UNIVERSITY OF SOUTHAMPTON

Resonant nano-electro-mechanical sensors for molecular mass-detection

by

Faezeh Arab Hassani

Thesis for the degree of Doctor of Philosophy

FACULTY OF PHYSICAL AND APPLIED SCIENCE
School of Electronics and Computer Science
Nano Research Group

Supervisors: Professor Hiroshi Mizuta
Dr. Yoshishige Tsuchiya

February 2012

UNIVERSITY OF SOUTHAMPTON

ABSTRACT

FACULTY OF PHYSICAL AND APPLIED SCIENCE
School of Electronics and Computer Science

Doctor of Philosophy

Resonant nano-electro-mechanical sensors for molecular mass-detection

by Faezeh Arab Hassani

This research is conducted as a part of EU FP7 project entitled NEMSIC (hybrid nano-electro-mechanical/integrated circuit systems for sensing and power management applications) with project partners, EPFL, TU Delft, IMEC-NL, CEA-LETI, SCIPROM, IMEC-BE, Honeywell Romania, and HiQSCREEN. Nano-electro-mechanical (NEM) sensors are getting an increased interest because of their compatibility with “In-IC” integration, low power consumption and high sensitivity to applied force, external damping or additional mass. Today, commercial biosensors are developed based on mass-detection and electro-mechanical principles. One of the recent commercial mass-detection biosensors is a quartz crystal microbalance (QCM) biosensor which achieves the mass sensitivity of a few tens pico g/Hz. The newly developed in-plane resonant NEM (IP R-NEM) sensor in this thesis achieves the mass sensitivity less than zepto g/Hz that is over nine orders smaller than that of the commercial QCM sensor using a much smaller sensing area compared to the QCM sensor. This fact will make the IP-RNEM sensor a world-unique sensor that shows a very high sensitivity to a very small change in mass. The stated mass sensitivity is achieved by modelling the functionalization and detection processes of the suspended beam. For modelling the linker molecules in the functionalization process, a conformal coating layer in different configurations are added to the suspended beam and the sparse distribution of target molecules in the detection process is modeled by changing the density of the coating layer. I would like to clarify that the scaling rule of the mass responsivity is given by k^4 regardless of the different functionalization configurations. I develop a completely new hybrid NEM-MOS simulation technology which combines three-dimensional finite element method (3D FEM) based NEM device-level simulation and circuit-level simulation for NEM-MOS hybrid circuits. The FEM device-level simulation module also includes new modelling of self-assembled monolayer for surface functionalization as well as adsorbed molecules to be detected and facilitates quantitative evaluation of mass responsivity of designed NEM sensor devices. The basic part of the sensor, the NEM structure, includes a suspended beam and two side electrodes and that is fabricated at the Southampton Nanofabrication Centre (SNC). The fabrication at SNC includes a new sensor that uses a free-free beam that improves the quality factor up to five orders of magnitude at room temperature and atmosphere based on the numerical results. The IP R-NEM sensor consists of a suspended beam that is integrated with an in-plane MOSFET and is fabricated by CEA-LETI. The monolithically integrated NEM with the MOSFET on the same SOI layer for the sensor is a real breakthrough which makes it a potential low-cost candidate among the mass-detection based sensors. With respect to the conducted radio-frequency (RF) characterization for nano-wire devices in collaboration with the Tokyo Institute of Technology and NEM structures, the designing of an RF contact pad to reduce the effect of parasitic frequencies and doing the measurement at high vacuum to reduce the motional resistance and increase the quality factor are necessary for the characterization of devices with nano-scale dimensions. The integrated MOSFET in the IP R-NEM sensor amplifies the output transmission signal from the resonating beam by its intrinsic gain. The fabricated sensors show a three orders of magnitude larger gain than that of the previously proposed resonant suspended gate FETs by biasing the MOSFET at the optimized voltage biases that are found based on the DC characterization of MOSFETs.

List of content

List of figures

List of tables

Declaration of authorship

I, Faezeh Arab Hassani, declare that the thesis entitled, “Resonant nano-electro-mechanical sensors for molecular mass-detection,” and the work presented in the thesis are both my own, and have been generated by me as the result of my own original research. I confirm that:

- this work was done wholly or mainly while in candidature for a research degree at this University;
- where any part of this thesis has previously been submitted for a degree or any other qualification at this University or any other institution, this has been clearly stated;
- where I have consulted the published work of others, this is always clearly attributed;
- where I have quoted from the work of others, the source is always given. With the exception of such quotations, this thesis is entirely my own work;
- I have acknowledged all main sources of help;
- where the thesis is based on work done by myself jointly with others, I have made clear exactly what was done by others and what I have contributed myself;
- parts of this work have been published in research journals. A list of publications is provided with this manuscript:

Signed: ……………………………………………………………………..

Date: ………………………………………………………………………..

Acknowledgement

My research was financially supported and conducted in European FP7 project NEMSIC (Hybrid nano-electro-mechanical/integrated circuit systems for sensing and power management applications).

I am sincerely and heartily grateful to my supervisors, Prof. Hiroshi Mizuta and Dr. Yoshishige Tsuchiya, for their support and guidance that they provided me throughout my PhD program and dissertation writing. I am sure it would have not been possible without their invaluable help, supervision and encouragement from the preliminary to the concluding level that empower me to develop an understanding of the subject.

I am truly thankful to the project and all of the partners, EPFL, TU Delft, IMEC-NL, CEA-LETI, SCIPROM, IMEC-BE, Honeywell Romania, and HiQSCREEN for their technical support throughout the project. I wish to thank Prof. Adrian Mihai Ionescu (project coordinator), Dr. Dimitrios Tsamados and Mr. Sebastian Bartsch for providing me with the opportunity to use their measurement facilities at the Nano Lab at EPFL, Dr. Eric Ollier and Dr. Cecilia Dupré from CEA-LETI for their help and effort on the layout design and fabrication of the sensor, Dr. Cornel. Cobianu from Honywell Romania for his technical discussions and Dr. Silvia Armini and Dr. Vladimir Cherman from IMEC-BE for their technical discussions and help on the functionalization of the sensor.

I am very obliged to all professors and colleagues in the Nano Research Group for the thoughtful discussions that I had with them about my research. I am grateful to Prof. Peter Ashburn for his permission to use the facilities at the Southampton Nano Fabrication Centre, Dr. Harold M. H. Chong for his thoughtful advice during the different steps of my PhD program, Dr. Martin D. Charlton for the training on the scanning electron microscope, Dr. Muhammad Khaled Husain for his continues help on the electron beam lithography, Dr. Kanad Mallik for the training on the radio-frequency probe station and ultra violet-ozone cleaning system and his help on the annealing furnaces, Dr. Ibrahim Sari for the training on the vapor hydrogen fluoride etcher, Mr. Feras M. Alkhalil for his help on the thinning down of the silicon-on-insulator wafers and annealing furnaces, Dr. Kai Sun for his help on the annealing furnaces, Dr. Mario Alberto Garcia Ramirez for his help on the focused ion beam, Mr. Marek E. Schmidt for the training on the rapid thermal annealing equipment and help on the focused ion beam, Dr. Ioannis Zeimpekis-Karakonstantinos for the training on the wirebonder, Mr. Yudong Wang for the training on the Lakeshore probe station, Mr. David Payne for the training on the atomic force microscopy, Mr. Mehdi Banakar for the training on the four-point prober, Dr. Xiaoli V. Li for the training on the DC probe station, Mr. Mohammad Adel Ghiass for his help on the DC probe station, Mr. Akhtar Rind for his help on the electron beam evaporator, and Dr. Zakaria Moktadir for his insightful discussions about my research. It is a pleasure to thank the cleanroom manager, Dr. Iain Anteney and all the technicians at the Southampton Nanofabrication Center who trained me on the different tools at the cleanroom, especially Dr. Kian S. Kiang for the photo-lithography and dicing saw, Dr. Owain Clark for the ellipsometry, profiler, reactive ion etching, plasma-enhanced chemical vapor deposition and wet room processing, Mr. Peter Ayliffe for the scanning electron microscope and the help on the electron beam lithography and Mr. James A. Farmer for the electron beam evaporator. I would also offer my regards to Mr. Richard S. Kean and Mr. Deniston F. Jack for their helps on my daily requests at the cleanroom and Mrs. Sally G. Lloyd for ordering the photo-lithography masks. I would also like to acknowledge the kind support of the group secretaries, Mrs. Glenys C. Howe and Mrs. Lucia Hewett.

I would like to thank to my parents and family who supported me throughout this process. They helped to boost my morale and provided me with great motivation through this challenging period of my life successfully. I believe that without their continuous love, I would have not been able to come to this stage.

Last but not least, I owe earnest thankfulness to my friends Mr. Seyed Hossein Ghotbi, Mrs. Jonali Das and Miss Sara Sadeghian who never stopped encouraging me to do my best.

List of abbreviations

AA	All-around
AFM	Atomic force microscopy
Al	Aluminium
APTES	Amino-propyltrimethoxysilane
Ar	Argon
BHF	Buffered hydrofluoric
BioMEMS	Biomedical or biological micro-electro-mechanical-systems
BOX	Buried oxide layer
CC	Clamped-clamped
CEA-LETI	Commissariat à l'Energie Atomique-Laboratoire d'Electronique et de Technologie de l'Information
Chem-FET	Chemical field-effect-transistor
CMOS	Complementary metal-oxide-semiconductor
CMP	Chemical-mechanical polishing/planarization
CNFET	Carbon nano-tube field-effect-transistor
DIBL	Drain-induced-barrier-lowering
DNA	Deoxyribonucleic acid
DRC	Design rules check
DUT	Device under test
EB	Electron beam
ECR	Electron cyclotron resonance
EPFL	École Polytechnique Fédérale de Lausanne
FEM	Finite element method
FF	Free-free
FGA	Forming-gas annealing
GOD	Glucose oxidase
GSG	Ground-signal-ground
HSQ	Hydrogen silsesquioxane
IMEC-BE	Interuniversitair Micro-Electronica Centrum-Belgium

IMOS	Impact ionization metal-oxide-semiconductor
IPA	Isopropyl alcohol
IP R-NEM	In-plane resonant nano-electro-mechanical
ISFET	Ion-sensitive field-effect-transistor
IUPAC	International union of pure and applied chemistry
JAIST	Japan Advanced Institute of Science and Technology
LCR	Inductance-capacitance-resistance
LOD	Limit of detection
LSW	Layer select window
MEMS/NEMS	Micro/nano-electro-mechanical-systems
MOS	Metal-oxide-semiconductor
NC-Si	Nano-crystalline-silicon
NWFET	Nano-wire field-effect-transistor
$\mathbf{N_2}$	Nitrogen
OSL	Open-short-load
OT	Only top
$\mathbf{O_2}$	Oxygen
PCR	Polymerase chain reaction
PD	Partially depleted
PSD	Phase sensitive detector
PECVD	Plasma-enhanced chemical vapor deposition
QCM	Quartz crystal microbalance
QCM-D	Quartz crystal microbalance with dissipation monitoring
redox	Reduction-oxidation
RF	Radio-frequency
RGT	Resonant gate transistor
RSG-FET	Resonant suspended gate field-effect-transistor
RSG-MOSFET	Resonant suspended gate metal-oxide-semiconductor field-effect-transistor
RIE	Reactive ion etching
RL	Return loss
SAM	Self-assembled monolayer
SAW	Surface acoustic wave

SEM	Scanning electron microscope
SET	Single electron transistor
SF_6	Sulfur hexafluoride
SG-FET	Suspended gate field-effect-transistor
SGSNM	Suspended gate silicon nano-dot memory
Si	Silicon
SiC	Silicon carbide
SiND	Silicon nano-dot
SMA	Sub-miniature version A
SNC	Southampton Nanofabrication Centre
SOC	System on chip
SOI	Silicon-on-insulator
SON	Silicon-on-nothing
STEM	Scanning transmission electron microscope
TB	Top-and-bottom
TIT	Tokyo Institute of Technology
UoS	University of Southampton
VB-FET	Vibrating body field-effect-transistor
VCO	Voltage controlled oscillator
WP	Work package
XeF_2	Xenon difluoride
2D/3D	Two/three-dimensional

List of symbols

$F \times Q$	Multiplication of the resonance frequency and quality factor
$V_{pi\_SG\text{-}MOSFET}$	Pull-in voltage of the gate for the RSG-FET
Δz	Deflection of the free end of the cantilever
$\Delta \sigma_1$	Change in the top surface stress
$\Delta \sigma_2$	Change in the bottom surface stress
Δm	Change of the mass
Δf	Change of the resonance frequency
f_0	Unloaded resonant frequency (for the cantilever)
f_1	Loaded resonant frequency (for the cantilever)
V_S	Volume of solution
x	Limit of detection (mol/L)
F_{elec}	Electro-static force
C_{gap}	Gap capacitance
C_{gap0}	Equilibrium gap capacitance
V	Applied voltage to the beam
V_{dc}	Applied DC voltage to the beam
A	Area ($l \times t$)
ε_0	Air permittivity
d_0, g	Initial gap
y	Displacement
V_{ac}	Applied AC voltage to the beam or electrode
V_G, V_g	Applied gate voltage
V_{Gint}	Divided gate voltage
C_{gc}	Gate-to-channel capacitance
C_{ox}	Oxide capacitance
C'_{ox}	Oxide capacitance per unit area
C_d	Depletion capacitance
C_{inv}	Inversion capacitance
U_{tot}	Total energy stored between two conductive plates

U_{elec}	Electro-static energy
U_{meca}	Mechanical energy
k	Gate rigidity
W_{beam}	Width of the gate
L_{beam}	Length of the gate
f_r	Resonant peak
f_a	Anti-resonant peak
L_x	Inductor
C_x	Capacitor
R_x	Resistor (motional resistance)
m	Mass
k	Spring
γ	Damper
$S_{11}, S_{12}, S_{21}, S_{22}$	S-parameters
Z_0	Characteristic impedance
Z_L	50 Ω-load
Z_S	Impedance of source
Γ_{in}	Input reflection coefficient
Γ_{out}	Output reflection coefficient
Z_{in}	Input impedance at port 1
R	Real part of Z_{in}
X	Imaginary part of Z_{in}
RL	Return loss
Z_{out}	Output impedance at port 2
E	Time harmonic voltage
V_1, V_2	Vector voltmeter
Z_x	Impedance of a device under test
V_{PSD}	Phase sensitive detector output
V_{ref}	External reference signal
ω_0	Signal frequency
θ_0	Signal phase
ω_L	Reference signal frequency
θ_L	Reference signal phase

G_{ac}	Gain of the AC signal amplifier
G_{dc}	Gain of the DC signal amplifier
V_{output}	DC output voltage of the lock-in amplifier
S_{11}	Reflection signal
S_{21}	Transmission signal
$P_{reflected}$	Power of a reflected signal
$V_{reflected}$	Voltage of a reflected signal
P_{in}	Power of an input signal
V_{in}	Voltage of an input signal
P_{out}	Power of a transmitted signal
V_{out}	Voltage of a transmitted signal
g_m	Transconductance
r_0	Output impedance of an MOSFET
n	Number of resonance mode for a resonator
β_n	nth mode constant
E	Young’s modulus
ρ	Density
w	Width of the beam
l	Length of the beam
t	Thickness of the beam
f_n	Mechanical resonance frequency of the nth mode
f_0	Mechanical resonance frequency of the first in-plane mode (for the beam and nano-wire)
m_b	Effective mass
k_b	Effective spring stiffness
k_{bm}	Mechanical spring stiffness
k_{be}	Electrical spring stiffness
f_r	Resonance frequency
V_P	Pull-in voltage for the beam
α	Damping factor
Q_{Total}	Total quality factor
W_{Total}	Total energy stored in the system
ΔW_{Loss}	Energy dissipated or lost per cycle of vibration

Q_{Air}	Gas damping
Q_{Anchor}	Anchor damping
$Q_{Material}$	Material loss
$Q_{Thermoelastic}$	Thermoelastic damping
$Q_{Anchor\text{-}phonon}$	Phonon-tunnelling anchor loss
b	Gas damping factor
μ	Viscosity
μ_0	Air viscosity
c	Spring factor
ω_c	Cut off frequency
K_n	Knudsen number
P_0	Operating pressure
P_{atm}	Atmosphere pressure
P_n	A known pressure
λ_0	Air mean-free path
λ_{atm}	Atmosphere mean-free path
λ_n	Mean-free path at P_n
l_T	Mean-free path of the thermal phonon
v	Phonon velocity
T	Operating temperature
C	Heat capacity
α'	Thermal expansion
χ	Thermal diffusivity
τ	Relaxation time
ϑ	Poisson’s ratio
X_n	nth mode shape factor
w_S	Width of the support beam
l_S	Length of the support beam
t_{top}	Thickness of the top coating layer in the top-and-bottom and only top configurations
t_{bottom}	Thickness of the bottom coating layer in the top-and-bottom configuration
t_a	Thickness of the coating layer in the all-around configuration
$k_{bm\text{-}TB}$	Mechanical spring stiffness for the beam with the coating layer in the top-

	and-bottom configuration
$m_{bm\text{-}TB}$	Effective mass for the beam with the coating layer in the top-and-bottom configuration
$k_{bm\text{-}AA}$	Mechanical spring stiffness for the beam with the coating layer in the all-around configuration
$m_{bm\text{-}AA}$	Effective mass for the beam with the coating layer in the all-around configuration
$\Delta m_{bl}/m_b$	Changing rate of the effective mass
Δm_{bl}	Change of the effective mass due to linker molecules
$\Delta k_{bml}/k_{bm}$	Changing rate of the mechanical spring stiffness
Δk_{bml}	Change of the mechanical spring stiffness due to linker molecules
S	Mass responsivity
Δm_{ba}	Changes of the mass due to adsorbed molecules
Δf_{BW}	Maximum allowable measurement bandwidth
DR	Effective dynamic range to the resonator
E_C	Maximum drive energy
k_B	Boltzmann constant
k	Scaling factor
l_C	Length of the MOSFET channel
l_S	Length of source
l_D	Length of drain
g_S	Side gap
ρ'	Resistivity
A'	Area ($w \times t$)
V_t	Threshold voltage
V_{FB}	Flat band voltage
φ_p	Substrate potential
ε_s	Electron permittivity
q	Electron charge
N_A	Substrate doping for the MOSFET
V_d	Drain voltage

List of publications

Journals

- F. A. Hassani, C. Cobianu, S. Armini, V. Petrescu, P. Merken, D. Tsamados, A. M. Ionescu, Y. Tsuchiya, and H. Mizuta, “Numerical analysis of zeptogram/Hz-level mass responsivity for in-plane resonant nano-electro-mechanical sensors,” *Microelectron. Eng.*, vol. 88, no. 9, pp. 2879-2884, 2011.
- C. Cobianu, B. Serban, V. Petrescu, J. Pettine, D. Karabacak, P. Offerman, S. Brongesma, V. Cherman, S. Armini, F. A. Hassani, M. A. Ghiass, Y. Tsuchiya, H. Mizuta, C. Durpe, L. Duraffourg, A. Koumela, D. Mercier, E. Ollier, D. Tsamados, and A M. Ionescu, “Towards nano-scale resonant gas sensors,” *Annals of the Academy of Romanian Scientists, Series on Science and Technology of Information*, vol. 3, no. 2, pp. 39-60, 2010.

Conferences

- H. Mizuta, J. Ogi, B. Pruvost, M. A. Ghiass, N. Kalhor, F. A. Hassani, M.A.G. Ramirez, Z. Moktadir, Y. Tsuchiya, C. Dupré, and E. Ollier, “Single-electron devices fused with nanoelectromechanical Systems (NEMS) (Invited talk),” *BIT’s First World Congress on NANO-S&T*, Dalian, 2011.
- H. Mizuta, F. A. Hassani, M. A. Ghiass, Y. Tsuchiya, S. Armini, T. Delande, J. Loyo Prado, V. Cherman, C. Dupre, and E. Ollier, “Silicon nanowires for advanced sensing: electrical and electromechanical characteristics and functionalisation technology (Invited talk),” *G-COE PICE Int. Symp. and IEEE EDS Minicolloq. Advanced Hybrid Nano Devices*, Tokyo, 2011.
- H. Mizuta, F. A. Hassani, M. A. Ghiass, Y. Tsuchiya, S. Armini, T. Delande, J. Loyo Prado, V. Cherman, C. Dupre, and E. Ollier, “Silicon nanowires for advanced sensing: Electrical and electromechanical characteristics and functionalisation technology (poster),” *G-COE PICE Int. Symp. and IEEE EDS Minicolloq. Advanced Hybrid Nano Devices*, Tokyo, 2011.

- H. Mizuta, M. Garcia Ramirez, F. A. Hassani, M. A. Ghiass, N. Kalhor, Z. Moktadir, Y. Tsuchiya, S. Sawai, J. Ogi, and S. Oda, “Scaled silicon nanoelectromechanical (NEM) hybrid systems (Invited talk),” *Int. Conf. Solid-State and Integrated Circuit Technology*, Shanghai, 2010.
- F. A. Hassani, Y. Tsuchiya, and H. Mizuta, “Design and analysis of a resonant nano-electro-mechanical sensor for molecular mass-detection (poster),” *Int. Symp. Atom-scale Silicon Hybrid Nanotechnologies for ‘More-than-Moore’ and ‘Beyond CMOS*, Southampton, UK, 2010 (unpublished).
- C. Cobianu, B. Serban, M. Mihaila, V. Dumitru, F. A. Hassani, Y. Tsuchiya, H. Mizuta, V. Cherman, , I. De Wolf, V. Petrescu, J. Santana, C. Dupre, E. Ollier, , T. Ernst, , P. Andreucci, L. Duraffourg, D. Tsamados, and A. M. Ionescu, “Nano-scale resonant sensors for gas and bio detection: expectations and challenges”, *Proc. 32nd Int. Semiconductor Conference,* 2009, pp. 259-262.
- F. A. Hassani, C. Cobianu, S. Armini, V. Petrescu, P. Merken, D. Tsamados, A. M. Ionescu, Y. Tsuchiya, and H. Mizuta, “Design and analysis of an in-plane resonant nano-electro-mechanical sensor for sub-attogram-level molecular mass-detection”, *Proc. Int. Conf. Solid State Devices and Materials*, Sendai, 2009.
- H. Mizuta, M. A. G. Ramirez, F. A. Hassani, M. A. Ghiass, Y. Tsuchiya, T. Nagami, B. Pruvost, J. Ogi, S. Sawai, and S. Oda, “Multi-scale simulation of hybrid silicon nano-electromechanical (NEM) information devices”, *8th Int. Conf. on Global Research and Education Inter-Academia,* 2009.

To my parents and family

for their love, support and encouragement

CHAPTER 1

Introduction

The development of future intelligent systems will be achieved by co-integrating solid-state semiconductor micro/nano- and micro/nano-mechanical devices [1]. System on chip (SOC) approach enables integration of micro-electro-mechanical systems (MEMS) and integrated circuit (IC) in vertical or horizontal architectures [2]. Vertical integration is used for the substrate-level integration, the interconnection level, the above-IC level or the module level. Horizontal integration allows integration of MEMS and IC on the same surface monolithically. The silicon-on-insulator (SOI) technology offers the ability to provide horizontal integration [2],[3]. By integrating nano-electro-mechanical-systems (NEMS) and IC, the cost of NEMS will continue to decrease [4]. Moreover, NEMS-IC devices show good performances because of the small distance between NEMS and IC that allows them to suppress a lot of the parasitic effects [2],[4]. Figure 1.1 shows an example of recent attempts of shrinking MEMS dimensions to nano-scale using SOI technology.

There are three main research domains for micro/nano-electronics that include: i) More Moore, ii) More than Moore and iii) Beyond CMOS (complementary metal-oxide-semiconductor) as shown in Fig. 1.2. More than Moore includes nano-technology hybridization with other platforms. Wearable and implantable systems, environmental monitoring associated to ambient intelligence and ultra-low power sensors are benefits of More than Moore platform. NEMS-IC integration was addressed in the ‘More than Moore’ era [5]. The fusion of NEMS and nano-CMOS provides three types of applications including: switch, memory and sensor.

- *Switch*: Scaling has played an important role in the improvement of performance and device density by doubling roughly every 18 months as per Moore’s law [6]. The scaling trend also causes an increase in the power dissipation that affects the device performance. As long as the sub-threshold leakage is becoming the dominant factor of power dissipation, massive efforts were made to find an alternative for CMOS technology [6-11]. Figure 1.3 shows the progress of emerged structures such as carbon nano-tube field-effect-transistors (CNFETs), nano-wire FETs (NWFETs), impact ionization MOSs (IMOSs) and NEM devices as suspended gate FETs (SG-FETs) that were used for switching applications [6]. These structures show subthreshold slopes less than 60 mV/decade that is the lowest achieved subthreshold slope by conventional MOSFETs. With respect to Fig. 1.3, NEM structure is considered as an alternative for CMOS technology because they gain the lowest subthreshold slopes among other emerged structures. Although NEM devices have extremely low OFF-current, a NEM device does not have as high ON current as CMOS transistors [6]. So, introduction of NEMS into conventional MOSFETs provides a very abrupt switch with superb performance and numerous new functionalities that have not been achieved using present devices [12-14].
- *Memory*: A flash memory plays an important role in the non-volatile memory market. The current scalability issue is challenging the conventional floating-gate memory technology in use for the flash memory. A new non-volatile memory concept based on bistable operation of the NEM structure combined with nano-crystalline-silicon (NC-Si) dots was proposed as an alternative for an extremely fast and non-volatile memory [15-17]. Another competitive candidate for a scalable non-volatile memory is the suspended gate silicon nano-dot memory (SGSNM) that was proposed due to the co-integration of NEMS, silicon nano-dots (SiNDs) and MOSFETs [18].
- *Sensor*: NEM sensors have attracted an increasing interest as a new technology because they not only offer compatibility with “In-IC” integration but also provide other specific advantages such as ultra miniature size elements, low power consumption, potential high resonance frequencies and quality factors, fast response time, high sensitivity to applied force, external damping or additional mass [5],[19-27]. Current research has started to focus on great efforts needed to improve the available technology and functionality limits of smart nano-systems of sensing in the ‘More than Moore’ era [28]. To present the NEM sensors that sense the molecules

with higher sensitivity compared to conventional sensors, the NEM structure was integrated with a MOSFET in order to improve its functionalities and use the capabilities of the MOSFET [29-31].

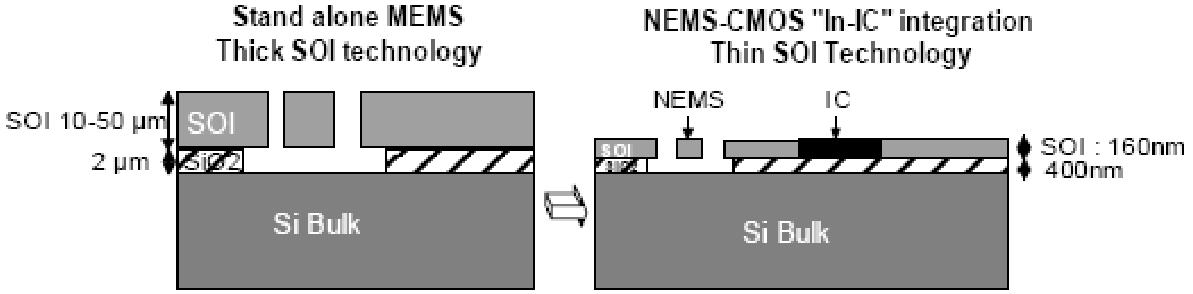

Fig. 1.1 From MEM to NEM devices on thin SOI substrate [2]

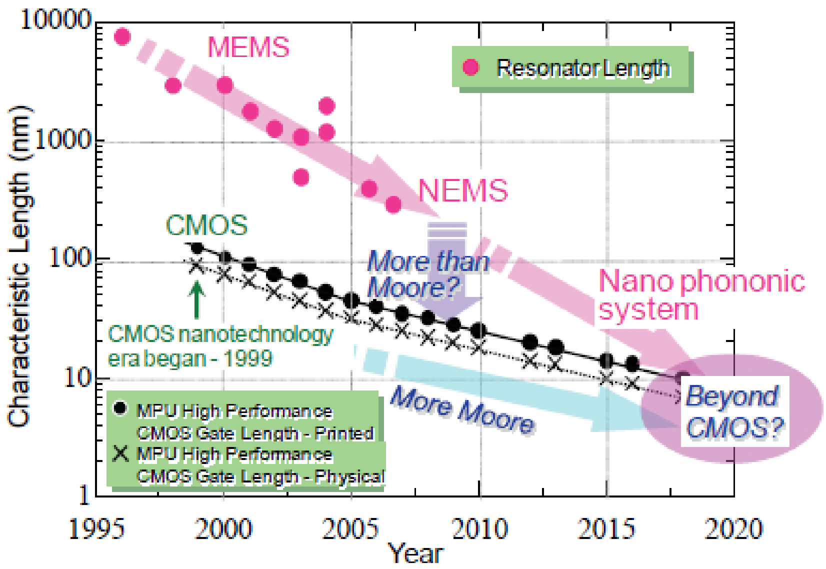

Fig. 1.2 Research domains for micro/nano-electronics [5]

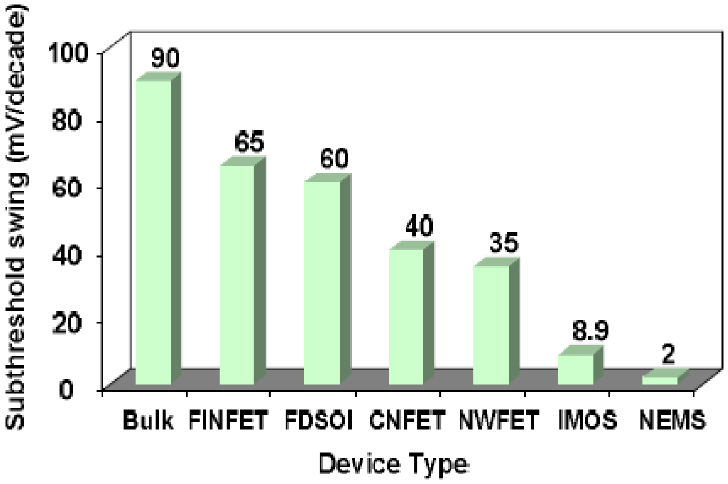

Fig. 1.3 Minimum subthreshold swings reported for advanced MOSFETs and other emerging devices [6]

1.1 Motivation and scope of the thesis

The current research project was a part of European FP7 NEMSIC (Hybrid nano-electro-mechanical/integrated circuit systems for sensing and power management applications) project [32] that included different work packages for sensing and power management applications of NEM devices. The NEMSIC research map is shown in Fig. 1.4. Designing and realizing multi-terminal resonant NEM devices, such as in-plane resonant NEM (IP R-NEM) sensor was the defined work package 1 (WP1) for the University of Southampton (UoS) as the leader of WP1. The resonant sensors are based on mass-detection principle and are sensitive to extremely small perturbations such as mobile gate mass loading or environment damping (in both gases and fluids). It is obvious that various applications in sensing [33-36] based on such resonant-gate FET necessitate the adaptation of functionalization of the mobile gate or the gate dielectric in order to attach the chemical or biological species that could be detected in order to generate an equivalent mass-loading (resulting in NEM resonance frequency shift) or damping (resulting in modification of the NEM quality factor at resonance).

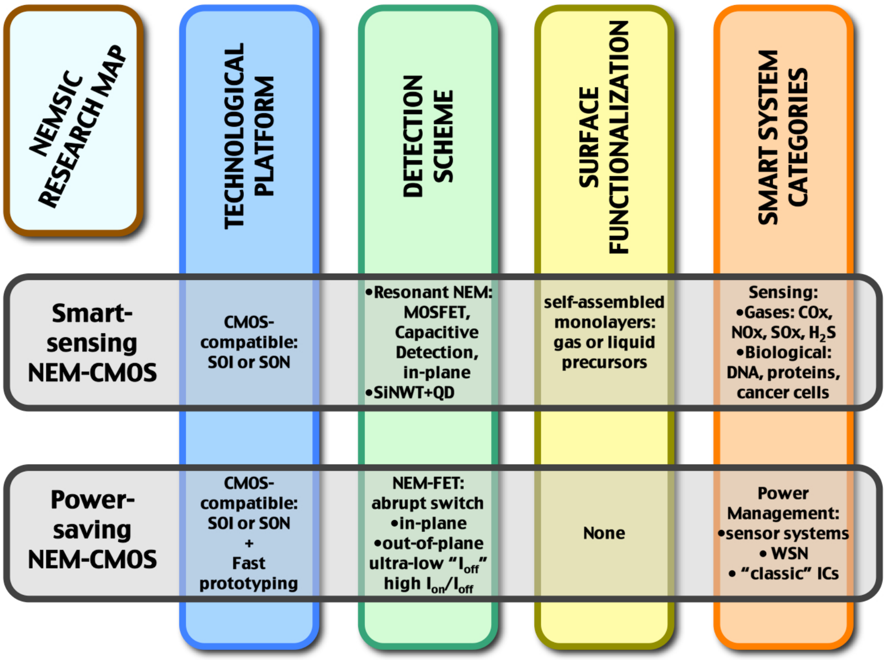

Fig. 1.4 The NEMSIC research map [32]

This thesis focused on the study of the IP R-NEM sensor as defined in WP1. This is a mass-detection based sensor that is used both in the biological and chemical-detection applications. This study started with the development of the sensor with a much higher sensitivity than that of the current commercial quartz crystal microbalance (QCM) mass-detection based biosensor. Figure 1.5 (a) shows the NEM structure that consists of a clamped-clamped (CC) suspended beam which has an in-plane movement. With respect to the advantages of NEMS-IC integration, the suspended beam is integrated with a MOSFET on the same SOI layer, the IP R-NEM sensor, which is shown in Fig. 1.5 (b) and is a real breakthrough which avoids unwanted parasitics associated with interconnects between MEMS and CMOS modules in the conventional CMOS-MEMS integration on the same platform. Moreover, the small footprint of the sensor makes it a potential low-cost candidate among the mass-detection based sensors. After doing the design of the NEM structure and the IP R-NEM sensor, the fabrication of the designed IP R-NEM sensor was done at the Commissariat à l'Energie Atomique-Laboratoire d'Electronique et de Technologie de l'Information (CEA-LETI) as a part of NEMSIC project and further characterization on the fabricated sensors was done at UoS. Apart from the defined tasks in WP1 for UoS, the fabrication and characterization of the NEM structure were also done at UoS as a part of my research project during the allocated fabrication time for CEA-LETI. Meanwhile, I also did some experimental measurements on the received non-suspended nano-wires (NWs) that were provided in collaboration with the Tokyo Institute of Technology (TIT). Non-suspended NWs were suspended and further characterization was done for them.

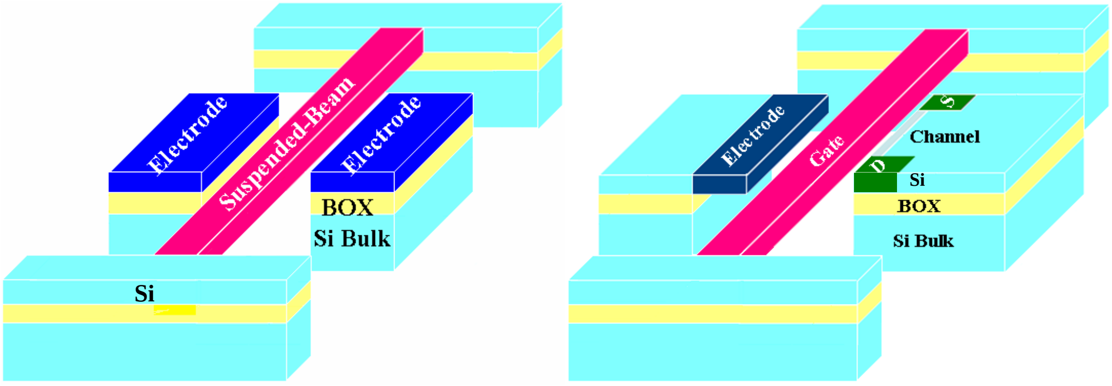

(a) (b)

Fig. 1.5 (a) The NEM structure and (b) the IP R-NEM sensor

1.2 Organization of the thesis

Chapter 2 provides an overview of the recent NEMS-IC functional devices that work as switch, memory and sensor. As to the biological application for the developed sensor in this thesis, I will also provide an overview on the available biosensors specially QCM biosensors that can be potential competitors to the IP R-NEM sensor. After that, the modelling and characterization of a resonant suspended gate FET (RSG-FET) that shows an out-of-plane movement with different applications for MEMS resonator, switch and memory are studied as a good example of the previously proposed suspended gate devices that are similar to the operation of the developed IP R-NEM sensor. Radio-frequency (RF) characterization methods and measurement setups are studied in this chapter for the resonant devices.

Chapter 3 shows the design and modelling of the NEM structure and the IP R- NEM sensor. Based on the analytical and numerical results of the developed sensor, I will study an alternative structure called free-free (FF) NEM structure that improves the quality factor of the previously introduced CC NEM structure. The IP R-NEM sensor is used as a resonant sensor to detect adsorbed target molecules after the functionalization of the resonator's surface. The functionalization process is modelled by adding a continuous coating layer on the beam and the detection process is modelled by changing the density of the coating layer. Different possible configurations for the coating layer are studied and the mass responsivity, scalability and limit of detection of the sensor are investigated.

In chapter 4, the post-processing for the provided NWs from TIT is discussed. Then the mask layout design and fabrication process for the NEM structure fabricated at the Southampton Nanofabrication Centre (SNC) and the IP R-NEM sensor fabricated at CEA-LETI are shown. The fabrication at SNC includes the FF NEM structure as well as the NEM structure.

In chapter 5, DC and RF characterizations of non-suspended and then suspended NWs are conducted that give me a good guideline for the characterization of NEM structures and IP R-NEM sensors. After that the DC characterization of NEM structures are done followed by their RF characterization. Finally, the DC characterization and optimization of the applied DC bias voltages to IP R-NEM sensors are done for the subsequent RF measurement. I perform some simulations for the fabricated IP R-NEM sensors to investigate their measured DC characteristics in more details. The summary and future plans of my research are given in chapter 6.

CHAPTER 2

Introduction to hybrid NEMS-IC devices and modern biosensors

Complementary metal-oxide-semiconductor (CMOS) technology has been facing difficulties due to its scaling issues that caused a great deal of interest to the micro/nano-electro-mechanical system (MEMS/NEMS) that is a promising technology today. These technologies had their own drawbacks and their integration together provided us with the benefits of both technologies that paved the way towards a scalable technology. In this chapter, an overview is first given on the recently proposed NEMS-integrated circuit (NEMS-IC) functional devices with different applications for switches, memories and sensors. The proposed in-plane NEM (IP R-NEM) sensor in this thesis is used for biological-detection applications. For this reason, the operation of a biosensor is first explained and then a comparison on the limit of detection (LOD) for various biosensors is given. The LOD for the IP R-NEM sensor will be calculated in the next chapter in comparison with the equivalent values for these biosensors. The IP R-NEM sensor is a mass-detection based sensor that can be compared to the various recent commercial mass-detection based quartz crystal microbalance (QCM) biosensors. So the operation of the QCM biosensor and its related mass responsivity and LOD are described for further comparison in the next chapter. The previously proposed resonant suspended gate field-effect-transistor (RSG-FET) is also studied here. The possible characterization methods and measurement setups for the RSG-FET and other resonant devices are investigated to provide us with a good guideline for the future characterization of the IP R-NEM sensor that has basically a similar operation to the RSG-FET.

2.1 NEMS-IC functional devices

C. Durand et. al gave an overview of the state-of-the-art micro/nano electro-mechanical resonators in Table 2.1, that is a very important component needed to integrate the frequency reference oscillator in chips [37]. There are different types of resonators that include vibrating beam, longitudinal beam, bulk square extensional plate, elliptic or contour mode disk, rings, solid dielectric capacitive gap resonator and bulk mode beam that are shown in Table 2.1. These resonators in Table 2.1 show various resonance frequencies that make the devices hard to compare. For this reason, the multiplication factor of the resonance frequency and quality factor, $F \times Q$, were used to compare the resonators. The quartz $F \times Q$ factor is 9×10^6 that shows the possibility of replacing quartz oscillators with the current resonators in Table 2.1 by taking advantage of their integrability on the chip.

Nano-beam resonators are considered as an important building block of NEMS. These resonators use the shift of the resonance frequency for example to detect the mass changes [38-45]. X. Han et. al [19] fabricated a clamped-clamped (CC) nano-beam resonator for the mass-detection application that was actuated by lateral electro-static force. Figures 2.1 (a) and 2.1 (b) show the schematic view and the scanning electron microscope (SEM) image of the nano-beam resonator made of poly-silicon, respectively. They showed that the resonance testing of NEM structures was always a bottleneck in this area, and for this reason they introduced a lumped parameter method to analyze the dynamic characterization of the system before observing the resonance frequency of the beam using a capacitance detection circuit. The displacement of the nano-beam is in the nanometre range (nearly 10-20 nm for the beam, 1-5 nm for the disk) thus making it difficult to detect using capacitive detection technique. Due to this fact, the necessity of integration of the NEM structure with IC technology is obvious [37] and it has attracted the attention of a number of researchers as in the following explanations.

N. Abelé [46],[47] proposed the RSG-FET that is a hybridization of a mechanical vibrating structure and a MOSFET. When the applied voltage to the suspended gate is less than the pull-in voltage, $V_{pi\_RSG\text{-}FET}$, of the gate, the MOSFET is OFF and then turned ON for the voltages larger than $V_{pi\_RSG\text{-}FET}$. The RSG-FET has the advantages of a high mechanical quality factor, the transistor intrinsic gain and ultra low-power that make this structure a candidate in quasi-static for MEMS switch and memory applications, and in dynamic for resonator application [6],[46-48]. Detailed description of this structure is shown later in this chapter. The cross-section of the n-channel silicon-on-insulator (SOI) RSG-FET that consists of a metal membrane MEMS switch and a partially depleted (PD) SOI MOSFET is shown in Fig. 2.2 (a). Figure 2.2 (b) shows the simplified equivalent electrical circuit for the RSG-FET that includes a MOSFET and a variable capacitance that is defined by the gap between the suspended gate and MOSFET channel.

Table 2.1 Electro-mechanical state-of-the-art resonators [37]

Resonator	Mode	Frequency	SEM view	Techno and material	Performances
Out of plane CC Beam (Bannon et al. 2000)	Flexion	$f_R = 1.03K\sqrt{\frac{E}{\rho}}\frac{h}{L^2}(1-g(V_P))^P$	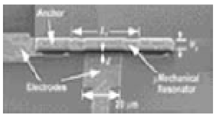	Surface technology Si substrate polySi resonator	f_R = 92.2 MHz Q = 7,450(vaccum) -12 ppm/°C R_m = 167 kΩ $F \times Q = 0.69 \times 10^6$
FF Beam (Koskenvuori et al. 2002)	Longitudinal	$f_R = \frac{0.76k_0x^3}{\omega^2}$	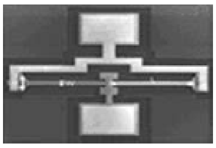	DRIE SOI substrate Si resonator	f_R = 13.1 MHz Q = 170,000(vaccum) Q = 2,000(air) R_m = 1.05 MΩ $F \times Q = 2.23 \times 10^6$
Plaque (Kaajakari et al. 2003)	Bulk square extensional	$f_R = \frac{1}{2L}\sqrt{\frac{Y_{2D}}{\rho}}$	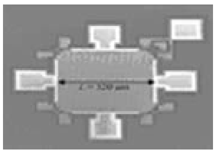	DRIE SOI substrate Si resonator	f_R = 13.1 MHz Q = 130,000 R_m = 4.47 kΩ $F \times Q = 1.70 \times 10^6$
Disk (Pourkamali et al. 2004)	Bulk elliptical	$f_R = \frac{k}{2\ \pi\ R}\sqrt{\frac{E}{\rho(1-\upsilon)^2}}$	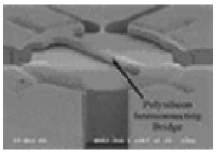	HARPSS SOI substrate Si resonator	f_R = 149.3 MHz Q = 45,700(vaccum) Q = 25,900(air) R_m = 91.2 kΩ $F \times Q = 6.82 \times 10^6$
Disk (Jing et al. 2004)	Bulk radial contour	$f_R = \frac{\alpha}{R}\sqrt{\frac{E}{\rho}}$	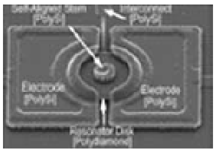	RIE Si substrate Diamond resonator	f_R = 1.51 GHz Q = 11,500(vaccum) Q = 10,000(air) -12.7 ppm/°C R_m = 1.22 MΩ $F \times Q = 17.37 \times 10^6$
Ring (Sheng-Shian et al. 2004)	Bulk contour	$L_S = \frac{n\sqrt{E/\rho}}{4f_R}$	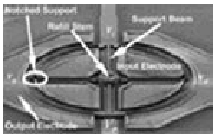	Surface technology Si substrate poly Si resonator	f_R = 1.2GHz Q = 15,000(vaccum) R_m = 282 kW $F \times Q = 18 \times 10^6$
Disk (Yu-Wei et al. 2005)	Solid dielectric capacitive gap		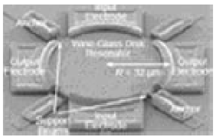	Surface technology poly Si resonator SiN gap	f_R = 164.4 MHz Q = 20,200(vaccum) R_m = 4.99 kΩ $F \times Q = 3.32 \times 10^6$
In plane CC Beam (Ayazi et al. 2006)	Bulk	$f_n = \frac{n}{2W}\sqrt{\frac{E}{\rho}}$	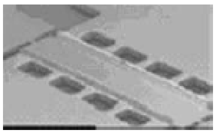	HARPSS SOI substrate Si resonator	f_R = 764.5 MHz Q = 17,300(vaccum) R_m = 23.7 kΩ $F \times Q = 13.23 \times 10^6$

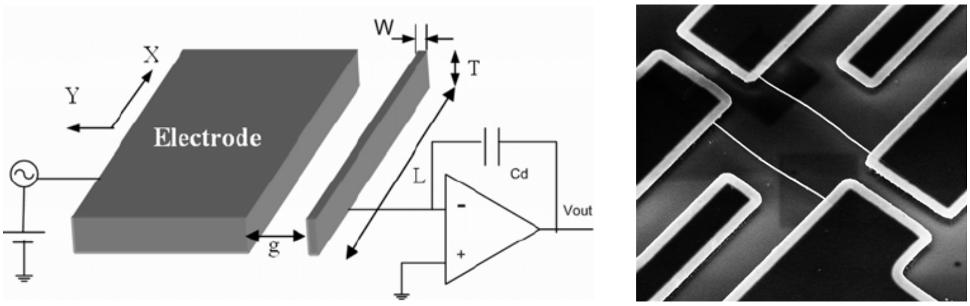

(a) (b)

Fig. 2.1 (a) A schematic view and (b) the SEM image of the nano-beam resonator made of poly-silicon [19]

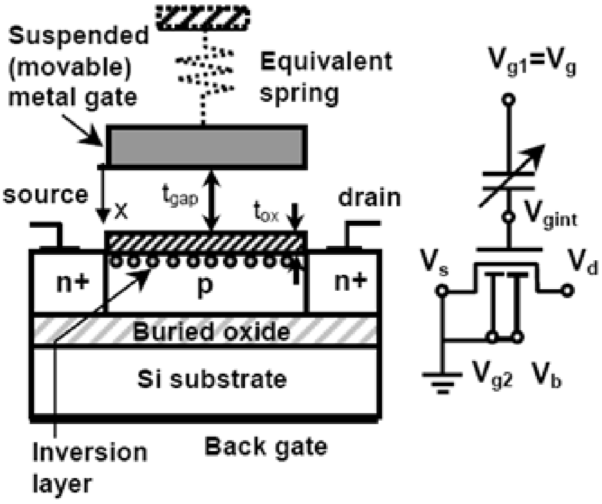

(a) (b)

Fig. 2.2 (a) The cross-section of the n-channel SOI SG-FET and (b) its simplified electrical equivalent circuit [19]

Integration of a NEMS beam and single electron transistors (SET) was studied using three-dimensional (3D) calculation and analytical modelling by B. Pruvost et. al [13]. Figure 2.3 (a) presents the integrated NEMS beam and SET that was simulated with a multi-physics modelling and simulation software, COMSOL [49]. By tuning the suspended gate capacitance of the SET, the periodicity and the level of the current is changed. Moreover, NEMS-gate architectures improves the behaviour of the conventional SETs with new functionalities such as threshold gate behaviour or abrupt current switching, and in general, further control of the device's behaviour [13]. Y. A. Pashkin et. al proposed a suspended Al-based SET that the island resonates freely between the defined drain and source on the clamps as shown in Fig. 2.3 (b). This improved the capability of detecting the motion of a mechanical resonator within the quantum limit [50]. In Fig. 2.3 (b), a bottom gate with a larger capacitance to the SET island is placed underneath to increase the SET coupling to mechanical motion.

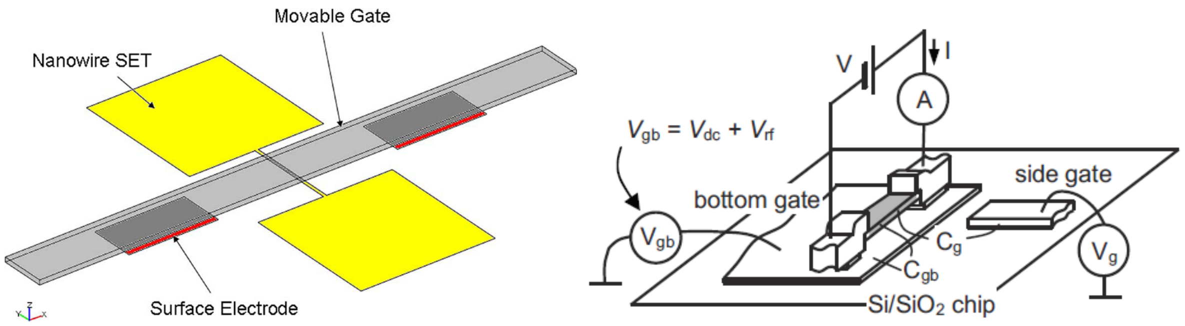

(a) (b)

Fig. 2.3 (a) The 3D simulation of an integrated NEMS beam with a SET using COMSOL [13], (b) schematics of the suspended SET and measurement circuit [50]

Y. Tsuchiya et. al [16] proposed a silicon NEM non-volatile memory that consists of a suspended floating gate beam in the cavity under the gate electrode, which contains the nano-crystalline-silicon (NC-Si) dots as charge storage. Figure 2.4 (a) shows the schematic of the NEM memory. The floating gate is bent naturally, either upward or downward. When the gate voltage is applied, the floating gate beam moves via electro-static interactions between the gate electrode and the charge in the NC-Si dots. A positional displacement of the floating gate may be sensed via a change in the drain current of the MOSFET underneath. The bistable nature of the NEMS beam causes the possibility of proposing a high speed non-volatile memory device with the operation speed of several GHz or higher [16]. Another new suspended gate silicon nano-dot memory (SGSNM) was proposed by co-integrating NEMS, silicon nano-dots (SiNDs), and MOSFETs by M. A. Garcia-Ramirez et. al [18],[51]. Figure 2.4 (b) shows a schematic of the SGSNM, which consists of a MOSFET as readout, SiNDs as a floating-gate (FG), and a movable suspended gate isolated from the FG by an air gap and a thin oxide layer. The advantages of the SGSNM cell include high speed programming/erasing operations, no gate leakage current and a serious non-volatility [18].

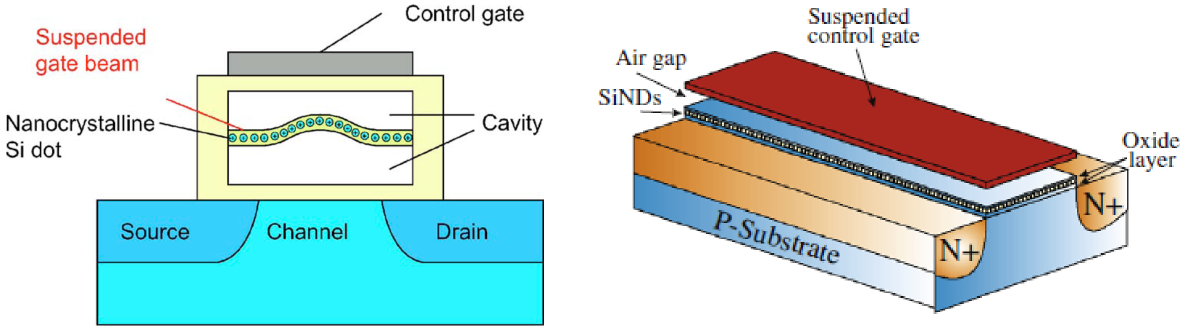

(a) (b)

Fig. 2.4 (a) The schematic of the silicon NEM non-volatile memory device incorporating NC-Si dots [16], (b) the schematic of the SGSNM [18]

Using the resonant NEM structures as sensors and integrating them with MOSFETs enable us to provide a wider range of functionality [29],[52]. E. Colinet et. al developed an in-plane SG-FET compatible with a front-end CMOS using the silicon-on-nothing (SON) technology and compared two capacitive and MOSFET detection methods for the SG-FET [52]. The SEM view of their developed lateral SG-FET is shown in Fig. 2.5. The integration of SG-FETs in MOS front-end enables the realization of more sophisticated system-on-chip architectures, including NEMS-based oscillators, low power switches and sensors [52].

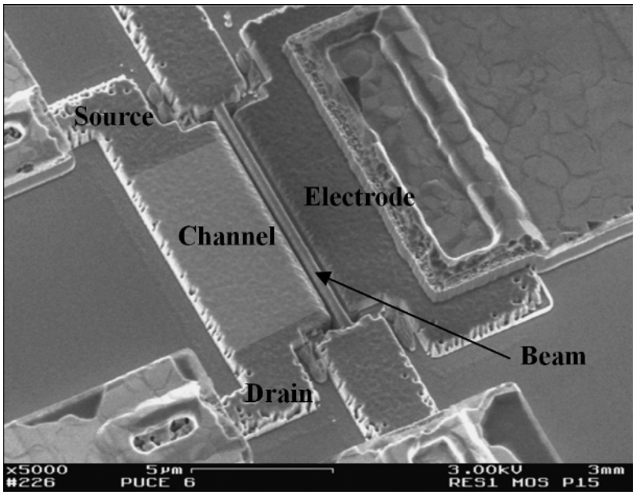

Fig. 2.5 The SEM view of the lateral SG-FET [52]

2.2 Biosensors

The growing market of molecular diagnostics motivates us to use new devices for biosensing procedures [53]. For this reason, biomedical or biological MEMS (BioMEMS) show a great interest among the researchers with a wide variety of important biomedical applications [54],[55]. BioMEMS cover a range of applications from diagnostics, such as Deoxyribonucleic acid (DNA) and protein micro-arrays, to micro-fluidics, surface modification, systems for drug delivery, etc. [56]. Figure 2.6 shows the resulting research areas on the integration of micro/nano-technology and biomedical sciences. The focus of this thesis is on the sensing application of NEMS-IC devices, and the proposed NEM sensor is used especially for the mass-detection based biological applications. This section first presents a brief review of various biosensors and BioMEMS sensors and compares their LOD. A particular attention is paid to the QCM biosensor as a commercialized mass-detection based biosensor.

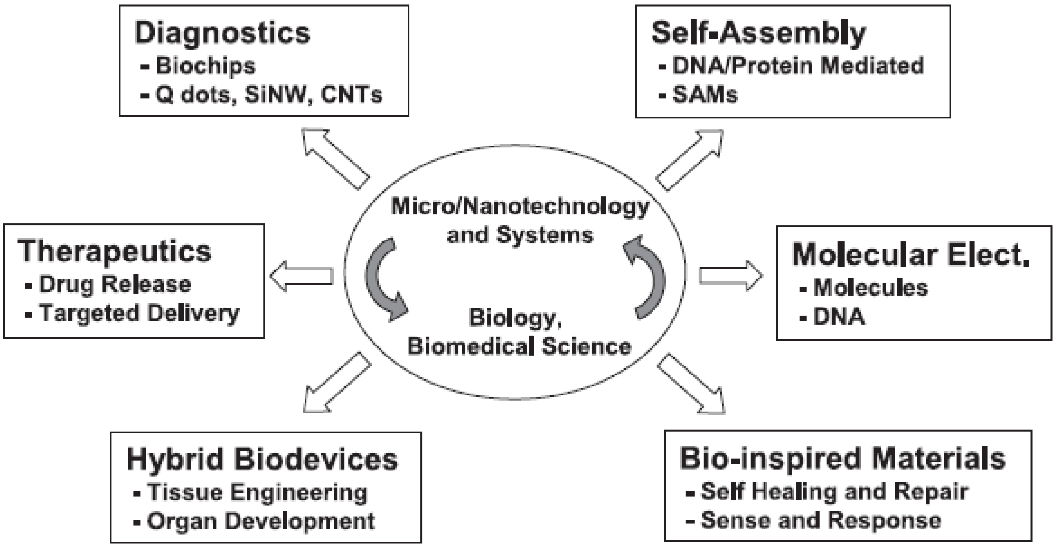

Fig. 2.6 The related research areas to the integration of micro/nano-technology and biomedical sciences [54]

In 1999, international union of pure and applied chemistry (IUPAC) proposed a definition of a biosensor [57]. They defined it: “a biosensor is a self-contained integrated device which is capable of providing specific quantitative or semi-quantitative analytical information using a biological recognition element (biochemical receptor) which is in direct contact with a transducer element”. A schematic of a biosensor is shown in Fig. 2.7. A biosensor consists of biochemical receptors and transducer as shown in Fig. 2.7. The biochemical receptor specifically reacts or interacts with the analyte of interest resulting in a detectable chemical or physical change that is used for the subsequent measurement [58].

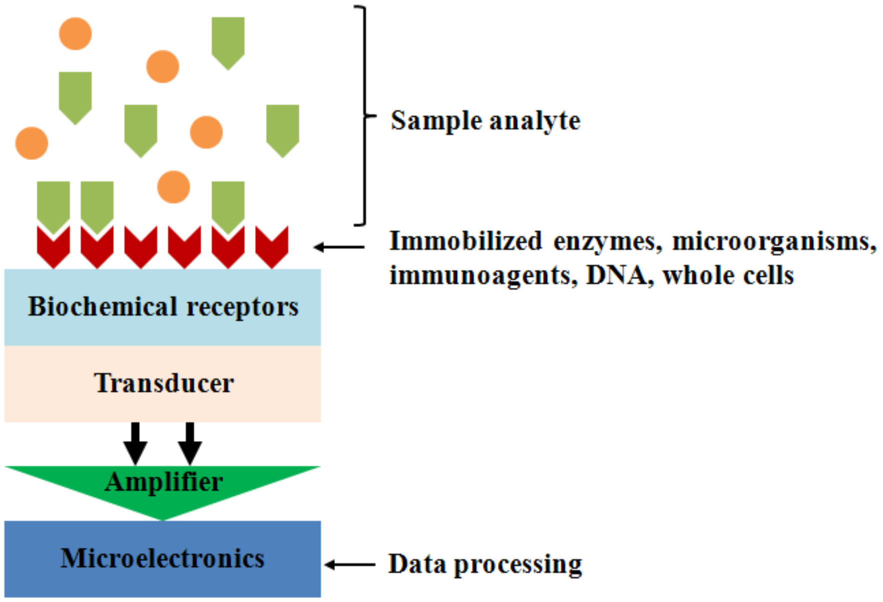

Fig. 2.7 A schematic of a biosensor [58]

The biochemical receptor has to be properly attached to the transducer and this process is called immobilization [57],[59],[60]. There are five main methods of doing this process as follows:

- *Adsorption:* This is the simplest method with a minimal preparation. Using this method, the bonding is weak and only suitable for exploratory work over a short time.
- *Micro-encapsulation:* This was a method for early biosensors in which the biochemical receptor is held in place behind a membrane to provide a close contact between the receptor and transducer.
- *Entrapment:* In this method, the biochemical receptor is mixed with a monomer which is then polymerized to a gel and consequently traps the receptor.
- *Cross-linking:* In this method, the biochemical receptor is chemically bonded to transducer or another supporting material such as gel.
- *Covalent bonding:* This approach involves a carefully designed bond between a functional group in the biochemical receptor and the transducer.

The lifetime of the biosensor is increased in respect to the immobilization method and the typical lifetime for the same biosensor using different immobilization methods include: Adsorption (1 day), membrane entrapment (1 week), physical entrapment (3-4 weeks) and covalent entrapment (4-14 months) [59].

2.2.1 Performance factors of biosensors

Due to different new emerging techniques for the biosensors, it is necessary to establish a criteria for the sensor by which we measure its performance. The following factors give us an idea of the performance requirements for a particular application [59],[61].

- *Selectivity:* It is rare to find a biosensor that only responds to one analyte and is more common to find a sensor that responds to one analyte with a limited response to other similar analytes. For example ion-selective electrodes respond to particular ions, like the glucose oxidase (GOD) as an enzyme is selective for glucose in the presence of other sugars in a blood solution.
- *Sensitivity:* It is important to know that, what concentration range is detected by the biosensor, range, and from calibration point of view, what section of this range shows

a linear response, linear range. The other parameter that is included in the definition of sensitivity of a biosensor is detection limit. Based on IUPAC, "detection limit is the minimum single result which, with a stated probability, can be distinguished from a suitable blank value. The limit defines the point at which the analysis becomes possible and this may be different from the lower limit of the determinable analytical range".

- *Time factors:* This factor includes response time, time to allow the system to come to equilibrium, recovery time, the time that should be passed before a sensor is ready for the next sample measurement, and lifetime, the time after which the response is declined by a given percentage.
- *Precision, accuracy and repeatability:* The analytical value of a senor must show the sufficient precision for the required purpose, accuracy close to the expected value and repetitive measurements in a certain range.

2.2.2 Classification of biosensors

Biosensors are classified as bioreceptor- or transducer-type [59],[60]. The most common forms of bioreceptor recognition mechanisms are: (i) antibody/antigen interactions, (ii) nucleic acid/DNA interactions, (iii) enzymatic interactions, (iv) cellular structure/cell interactions (i.e. microorganisms, proteins) and (v) interactions using bio-mimetic materials (i.e. synthetic bioreceptors). Classification of biosensors based on transducer-type includes:

- *Optical transducers*: They determine changes in light absorption between the reactants and products of a reaction, or measuring the light output by a luminescent process in which the light is guided with optical fibres into the sensor. Taking advantage of the development of fibre optics, a greater flexibility and miniaturization are achieved for these types of transducers. An example for the integrated optical transducer on a chip for the detection of DNA is shown in Fig. 2.8. In Fig. 2.8, the target DNA strands are fluorescence labelled for further detection and are adsorbed to the surface by the capture probes.
- *Electro-chemical transducers*: They convert the biological recognition event into a detectable electrical signal (current, potential and resistance). There are three basic electro-chemical processes that include:

- *Potentiometry:* The measurement of a cell potential at zero current.
- *Voltammetry (ampermetry)*: The measurement of cell current in which an oxidizing (or reducing) potential is applied between the cell electrodes.
- *Conductometry*: The measurement of the conductance of the cell by an alternating current bridge method.

It is important to note that, all of the above types of electro-chemical transducers particularly potentiometric detection method can be constructed on a silicon-based FET [59],[62]. The general form of potentiometric sensors are the ion-sensitive FETs (ISFETs) or chemical FETs (Chem-FETs) in which the potential of an electrode is measured compared to another electrode. The schematic of a NW potentiometric sensor for pH detection is shown in Fig. 2.9 (a). In this sensor, the conductance of the NW changes due to the biochemical reaction on the surface of NW as shown in Fig. 2.9 (b). The micro-potentiometric sensors on a chip perform the label-free detection of hybridization of DNA [63]. Label-free detection provides direct monitoring of the target molecules without modifying them with labels [64]. The schematic views of the operation of conductometric and amperometric biosensors on a chip are shown in Fig. 2.10. The conductometric biosensor in Fig. 2.10 (a) measures conductance changes induced by changes in the overall ionic medium between the two electrodes. Figure 2.10 (b) shows the electric current in the amperometric sensor due to the involved electrons in reduction-oxidation (redox) processes due to the interaction between glucose molecules and GOD.

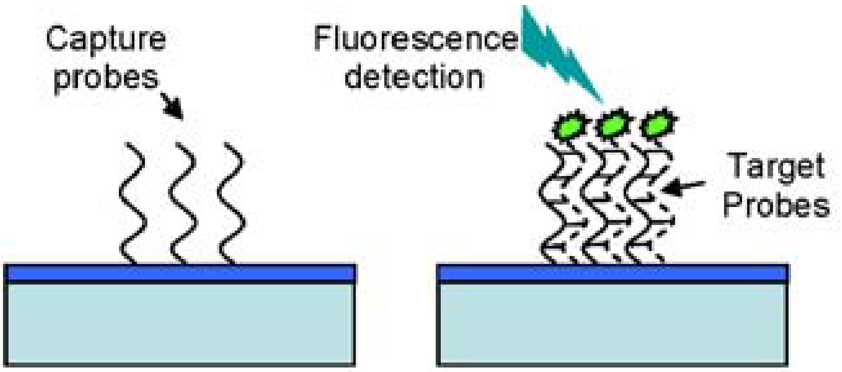

Fig. 2.8 The optical transducer on a chip for DNA detection [54]

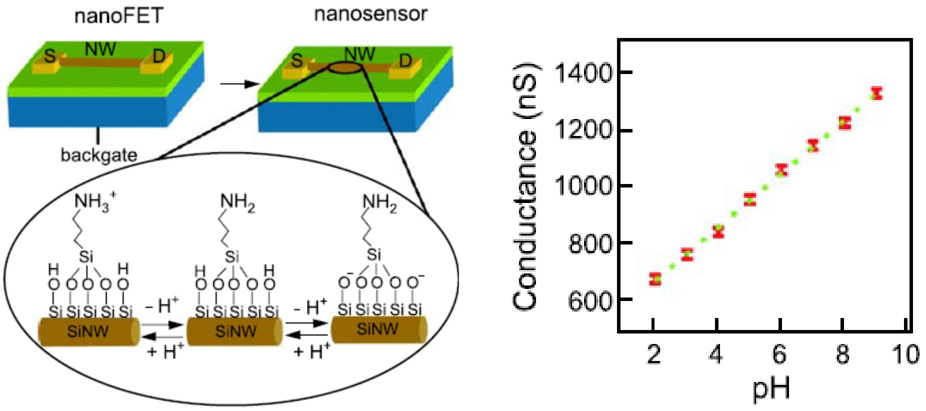

(a) (b)

Fig. 2.9 (a) The schematic of a NW potentiometric sensor for pH detection and (b) conductance of the NW versus pH of the target analyte [54]

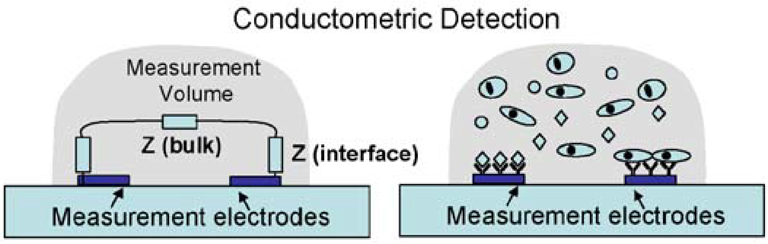

(a)

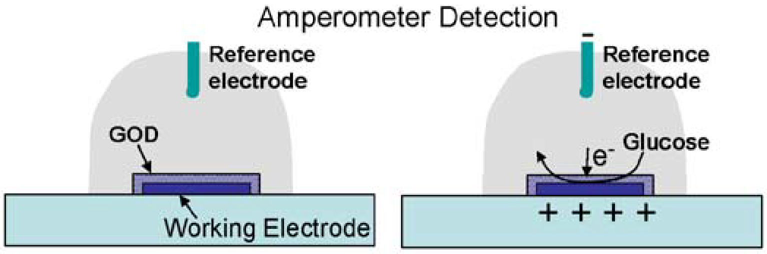

(b)

Fig. 2.10 The schematic views of the operation of [56]: (a) Conductometric and (b) amperometric biosensors on a chip

- *Mechanical transducers*: They convert the biological recognition event into a detectable mechanical output such as resonance frequency, velocity, displacement, etc. This type of transducers includes:
    - *Piezo-electric transducers*: They convert the changes in recognized mass into changes in resonance frequency of mainly crystals under the influence of an electric field.
    - *Acoustic wave transducers*: They sense the changes in the velocity or amplitude of the acoustic wave as it propagates through or on the surface of the material.

  - *Micro/nano-scale cantilever transducers on a chip*: This type of transducers have recently been used for stress sensing and mass sensing and one of their main advantages is the capability of label-free detection similar to the micro-potentiometric sensors [54]. In stress sensing mode that is also referred to as the static mode, the biochemical reaction on one side of the cantilever causes changes in the stress of the surface that leads to a measureable bending of the cantilever. The bending is detected using optical methods like laser or electrical methods like the integrated piezo-resistor on the cantilever [54],[65]. A schematic view of the stress sensing mode for the cantilever and the relation between the displacement and surface stress are shown in Fig. 2.11 (a). This thesis is interested in the mass sensing mode that is referred to as the dynamic mode and details will be discussed in the next chapter. In this mode, the captured biological entity on the surface of the cantilever will change the mass of the cantilever and consequently the resonance frequency of the vibrating cantilever [54],[65]. This mode is preferable because there is no need for the optical setup and the cantilever constitutes the frequency-determining element of an oscillator circuit [65],[66]. Figure 2.11 (b) shows the schematic view of the cantilever for mass sensing and the relation between the mass and resonance frequency.

- *Thermal transducers:* They detect heat released or absorbed during a biochemical reaction that is proportional to the molar enthalpy and the total number of product molecules created in the reaction [67]. MEMS thermal biosensors offer improved sensitivity and linear range, reduced power consumption and shortened measurement times and they can be either thermistors or thermopiles [68]. Figures 2.12 (a) and 2.12 (b) show the cross-section and top view of a MEMS thermal biosensor respectively that consists of a thermopile integrated with a microfluidic system [68]. The microfluidic system includes two identical chambers that have their surfaces functionalized with enzymes and are filled with the analyte and buffer solutions. The enzyme-catalyzed reactions of the analyte produce a thermal power that is measured by using the temperature difference between the sample and reference chambers.

Among the different existing biosensors, the resonant-based sensors have recently been particularly popular because of the higher resolution and accuracy of frequency measurements compared to voltage or current measurements in the modern digital measurement circuits [69],[70]. Moreover, the resonance-based sensors share the same platform with the frequency counter circuits monolithically as a regular pulse generator [69]. The performance of a biosensor is also distinguished by its detection limit and the device sensitivity [71]. Table 2.2 shows a summary on the performance of a few available biosensors [72-78] including their detection target, detection limit, response time, detection time, detection range and the lifetime of the biosensor. The detection limit is explained in the following section.

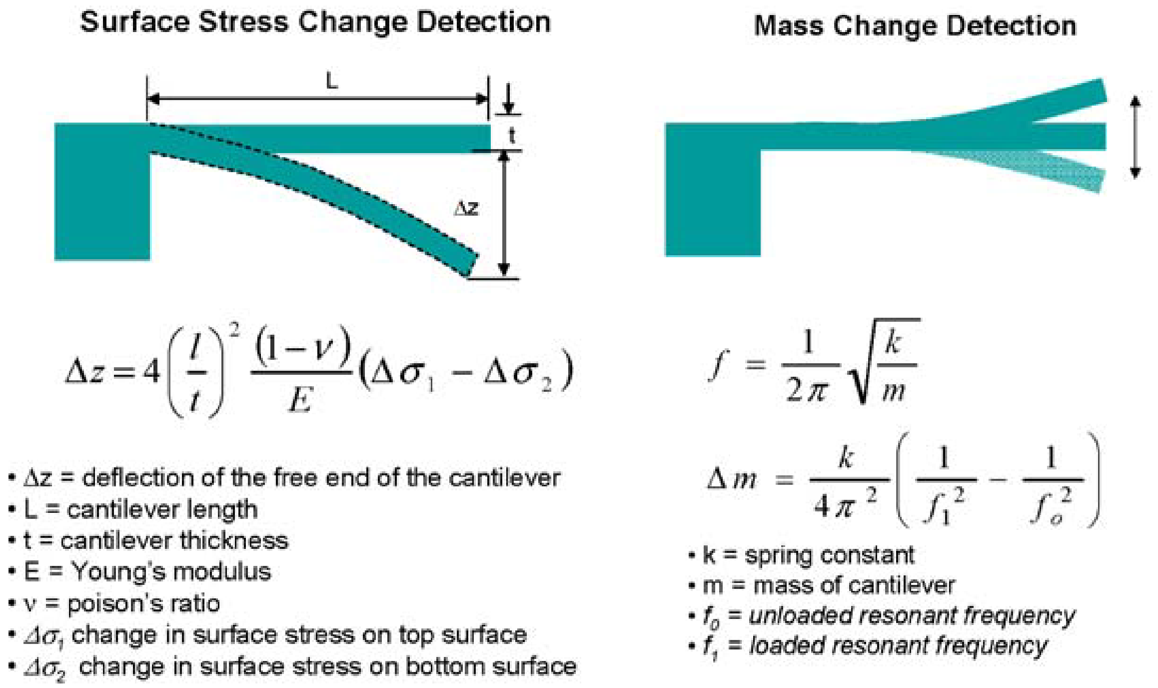

(a) **(b)**

Fig. 2.11 A schematic view of the cantilever for [54]: (a) The stress and (b) the mass sensing mode

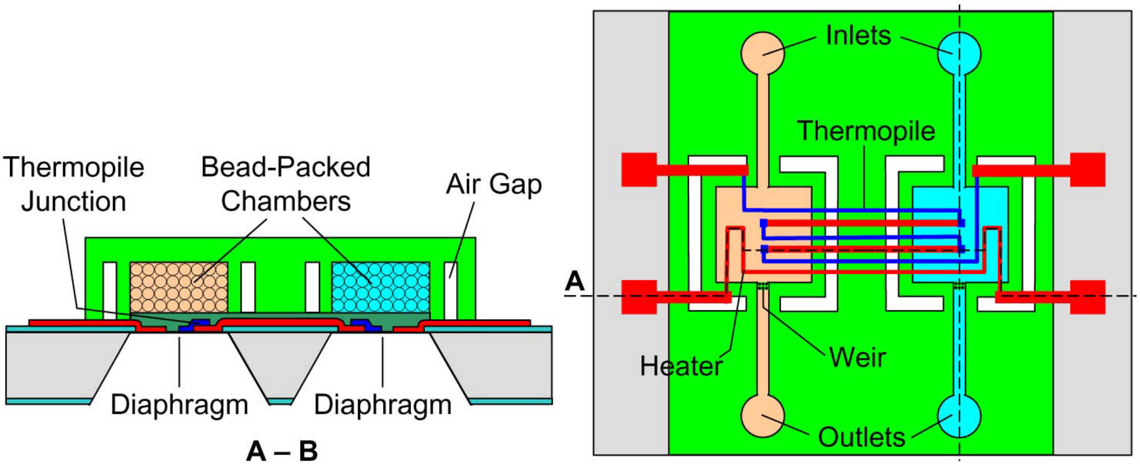

(a) **(b)**

Fig. 2.12 A MEMS thermal biosensor [68]: (a) The cross-section and (b) the top view of the sensor

Table 2.2 The performance of recent biosensors

Ref.	Sensing mechanism	Detection target	Detection limit	Response time [1]	Detection time	Detection range	Lifetime
[72]	Electro-chemical (Amperometric)	Glucose	47 uM	8 s	-	1.5-7 mM	20 days
[73]	Electro-chemical (Potentiometric)	DNA	6.8×10^{-9} molL^{-1}	-	-	1.76×10^{-8}-1.07×10^{-6} molL^{-1}	1 week
[74]	Electro-chemical (Impedimetric)	Protein	0.5 nM	-	-	0.5-500 nM	-
[75]	Optical	Methyl parathion pesticide	0.3 uM	< 3 min	-	4-80 uM	1 month
[76]	Piezo-electrical	Foodborne pathogens	1.2×10^{2} CFU/ml [2] 1.2×10^{6} CFU/ml [3]	-	3 hr [4]	1.2×10^{2} - 1.2×10^{6} CFU/ml	-
[77]	Thermal	Glucose	0.06 mM	2 min	-	0.2-30 mM	3-6 months
[78]	Acoustic wave	DNA	-	-	-	1.2-14 ug/ml	-

[1] Response time is the time of injection to maximum height of the response peak [77].

[2,3] The detection limit values are for with out and with Au particle, respectively.

[4] Total detection time includes DNA extraction for 0.5 hr, polymerase chain reaction (PCR) for 1.5 hr and real-time extraction for 1 hr [76].

2.2.3 Definition of detection limit for DNA biosensors

This thesis focuses on DNA and protein as the major targets for the sensor among different types of targets available. Figure 2.13 shows the transduction mechanisms and LOD for several bibliographic references on DNA biosensing. With respect to Fig. 2.13, a massive number of DNA biosensors have been studied in research laboratories based on the electro-chemical transduction mechanisms with a wide range of LODs down to zepto M (Molar=mol/L) regime. For the mass-detection principle only a few have been reported based on resonance frequency and surface acoustic wave (SAW) methods with relatively moderate LODs (10 µM- 10 nM). These days the mass-detection based mechanical sensors have attracted a great interest due to their excellent capability of scaling as the physical size is reduced. Their scalability results in higher sensitivity to mass changes and applied forces as well as faster response time [33]. J. L. Arlett et al. showed LODs down to 1 femto M for micro-cantilever resonators in their recently reviewed article that were compared to NW biosensors, which are a type of electro-chemical transducers, with the minimum LODs down to 0.1 pico M [33]. For this reason, the minimum LOD of 1 femto M is considered as a target value for the introduced sensor in this thesis that is specified with a red dot in Fig. 2.13.

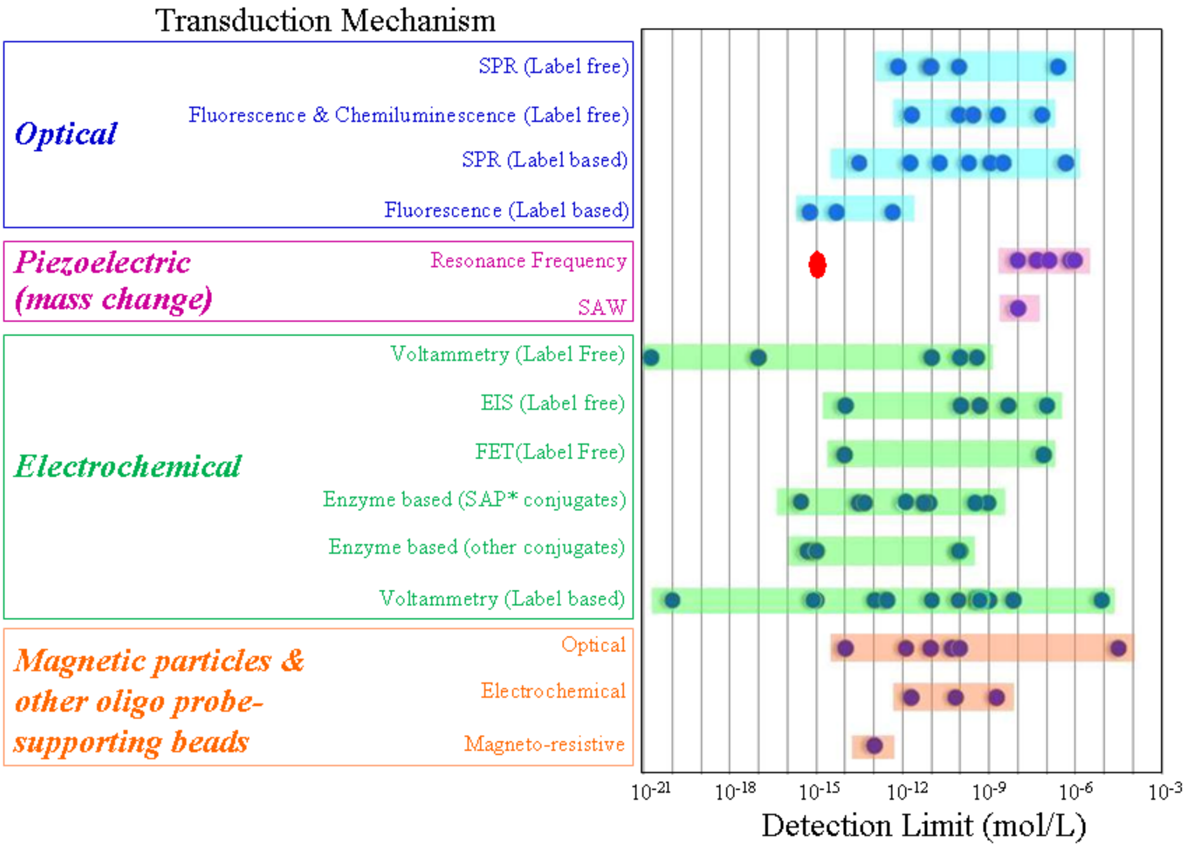

Fig. 2.13 The transduction mechanism and LOD for several bibliographic references on DNA biosensing drawn based on the data published in [53]

In order to define the LOD for mass-detection DNA sensors, it is necessary to convert the unit of LOD from mol/L to g/cm^2. A preliminary method is described for this unit conversion. Figure 2.14 shows a suspended beam that is anchored in both ends and two side electrodes. It was assumed that all the DNA molecules in the solution surrounding the suspended beam were captured on the beam surface during a certain detection time. If we consider that the volume of the red part, V_s, that is shown in Fig. 2.14, is filled by the target solution and also assume that the detection time is long enough in order that, all of the available DNA molecules can attach to the beam surface, changes of the mass due to adsorbed molecules, Δm_{ba}, is calculated by:

$$\Delta m_{ba}\,(g) = V_s\,(cm^3) \times x\,(mol/L) \times (molecular\ weight)\,(g/mol) \qquad (2\text{-}1)$$

Today, commercial biosensors have been developed based on the mass-detection principle. One of the recent mass-detection biosensors is a QCM biosensor that will be discussed in the following section.

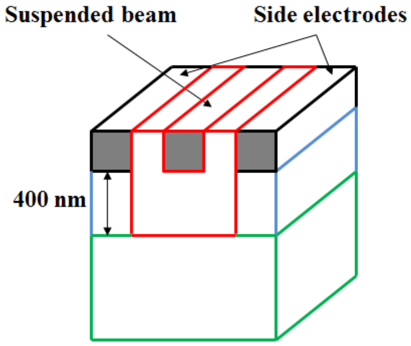

Fig. 2.14 The volume of the target solution surrounding the suspended beam shown in red

2.2.4 Quartz crystal microbalance biosensors

A QCM crystal consists of a thin (≈200- 400 µm) circular disk (diameter~0.5-3 cm) of crystal sandwiched between a pair of circular metal electrodes typically gold or platinum. Figure 2.15 (a) shows both sides of a typical quartz resonator used for the QCM and metallised with gold electrodes [79]. The front side is in contact with the analyte of interest and the back side is exposed to air. The crystal will start resonating when the frequency of the applied field is equal to its resonance frequency. The resonance frequency of the crystal is thus directly proportional to the total mass of the crystal. The application of a mechanical stress to the quartz causes the generation of electricity (piezo-electricity) that is the basis of the QCM [79]. Applied stresses lead to the displacement of the atoms and subsequent shifting of the dipoles, causing a change in the net charge at the crystal face and consequently the change of electrical potential. Other way, the QCM operates by applying a potential across the electrodes connected to the quartz crystal surface and generating a shear force. The QCM measures a mass per unit area by measuring the change in frequency of a quartz crystal resonator. The resonance is changed by adding or removing of a small mass at the surface of the resonator. A linear relation between the changes of resonance frequency, Δf, and changes of mass, Δm, for the QCM is considered if the added mass to the surface is small compared to the weight of the crystal, rigidly adsorbed and smoothly distributes on the surface of the resonator [80]. Changes in the energy dissipation of the oscillating system in the QCM will violate the linear relation between Δf and Δm [80]. In antigen-antibody applications, both the sensing template and the captured molecules are often relatively small and rigid proteins, consequently the linear relationship between changes in frequency and coupled mass is very accurate [80]. QCMs are known to provide very sensitive mass-measuring devices in gas phase and in aqueous solution [81]. Different types of cut for the crystal cause different properties. The two common cuts for the crystal are [82]:

- *Stress-compensated (SC) crystals*: These crystals are available with a doubly-rotated cut that minimizes the frequency changes due to temperature gradients when the system is operating at high temperatures, and reduces the reliance on water cooling. However, due to the more difficult manufacturing process, they are more expensive and are not widely commercially available.
- *AT-cut crystals*: These crystals are single-rotated cuts from rods of quartz at a 35° 15' angle from the z-axis perpendicular to the surface. By applying an alternating potential across the electrodes, a vibrational wave with an amplitude parallel to the crystal surface is generated. The vibrational motion of crystal causes a transverse acoustic wave with the speed of sound that is reflecting back into the crystal at the surfaces, as shown in Figure 2.15 (b). When the wavelength of the acoustic wave in crystal is twice the crystal thickness, a standing wave is created and the crystal is oscillating at its resonance frequency. The AT-cut crystal is easily manufactured and ensures high temperature stability and pure shear motion when subjected to an electric field. The frequency of crystals is inversely proportional to the thickness of the crystals. So for mechanical processing there is an upper limit of about 50 MHz for crystals operating on the fundamental mode [82].

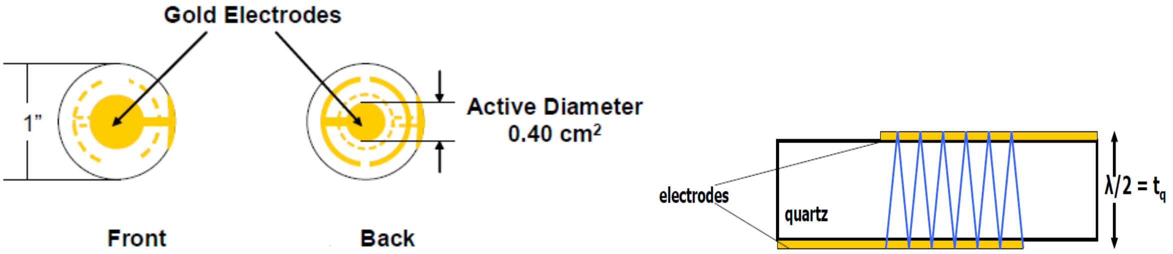

(a) (b)

Fig. 2.15 (a) Both sides of a typical quartz resonator as used for the QCM and metallised with gold electrodes and (b) the created transverse acoustic wave in the crystal by applying a potential to the electrodes [79]

Y. Okahata et. al [83] proposed a new methodology in 1992 to detect the one-to-one hybridization between the oligonucleotides immobilized on Au electrodes of a QCM and target M13 phage DNAs in aqueous solutions. The detection was done using the frequency changes of the QCM and the methodology is shown in Fig. 2.16. The fundamental frequency of the QCM in their methodology is 9 MHz. In 1998, Y. Okahata et. al proposed the 27 MHz QCM that is ~10 times more sensitive than the last conventional 9 MHz QCM [83].

Y. Okahata has developed a commercial product, AFFINIX Q, that is a single channel QCM biosensor (Fig. 2.17 (a)) and a 4-channel QCM biosensor that is called AFFINIX Q4 (Fig. 2.17 (b)) in 2003 [84],[85]. AFFINIX Q and AFFINIX Q4 are used for quantification of interaction between biomolecules (such as proteins, enzymes and DNA) and enzyme reaction. A. Sellborne et. al developed a methodological system that includes a QCM with dissipation monitoring (QCM-D) purchased from Q-sense AB [86]. Q-sense E4 is the latest generation of QCM-D technology from Q-Sense AB that consists of four QCM sensors that can be used in any series or parallel configuration and it obtains the kinetics of both structural changes and mass changes [87]. Another example for the commercial biosensor is the Mark 21 QCM from QCM research that is based on the first award winning Mark 8 QCM design in 1975 [88]. Table 2.3 shows characteristics of the first and recently developed QCM biosensors. As the IP R-NEM sensor will be used as mass-detection biosensor, a comparison between these QCM biosensors and the IP R-NEM sensor will be done in the next chapter.

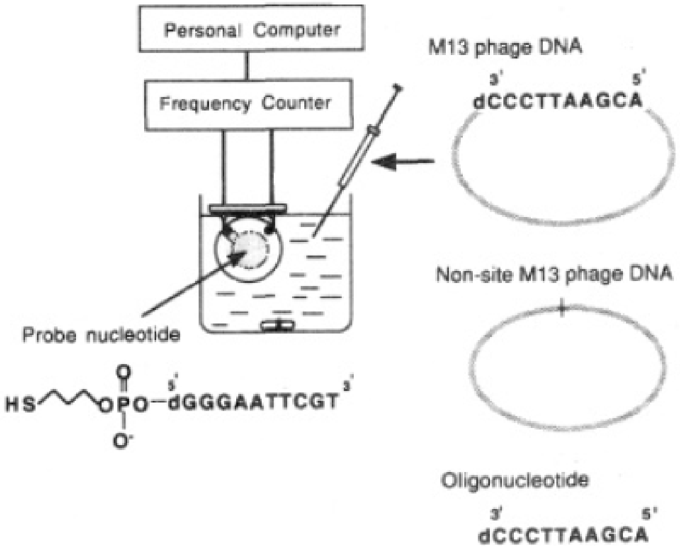

Fig. 2.16 The methodology to detect the one-to-one hybridization between the oligonucleotides immobilized on Au electrodes of a QCM [81]

(a) **(b)**

Fig. 2.17 (a) AFFINIX Q and (b) AFFINIX Q4 [84]

Table 2.3 Comparison of the commercial QCM biosensors

Biosensor	Mass detection limit	Q-factor	Mass responsivity	Sensing area	Fundamental frequency	Ref.
QCM Okahata et al. (1992)	-	-	1.05 ng /Hz	0.16 cm^2	9 MHz	[83]
Q-Sense E4	-	$\geq 10^5$	27 ng/Hz	1.54 cm^2	5 MHz	[87]
QCM Initium AFFINIX Q	100 pg	$\geq 10^5$	30 pg /Hz	0.049 cm^2	27 MHz	[85]
Mark 21 QCM sensor	56.6 µg	-	18 pg/Hz	0.1007 cm^2	50 MHz	[88]

2.3 Resonant suspended gate FET

Flexural mode architecture is one of the electro-static MEMS resonators that can be single or double clamped beam [47],[89]. The beam resonates in-plane or out-of-plane at its intrinsic resonance frequency depending on the material and dimensions of the beam. Two ports lateral CC beam resonator is shown in Fig. 2.18. This architecture uses the capacitive detection that gives a current related to the capacitance between the resonator and the electrode. Simply, the attractive force between two movable conductive plates will produce an electro-static actuation. The actuation electrode in the MEMS resonator is fixed and only the suspended conductive structure is moving. The electro-static force is calculated using [47]:

$$F_{elec} = \frac{1}{2}(\Delta C_{gap})V^2 = \frac{1}{2}\frac{\varepsilon_0 A V^2}{(d_0 - y)^2} \tag{2-2}$$

where, ε_0, is the air permittivity, C_{gap}, is the capacitance between the two plates, V, is the applied voltage, d_0, is the initial gap between the two plates, A, is the area of the two conductive parts and, y, is the lateral displacement.

By applying both AC, $V_{ac}sin\omega t$, and DC voltages, V_{dc}, where $V=V_{dc}+V_{ac}sin\omega t$, the structure is actuated at its resonance frequency, ω, and the electro-static force is rewritten as follows [47]:

$$F_{elec} = \frac{1}{2}\frac{\varepsilon_0 A}{(d_0 - y)^2}(V_{dc}^2 + 2V_{dc}V_{ac}\sin\omega t + V_{ac}^2 \sin^2 \omega t) \tag{2-3}$$

This architecture is typically used for applications with the frequency range of 10 kHz to 100 MHz. Higher frequencies are achieved by scaling down the dimensions of the beam which increase the rigidity and consequently decrease the mechanical displacement. So with low mechanical displacement, the capacitance measurement will face some difficulties in measuring the induced low capacitance variations which is lower than the detection threshold. Moreover, scaling down the dimensions of the beam causes a negative impact on the power handling capability of the resonator [90].

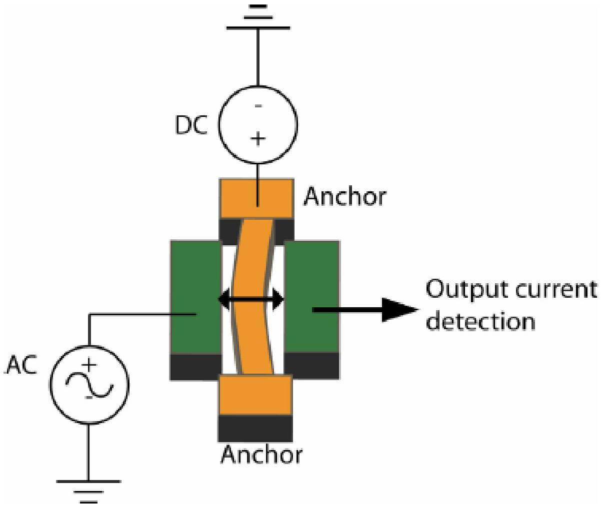

Fig. 2.18 Schematic of a lateral flexural CC beam resonator [47]

Electro-static MEMS/NEMS is a CMOS-compatible technology and their integration with transistors has attracted a great of interest due to the larger output current capability [91]. H. C. Nathonsan et. al described the first resonant gate transistor (RGT) in 1967 that was an electro-statically excited tuning fork using FET as readout [92]. A new approach was introduced based on MOSFET detection for the MEMS resonators in high frequencies as wireless application requires working in the intermediate and ultra-high frequency domains, from 30 MHz to 300 MHz and from 300 MHz to 3 GHz, respectively [47]. The introduced RSG-FET in Fig. 2.19 (a) consists of a mobile gate resonating over the channel that modulates the channel charge and induces the drain current. The cross-section of the RSG-FET along the channel is also shown in Fig. 2.19 (b). DC and AC signals are applied to the suspended gate electrode that can be a CC beam. The electrical and electro-mechanical modelling of the CC RSG-FET [47] is presented in the following section.

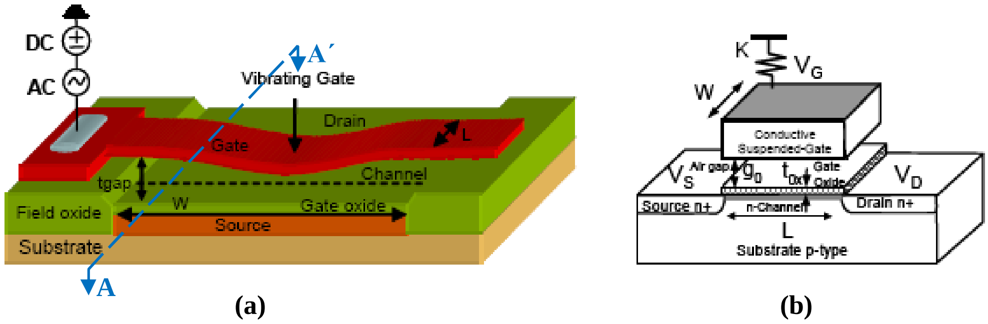

(a) **(b)**

Fig. 2.19 Schematics of [47]: (a) The resonant SG-FET and (b) the transverse view of the device along the line AA´

2.3.1 The electrical and electro-mechanical modelling of the CC RSG-FET

The equivalent electrical circuit of the RSG-FET [47] is shown in Fig. 2.20 that consists of a gap capacitance, C_{gap}, and an integrated MOSFET. C_{gap} is a variable capacitance as it shows the capacitance between the MOSFET oxide surface and the movable gate. The MOSFET itself is modelled with a gate-to channel capacitance, C_{gc}, in the linear region consisting of an oxide capacitance, C_{ox} , a depletion capacitance, C_d , and an inversion capacitance, C_{inv} that are the capacitances of a classical MOSFET. C_{gap}, C_{ox}, C_d and C_{inv} are capacitively dividing the applied gate voltage, V_G. The divided gate voltage is calculated as [47]:

$$V_{G\,int} = \frac{V_G}{(1+\dfrac{C_{gc}}{C_{gap}})} \tag{2-4}$$

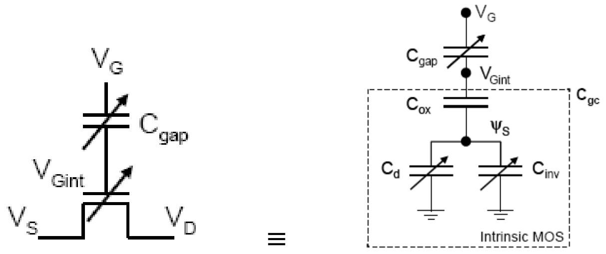

Fig. 2.20 The electrical modelling of an RSG-FET [47]

Considering the electro-mechanical analysis, the total energy stored between two conductive plates is as follows [47]:

$$U_{tot} = U_{elec} - U_{meca} = \frac{1}{2} C_{gap} V^2 - \frac{ky^2}{2} \tag{2-5}$$

where, U_{elec}, and, U_{meca}, are the electro-static and mechanical energy respectively and, k, is the gate rigidity. C_{gap} is calculated as [47]:

$$C_{gap} = \frac{\varepsilon_0 A}{d_0 - y} \tag{2-6}$$

C_{gap0} represents the equilibrium C_{gap} considering y=0. When the gate is in mechanical equilibrium, the derivative of eq. (2-5) over y is null. Moreover, the voltage drop between the gate and the substrate is equal to V_G-V_{Gint} and as the initial gap is, $d_{0,}$ the displacement is equal to d_0-y. So the pull-in voltage of the gate is calculated as [47]:

$$V_{pi\_RSG-FET} = \sqrt{\frac{8k(1+\frac{C_{gap}}{C_{gc}})^2 d_0^3}{27\varepsilon_0 W_{beam} L_{beam}}} \tag{2-7}$$

where, W_{beam}, and, L_{beam}, are the width and length of the gate, respectively. Electro-static MEMS resonators are mechanically and electrically modelled by a resonating damped system as shown in Fig. 2.21. The electrical model is represented by the series inductor, L_x, capacitor, C_x, and resistor, R_x, that are respectively the equivalent of mass, m, spring, k, and damper, γ , in the mechanical model, and a parallel C_{gap} that is variable with gap, d_{gap}. The series resonant circuit is responsible for the resonant peak, f_r, and the parallel circuit causes anti-resonant peak, f_a, that are discussed later. The two resonance frequencies are [47]:

$$f_r = \frac{1}{2\pi\sqrt{L_x C_x}} \tag{2-8}$$

$$f_a = f_r\sqrt{1+\frac{C_x}{C_{gap}}} \tag{2-9}$$

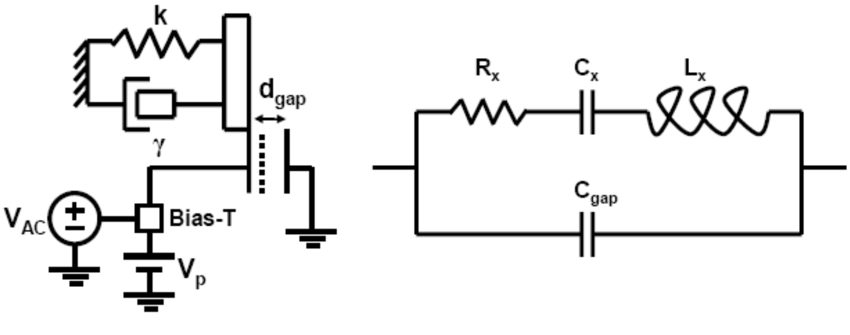

Fig. 2.21 Schematics of the mechanical (left) and electrical model (right) of an electro-static resonator [47]

2.3.2 Characterization of the RSG-FET

At low frequencies, most circuits are modelled using a group of replaceable lumped-equivalent elements but at high frequencies, such a simplified modelling becomes inaccurate [93],[94]. Assuming the passive and active circuit devices as a "black box" irrespective of their complicated behaviour has many advantages and is especially important in high frequency circuits [95]. A general two-port network using the "black box" methodology is shown in Fig. 2.22. This methodology is based on establishing the input-output parameter relations such as impedance, admittance, hybrid, ABCD and scattering parameters (S-parameters). In the following sections, first S-parameters and their practical measurement using network analyzer are explained followed by the impedance measurement as an alternative method for high-frequency measurement. The RSG-FET is considered as a two-port network and two characterization setups for the RSG-FET, capacitive and MOSFET detections [47] that are presented in the following sections. Besides the network and impedance analyzers, lock-in amplifier measurement is also used as an alternative characterization technique for the resonant devices [96-98]. The quality factor of a flexural beam resonator is strongly dependent to air damping so the resonators should be then either tested in a vacuum chamber or preferably encapsulated in thin film vacuum package [37].

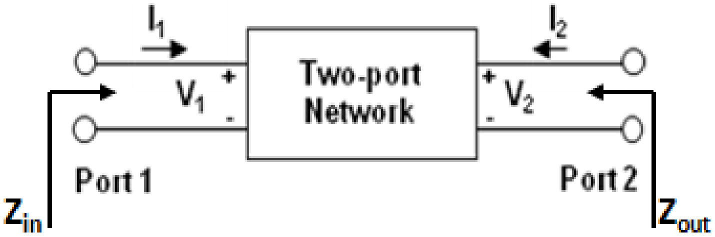

Fig. 2.22 A general two-port network [94]

2.3.2.1 Measuring S-parameters by network analyzer

At high frequencies the characterizing of multi-port devices is no longer possible using simple open or short-circuit measurements and S-parameters are important for the characterizing high frequency circuits [93],[95]. S-parameters define the input-output relations of a network in terms of incident and reflected power waves as shown in Fig. 2.23. S-parameters are usually measured with the device under test (DUT) imbedded between a 50 Ω-load, Z_L, and source [93]. S-parameters are defined as follows [95]:

$$\begin{Bmatrix} b_1 \\ b_2 \end{Bmatrix} = \begin{bmatrix} S_{11} & S_{12} \\ S_{21} & S_{22} \end{bmatrix} \begin{Bmatrix} a_1 \\ a_2 \end{Bmatrix} \qquad (2\text{-}10)$$

where:

$$S_{11} = \left.\frac{b_1}{a_1}\right|_{a_2=0} \equiv \text{reflected power wave at port 1/incident power wave at port 1}$$

$$S_{12} = \left.\frac{b_1}{a_2}\right|_{a_1=0} \equiv \text{transmitted power wave at port 1/incident power wave at port 2}$$

$$S_{21} = \left.\frac{b_2}{a_1}\right|_{a_2=0} \equiv \text{transmitted power wave at port 2/incident power wave at port 1}$$

$$S_{22} = \left.\frac{b_2}{a_2}\right|_{a_1=0} \equiv \text{reflected power wave at port 2/incident power wave at port 2}$$

(2-11)

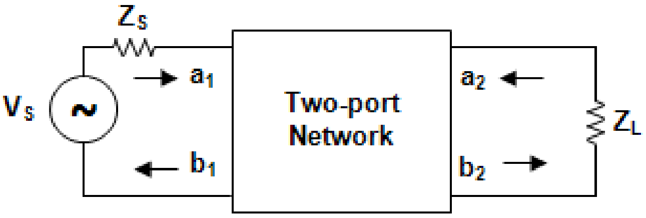

Fig. 2.23 Two-port network showing incident waves (a_1, a_2) and reflected waves (b_1, b_2) [95]

In a symmetrical network $S_{11}=S_{22}$ and $S_{12}=S_{21}$. If the characteristic impedance, Z_0, is considered for the connecting lines on the input and output sides of the two-port network, S-parameters are measured by a matched load that is $Z_L=Z_0$ when $a_2=0$ in the case of S_{11} and $Z_S=Z_0$ when $a_1=0$ in the case of S_{22}. The input reflection coefficient, Γ_{in}, and output reflection coefficient, Γ_{out}, are defined as follows [93]:

$$S_{11} = \Gamma_{in} = \frac{Z_{in} - Z_0}{Z_{in} + Z_0} = |\Gamma_{in}| e^{j\theta_{in}} = |\Gamma_{in}| \angle \theta_{in} \qquad (2\text{-}12)$$

$$S_{22} = \Gamma_{out} = \frac{Z_{out} - Z_0}{Z_{out} + Z_0} = |\Gamma_{out}| e^{j\theta_{out}} = |\Gamma_{out}| \angle \theta_{out} \qquad (2\text{-}13)$$

where Z_{in} is the input impedance at port 1 and Z_{out} is the output impedance at port 2. In a symmetrical network $S_{11} = S_{22} = \Gamma_0 = |\Gamma_0| \angle \theta_L$. Forward and reverse voltage gain of the network is found by $|S_{12}|^2$ and $|S_{21}|^2$, respectively. Taking the logarithm of the reflection coefficient gives the return loss (RL) as follows [93]:

$$RL = -20\log|\Gamma_0| \tag{2-14}$$

If Z_{in} consists of a real and imaginary part as follows, the relationship between reflection coefficient and impedance is shown on Smith chart [99],[100]:

$$Z_{in}(\omega) = R(\omega) + jX(\omega) \tag{2-15}$$

The smith chart is shown in Fig. 2.24. Figure 2.24 shows constant resistance and reactance circles that the points situated on a circle have a same real impedance part value and a same imaginary impedance part value, respectively. Positive imaginary part of the impedance shows the capacitive behaviour of the circuit while the negative imaginary part shows the inductive behaviour of the circuit. $\Gamma_0 = -1, 0, +1$ represents the short circuit, 50 Ω-resistance and open circuit, respectively. The resonance and anti-resonance frequencies occur when $X(\omega)$=0 [99],[100]. When $X(\omega)$=0 the curve crosses the x-axis. An example for the resonance and anti-resonance frequency of an acoustic resonator in Smith chart is given in Fig. 2.25.

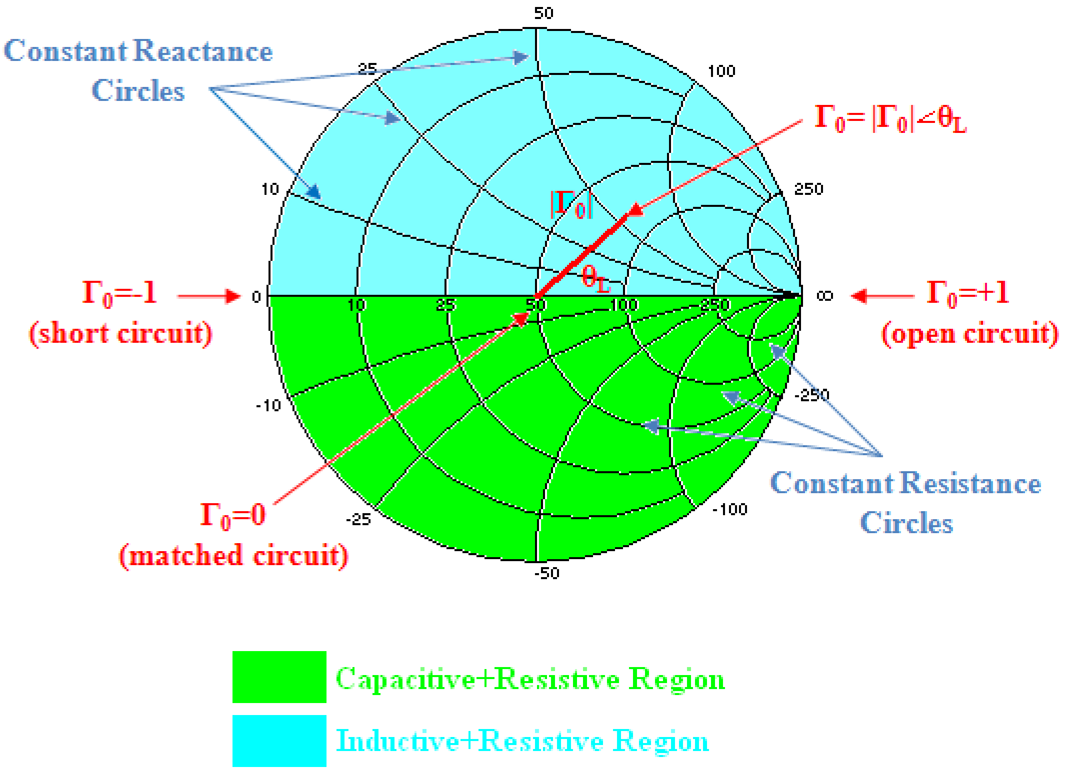

Fig. 2.24 Smith chart [100]

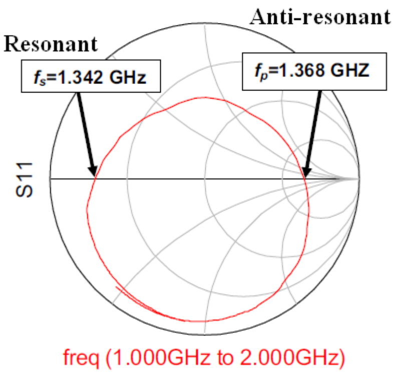

Fig. 2.25 An example of the Smith chart for the reflection parameter of the acoustic resonator [100]

One of the most popular ways for measuring S-parameters is to use the vector network analyzer. The vector network analyzer measures voltages in terms of magnitude and phase. Usually network analyzer has an output that provides the radio-frequency (RF) signal and three measurement channels named as *R*, *A* and *B* in Fig. 2.26 [93]. The RF source is set to sweep over a range of frequency. Channel *R* is a reference port while channels *A* and *B* measure the reflected and transmitted waves. The setup in Fig. 2.26 allows the measurement of S_{11} and S_{21} signals. The bias-T provides the necessary biasing conditions for the DUT. Before starting the measurement we need to do the open-short-load (OSL) calibration procedure to reduce the effect of all undesired influences or parasitics.

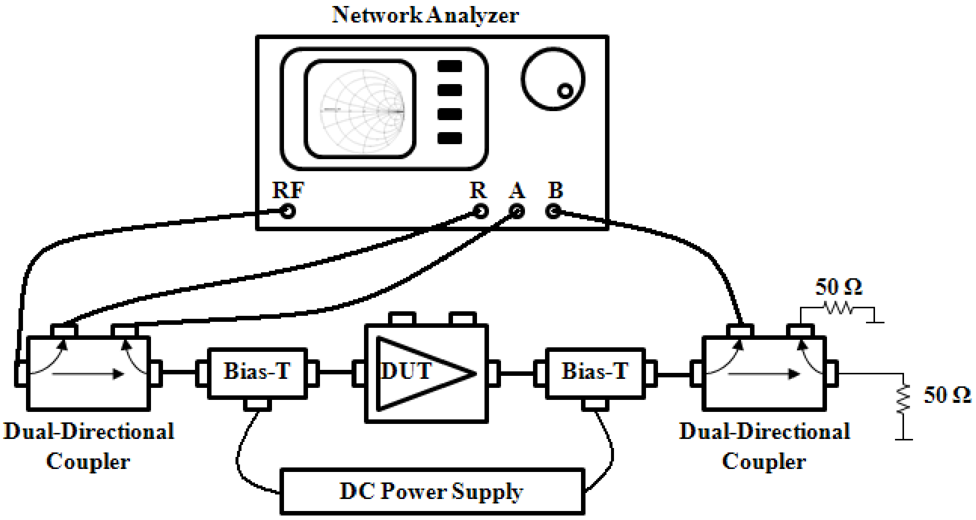

Fig. 2.26 The measurement system using a network analyzer [93]

2.3.2.2 Measuring impedance by impedance analyzer

A DUT may have much greater or smaller impedance than the 50 Ω-reference impedance in network analyzer at the operating frequencies. Due to this issue, inductance-capacitance-resistance (LCR) or impedance analyzer measures more accurately than network analyzer [101],[102]. The impedance analyzer is limited to the frequency range, as an example, HP 4291A measures up to 2 GHz. It is also a one-port analyzer that only measures the input impedance of one port among multi-ports of the device [102]. The analyzer applies a time-harmonic voltage, *E*, over the input port of DUT and measures the amplitude and phase of the current in the port. The input impedance of the port is calculated by dividing the voltage by the current [102]. A general impedance measurement schematic using two vector voltmeters, V_1 and V_2, is shown in Fig. 2.27. The true impedance of DUT, Z_x, is calculated by measuring the voltages between any two points in a linear circuit as follows [101]:

$$Z_x = K_1 \frac{K_2 + V_r}{1 + K_3 V_r} \tag{2-16}$$

where $V_r = V_2/V_1$ and K_1, K_2 and K_3 will be found by OSL calibration.

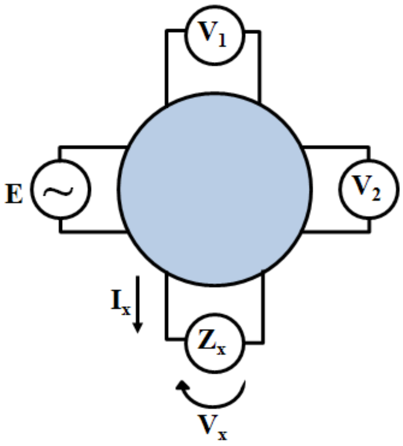

Fig. 2.27 The general schematic for the impedance measurement [101]

2.3.2.3 Lock-in amplifier measurement

Lock-in amplifier detects and measures very small AC signals even if the signal is obscured by noise sources [103]. Lock-in amplifiers use a phase-sensitive detection technique to separate the input signal at a specific reference frequency and phase from noise signals at frequencies other than the reference frequency [103]. The block diagram of a lock-in amplifier is shown in Fig. 2.28 that includes: i) an AC signal amplifier, ii) a voltage controlled oscillator (VCO) that synchronizes with an external reference signal, iii) a multiplier that is called the phase sensitive detector (PSD), iv) a low-pass filter, and v) a DC amplifier. If the input signal is $V_{ac}(t) = G_{ac} V_0 \sin(\omega_0 t + \theta_0)$, where V_0 is the signal amplitude, ω_0 is the signal frequency, θ_0 is the signal phase, and G_{ac} is the gain of AC signal amplifier, and the internal reference signal which is locked to the external reference signal is $V_{ref}(t) = V_L \sin(\omega_L t + \theta_L)$, where V_L is the reference signal amplitude, ω_L is the reference signal frequency, and θ_L is the reference signal phase, the PSD output is calculated by [103],[104]:

$$\begin{aligned} V_{PSD} &= G_{ac} V_0 \sin(\omega_0 t + \theta_0) V_{ref} \sin(\omega_L t + \theta_L) \\ &= \frac{1}{2} G_{ac} V_0 V_{ref} \cos((\omega_0 - \omega_L)t + (\theta_0 - \theta_L)) \\ &- \frac{1}{2} G_{ac} V_0 V_{ref} \cos((\omega_0 + \omega_L)t + (\theta_0 + \theta_L)) \end{aligned} \tag{2-17}$$

If $\omega_0 = \omega_L$ the final DC output voltage that is proportional to the amplitude of the input signal is calculated by [103],[104]:

$$V_{output} = \frac{1}{2} G_{dc} G_{ac} V_0 V_L \cos(\theta_0 - \theta_L) \tag{2-18}$$

where G_{dc} is the gain of DC amplifier.

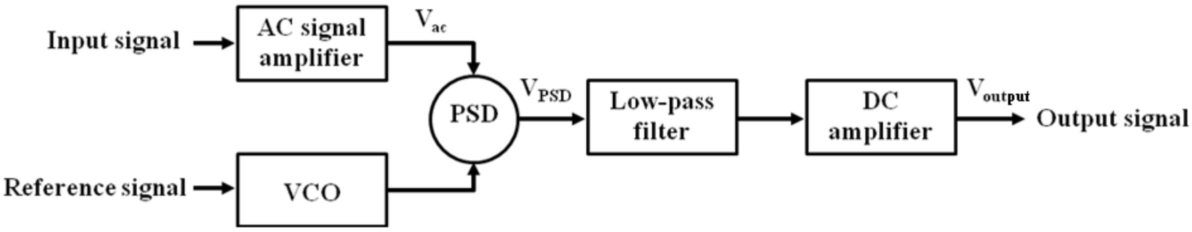

Fig. 2.28 The schematic of a lock-in amplifier [104]

2.3.2.4 Capacitive response of the RSG-FET

In capacitive detection resonator, the reflected signal from the resonator is sensed on the resonating structure or on the actuation electrode. A 1-port characterization setup is considered in Fig. 2.29 to evaluate the capacitive response of the RSG-FET. By connecting the source, drain and bulk of the MOSFET to the ground, the transistor behaves as a capacitor and the surface potential is considered constant in the accumulation regime and in the strong inversion regime. The equivalent circuit model of the RSG-FET in this setup is also shown in Fig. 2.29 that is explained in section 2.3.1. The bias-T circuit in Fig. 2.29, includes an inductance which stops all AC signal towards the DC source and a capacitance to stop all DC signal towards the analyzer. The analyzer injects a signal to the vibrating gate and compares this signal amplitude with the reflected signal sensed at the same port. Reflection is calculated as [47]:

$$S_{11} = 10\log(\frac{P_{reflected}}{P_{in}}) = 20\log(\frac{V_{refelected}}{V_{in}}) \tag{2-19}$$

where P_{in} and V_{in} are the power and voltage of input signal respectively while $P_{reflected}$ and $V_{reflected}$ denote the power and voltage of the reflected signal. Fig. 2.30 shows the reflection signal versus frequency. At the mechanical resonance, the impedance of the resonator is low, therefore inducing a high transmission response and low reflection amplitude, as seen in Fig. 2.30. The amplitude of the reflection peak is related to the applied DC gate voltage and the gap capacitance.

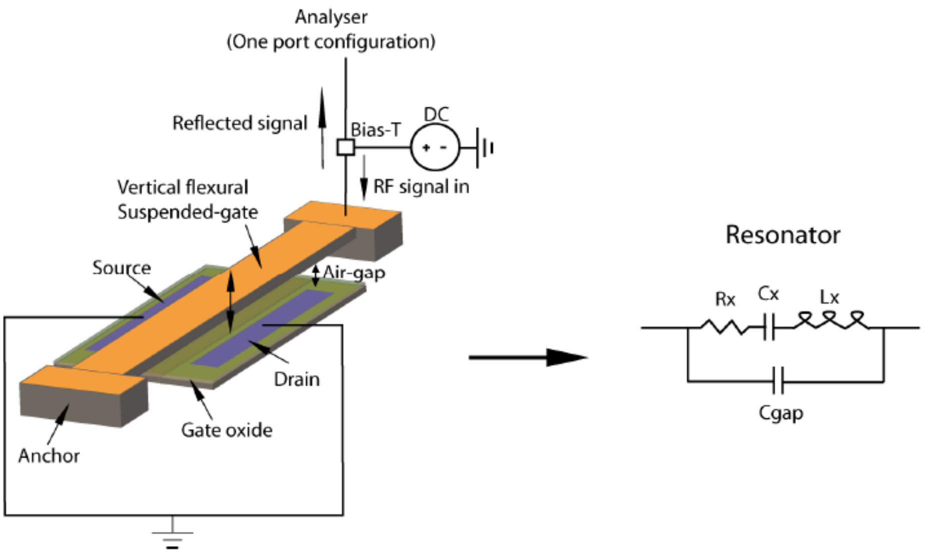

Fig. 2.29 The schematic of 1-port characterization technique for the RSG-FET pure capacitive response (left) and its equivalent circuit model (right) [47]

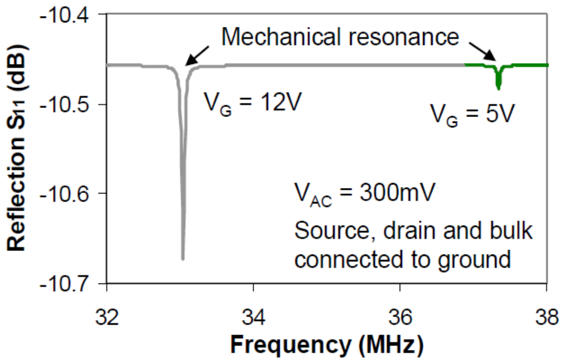

Fig. 2.30 The 1-port reflection response of the RSG-FET [47]

2.3.2.5 Transistor response of the RSG-FET

The transistor response is extracted from a two port measurement of the RSG-FET. The schematic of this measurement setup and the equivalent circuit model are shown in Fig. 2.31. The excitation signal from the analyzer is applied to the suspended-gate and the drain current is sensed across the analyzer output impedance. This setup includes a FET as well as the electrical model of the resonator in Fig. 2.29. The resulting voltage variation across the 50 Ω-output impedance is compared to the applied signal amplitude on the gate. The transmission response is then a function of the intrinsic gain of the transistor, g_m, and is related to the small signal analysis. Transmission signal is derived by [47]:

$$S_{21} = 10\log\left(\frac{P_{out}}{P_{in}}\right) = 20\log\left(\frac{g_m V_{G\,int}\, r_0}{V_{in}}\right) \tag{2-20}$$

where P_{out} is the power of the transmission signal, V_{Gint} is the input voltage to the FET through the CC beam and r_o is the output impedance of the FET.

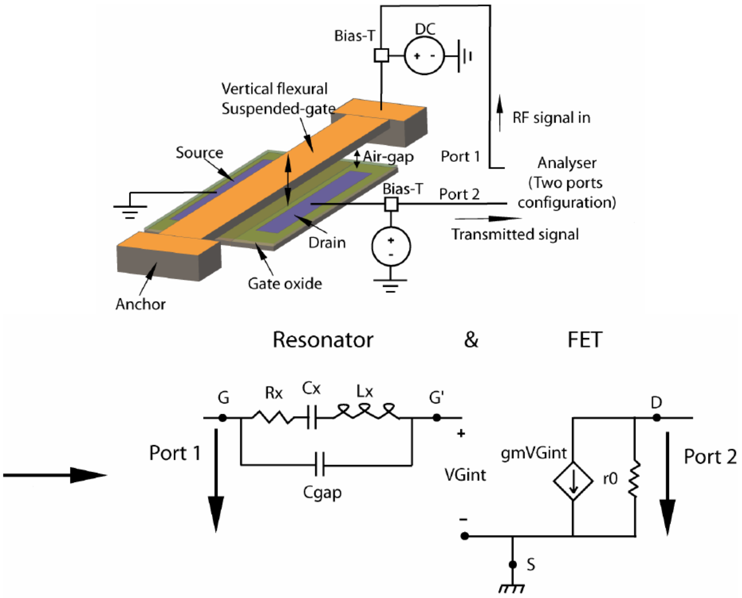

Fig. 2.31 The schematic of 2-ports characterization technique for the RSG-FET transistor response (top) and its equivalent circuit model (bottom) [47]

The transmission signal versus frequency for the RSG-FET is shown in Fig. 2.32 that is set by a series and a parallel resonance. The circuit behaves like a simple capacitor at frequencies below f_r and like an inductor between f_r and f_a. After f_a the impedance decreases with frequency, indicating typical capacitor behaviour again. In Fig. 2.33 (a), by increasing the gate voltage, C_x increases while C_{gap} increases. Respect to eq. (2-8), the resonance frequency decreases due to the reduction of C_x for higher gate voltages while the anti-resonance frequency is constant because the ratio of C_x/C_{gap} in eq. (2-9) is not changing by increasing the gate voltage. The magnitude of the transmission signal is directly related to the gain of the transistor and increases for a larger gate voltage. Figure 2.33 (b) shows the effect of reducing the gap on the transmission response. The resonance frequency is constant by decreasing the gap but the anti-resonance frequency increases for smaller gaps and the reason for this behaviour is not explained in [47]. The transmission response amplitude strongly depends on R_x and R_x is proportional to the gap. For smaller gap, the smaller R_x results in larger amplitude response.

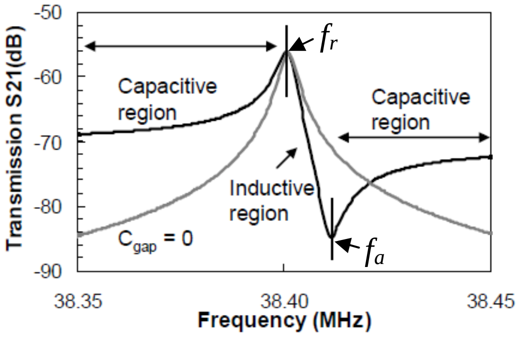

Fig. 2.32 The transmission parameter versus frequency [47]

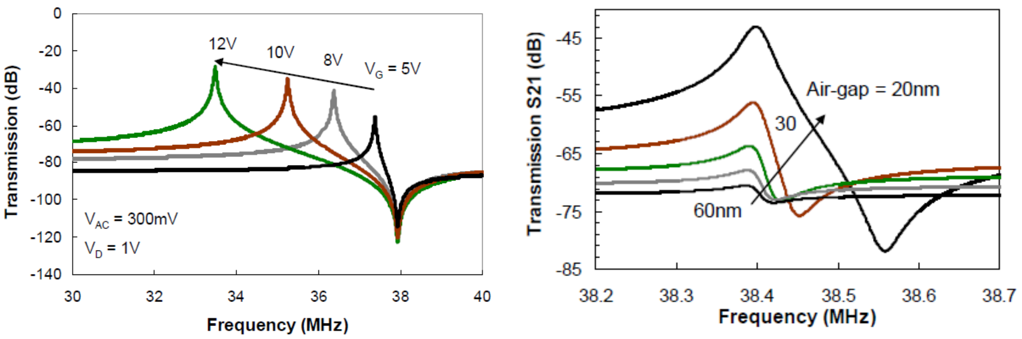

(a) **(b)**

Fig. 2.33 The 2-port transmission response of the RSG-FET [47]:
(a) The effect of increasing the gate voltage for the gap=50 nm and (b) the effect of reducing the gap on the transmission response of the RSG-FET

2.3.2.6 Practical characterization of the resonant devices

Impedance and network analyzer are two methods for characterizing the RSG-FET [47]. It is easier to detect the resonant response using impedance analyzer. The Agilent 4294A impedance analyzer is suitable for impedance measurement comprised between 1 mΩ to 100 MΩ, at a frequency ranging from 40 Hz to 110 MHz. A four-terminal pair cable configuration was used for the impedance analyzer as shown in Fig. 2.34 (a). As the second method, network analyzer measurements are used to obtain the transmission and reflection signals. For the transmission setup in Fig. 2.34 (b) ground-signal-ground (GSG) RF probes are used that are connected to a network analyzer HP8753D. The analyzer is suitable for frequency measurement between 30 kHz and 3 GHz. Polarization voltages are set with external voltage source connected to the network analyzer by its internal bias-T. The gate and drain are respectively connected to the output and input of the analyzer.

The alternative technique for measuring the resonance frequency of resonant devices is the lock-in measurement technique [96-98]. S. T. Bartsch et. al [96] used the lock-in amplifier setup for the characterization of a resonant body FinFET (RB-FinFET) in Fig. 2.35 (a). The RB-FinFET has a vibrating channel that is controlled by two side gates. The lock-in amplifier measurement setup for RB-FinFET is shown in Fig. 2.35 (b). In this setup an RF signal with the frequency of $\omega + \Delta\omega$ is applied to the drain while applying another RF signal with the frequency of ω to the side gate. The output low-frequency signal from the FET and the provided reference signal are applied to the lock-in amplifier for the extraction of the resonant frequency as was explained in section 2.3.2.3.

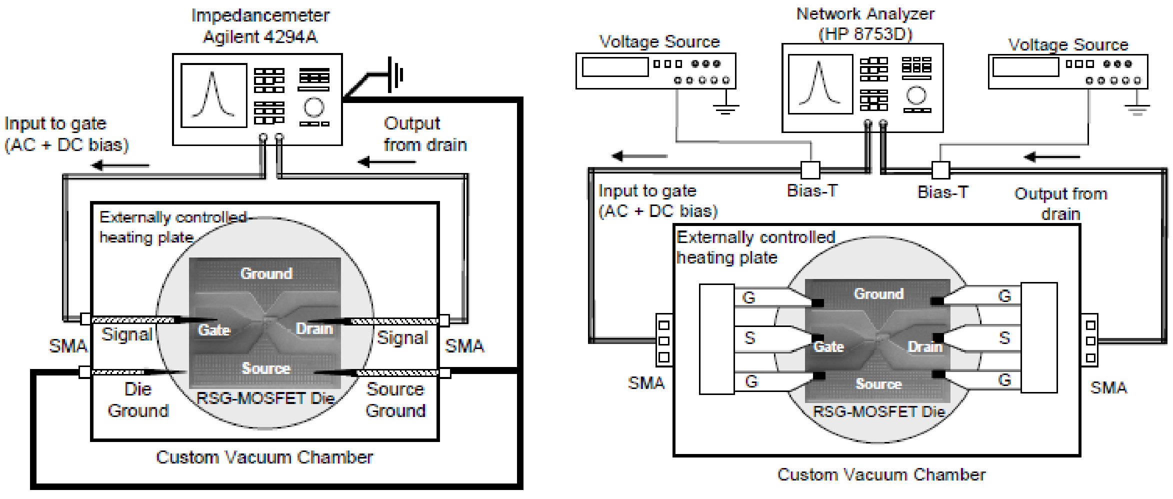

(a) **(b)**

Fig. 2.34 The measurement setup for the RSG-FET [47]: (a) The impedance analyzer setup and (b) the network analyzer setup

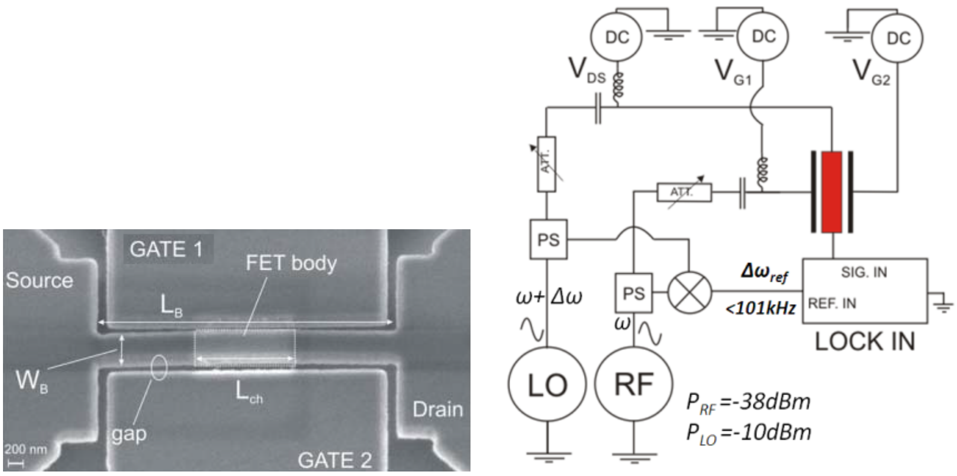

(a) **(b)**

Fig. 2.35 (a) The RB-FinFET and (b) its lock-in amplifier measurement setup [96]

2.4 Summary

In this chapter, the available NEM-IC devices that work as switches, memories or sensors were presented and the sensing application particularly for biosensing was chosen for the developed IP R-NEM sensor. The available biosensors were classified into different types and their performance factors including the detection limit were discussed. The IP R-NEM sensor uses the mass-detection technique for its sensing and was compared to the commercialized QCM biosensor that has the same sensing technique. The similar operation of the RSG-FET to the IP R-NEM sensor makes it a good example for further investigation on the operation of the IP R-NEM sensor. For this reason, the electrical and electro-mechanical modelling of the CC RSG-FET with the out-of-plane movement for the suspended gate were studied. Network and impedance analyzer as well as lock-in amplifier are the available measurement instruments for the characterization of high frequency devices. The capacitive and transistor responses of the RSG-FET and its practical characterization in the network and impedance analyzer setups as well as the lock-in measurement setup for the RB-FinFET were explained. Similar measurement setup for the RSG-FET will be used for the IP R-NEM sensor in future.

CHAPTER 3

In-plane resonant NEM sensor: Design and simulation

This chapter describes the design and simulation methodologies developed for the newly in-plane resonant nano-electro-mechanical (IP R-NEM) sensor. This sensor features an in-plane metal-oxide-semiconductor field-effect-transistor (MOSFET) integrated with a suspended gate that moves in-plane and works as a mass-detection based sensor for the biological and chemical detections. In the beginning, the fundamental characteristics for the NEM structure that includes a clamped-clamped (CC) beam and two side electrodes are investigated at the physical-level. These characteristics include the resonance frequency, pull-in voltage and quality factor. Different sources of damping that affect the quality factor of the resonator are investigated both analytically and numerically. A new design is then introduced for the NEM structure using a free-free (FF) beam that improves the quality factor of the resonator. Hybrid circuit analysis of the IP R-NEM sensor is done afterwards for characterizing the sensor fully, and a complete investigation is conducted on the effect of the different parameters such as the gap and gate voltage on the resonance frequency of the sensor. The mass responsivity of the sensor is evaluated by modelling the functionalization and detection processes then followed by presenting the scaling rules for key structure parameters. The limit of detection (LOD) for the sensor is calculated and a comparison of the detection ability with other available biosensors is made.

3.1 Mass-detection based NEM structure and IP R-NEM sensor

The NEM structure consists of a suspended CC beam and two side electrodes (Fig. 3.1 (a)). The CC beam is excited by using the applied AC voltage. When the frequency of the AC voltage source is equal to the resonance frequency of the beam, it starts resonating. The suspended CC beam is the sensing head of the NEM structure in which the variation of the resonance frequency, Δf, is detected depending on the mass variation of the beam due to the chemical or biological species adsorption on its surface, Δm_{ba}. In order to make the surface of the CC beam sensitive to the target molecules of interest, we need to functionalize the surface by using various self-assembled linker molecules that react with the target molecules. After the functionalization process, the target molecules are introduced on the beam in a liquid or gas phase during the detection process. More details on the functionalization and detection processes are given later. The adsorbed linker and target molecules on the surface of the CC beam change the primary resonance frequency of the CC beam due to Δm_{ba}. In order to amplify Δf after the molecules are adsorbed onto the surface of the suspended beam, the beam is integrated with a MOSFET as shown in Fig. 3.1 (b) and named IP R-NEM sensor. In this structure, the suspended beam plays the role of the gate for the MOSFET that moves in-plane and induces a channel in the MOSFET. After the molecules are adsorbed onto the surface of the resonant beam during the functionalization and detection processes, the resonance frequency of the beam changes and consequently causes variation in the MOSFET current.

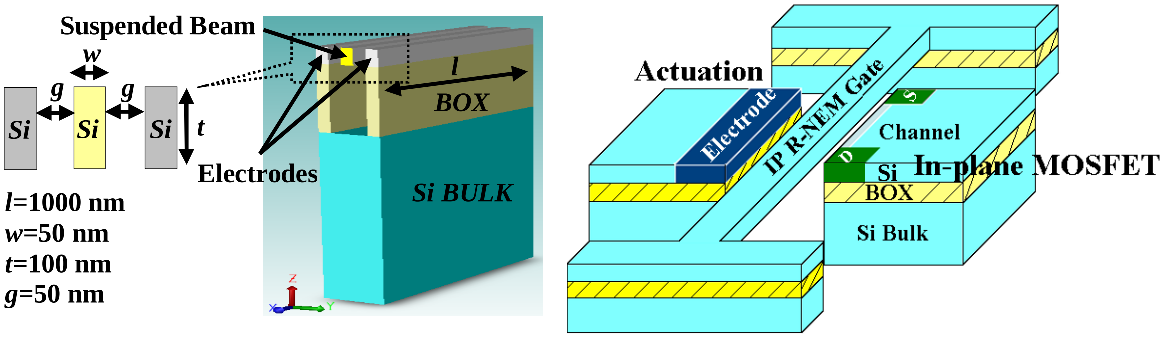

(a) (b)

Fig. 3.1 The simulated mass-detection based devices: (a) The NEM structure and (b) the IP R-NEM sensor

The fabrication process of the NEM structure and the IP R-NEM sensor are based on the silicon-on-insulator (SOI) technology in which the SOI layer is thinned down to 50 nm. The simplified fabrication process for the NEM structure is shown in Fig. 3.2. The CC beam and double side electrodes are patterned using electron beam (EB) lithography and the following reactive ion etching (RIE) on a heavily-doped SOI layer (Fig. 3.2 (a)) as shown in Fig. 3.2 (b). An oxide layer is then deposited on the patterned SOI layer in order to pattern contact holes above silicon pads later (Fig. 3.2 (c)). Contact holes (Fig. 3.2 (d)) are considered in the fabrication process to make the process more compatible with the regular MOSFET process technology and avoid the leakage current from the later deposited metal layer to the substrate. A metal layer is deposited for patterning the interconnections and contact pads in Fig. 3.2 (e). Figure 3.2 (f) shows the patterned metal layer using metal etchant. The buried oxide layer (BOX) will act as the sacrificial layer that will be removed for the suspension of the beam. The final structure is shown in Fig. 3.2 (g). Further details on the complete fabrication process for the NEM structure and IP R-NEM sensor are given later. The analytical values for the key parameters of the NEM structure are explained and calculated later.

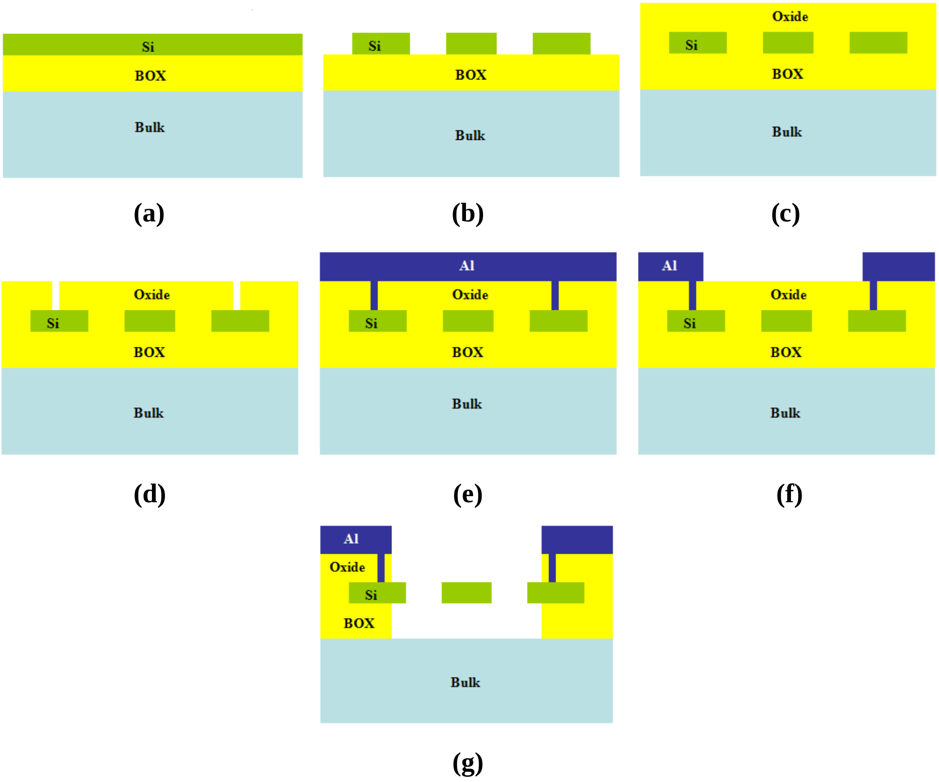

Fig. 3.2 The fabrication process of the NEM structure: (a) A heavily-doped SOI layer, (b) the patterned SOI layer using EB and the following RIE step, (c) the deposited oxide layer on the patterned SOI layer, (d) the patterned contact holes above silicon pads, (e) the deposited aluminium layer on the patterned oxide layer, (f) the patterned aluminium layer using wet etching and (g) the NEM structure after the suspension of the beam

3.2 Key characteristics for the NEM structure

The mechanical resonance frequency of the nth mode of the CC beam for the lateral displacement is given using the following equation [105-110]:

$$f_n = \frac{\pi\beta_n^2}{2\sqrt{12}}\sqrt{\frac{E}{\rho}}\frac{w}{l^2} \tag{3-1}$$

where β_n is the mode constant, E is Young's modulus, ρ is density, and, w, and, l, the width and length of the beam, respectively, m_b, the effective mass of the beam and, k_{bm}, the mechanical spring stiffness of the beam. Using β_n for the first mode, β_0, the resonance frequency of the first mode, f_0, is calculated as [105-110]:

$$f_0 = 1.03\sqrt{\frac{E}{\rho}}\frac{w}{l^2} = \frac{1}{2\pi}\sqrt{\frac{k_{bm}}{m_b}} \tag{3-2}$$

where m_b is given by [111]:

$$m_b = 0.735\rho wlt \tag{3-3}$$

where t is the thickness of the beam. By using eq. (3-2), k_{bm} is calculated as follows:

$$k_{bm} = 30.78Et(\frac{w}{l})^3 \tag{3-4}$$

For biasing the beam, a DC voltage was applied to the beam, V_{dc}, and an AC voltage, V_{ac}, was applied to the side electrode in Fig. 3.1 (a). More details on the applied voltages are provided later. The induced electro-static force in eq. (2-2) due to the applied voltages causes the electrical spring stiffness, k_{be}, that is added to the mechanical spring stiffness and gives the effective spring stiffness, k_b:

$$k_b = k_{bm} + k_{be} \tag{3-5}$$

k_{be} is calculated by [92],[108],[112]:

$$k_{be} = \frac{-\varepsilon_0 A V_{dc}^2}{g^3} \tag{3-6}$$

where ε_0 is the air permittivity, g, the gap between the beam and electrodes, and, A, the beam area and is equal to $l \times t$. As a result, the resonance frequency is calculated as follows:

$$f_r = \frac{1}{2\pi}\sqrt{\frac{k_b}{m_b}} \tag{3-7}$$

The pull-in effect, that is an important issue to design NEM/MEM structures, occurs when the beam passed approximately two-thirds of the gap in the parallel-plate model. The pull-in voltage, V_p, for this model is calculated as [48],[113]:

$$V_p = 0.54\sqrt{k_b g^3 / \varepsilon_0 A} \tag{3-8}$$

In order to operate the NEM sensor with a safe margin, V_{dc} was chosen to be well below V_p and assumed that $k_b \approx k_{bm}$ and consequently $f_r \approx f_0$. Considering the equivalent circuit model for the NEM structure in Fig. 2.21, C_{gap0} is derived using eq. (2-6) considering $d_0 = g$, $y=0$ and $A = l \times t$ and the inductor, L_x, the capacitor, C_x, and the resistor, R_x are calculated as following [46]:

$$L_x = \frac{m_b}{\eta^2} \tag{3-9}$$

$$C_x = \frac{\eta^2}{k_b} \tag{3-10}$$

$$R_x = \frac{\alpha}{\eta^2} \tag{3-11}$$

where the damping factor, α , and η are calculated by [47]:

$$\alpha = \frac{2\pi f_0 m_b}{Q_{Total}} \tag{3-12}$$

$$\eta = \frac{V_p \varepsilon_0 A}{g^2} \tag{3-13}$$

where Q_{Total} is the total quality factor that is discussed in the next section.

3.3 Damping sources for resonators

Energy is dissipated from the resonator in different damping mechanisms. Q_{Total} is defined as the ratio of the total energy stored in the system, W_{Total}, to the energy dissipated or lost per cycle of vibration, ΔW_{Loss} [114]:

$$Q_{Total} = 2\pi \frac{W_{Total}}{\Delta W_{Loss}} \tag{3-14}$$

Q_{total} consists of several individual Q-factors as following [114]:

$$\frac{1}{Q_{Total}} = \frac{1}{Q_{Air}} + \frac{1}{Q_{Anchor}} + \frac{1}{Q_{Structural}} \tag{3-15}$$

The normal mode of vibration of an elastic resonator (an acoustic mode) faces damping due to its interaction with the ambient (liquid or gas), crystallographic defects, elastic waves and phonons. In general, the energy in the resonator is dissipated via the ambient, Q_{Air} (gas damping), through the anchors, Q_{Anchor} (anchor damping or loss) and its material itself, $Q_{Structural}=Q_{Material}+Q_{Thermoelastic}$ (material loss and thermoelastic damping) [114]. By scaling the resonator from the micro to the nano-scale and use of the vacuum as the working medium for the resonator, it seems that the thermoelastic and support loss play the dominant role in the damping sources that are later discussed [115-117]. It is important to note that, the Q-factor significantly decreases with size even when the resonators are made from the pure single-crystal materials and working in the vacuum and low temperature environments. Due to this reason, it is necessary to study the Q-factor precisely in nano-scale resonators. Individual Q-factors of a resonator are studied in next sections.

3.3.1 Gas damping

When a beam is moving in a fluid or gas, it collides with molecules of the fluid or gas and transfers some of its energy to them. When the beam moves perpendicular to a parallel plate with a small gap between them, it pushes the gas out of the gap and causes a damping force. Moreover, it compresses the gas in the gap and causes a spring force. The damping force is proportional to the gas damping factor, *b*, which is calculated as following [118],[119]:

$$b = \frac{96}{\pi^4} \frac{\mu l t^3}{g^3} \tag{3-16}$$

where μ is the viscosity of the medium around the beam. The spring force is proportional to the spring factor, *c*, which is defined as follows [119]:

$$c = \frac{1}{b\omega_c} \tag{3-17}$$

ω_c is the cut off frequency of the beam that is calculated by [119]:

$$\omega_c = \frac{\pi^2 g^2 P_0}{12\mu t^2} \tag{3-18}$$

where P_0 is the operating pressure. When the resonance frequency of the beam is larger than the cut off frequency, the spring force is more important than the damping force. The air mean-free path, λ_{atm}, at the atmosphere pressure, P_{atm}=101325 Pa, is 68 nm. When this value is larger than the gap, the viscosity is not independent of pressure and is defined as following in respect to the Reynolds equation [120]:

$$\mu = \frac{\mu_0}{1 + 9.638 K_n^{1.159}} \tag{3-19}$$

where μ_0 is the air viscosity and K_n is the Knudsen number that is calculated by [119]:

$$K_n = \frac{\lambda_0}{g} = \frac{P_n \lambda_n}{P_0 g} \tag{3-20}$$

where λ_0 is the air mean-free path at the operating pressure and λ_n is the air mean-free path at a known pressure, P_n. The quality factor due to the gas damping, Q_{Air}, is calculated by [121]:

$$Q_{Air} = \frac{\sqrt{k_b m_b}}{b} \tag{3-21}$$

3.3.2 Thermoelastic damping

When the resonator is in motion, it is taken out of the equilibrium and has excess energy. The movement of the resonator results in the strain gradient in the structure and consequently a temperature gradient. As the resonator tries to relax back to the equilibrium, the energy is dissipated within the irreversible heat flow. This damping basically shows the interaction of the normal mode of vibration of a resonator with the thermally-excited phonons. Two regimes for these thermal phonons are considered: Diffusive and ballistic regimes [116]. In the diffusive regime, the mean free path of the thermal phonon, l_T, is much smaller than the wavelength of the acoustic mode (dimensions of the resonator) and there is no need to treat them as individual excitations. In this regime, changes of length are related to changes of temperature with the material's thermal expansion coefficient, α', that defines the resonator mode and thermal phonons interaction. When l_T becomes much larger than the dimensions of the resonator, the regime becomes ballistic. In this regime the phonon-phonon scattering (Akheizer effect), ballistic transport of phonons between hot (the part of resonator in compression) and cold (the part in tension) parts of the resonator and the interaction of thermal and acoustic phonons are important. The material's thermal expansion coefficient is not valid in this regime.

In a resonator, there are torsional, flexural and longitudinal modes. The torsional mode has no local volume changes in the resonator and will not experience thermoelastic loss. In the longitudinal mode, we only have dissipation with a fixed peak that depends on the thermodynamic properties of the material as a function of temperature and does not change due to the scaling. The flexural mode is an important mode in resonators that was studied primarily by Zener [115]. He showed the damping behaviour of the anelastic thin beam in low order of flexural modes. The thermoelastic behaviour in the diffusive regime is defined by a single relaxation peak with a characteristic relaxation time, τ, that is proportional to w^2/χ. χ is the solid's thermal diffusivity. When the frequency of the resonator is much larger or smaller than τ, the system has small energy dissipation. In some papers they have tried to expand this formula for more general shapes of resonators except for beams or thin structures. In the ballistic regime τ is proportional to w/v where v is the phonon velocity. Later, R. Liftshitz et. al [115] showed that for the flexural mode even in the diffusive regime, the thermoelastic damping in silicon was playing an important role down to nano-metre scales in the temperatures above 100 K. The inverse quality factor due to the thermoelastic damping, $Q^{-1}_{Thermoelastic}$, is calculated by [115]:

$$Q^{-1}_{Thermoelastic} = \frac{E\alpha'^2 T}{C}\left(\frac{6}{\xi^2} - \frac{6}{\xi^3}\frac{\sinh\xi + \sin\xi}{\cosh\xi + \cos\xi}\right) \tag{3-22}$$

where α' is the thermal expansion, T is the operating temperature and C is the heat capacity of the beam. ξ is defined by [115]:

$$\xi = w\sqrt{\frac{2\pi f_0}{2\chi}} \tag{3-23}$$

3.3.3 Anchor damping

Each resonator is fixed to the surrounding structure and this provides a path for the radiation or vibrational energy to dissipate from the resonator. The quality factor due to the anchor damping, Q_{Anchor}, is calculated by [109]:

$$Q_{Anchor} = \frac{2 \times 2.43}{(3-\vartheta)(1+\vartheta)(\beta_n X_n)^2} \left(\frac{l}{w} \right)^3 \qquad (3\text{-}24)$$

where ϑ is the Poisson's ratio, X_n is the shape factor for a CC beam, where n shows the mode number of the resonator. This damping can be reduced by properly designing of the resonator so that it has a symmetrical vibration and a fixed centre of mass. G. Stemme [122] showed that an unbalanced resonator vibration yield energy losses at the mounts. In order to have a balanced resonator, it should have a fixed centre of gravity and sum of forces and moments due to vibration should be zero. An example for a balanced resonator is shown in Fig. 3.3.

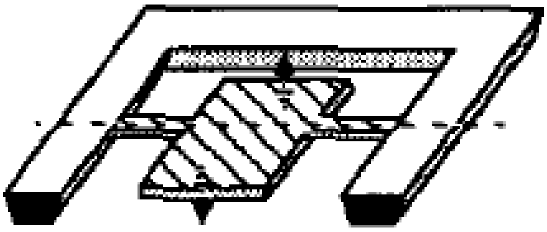

Fig. 3.3 A balanced resonator [122]

There are two places in the vibrating elements that do not have translational motion and are known as nodal points. The vibrating element is not suspending at the ends but at the nodal points so that we can use a few support elements at these points that allows minimal coupling and results in reduced energy dissipation through the anchors [114]. W. -T. Hsu et. al [123] studied a free-free beam micro-mechanical resonator (Fig. 3.4) that has the Q-factor greater than 10000. They showed that by using the support beams on opposite sides and placing them in the nodes of the FF beam, the energy loss was suppressed. Support beams vibrate in their second modes. Based on this structure, the resonance frequency and Q-factor were found to be sensitive to the length of the support beams.

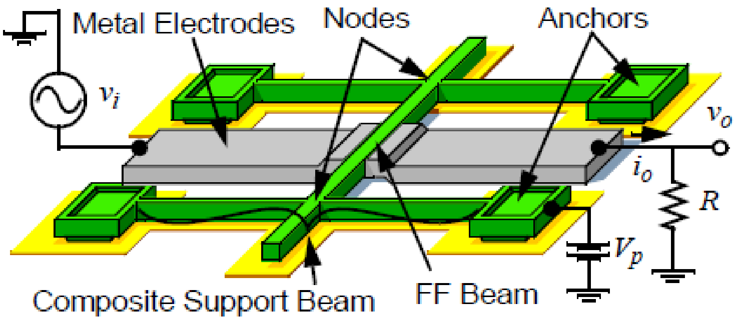

Fig. 3.4 The FF resonator [123]

G. D. Cole et. al [117] explained the reduction in anchor loss using the FF beam based on the “phonon-tunnelling”. They showed that anchor loss was becoming a dominant source of damping even in nano-scale resonators as the other damping sources could be reduced in low temperature and high vacuum. The phonon-tunnelling is explained as follows: The mechanical resonance is regarded as a phonon cavity that is coupled weakly to the exterior by a hopping process where the elastic energy leaks out of the resonator through the anchors [117]. They used the FF beam as an ideal platform to measure the phonon-tunnelling. They stated that the phonon tunnelling was reduced in the FF beam and the Q-factor was increased from 10^3 in CC beam to 5.1×10^4. By changing the place of the support beams and keeping the frequencies and surface-to-volume ratios of the resonators, they proved that this anchor loss was independent of scaling with a strong geometric dependency of the beam that was present in any suspended structure. The anchor loss in this structure is proportional to the radiated energy from support beams and is scaled like the squared deflection of contacts of the support beams with the main beam [124]. The quality factor due to phonon-tunnelling anchor loss, $Q_{Anchor\text{-}phonon}$, for a CC beam that has an in-plane movement in its first mode, is calculated by [124]:

$$Q_{Anchor-phonon} = \frac{3.9l^5}{2\pi^4 \tanh^2 \frac{1.5\pi}{2} tw^4} \tag{3-25}$$

3.3.4 Analytical values of damping sources for the NEM structure

This thesis assumes the resonator works at the atmosphere and at the temperature of 300 K. The Q_{Total} was calculated based on the three important damping sources (air, anchor and thermoelastic damping) that were explained in the previous sections. The $Q_{Anchor\text{-}phonon}$ was not considered for the calculation of Q_{Total} as this factor is a few orders of magnitude larger than other quality factors. The parameters used for the calculation of Q_{Total} are given in Table 3.1 and the calculated analytical parameters and quality factors are given in Table 3.2. As shown in Table 3.2, first the air and then the anchor dampings are smaller than the thermoelastic damping and put a limit on the Q_{Total}.

Table 3.1 Parameters used for calculations of the NEM structure

Dimensions	Silicon properties	Air properties	Other parameters
t=100 nm	E=130.18 GPa	ε_0 =8.85×10^{-12} F/m	β_0=1.5056
w=50 nm	ρ=2331 kg/m^3	μ_0=1.86×10^{-5} kg/(m.s)	X_0=-0.983
l=1 µm	α' =2.616×10^{-6} 1/K	P_n=P_0=P_{atm}=101325 Pa	
g=50 nm	C=700 J/kgK	λ_n=λ_0=λ_{atm}=68 nm	
	χ=0.86 cm^2/s	T_0=300 K	
	ϑ=0.33		

Table 3.2 Analytical values for the NEM structure

Key quantities	Quality factors
f_0=384.95 MHz	Q_{Air}=2085.90
m_b=8.56 fg	$Q_{Thermoelastic}$=868351.56
k_{bm}=50.08 N/m	Q_{Anchor}=4998.47
V_p=45.41 V	Q_{Total}=1469.24
C_{gap0}=17.7 aF	$Q_{Anchor\text{-}phonon}$=18961274.91
L_x=33.12 mH	
C_x=5.15 aF	
R_x=54.68 kΩ	
η=1.6×10^{-8} (V.F)/m	
ω_c=16.54 GHz	
μ= 1.259×10^{-6} kg/(m.s)	
b=9.926×10^{-12} (N.s)/m	
α=1.4×10^{-11} (N.s)/m	

3.4 Three-dimensional finite-element-method (3D FEM) analysis for the NEM structure

CoventoreWare software (see Appendix A.1) [125] was used for modelling the mechanical and electrical parts of the NEM structure. For modelling the NEM structure using the Designer, the metal contact pads were ignored as the side electrodes were heavily-doped silicon and a voltage could be applied to them directly. The preliminary dimensions for the modelled structure in Fig. 3.1 (a) were derived in a way that the highest displacement was gained by applying a specific pressure load to the beam or a voltage to side electrodes. Moreover, using these dimensions the in-plane movement for the dominant mode was gained. The effect of using different dimensions for the beam on its in-plane displacement and resonance frequency are shown in Appendix A.2. The mesh size for simulating the structure is 20 nm which is an optimized size to gain both speed and accuracy of the simulation. Different analyses are done for the NEM structure in next sections.

3.4.1 Mechanical analysis for the NEM structure

The mechanical analysis was done using the Analyzer to understand the stress distribution of the structure in the presence of an applied pressure load. A pressure load equal to 10 MPa was applied to one side of the beam and the corresponding von Mises stress distribution and displacement magnitude are shown in Figs. 3.5 (a) and 3.5 (b), respectively. Von Mises stress is a scalar stress value that is computed from the stress tensor. The central point of the beam has the largest displacement and clamped ends of the beam show the maximum Mises stress. In this simulation, the modal analysis was done by removing the applied pressure load. The modal analysis was used to verify that the suspended beam had an in-plane movement in the dominant mode. Three modes of the modal analysis are shown in Fig. 3.6 and their resonance frequencies are shown in Table 3.3. The modal analysis for the suspended beam was done in the absence of any type of external applied force and because of this the shown displacement in Fig. 3.6 is zero for all modes. The first mode shows the beam movement in y direction and is equal to 432.47 MHz. The frequency of the first mode was considered as the resonance frequency of the beam.

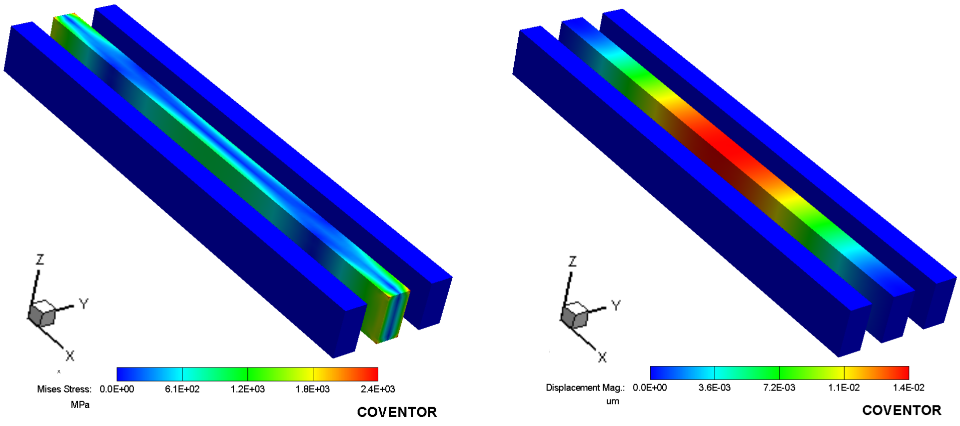

(a) (b)

Fig. 3.5 (a) Von Mises stress distribution and (b) the displacement magnitude of the NEM structure in the presence of 10 MPa pressure load

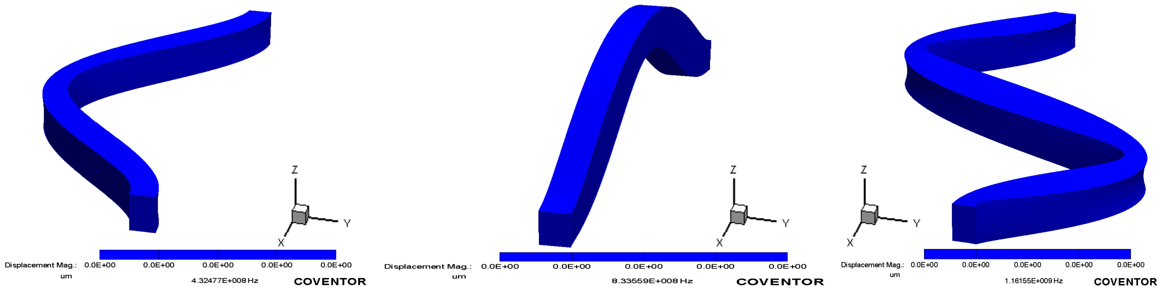

First Mode **Second Mode** **Third Mode**

Fig. 3.6 The modal analysis for the suspended beam of the NEM structure

Table 3.3 The resonance frequencies of the first three modes of the NEM structure

Mode no.	Frequency (MHz)
1	432.477
2	833.559
3	1161.55

Harmonic analysis was also done as a part of the mechanical analysis. In this analysis a sinusoidal pressure load with the magnitude of 1 kPa was applied to the side of the beam by considering a range of frequency. The full movement of the suspended beam in this analysis is shown in Fig. 3.7. The magnitude and phase of the in-plane displacement versus frequency are shown in Figs. 3.8 (a) and 3.8 (b), respectively. When the frequency of the applied pressure is equal to the resonance frequency of the beam, it resonates and shows a large peak for the displacement at the resonance frequency as shown in Fig. 3.8 (a). Figure 3.8 (b) shows also a change of 180 deg for the displacement of the beam at the resonance frequency.

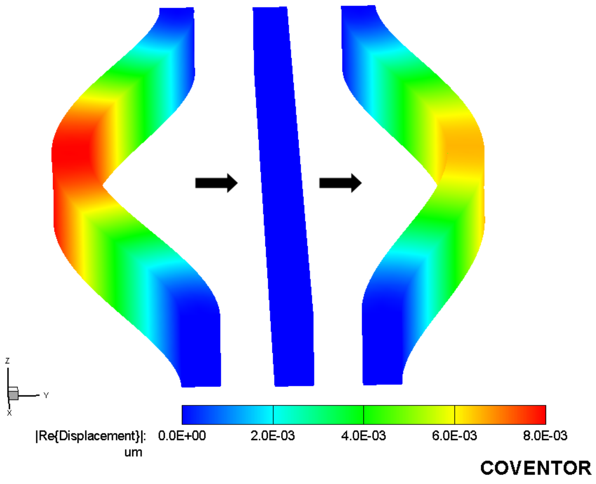

Fig. 3.7 The lateral displacement of the suspended beam in the presence of a sinusoidal pressure load

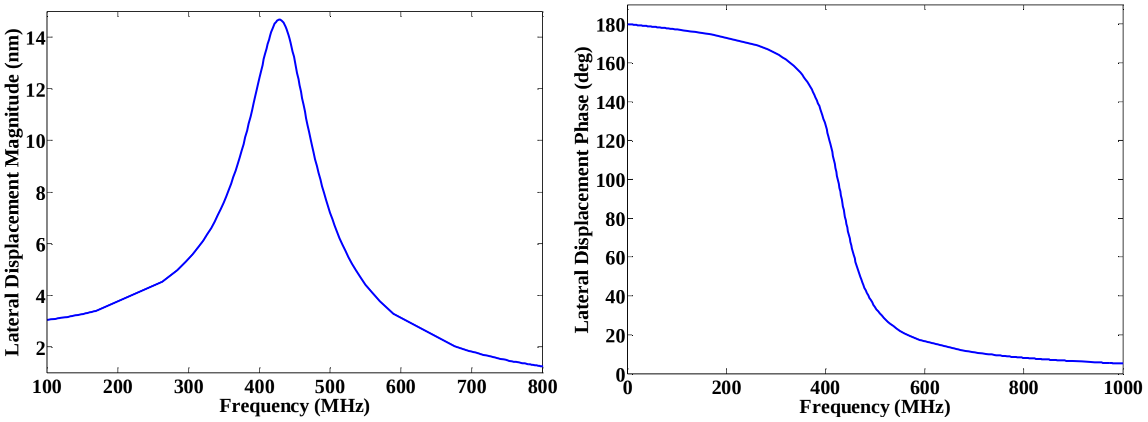

(a) **(b)**

Fig. 3.8 (a) The magnitude and (b) phase of in-plane displacement of the suspended beam versus frequency in the presence of a sinusoidal pressure load

3.4.2 Electro-mechanical analysis for the NEM structure

In the electro-mechanical analysis, a DC voltage was applied instead of the applied pressure load in the mechanical analysis. The stress distribution was then investigated in the presence of electro-static force using this method. For this structure the “detect pull-in” analysis was chosen in order to obtain the pull-in voltage. A range of constant voltage 0-60 V was applied to one of the electrodes to measure the pull-in voltage. The present beam design results in the pull-in voltage of 56.95 V as shown in the displacement versus voltage characteristics in Fig. 3.9. Figure 3.9 shows a good compatibility between the simulated pull-in voltage and the analytical value in Table 3.2. The pull-in happens when the displacement is about half of the gap due to the fact that the displacement of the central point is significant for the CC beam. In order to operate the NEM structure within a safe margin, the operating voltage was chosen to be well below the pull-in voltage.

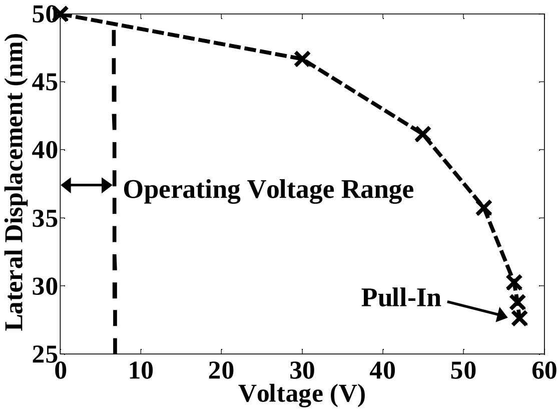

Fig. 3.9 The lateral displacement of the suspended beam versus voltage

3.4.3 Numerical values of damping sources for the NEM structure

CoventorWare has the capability of simulating the air, anchor and thermoelastic damping for the resonator using the mechanical analysis. The derived numerical values generated by the software are shown in Table 3.4. An infinite substrate was defined for the beam in order to simulate the anchor damping and avoid the reflection from the substrate back into the resonator. Considering a BOX layer for the substrate affects this assumption and causes a difference between the analytical and numerical values for the Q_{Anchor}. The software uses slightly different parameters for silicon and air as well as using Zener model for the thermoelastic simulation that causes difference between the analytical and numerical values for the Q_{Air} and $Q_{Thermoelastic}$.

Table 3.4 Numerical values for the NEM structure

Key quantities	Quality factors
f_0=432.47 MHz	Q_{Air}=2563.08
b=9.075x10^{-12} (N.s)/m	$Q_{Thermoelastic}$=680632.73
V_p=56.95 V	Q_{Anchor}=3153.67
	Q_{Total}=1411

3.4.4 The alternative FF beam for the NEM structure

As explained in section 3.3.4, the anchor damping after the air damping will put a limit on the quality factor of the sensor. The air damping is reduced by using vacuum as the operating medium for the beam, but the anchor loss cannot be avoided until there is optimization of the design for the resonator. Using a FF beam for the resonator is a suitable candidate that may reduce the anchor damping [126]. The designed FF NEM structure is shown in Fig. 3.10 (a). Four support beams are connected to the sides of the main beam. There are two nodes in the main beam that experience zero-displacement. Each pair of support beams will be connected to the sides of the main beam in these zero-displacement nodes. The support beams are designed to vibrate in the second vibration mode of the FF beam. The vibration mode of the structure is shown in the inset to Fig. 3.10 (a). The width of the support beams, w_s, is extracted from [123] and the length of the support beams, l_s, is calculated as follows:

$$l_S = 1.683\left[\sqrt{\frac{E}{\rho}}\frac{w_S}{f_0}\right]^{1/2} \tag{3-26}$$

The anchor damping of the structure is changed by changing the position of the support beams and minimized at a specific position along the main beam. Figure 3.10 (b) shows the anchor dissipation versus the distance of the support beams from the centre of the main beam. The same dimensions as the suspended beam in Fig. 3.1 (a) were used for the main beam. The dimensions of the support beams and the electrodes are given in Table 3.5. As shown in Fig. 3.10 (b), by positioning the support beams 300 nm away from the centre of the main beam, the anchor damping or dissipation is minimum and almost zero. Numerical value of quality factors for the NEM structure with the designed FF beam positioned at 300 nm away from the centre of the main beam, are shown in Table 3.5. Table 3.5 shows that using the FF beam for the NEM structure, the Q_{Anchor} was improved about four orders of magnitude and it did not limit the Q_{Total} of the structure. Furthermore, the $Q_{Thermoelastic}$ is reduced by using low operating temperature. Even if the resonator works in the atmosphere and at room temperature, the Q_{Total} was larger for the designed FF NEM structure than that of the CC NEM structure.

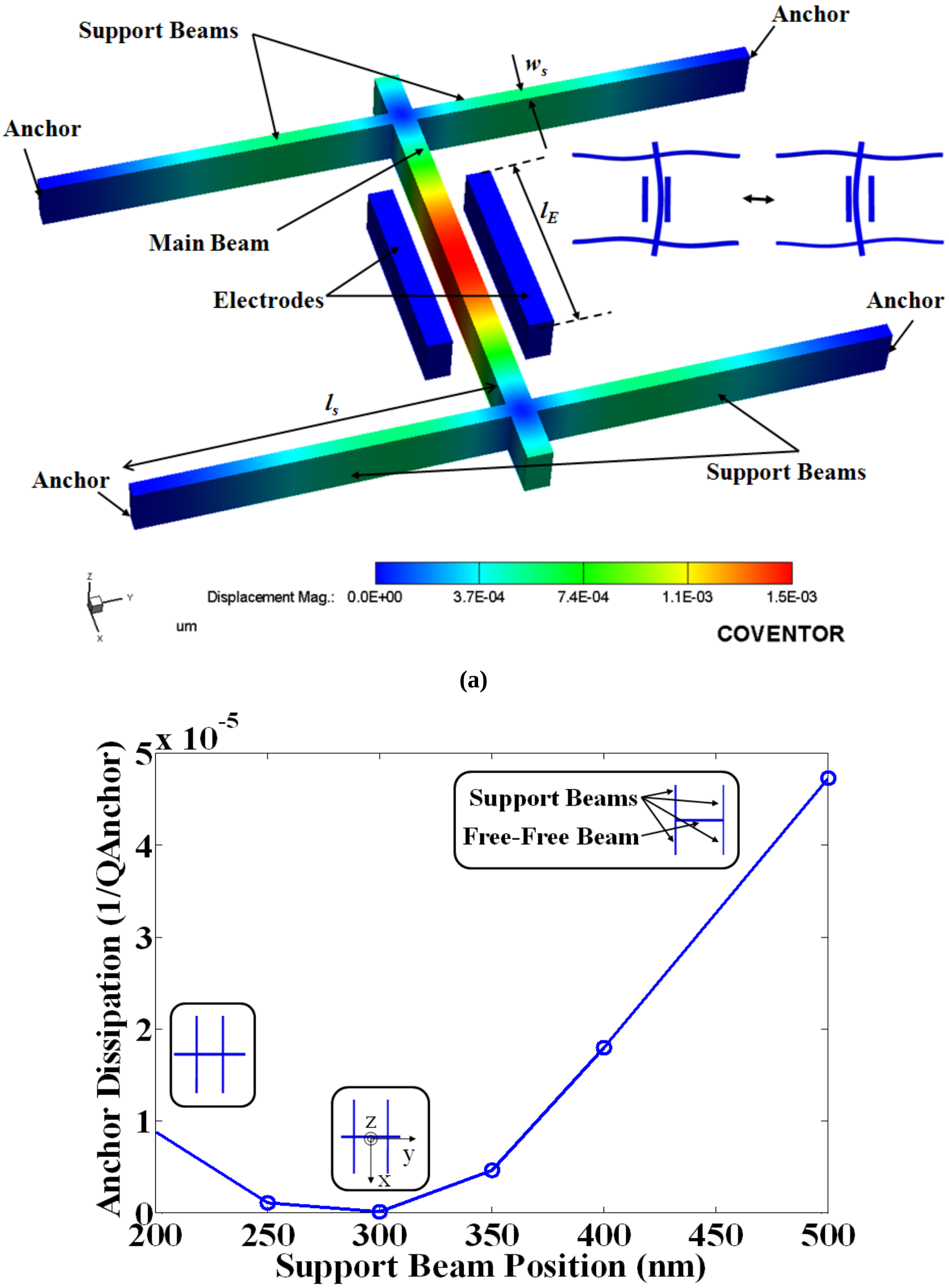

(a)

(b)

Fig. 3.10 (a) The FF NEM structure and (b) the anchor dissipation of the structure versus the distance of support beams from the centre of the main beam

Table 3.5 Parameters used and numerical values for the FF NEM structure (support beam position= 300 nm)

Dimensions for the support beams	Dimension of the side electrode	Key quantities	Quality factors
w_s=30 nm	l_e=400 nm	f_0=368.75 MHz	Q_{Air}=8348.71
l_s=1.178 µm		b=3.5632x10^{-12} (N.s)/m	$Q_{Thermoelastic}$=1462838.84
			Q_{Anchor}=10535972.28
			Q_{Total}=8294.79

3.4.5 Impacts of surface modification on the resonance frequency of the NEM structure

In order to detect biological and chemical molecules, the surface of the suspended beam will be functionalized by using various self-assembled monolayer (SAM) linker molecules. For example, the silane couplers such as Amino-propyltrimethoxysilane (APTES) are used to convert the silanol groups of the native oxide to active amino groups. The other method is to make the H-terminated silicon surface active for sensing by using alkenes or alkyne-based molecules. Most likely the distribution of linker molecules on the surface will be conformal while the target molecules may adsorb sparsely onto the linker molecules. Figure 3.11 shows a schematic view of the linker and adsorbed target molecules to the surface. The sensing process consists of two steps of functionalization and detection processes.

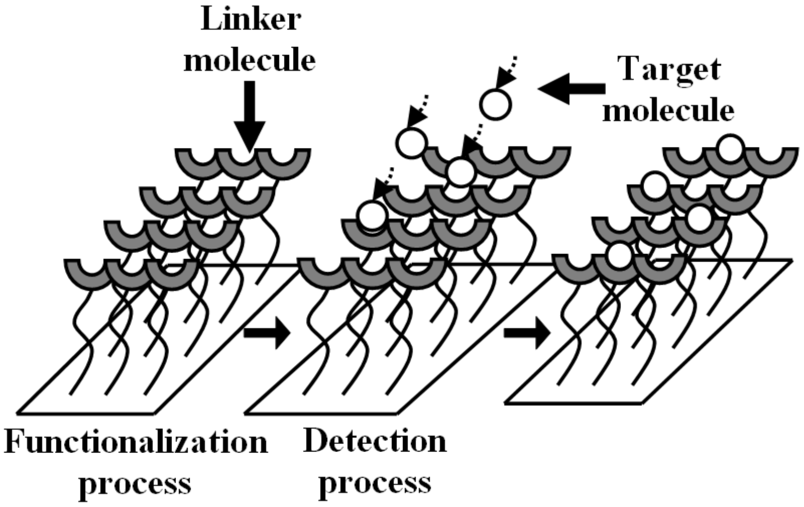

Fig. 3.11 A schematic view of the linker and adsorbed target molecules to the surface

3.4.5.1 Modelling of the functionalization process

In the present simulations, such self-assembled linker molecules on the silicon beam surface are modelled simply by adding an extra surface coating layer onto the suspended beam as linker molecules are coated on the surface homogeneously. The surface coating layer was introduced in Designer [125], by using various insulator/polymer materials. In practice, the surface functionalization processes are performed either in liquid or in vapor and may result in different surface coating configurations. The three coating configurations are studied: Top-and-bottom (TB), only top (OT) and all-around (AA) coating.

With the TB configuration, two surface layers with the same thickness are considered on the top and bottom of the beam. The TB configuration is shown schematically in Fig. 3.12 (a). This configuration may be suitable to describe the coating in liquid as it is unlikely that molecular solution flows through the nano-scale gap between the suspended beam and the electrodes as freely as above and under the beam. The OT configuration is considered in Fig. 3.12 (b) as the molecular solution does not flow under the beam when the bottom air gap is also narrow. If both the side and bottom gaps are designed to be wide enough, all the surfaces maybe coated equally as shown in Fig. 3.12 (c). This is also the likely case for the coating in vapor as the vapor flow can go through narrow gaps more easily than the liquid flow.

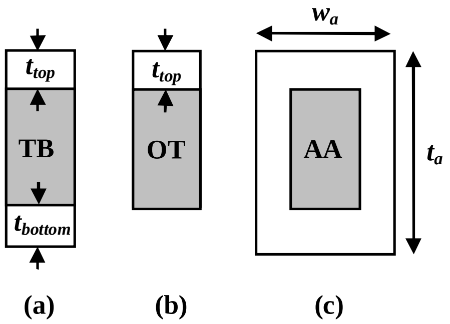

Fig. 3.12 The coating configurations: (a) Top-and-bottom (TB) (b) only top (OT) and (c) all-around (AA)

With the TB configuration, three parallel springs should be considered to calculate the mechanical spring stiffness of the coated beam analytically. For this reason both ends of the coating layers were clamped similar to the clamped ends of the beam. The total mechanical spring stiffness, $k_{bm\text{-}TB}$, is:

$$k_{bm-TB} = 30.78\left(\frac{w}{l}\right)^{3}[Et + E_c(t_{top} + t_{bottom})] \tag{3-27}$$

where, E_c, is the young's modulus of the coating layer, t_{top}, and, t_{bottom}, the thickness of top and bottom layers ($t_{top}=t_{bottom}$). The calculated mass for the beam with the TB configuration is:

$$m_{b-TB} = m_b + 0.735\rho_c w(t_{top} + t_{bottom})l \qquad (3\text{-}28)$$

where, ρ_c, is the density of the coating layer. Eqs. (3-27) and (3-28) are used for the OT considering t_{bottom}=0. For the analytical study of the total mechanical spring stiffness, $k_{bm\text{-}AA}$, of the AA configuration, two parallel springs were used considering the assumption of anchored ends of the coating layer similar to the TB configuration. $k_{bm\text{-}AA}$ is calculated by:

$$k_{bm-AA} = 30.78\{ Et\left(\frac{w}{l}\right)^3 + [\frac{E_c}{l^3}(t_a w_a^3 - tw^3)]\} \qquad (3\text{-}29)$$

where, t_a, and, w_a, are the thickness and width of the beam after adding the coating layer, respectively. The calculated mass for the beam for the AA configuration is:

$$m_{b-AA} = m_b + 0.735\rho_c l(w_a t_a - wt) \qquad (3\text{-}30)$$

A previous study [127],[128] on a micro-resonator showed that the deposition of coating materials over a resonating beam affects not only the mass but also the mechanical spring stiffness that results in a change in the resonance frequency both toward higher or lower frequencies with respect to the resonator structural materials. The effect of adding surface coating on the resonance frequency due to changes in both mass and spring stiffness of the beam was studied first analytically and then using numerical simulation. Eqs. (3-27)-(3-30) indicate both spring stiffness and mass increase by increasing the thickness of the coating layer. The changing rates of mass, ($\Delta m_{bl}/m_b$), and mechanical spring stiffness, ($\Delta k_{bml}/k_{bm}$), depend on the configuration of the coating layer. Here, Δm_{bl} and Δk_{bml} are changes of the mass and spring stiffness due to linker molecules. For example for a 1 nm-thick coating layer in the TB configuration, the mass of the beam changes by 1.75% while the spring stiffness changes by 1.07%. According to eq. (3-2), a larger change in the mass leads to a lower resonance frequency after adding the coating layer. Due to a 0.81% change in the mass and a 0.51% change in the spring stiffness for the 1 nm-coating layer in the OT configuration, the resonance frequency decreases. On the other hand, for the AA configuration, a 5.60% change in mass and a 7.90% change in spring stiffness result in a resonance frequency larger than that for an un-coated beam. In conclusion, the coating layer on the side surfaces of the beam, which is in the direction of the beam displacement, affects the spring stiffness more significantly than its mass. This effect is also validated using the simulation later on in Fig. 3.14.

3.4.5.2 Modelling of the detection process

The linker molecules in the previous section were modelled as a uniform coating layer because it is expected the homogenous and dense SAM layer is formed on the beam surface after the functionalization process. In contrast, the adsorption of target molecules to the functionalized surface is random and sparse as shown in Fig. 3.11. The sparse adsorption of target molecules changes the effective mass of the beam without much affecting the spring stiffness of the beam. In order to model the random distribution of target molecules, simply the density of the modelled coating layers with various configurations increased only rather than introducing random target molecules explicitly. This method allows us to only study the impact of the mass increase due to adsorbed target molecules on the resonance frequency.

3.5 3D FEM and hybrid circuit analysis for the IP R-NEM sensor

The modelling of linker and target molecules for the functionalization and detection processes described in sections 3.4.5.1 and 3.4.5.2 were then introduced into the 3D FEM analysis to simulate the impact of different functionalization schemes and evaluate the mass responsivity of the IP R-NEM sensor for the detection process. For the present 3D FEM simulation, it was assumed that the both ends of the coating layer were not anchored. This assumption may cause some differences with the results of the analytical calculations, which assumed the coating layer was also doubly clamped. In reality, it does depend on the details of the surface coating of the resonator at the clamping points whether or not the non-anchored model is more appropriate. The thickness of the added layers for the functionalization process was varied in 3D FEM analysis to see its effect on the resonance frequency. As the other part of 3D FEM analysis, the density of the coating layer was varied to model the sparse target molecules in the detection process. Further details on the simulation results of the 3D FEM analyses are given in the next section.

After conducting the 3D FEM analysis of the NEM structure, a hybrid NEM-MOS circuit model was prepared using Architect [125] to analyze the complete IP R-NEM sensor as shown in Fig. 3.1 (b). Figure 3.13 (a) shows the beam and side electrode components that exist in the Architect library and are used for the circuit model of the sensor. Figure 3.13 (b) shows the hybrid circuit model for the IP RNEM sensor, which consists of a NEM part including the electrodes and a suspended beam and a MOSFET detection part. The suspended beam was modelled by using two central beam components and two extra side beam components. Two central beam components were used in order to define the node at the centre and measure the displacement, *y*, as shown Fig. 3.13 (b). The length of the side beam components are set in order to keep the design similar to the Designer modelling in section 3.4.1. A DC voltage was applied to the beam, V_{dc}, for biasing and an AC voltage, V_{ac}, was applied to the electrode. The amplitude of V_{ac} is smaller than V_{dc} and its frequency is equal to the mechanical resonance frequency of the suspended beam. The output AC voltage is defined at the node shown by *out* in Fig. 3.13 (b). The mechanical part is connected to the electrical part using resistances. R_1 was used to model the resistance of the gate but R_2 was applied to connect the mechanical and electrical parts without receiving any error from software. The value of R_1 and R_2 were set to 10 MΩ but later the R_2 value was reduced to the smallest value as possible, so as the resonance behaviour of the sensor could be still valid for the small values of R_2. The n-MOSFET has the 1 μm-channel length same as the length of the beam. To study the impact of adding the coating layer on the output voltage of the designed sensor, the coating layer onto the beam was introduced in the circuit model. The same assumption of non-anchored ends for the coating layer was also applied here. The results are discussed in next section.

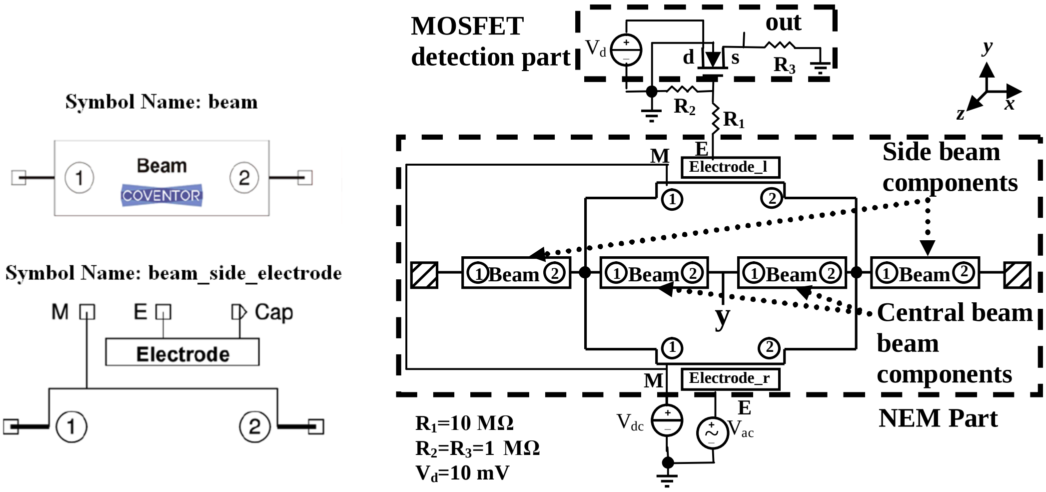

(a) (b)

Fig. 3.13 (a) Beam and side electrode components in the Architect library [125], (b) the circuit model for the IP R-NEM sensor

3.5.1 Simulation results for the IP R-NEM sensor

In this section, the impact of functionalization process on the resonance frequency is discussed by using the 3D FEM and hybrid circuit analysis. The evaluation of the mass responsivity for the detection process and the scalability issue of the sensor are discussed finally.

3.5.1.1 Impact of different functionalizations

A coating layer was added to the beam surface in different configurations (Fig. 3.12) in order to model the liquid and vapor phase techniques for the functionalization process in Fig. 3.11. Figure 3.14 shows the resonance frequency versus the coating layer thickness for the TB, OT and AA configurations. In Fig. 3.14, the frequency decreases in the TB and OT configurations by increasing the coating layer thickness that shows the dominant effect of mass as was expected from the analytical model in section 3.4.5.1. Change in the resonance frequency is lower for the OT configuration than the TB configuration due to its smaller value of the coating layer mass using eq. (3-2). Higher resonance frequencies for the OT configuration are explained by the smaller mass of coating layer for the OT configuration than in the TB configuration. On the contrary, the resonance frequency increases by increasing the coating layer thickness in Fig. 3.14 as was expected from section 3.4.5.1 because of the dominant effect of the spring stiffness enhancement for the AA configuration.

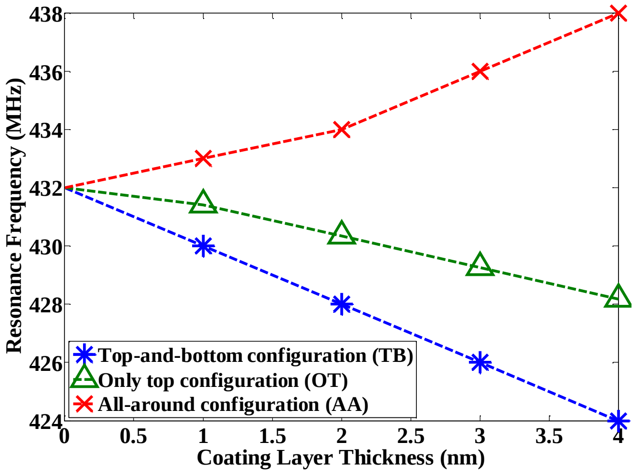

Fig. 3.14 The resonance frequency versus thickness of the coating layer for the TB, OT and AA configurations

The harmonic analysis was done for the structure with the AA configuration. A sinusoidal pressure load with the magnitude of 1 kPa was applied in a specified range of frequency that resulted in a peak of the lateral displacement of the beam at the resonance frequency. The magnitude of the in-plane displacement versus frequency for different thicknesses of coating layer are shown in Fig. 3.15. The resonance frequency was increased slightly by increasing the coating layer thickness in the AA configuration as was expected from Fig. 3.14.

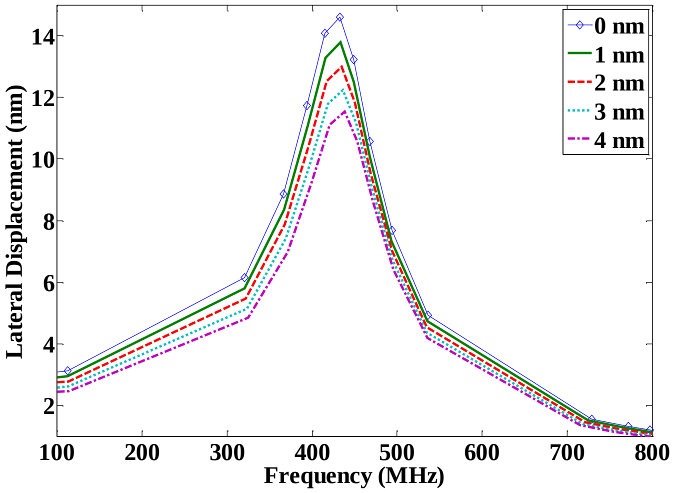

Fig. 3.15 The lateral displacement versus frequency for different thicknesses of coating layer in the AA configuration

After investigating the 3D FEM analysis of the NEM part of the sensor after the functionalization process, the behaviour of the full sensor including the MOSFET detection part was studied using the hybrid NEM-MOS circuit model presented in section 3.5. For the DC transfer analysis, a range of DC voltages were applied to the electrode and the pull-in and pull-out cycles were investigated for the sensor. The IP R-NEM sensor operates by applying low voltages and shows small displacements. So, the pull-in will not happen as a wanted event. For small voltages the achieved displacement from Designer and Architect are similar even though the physical phenomena of the sensor was modelled more precisely using Designer. The displacement and capacitance versus voltage is shown in Figs. 3.16 (a) and 3.16 (b), respectively. By increasing the applied voltage to the side electrode, the displacement of the suspended beam increases and the gap between side electrode and beam decreases. Smaller gap results in larger capacitance. At pull-in voltage the electro-static and spring forces are equal and the beam will collapse against the electrode. If the voltage decreases from this value, the electro-static force becomes larger than the spring force at the voltage called pull-out voltage and the beam becomes separated from the electrode. By decreasing the voltage, the gap increases and smaller capacitance is obtained.

For the small signal ac analysis, a range of frequency was chosen to derive the frequency spectrum of the sensor. The lateral displacement, y, versus frequency for the beam at V_{dc}=50 V is shown in Fig. 3.17 (a). The y-axis shows the decibel value of displacement. The derived resonance frequency for the displacement, that is equal to 443.87 MHz, is near to the resonance frequency obtained using the Analyzer, and this value is used to perform the transient analysis in the next step. The output voltage versus frequency at V_{dc}=50 V is also shown in Fig. 3.17 (b). The peak and dip presumably present the resonance and anti-resonance frequency [47] of the beam as shown in Fig. 2.32, that are 448.87 MHz and 497.41 MHz, respectively.

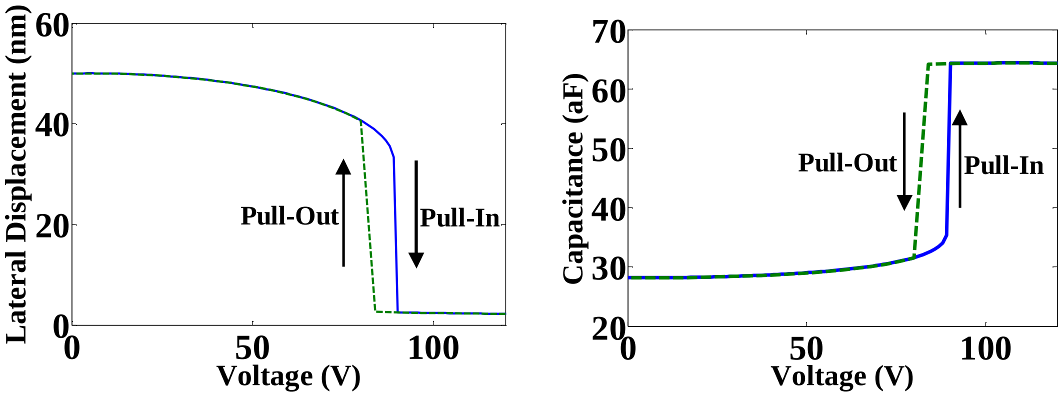

(a) (b)

Fig. 3.16 (a) The displacement versus voltage and (b) the capacitance versus voltage

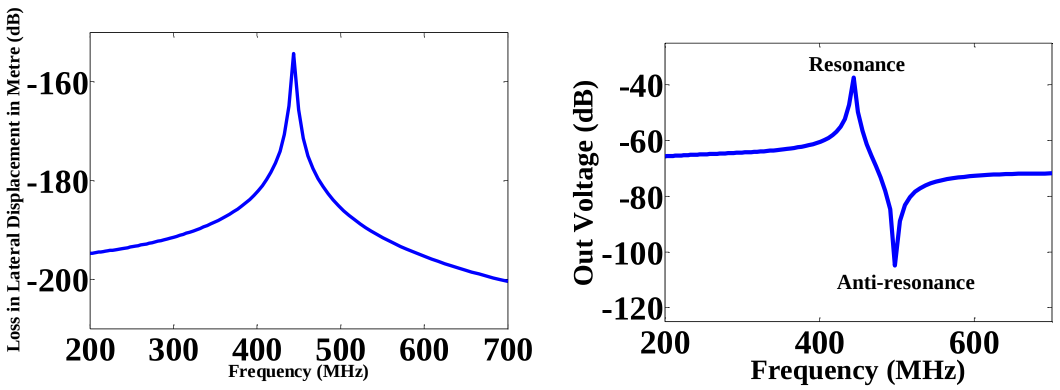

(a) (b)

Fig. 3.17 (a) The loss in lateral displacement versus frequency and (b) the out voltage versus frequency

To investigate the effects of gap changes on the resonance frequency, the gap was changed from 50 to 30 nm for three different DC voltages. The displacement versus frequency for different gaps and voltages are shown in Fig. 3.18. Figure 3.18 (a) shows that at V_{dc}=50 V, if the gap is decreased, the spectrum shifts to lower frequencies. This trend is compatible with eq. (3-6) that shows by reducing the gap, k_{be} increases and results in smaller k_b with respect to eq. (3-5) and consequently lower f_r with respect to eq. (3-7). For V_{dc}=30 V in Fig. 3.18 (b), this effect is only visible when the gap reduced from 40 nm to 30 nm. By reducing the applied voltage to V_{dc}=10 V in Fig. 3.18 (c) and also reducing the gap, there will not be a shift for the resonance frequency as the effect of k_{be} on k_b is smaller for smaller V_{dc}. Figure 3.18 shows that by reducing the gap in different applied DC voltages, the widening of the resonance frequency spectrum is larger which means a smaller Q-factor. This is due to the fact that only Q_{Air} is considered as the dominant factor in these results that included assumption that the resonator was working in the atmosphere and at room temperature. By reducing the gap with respect to eq. (3-16), the damping factor increases and results in smaller Q-factor due to eq. (3-21).

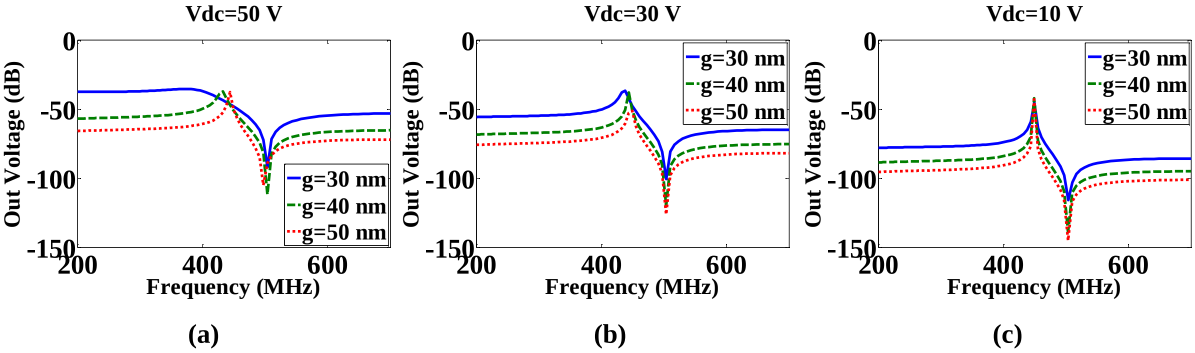

Fig. 3.18 The out voltage versus frequency at V_d=10 mV for different gaps at: (a) V_{dc}=50 V, (b) V_{dc}=30 V and (c) V_{dc}=10 V

The resonance frequency for g=50 nm at V_{dc}=10 V to 70 V are shown in Fig. 3.19. Figure 3.19 shows that by increasing V_{dc} from 10 V to 70 V, the resonance frequency decreased due to increasing of k_{be} with respect to eq. (3-6) and causes reduction in k_b and consequently reduction in the resonance frequency with respect to eq. (3-7). The reduction of the resonance frequency with increasing of V_{dc} is called spring softening [108]. Reduction in k_b causes smaller Q_{Air} with respect to eq. (3-21) and results in wider resonance frequency spectrum as shown in Fig. 3.19.

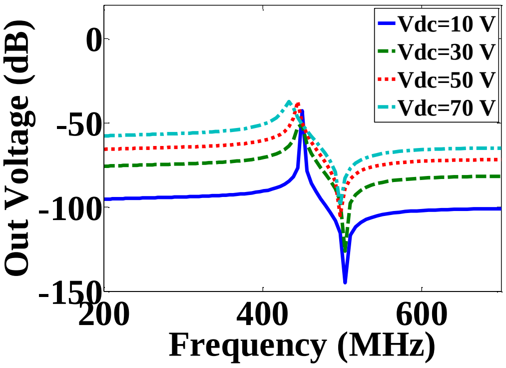

Fig. 3.19 The out voltage versus frequency for g=50 nm at different V_{dc}

The width of the beam was increased to 53 nm to study the effect of increasing the mass of the beam on the resonance frequency. Figure 3.20 shows the comparison of displacement versus frequency for two different masses for the beam. The changes in the mass, Δm= 1.11 fg, causes the variation of the resonance frequency, Δf, equal to 28.992 MHz. This result emphasizes the high sensitivity of the sensor response to small changes in the mass and makes it suitable for molecular biosensing. It is important to note that, using eq. (3-2), even though the mass of the beam is increased by increasing its width, the effect of increasing of the spring stiffness remained dominant and resulted in higher resonance frequency for the wider beam.

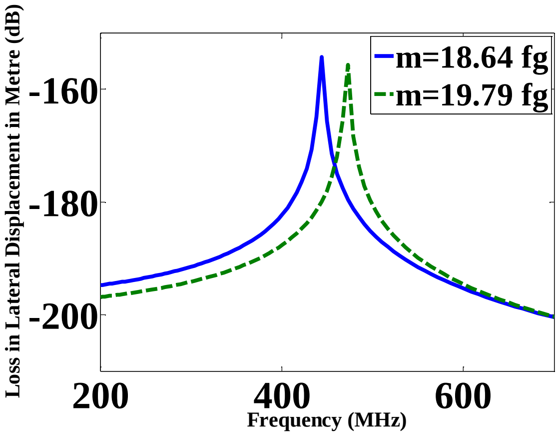

Fig. 3.20 The comparison of loss in lateral displacement versus frequency for different mass values

Figure 3.21 shows the output voltage versus frequency calculated with different coating layer thicknesses of the TB and AA configurations. The frequency spectra of the output voltage shift to low frequencies by increasing the thickness of the coating layer for the TB configuration (Fig. 3.21 (a)) while the trend is reverse for the AA configuration (Fig. 3.21 (b)). These results show the effect of the mass change is dominant for the TB configuration and the effect of the spring stiffness change is dominant for the AA configuration as explained previously in this section. These results are consistent with the previous 3D simulation results in Fig. 3.14.

Transient response analysis was also conducted by setting the frequency of the ac voltage equal to the resonance frequency of the un-coated beam obtained from the small signal analysis. The transient response is shown in Fig. 3.22. The transient output signal reaches the steady state with the response time of approximately 400 ns after the ac signal was applied. The sinusoidal behaviour of the output voltage shows that the beam is resonating with high speed and the overall damping of the output is determined by the intrinsic mechanical damping of the beam.

The piezo-resistive effect is widely applied to NEM/MEM sensors to improve their performance [129-132]. For this reason applying this effect to the IP R-NEM sensor is studied in Appendix A.3.

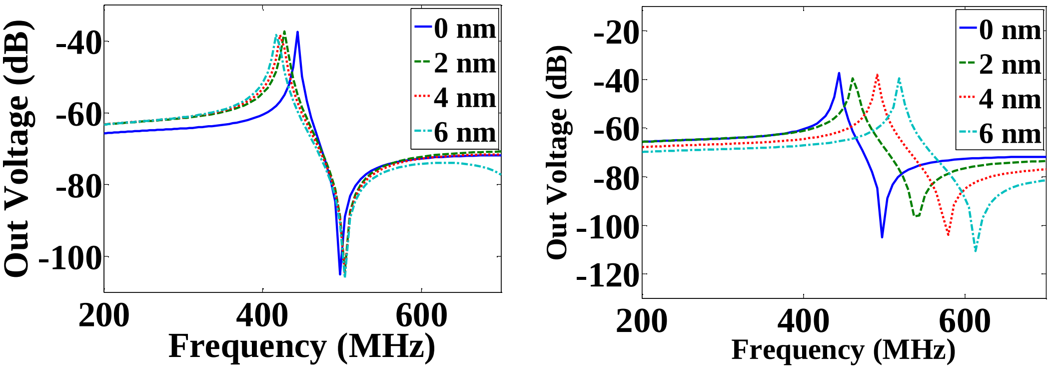

(a) **(b)**

Fig. 3.21 The output voltage versus frequency for different coating layer thicknesses of the (a) TB and (b) AA configurations

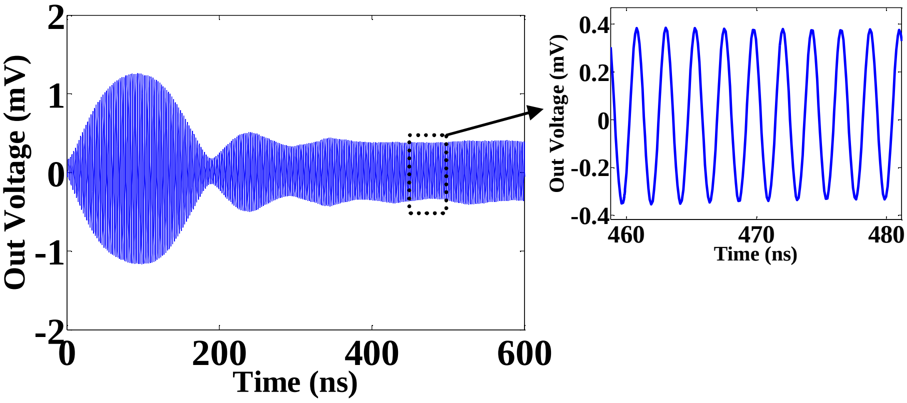

Fig. 3.22 The transient out voltage for the IP R-NEM sensor

3.5.1.2 Evaluation of mass responsivity

To model the target molecules adsorption, the density of the coating layer for different configurations was increased as explained in section 3.4.5.2. Figure 3.23 shows the resonance frequency calculated for the TB, OT and AA coating configurations as a function of total mass of the surface coating layer and adsorbed target molecules. Regardless of the different coating schemes, the increase in the mass due to adsorbed molecules decreases the resonance frequency linearly. The inverse slope of the resonance frequency versus mass shows the mass responsivity, *S*. *S* is calculated as follows:

$$S \approx \frac{\Delta m_{ba}}{\Delta f} = \frac{\Delta m_{ba}^{3/2}}{k_{bm}^{1/2}} \tag{3-31}$$

where Δm_{ba} is changes of the mass due to adsorbed molecules and are also considered as the minimum detectable mass [39]. Figure 3.23 shows virtually the same S values of 0.05 zepto g/Hz for all configurations regardless of modified resonance frequency with different functionalization schemes and independent of the surface area of the beam that was used for adsorption.

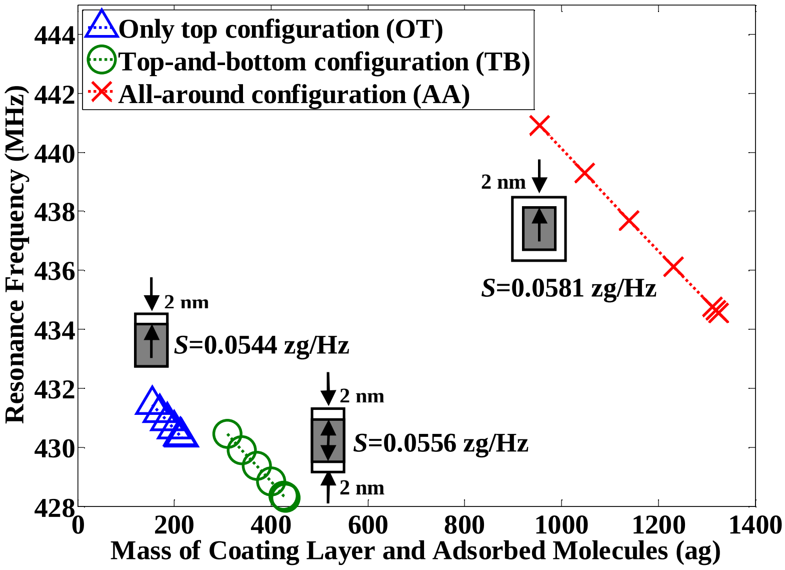

Fig. 3.23 The resonance frequency versus mass for different coating configurations

Considering several noise processes in the operation of a resonator Δm_{ba} is calculated as following [39]:

$$\Delta m_{ba} \approx S\left(\Delta f_{BW} \frac{2\pi f_0}{Q_{Total}}\right)^{1/2} 10^{(-DR/20)} \tag{3-32}$$

where Δf_{BW} is the maximum allowable measurement bandwidth that is $\sim f_0/Q_{Total}$ and DR represents the effective dynamic range intrinsic to the resonator:

$$DR(dB) = 10\log(E_C / k_B T) \tag{3-33}$$

where Boltzmann constant, k_B, is 1.38×10^{-23} J/K and the maximum drive energy for the in-plane CC beam is $E_C \approx m_b 4\pi^2 f_0^2 0.53^2 w^2$. Using eqs. (3-31)-(3-33) Δm_{ba} is calculated equal to 11.73 atto g.

In Table 3.6, characteristics of the IP R-NEM sensor is compared to that reported for recent commercial mass-detection biosensors based on the QCM technique in Table 2.3. As an example, a type of protein was considered as the target molecule in the IP R-NEM sensor. By assuming that the protein has a sphere shape with a minimal radius of near 2 nm, same as the thickness of 2 nm for the coating layer in Fig. 3.23, it has the molecular weight of 20 kDa (1 Da= 1.6605×10^{-24} g) [133]. Considering the mass detection limit of the order of 11.73 atto g for the IP R-NEM sensor, about maximum number of 353 protein molecules can be detected by the sensor in the case of conformal and full coverage of the protein molecules onto the surface of the beam.

Table 3.6 Comparison of the IP R-NEM sensor and the commercial QCM biosensors

Biosensor	Mass detection limit	Q-factor	Mass responsivity	Sensing area	Fundamental frequency	Ref.
Q-Sense E4	-	$\geq 10^5$	27 ng/Hz	1.54 cm^2	5 MHz	[87]
QCM Initium AFFINIX Q	100 pg	$\geq 10^5$	30 pg/Hz	0.049 cm^2	27 MHz	[85]
Mark 21 QCM sensor	56.6 μg	-	18 pg/Hz	0.1007 cm^2	50 MHz	[88]
IP R-NEM sensor	11.73 atto g	1411	0.05 zepto g/Hz	3×10^{-9} cm^2	448.87 MHz	-

Using the conversion method for the LOD presented in section 2.2.3, the LOD for the IP R-NEM sensor will be calculated as follows. If the molecular weight of one mole of DNA is equal to 20×10^3 kg, V_s = 7 $\times10^{-14}$ cm^3 based on the beam dimensions in Fig. 3.1 (a) and Δm_{ba}=11.73 atto g for the IP R-NEM sensor, eq. (2-1) shows x= 8.37×10^{-9} mol/L. The derived LOD is located just below the LOD reported for other mass-detection based biosensors in Fig. 2.13. It should be noted that the solution concentration LOD is not necessarily a must requirement because some of recent products such as AFFINIX system recommend that users prepare the target solution with molar concentration as high as possible. Such QCM biosensors are not intended to detect a small amount of biomolecules from very dilute solution but to study real-time monitoring of biomolecular interaction.

A few of the most recent research works on mass-detection based NEM sensors using a CC beam with different materials [89],[111],[134-136] are given in Table 3.7. The IP R-NEM sensor shows higher sensitivity than that of the stated sensors in Table 3.7. One of the silicon carbide (SiC) CC beams in Table 3.7 shows the same order of mass responsivity for the IP R-

NEM sensor which is due to the larger Young's Modulus of SiC than that of Si. The calculated mass responsivity for the FF NEM structure in Fig. 3.10 (a) with the support beams 300 nm away from the centre of the main beam and with the OT configuration is S=0.2363 zg/Hz. This value shows that even though a larger quality factor was achieved for the sensor using the FF beam compared to the CC beam, but the FF NEM structure had also a larger value for the mass responsivity that shows a trade off between the quality factor and the mass responsivity.

Table 3.7 Comparison of the recent mass-detection based NEM sensors

Ref.	Material	Type of beam	Frequency (Hz)	Quality factor	Temperature	Medium	Mass responsivity or detection limit
[111]	SiC	CC	32.8 M	3000	17 K	Ultra High Vacuum	0.06 zepto g Hz $^{-1}$
[134]	SiC	CC	428 M	2500	22 K	Vacuum	0.27 zepto g Hz $^{-1}$
[135]	SiC	CC	190 M	5000	300 K	Ultra High Vacuum ($<10^{-10}$ Torr)	0.86 zepto g Hz $^{-1}$
[136]	Carbon nano-tube	CC (Fe-coated)	470 M	15	Room	Vacuum (10^{-6} Torr)	~1 atto g
[89]	Silicon nano-wire	CC (Metallized)	200 M	2000	25 K	Vacuum	0.71 zepto g Hz $^{-1}$

3.5.1.3 Scalability of mass responsivity

Downscaling MEMS leads to novel applications that are capable to achieve remarkable sensitivity in the detection of displacement, mass, force and charge [135-139]. The unprecedented mass responsivity of the designed IP RNEM sensor is the result of the reduction of dimensions. To study the scalability for the presented mass-detection based sensor, the dimensions of the beam were enlarged by the scaling factors, k, of 10, 100 and 1000. Table 3.8 shows the scaling rule for mass, spring stiffness, resonance frequency and mass responsivity evaluated by using the analytical models given by eqs. (3-2)-(3-4) and eq. (3-31). The numerical simulation was conducted using the above-mentioned scaling factors, k, to clarify the scaling rule for the present structure accurately. For this simulation the beam that is functionalized in the AA configuration was chosen because the mass responsivity is virtually independent of the functionalization process as shown in Fig. 3.23. Figure 3.24 shows the calculated mass responsivity versus the scaling factor, which indeed shows that the mass responsivity increases from zg/Hz to pg/Hz with the scaling rule of k^4 by increasing the scaling factor as indicated by the analytical model. This scaling rule provides a good guiding principle for the resonator design depending on the needs of mass responsivity.

Table 3.8 Scaling rules for key parameters of the IP R-NEM sensor

Parameter	Scaling rule
w, l, t	k
m_b	k^3
k_{bm}	k
f_r	k^{-1}
S	k^4

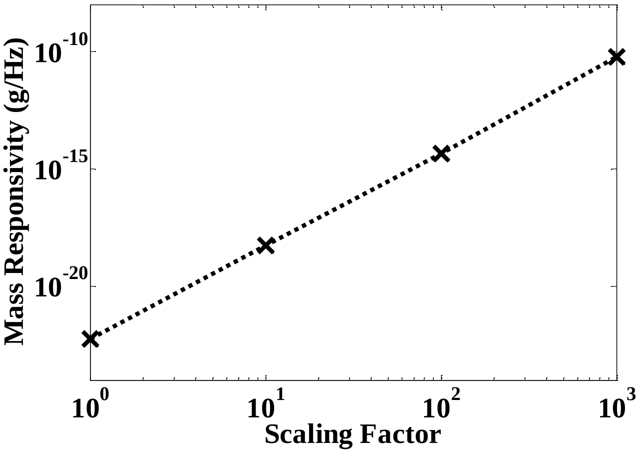

Fig. 3.24 The calculated mass responsivity versus the scaling factor

3.6 Summary

I presented the design and analysis of the NEM structure and then the IP R-NEM sensor that is based on mass-detection principle and can be used as a bio/chemical sensor with a higher responsivity than that of the recent commercial QCM sensor and mass-detection based NEM sensors. The proposed sensor was designed and simulated using both 3D FEM simulation and hybrid NEM-MOS circuit simulation in order to investigate its characteristics both in physical and circuit-level. Linker species are adsorbed onto the suspended beam in the functionalization process and they have been modelled by adding extra layers to the beam in different configurations. The target molecules in detection process have been modelled by changing the density of the coating layer. By modelling the functionalization and detection processes, the simulation results have shown that the IP R-NEM sensor achieves an extreme mass responsivity of the order of zepto g/Hz that is unique among available mass-based sensors. The calculated scaling rule of k^4 for the resonator provides a good guiding principle for the resonator design depending on the needs of mass responsivity. The fabrication of the NEM structure and IP R-NEM sensor are discussed in the next chapter along with further processing of available NWs.

CHAPTER 4

In-plane resonant NEM sensor: Fabrication

In this research three devices are fabricated for different purposes. First, some post-processing is conducted for the provided non-suspended nano-wires (NWs) in collaboration with the Tokyo Institute of Technology (TIT). The fabrication process of NWs is based on Fig. 4.1. J. Ogi et. al [140] first patterned a silicon (Si) NW and double side gate electrodes on a 50 nm-thick silicon-on-insulator (SOI) layer heavily-doped with ion implantation, by using electron beam (EB) lithography and anisotropic electron cyclotron resonance reactive ion etching (ECR RIE). Then the buried-oxide (BOX) layer under the NW channel was isotropically etched with liquid hydrofluoric (HF) acid, and a suspended NW channel was formed. Both liquid and vapor HF etching are used for the suspension of NWs. For the second device, the NEM structure is fabricated at the Southampton Nanofabrication Centre (SNC) in the University of Southampton. Figure 4.2 illustrates an outline of the fabrication process for the NEM structure that includes a clamped-clamped (CC) beam with two side electrodes. Moreover, the fabrication includes a free-free (FF) NEM structure. The fabrication is planned in four steps of lithography that are EB lithography of the structures on the heavily-doped SOI wafer that is thinned down, photo-lithography for patterning the contact holes above the silicon-pads of the beam and side-electrodes, photo-lithography for patterning the wiring and contact pads in Aluminium (Al) and photo-lithography for patterning the windows above the beam for making it suspended using HF etching. For the third device, one of our partners in the NEMSIC project, Commissariat à l'Energie Atomique-Laboratoire d'Electronique et de Technologie de l'Information (CEA-LETI), is responsible for the fabrication of the in-plane resonant NEM (IP R-NEM) sensor. For this reason, the mask layout for the IP R-NEM sensor as well as the NEM structure is designed with respect to the CEA-LETI's process technology. The mask layout is designed before starting the fabrication at SNC. The simplified steps of CEA-LETI's fabrication technology for the IP R-NEM sensor are given in Fig. 4.3. The details of the mask layout and the fabrication process are discussed later. A summary for the devices that includes their structures, features including beam and MOSFET dimensions, the frequency range based on the numerical analysis, the purpose of the fabrication and finally the reason for moving towards the fabrication of the next device are given in Table 4.1.

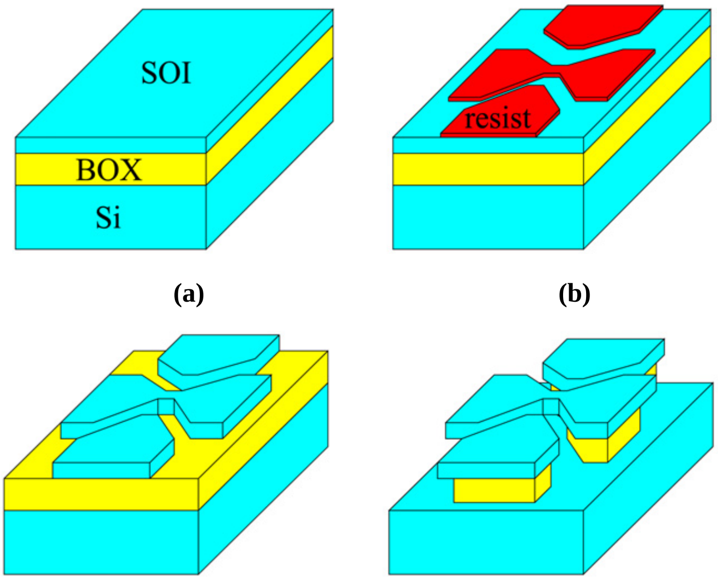

(a) (b)

(c) (d)

Fig. 4.1 Basic fabrication process of the suspended NW [140]: (a) Thinned down heavily-doped SOI wafer, (b) EB lithography for patterning the NW in resist, (c) anisotropic dry etching to pattern the NW in the SOI layer and (d) isotropic wet etching for releasing the NW

4.1 Post-processing on NWs

The non-suspended NWs were fabricated on an SOI wafer with the SOI thickness of 53 nm and BOX thickness of 200 nm using the fabrication process as explained earlier in this chapter. NWs have the width, *w*, of 100 nm, gap, *g*, of 150 nm and different lengths, *l*, of 500 nm, 1000 nm, 1500 nm and 2000 nm and the working in-plane frequency range, f_0, of 218.4 MHz-3.2 GHz. The N-type doping for the wires is 2×10^{19} cm^{-3}. Figure 4.4 shows the design of NWs in one chip. Each chip contains four NWs. The scanning electron microscope (SEM) views of NWs with different lengths in a chip are shown in Fig. 4.5.

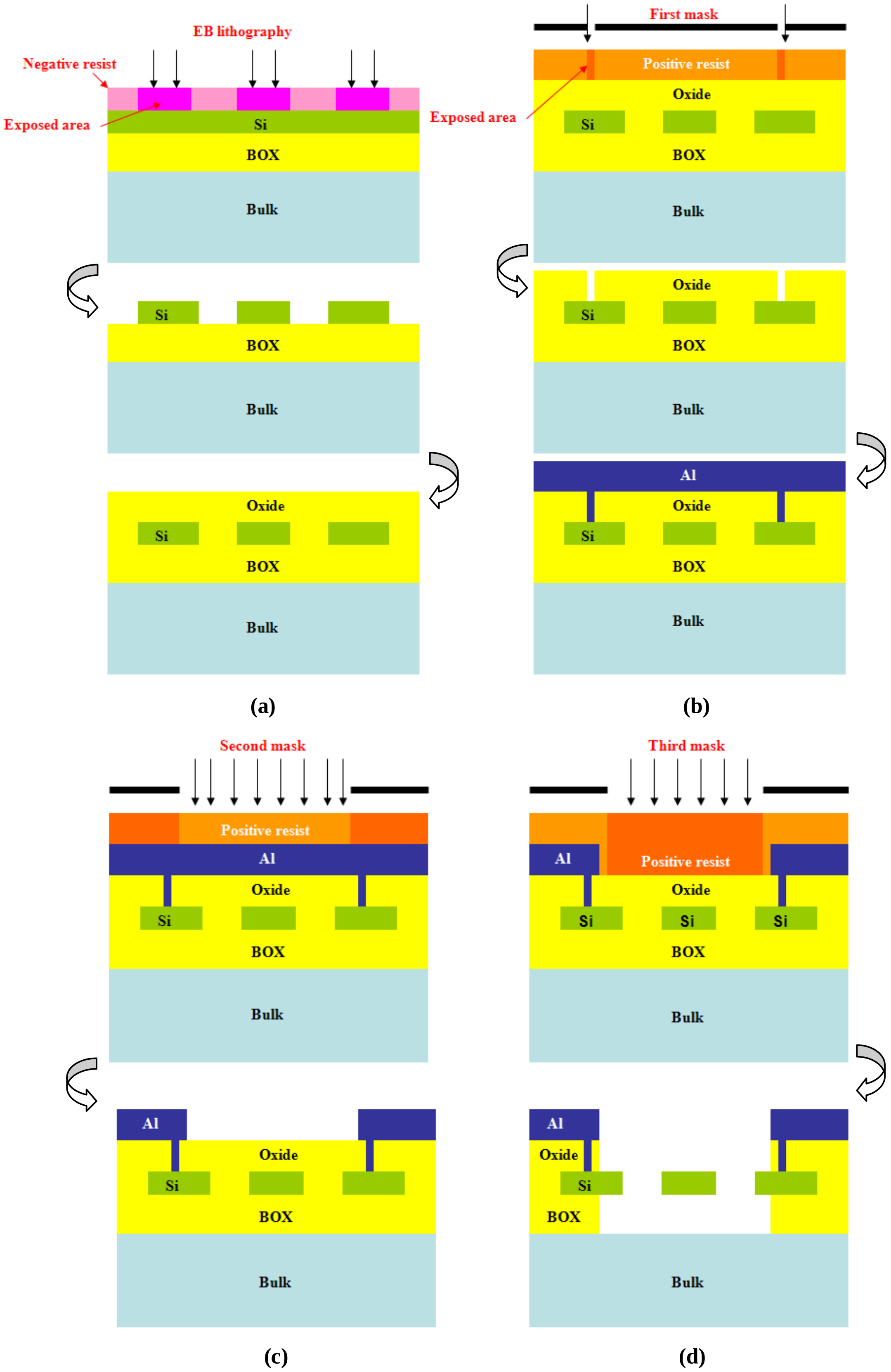

Fig. 4.2 Four steps of the fabrication process for the NEM structure: (a) EB lithography for patterning the SOI layer, (b) photo-lithography for patterning contact holes, (c) photo-lithography for patterning contact pads and wiring and (d) photo-lithography for opening a window above the beam for its subsequent release

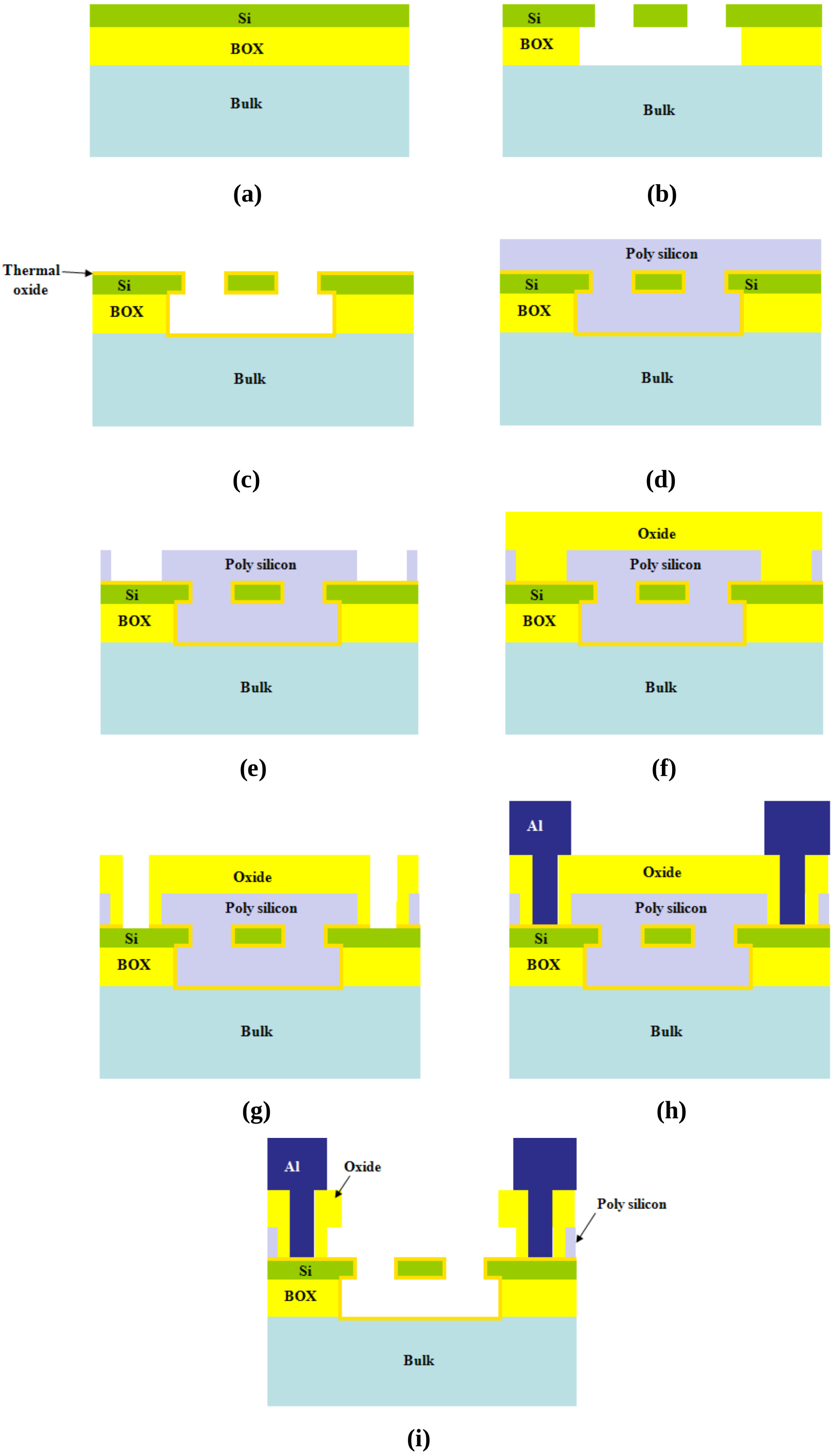

Fig. 4.3 Fabrication process steps of the IP R-NEM sensor: (a) Doping implantation for the whole wafer except some protected parts by resist, (b) silicon patterning and vapor HF release of beams, (c) oxidation, (d) poly silicon deposition, (e) opening contact holes in poly silicon, (f) oxide deposition, (g) opening contact holes in oxide (h) Al deposition and patterning for contact pads and wiring and (i) open window in oxide and poly silicon above the beam for its subsequent release

Table 4.1 A summary on the structures and features of the fabricated devices

Device	Fabricated at	Device name	Device structure	Device features			Purpose	Motivation for the next fabrication step
				Beam	MOSFET	Resonance frequency (Numerical)		
A	TIT+SNC	NW	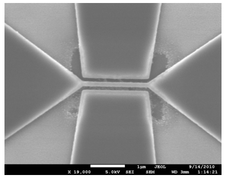	▪ Dimensions: l=500-2000 nm w=100 nm t=53 nm g=150 nm ▪ Doping: $N^+=2\times10^{19}$ cm^{-3}	-	First in-plane mode: 218.4 MHz-3.2 GHz	▪ Suspension of NWs using both liquid and vapor HF ▪ DC and RF measurement using capacitive response	No existing metal contact pad
B	SNC	NEM structure	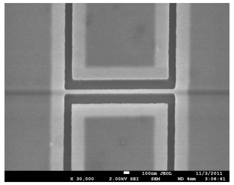 CC	▪ Dimensions: l=400 -2000 nm, l=4-32 µm t=50 nm w=45-135 nm g=80-200 nm ▪ Doping: $N^+=2\times10^{19}$ cm^{-3}	-	First in-plane mode: 1.9-22.7 MHz 98.3 MHz-4.4 GHz	DC and RF measurement using capacitive response	Improve the output signal using transistor response
			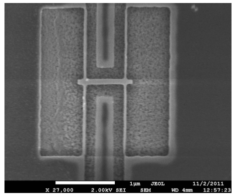 FF	▪ Dimensions: l=1000 nm t=50 nm w=45,135 nm g=80-140 nm w_s=28,82 nm l_s=1010,1192 nm ▪ Doping: $N^+=2\times10^{19}$ cm^{-3}	-	First in-plane mode: 176.3 MHz,380.2 MHz	▪ Improve the quality factor of the CC NEM structure ▪ DC and RF measurement using capacitive response	
C	CEA-LETI	IP R-NEM sensor	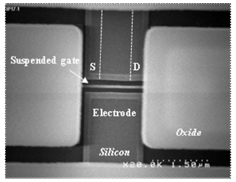	▪ Dimensions: l=400-2000 nm t=40 nm w=45-135 nm g=80-200 nm ▪ Doping: $N^+=4\times10^{19}$ cm^{-3} $P^+=1\times10^{19}$ cm^{-3}	$l_S=l_D$=295 nm l_C=250-1250 nm Type $N^+/P/N^+$ $P=1\times10^{16}$ cm^{-3} Type $P^+/P/P^+$ $P=1\times10^{15}$ cm^{-3}	First in-plane mode: 98.2 MHz-2.3 GHz	DC and RF measurement using transistor response and lock-in technique	-

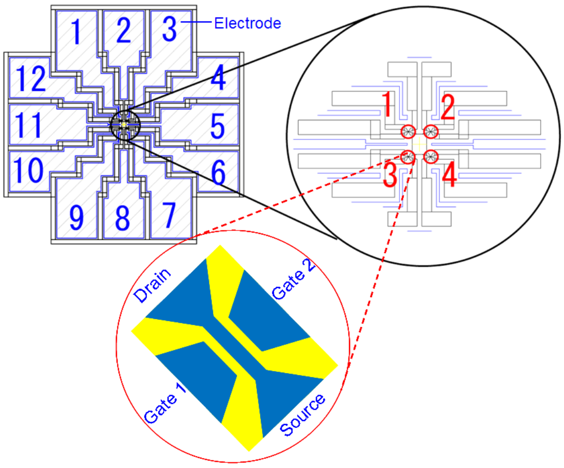

Nano-wire	Lenght
1	500 nm
2	1000 nm
3	1500 nm
4	2000 nm

Fig. 4.4 The layout of NWs and their dimensions

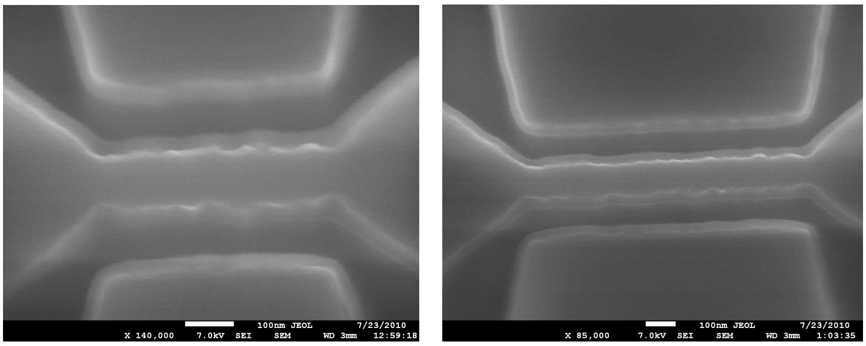

Length= 500 nm **Length= 1000 nm**

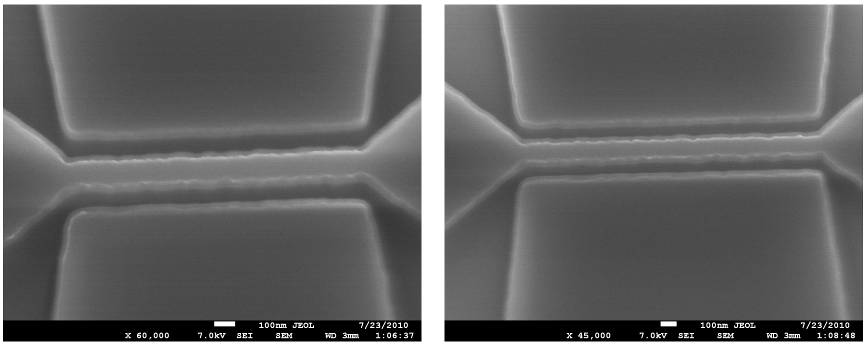

Length= 1500 nm **Length= 2000 nm**

Fig. 4.5 SEM views of the non-suspended NWs

After doing some measurement on the non-suspended NWs that are explained in the next chapter, two chips of NWs are separately released using liquid and vapor HF. For releasing NWs in the first set, buffered HF (BHF) 20:1 was used for ~9 minutes to etch 200 nm of BOX layer underneath the NWs. The etch rate for BHF 20:1 is 24 nm/min. The SEM views of the suspended NWs are shown in Fig. 4.6. The suspension using liquid HF caused the problem of producing fibres around NWs as shown in Fig. 4.7 (a). BHF 20:1 was used for 1 minute to remove the fibres that were assumed to be silicon fibres. BHF did not remove the fibres which led me to assume they were polymer fibres. The cleaning process included: O_2 plasma ashing for 5 minutes, rinsing with acetone and isopropyl alcohol (IPA) followed by drying with nitrogen gun to remove the fibres. The cleaned NW is shown in Fig. 4.7 (b). In the next chapter, the suspended NWs showed high current at the applied zero voltage across NWs due to the trapped charges in the native oxide layer around the NW that could be passivated by annealing. NWs were annealed in tube furnace at 400 ^{o}C for 30 minutes in the (argon) Ar and (nitrogen) N_2 environment. Further details on the DC characterization of the cleaned and annealed NWs are given in the next chapter.

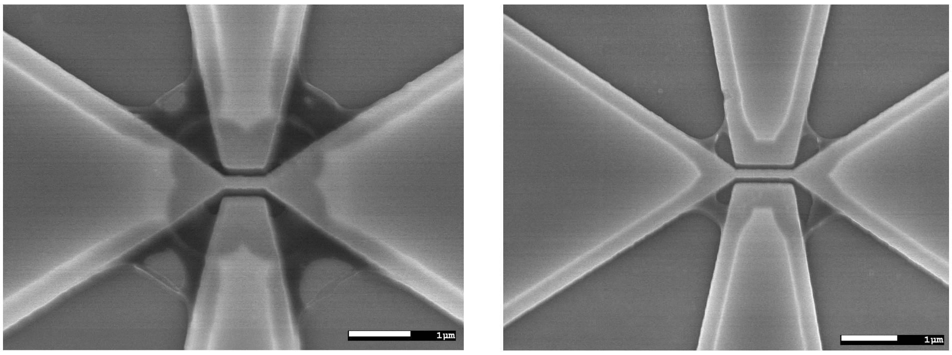

Beam length= 500 nm **Beam length = 1000 nm**

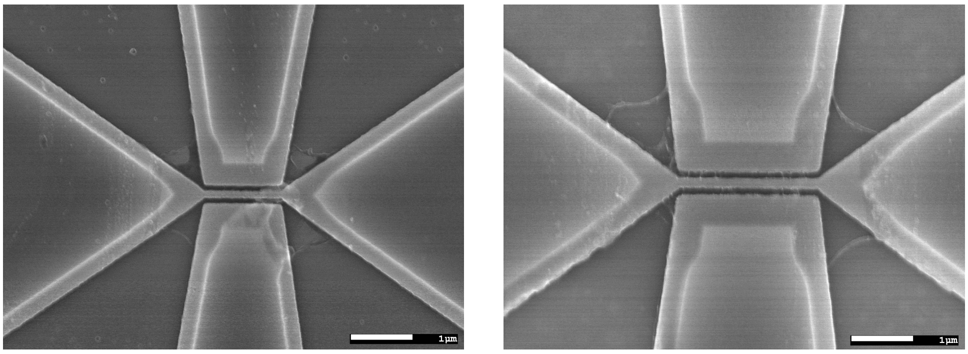

Beam length = 1500 nm **Beam length = 2000 nm**

Fig. 4.6 SEM views of the suspended NWs using BHF 20:1

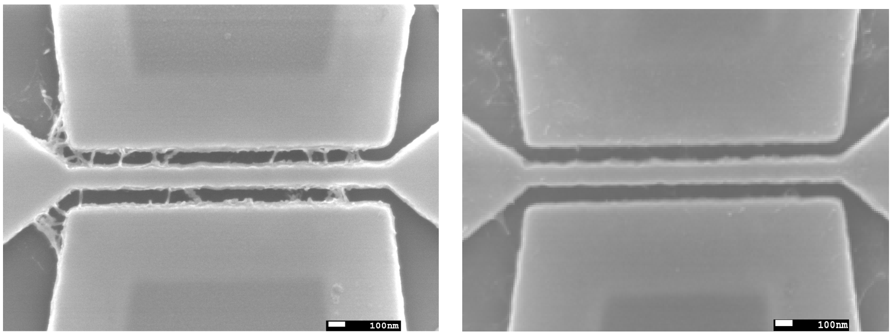

(a) **(b)**

Fig. 4.7 The suspended NW with the length of 2000 nm released by BHF 20:1: (a) Polymer fibres around the NW after the releasing process and (b) the cleaned NW from polymer fibres

To avoid the possible contamination in wet etching process and the possible bending of NWs and their stiction to the substrate [141] especially for the longer NWs, vapor HF was used for the etching of the BOX layer and releasing NWs. Vapor HF used for 2 minutes at temperature=45 ^{o}C did not produce polymer fibres around NWs. Further details of the benefits of using vapor HF for the suspension are discussed in the next chapter. The SEM views of the suspended NWs with different lengths are shown in Fig. 4.8.

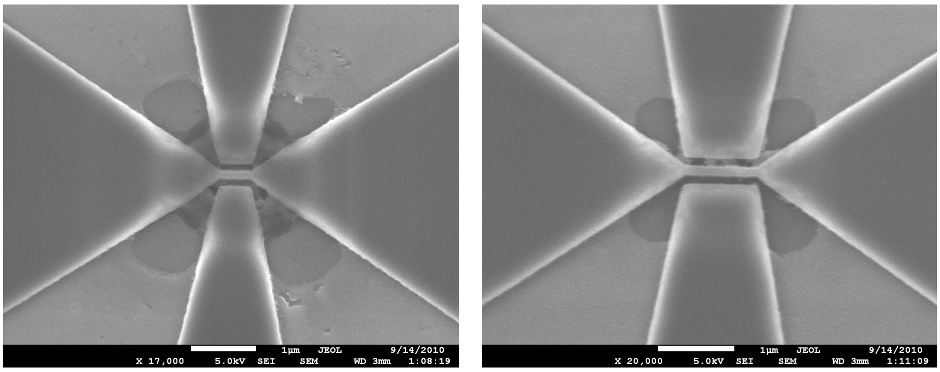

Beam length = 500 nm **Beam length = 1000 nm**

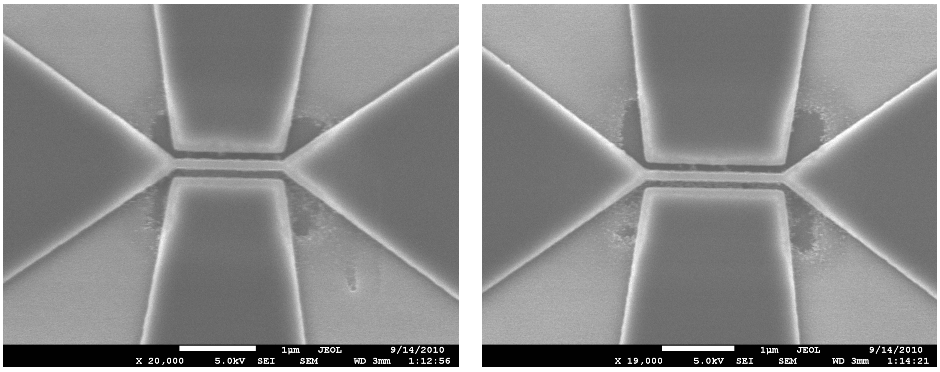

Beam length = 1500 nm **Beam length = 2000 nm**

Fig. 4.8 SEM views of the suspended NWs using vapor HF

4.2 Fabrication of CC and FF NEM structures

The mask layout of the CC and FF NEM structures were designed for different dimensions of beam, electrode length, gap and radio frequency (RF) measurement pad structures. The details of mask layout and the fabrication process are given in the following sections.

4.2.1 Mask layout

The mask layout includes the NEM structure with the working in-plane frequency range, f_0, of 1.9-22.7 MHz and 98.3 MHz-4.4 GHz. For each device, a 50 Ω-resistance measurement pad was used that had been designed in collaboration with the École Polytechnique Fédérale de Lausanne (EPFL) (Fig. 4.9). The RF pads in Fig. 4.9 are compatible with a ground-signal-ground (GSG) probe with the pitch of 150 µm as shown in Fig. 2.34 (b). Figure 4.9 (a) shows the suitable RF pad for the gas-detection. In the other configuration for the RF pad in Fig. 4.9 (b), the metal contact pads are far from the device that helps us to use this space for introducing the target liquid to the structure for the bio-detection.

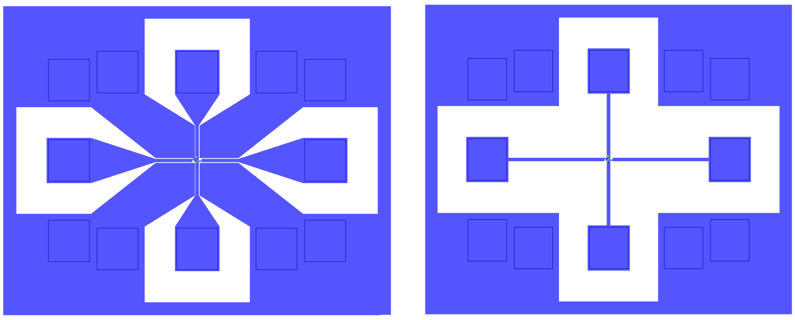

(a) **(b)**

Fig. 4.9 RF measurement pads for: (a) Gas-detection and (b) bio-detection

The layout of the RF pad and its wiring to the NEM structure are shown in Fig. 4.10. The contact holes in Fig. 4.10 have different dimensions of 2.5×2.2 cm^2 and 3×3 cm^2 in mask layout. The minimum wiring-width of 2 µm and the minimum spacing of 1.5 µm between wires were used. The dimensions for beams of NEM structures are given in Table 4.2.

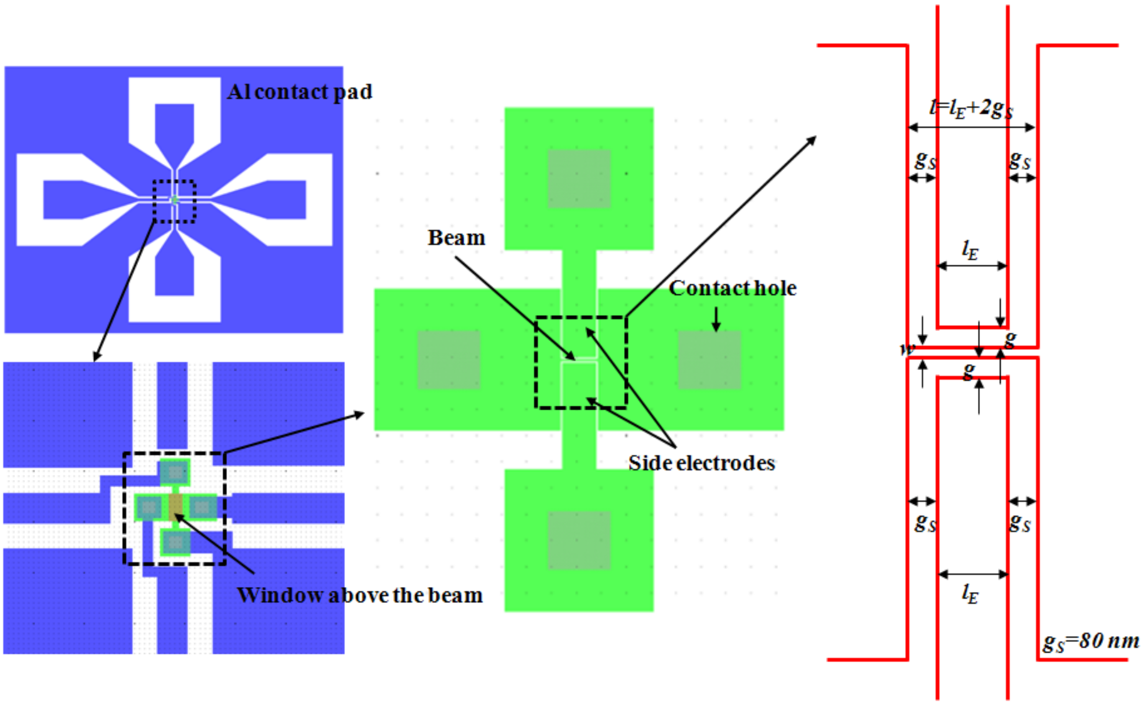

Fig. 4.10 The layout of the CC NEM structure and its wiring to the RF pad

Table 4.2 Dimensions for CC NEM structures

f_0	w	g	l
1.9-22.7 MHz	45 nm	80 nm	4.16, 4.80, 5.88, 8.32, 14.39 µm
	135 nm	80 nm	7.20, 8.32, 10.19, 14.41, 32.23 µm
98.3 MHz-4.4 GHz	45, 75, 105, 135 nm	80, 120 nm	400, 800, 1000,1500, 2000 nm

The FF NEM structure in section 3.4.4 is also added to the mask layout. The layout of the FF NEM structure and its wiring is shown in Fig. 4.11. Table 4.3 shows dimensions of FF NEM structures. Three 5-inch masks were ordered for three steps of photo-lithography. The plots of three masks are shown in Fig. 4.12 note that the coloured parts in the plots are transparent on the actual masks. Figure 4.12 shows (a) the first mask for patterning the contact holes, (b) the second mask for patterning the contact pads and wiring and (c) the third mask for patterning the windows above the beams for their subsequent suspension.

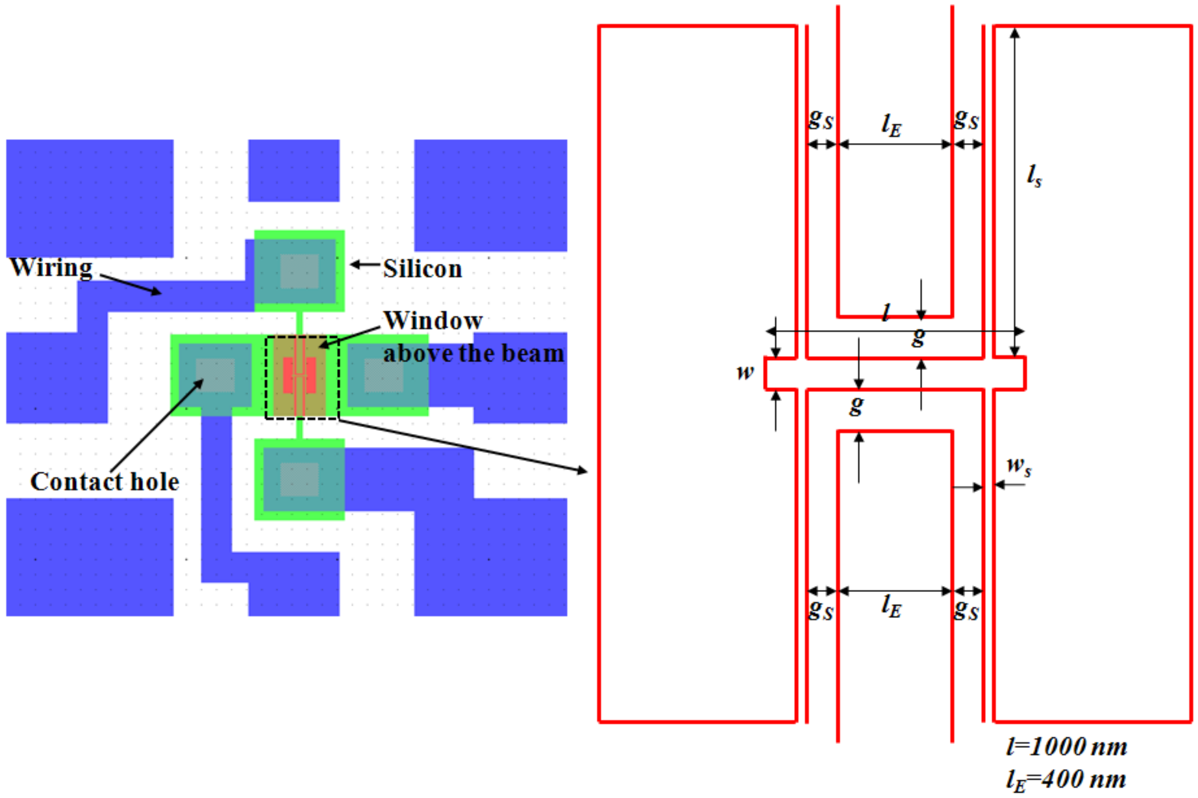

Fig. 4.11 The layout of the FF NEM structure and its wiring

Table 4.3 Dimensions for FF NEM structures

g	w, w_s, l_s, g_s	Support beam position
80,100,120,140 nm	45, 28, 1010, 170 nm 135, 82, 1192, 118 nm	384 nm 359 nm

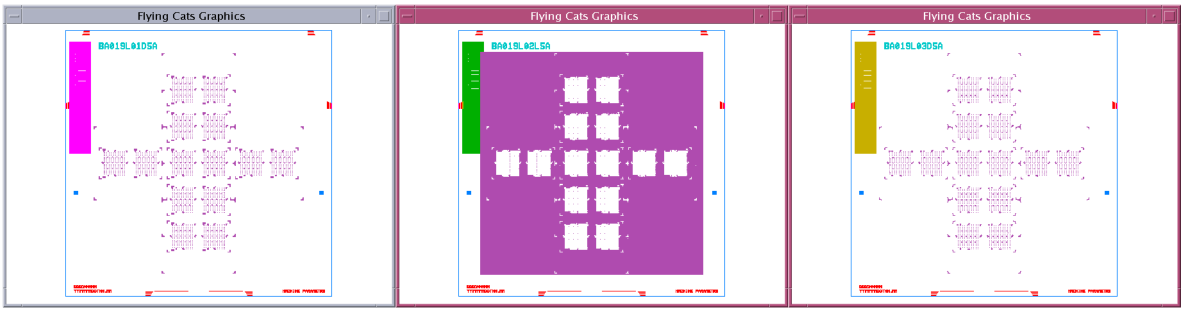

(a) **(b)** **(c)**

Fig. 4.12 Plots of three photo-lithography masks for: (a) Patterning contact holes, (b) patterning contact pads and wiring and (c) patterning windows above the beams for their subsequent release

4.2.2 Fabrication process

The fabrication is based on SOI technology and the phosphorus-doped SOI wafers of 1×10^{14} cm^{-3} with SOI thickness of 100 nm and BOX thickness of 200 nm were used. The SOI layer was thinned down to 50 nm by thermal oxidation at 950 ^{o}C for 30-40 minutes in collaboration with Mr. Feras M. Alkhalil. A 100 nm-thick oxidized layer was formed on the SOI layer by thinning down of 100 nm-thick SOI layer to 50 nm. The phosphorus ion was implanted in the oxidized SOI wafer at the University of Surrey with the energy of 90 keV and doping of 1×10^{15} cm^{-3}. The 100 nm-oxidized layer was kept on the wafer during the implantation process as a buffer layer to avoid the damages due to implantation. The implanted ions drive-in step is done in N_2 gas at 1000 ^{o}C in the annealing furnace for 30 minutes in collaboration with Dr. Kai Sun and Mr. Feras M. Alkhalil. ATHENA provides a convenient platform for simulating semiconductor industry processes [142] and was used to simulate the doping profile in the SOI layer after the implantation and drive-in steps with the previously stated conditions (see Appendix A.4). Along the specified cutline in Fig. 4.13 (a), ATHENA shows the net doping of ~8×10^{19} cm^{-3} for the SOI layer in Fig. 4.13 (b). The four-point prober, JANDEL RM3000, was used to measure the sheet resistance and consequently doping of the SOI layer. The measurement showed the doping of ~2×10^{19} cm^{-3} for the SOI layer that is compatible with the simulated value using ATHENA. BHF 20:1 was used to remove the oxidized layer on the SOI wafer. The wafer was cut to sample sizes of 3.5×3.5 cm^2 in order to fit the sample holder of the EB lithography system. Four samples were fabricated in sequence to optimize the fabrication process. The sample A and sample B contain one set of devices while the sample C and D contain two sets of same dimensions of devices.

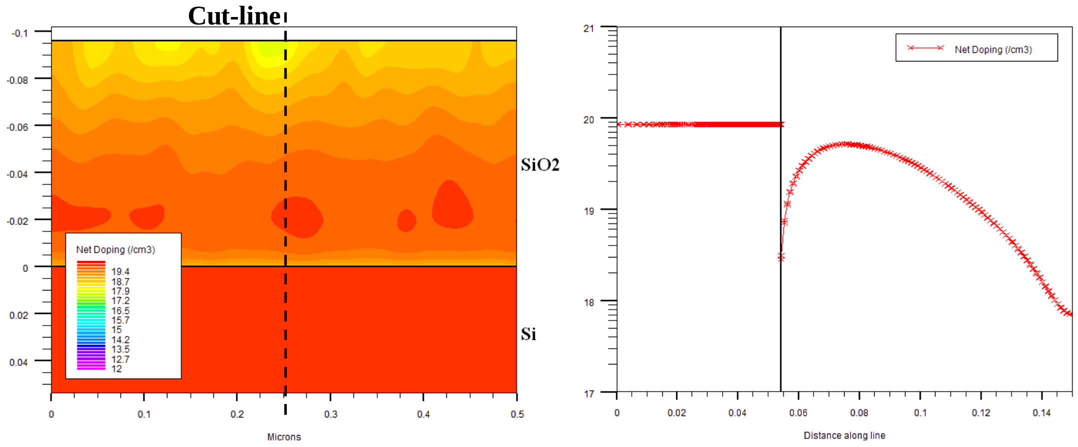

(a) (b)

Fig. 4.13 (a) ATHENA simulation for the net doping profile of the SOI layer and the oxidized layer on top after implantation and drive-in steps and (b) the net doping versus distance along the cutline

The fabrication of samples is followed by one step of EB lithography in collaboration with Dr. Muhammad Khaled Husain and three steps of photo-lithography as shown in Fig. 4.2. For the EB lithography step (Fig. 4.2 (a)), in the beginning a negative tone resist called UVN30 was used for patterning structures on the SOI layer of a test sample. UVN30 was spin-coated on the sample at the speed of 6000 rpm for 30 seconds. The pre-bake of temperature=95 ^{o}C was used for 2 minutes after the spin-coating of UVN30. After several trials, the exposure dose of 15 μC/cm^{2} was used as the optimized value for the subsequent exposures. MFCD-26 was used for developing the sample for 50 seconds. The adhesion of UVN30 to the silicon surface, especially for the beam, was not good as shown in Fig. 4.14 (a) and only the good resolution was obtained for a few devices with the *w* of 135 nm and *g* of 120 nm as shown in Fig. 4.14 (b). For better adhesion of UVN30 to the surface, HMDS prime was first spin-coated on the silicon sample at the speed of 3000 rpm for 30 seconds. The resolution was worse compared to the process that used only UVN30 and was due to the difficulties in the development step.

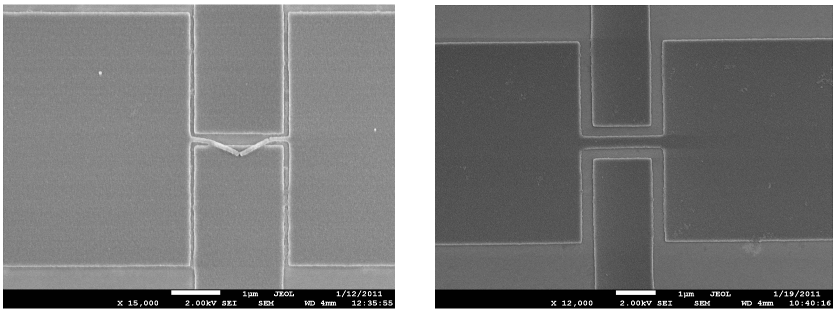

(a) (b)

Fig. 4.14 (a) The poor adhesion of UVN30 to the silicon surface, (b) the EB patterned beam using UVN30 with *w*= 135 nm and *g*=120 nm

To get finer structures and better resolution, Hydrogen silsesquioxane (HSQ) was used as the EB resist. HSQ is a negative resist that is known for the highest available resolution of EB resists [143]. HSQ is a subset of a cage-like structure $(HSiO_{3/2})_{2n}$ (n=2, 3, 4, etc.) as shown in Fig. 4.15 (a) and a part of it transforms to a network structure after curing as shown in Fig. 4.15 (b). Four stages can be considered during the curing of the HSQ layer [143-146]:

Up to 200 ^{o}C: Solvent loss

250-320 ^{o}C: Cage-network redistribution

$$2HSiO_{3/2} \rightarrow H_2SiO_{2/2} + SiO_{4/2}$$

$$H_2SiO_{2/2} + HSiO_{3/2} \rightarrow SiO_{4/2} + H_3SiO_{1/2}$$

$$H_3SiO_{1/2} + HSiO_{3/2} \rightarrow SiO_{4/2} + SiH_4$$

350-450 ^{o}C: Si-H thermal dissociation and network redistribution

$$4HSiO_{3/2} \rightarrow 3SiO_{4/2} + SiH_4$$

$$SiH_4 \rightarrow Si + 2H_2 \text{ or cleavage or Si-H}$$

>450 ^{o}C: Collapse of the pore structure

Figure 4.16 shows the SEM of a test patterned cross in HSQ after RIE step, imaged by focused ion beam (FIB) in collaboration with Dr. Mario A. G. Ramirez. Without the curing of the HSQ before RIE step, the plasma etches the resist as well as silicon. Accordingly, the curing at 250 ^{o}C for 4 minutes and 30 seconds using a hotplate was used to improve the hardness of HSQ during RIE of the SOI patterns. Using HSQ, the beam structures with the minimum *w* of 15 nm and with *g* of 80 nm were patterned using the optimized exposure dose of 900-1000 μC/cm^2. SEM views of patterned CC and FF beams in HSQ are shown in Figs. 4.17 (a) and 4.17 (b), respectively.

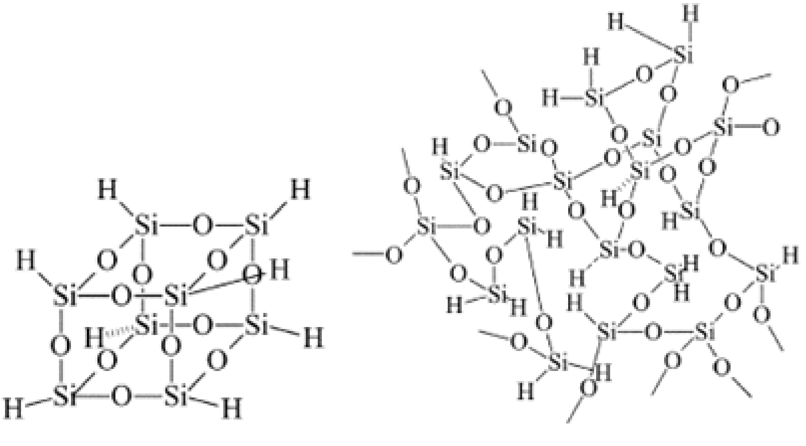
(a) **(b)**

Fig. 4.15 HSQ chemical structures [146]: (a) The cage-like structure and (b) the network structure

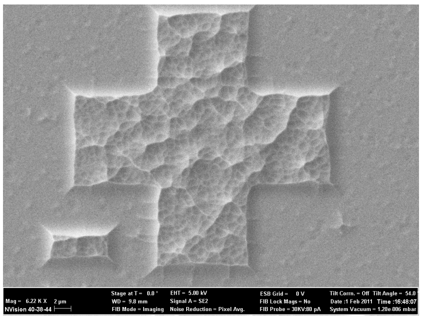

Fig. 4.16 The plasma attacking the silicon surface after the RIE step for the patterned cross in HSQ

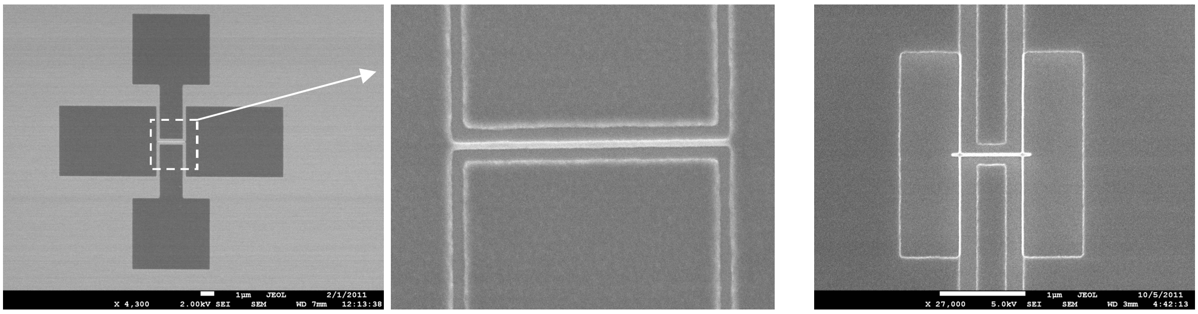

(a) **(b)**

Fig. 4.17 An EB patterned beam in HSQ: (a) The CC beam with w=45 nm, l=2000 nm and g=80 nm and (b) the FF beam with w=45 nm, w_s=28 nm, l=1000 nm, l_S=1010 nm, g=140 nm and g_S=170 nm

The RIE recipe of silicon, using the HSQ resist as the etching mask, was optimized with the etch rate of 107 nm/min and selectivity of (silicon:HSQ 8:1). The etch rate and selectivity was calculated based on the measurement by atomic force microscopy (AFM). Figure 4.18 shows the surface of HSQ for different exposure times to the plasma during RIE step for a test structure. It was found that the exposure time above 30 seconds caused the corrosion of the surface of HSQ and the plasma etches the resist quicker than the stated selectivity of silicon:HSQ. To avoid this effect, the RIE step should not last longer than 30 seconds. Therefore, several steps were used with the maximum step time of 30 seconds.

By optimizing the gas flow ratio of sulfur hexafluoride (SF_6)/oxygen (O_2) to 36 sccm/36 sccm, the vertical side walls for the silicon beam were obtained. A few of the etched silicon beams using the optimized etching recipe are shown in Figs. 4.19 (a) and 4.19 (b). The 3D image of the SOI pattern using AFM and its SEM image are shown in inset to Fig. 4.20 that presents the cross-section of the SOI pattern along the cutline. Even though the SEM image in Fig. 4.20 shows the vertical side walls for the beam, the AFM tip is not able to sense vertical sidewalls due to the available angle in the tip of AFM. The exposed and cured HSQ behaves similar to a layer of SiO_2, so RIE or HF etching is used for removing this layer. Early-suspension of the beams will happen before starting the following photo-lithography steps if HF etching is used for removing the HSQ layer. For this reason, the removal of HSQ at the contact holes above silicon were done using BHF 20:1 after the first photo-lithography step which covered beams by the photo-resist.

After the EB lithography for the sample A, the SOI layer was patterned using RIE and a 200 nm-SiO_2 layer was deposited using plasma-enhanced chemical vapor deposition (PECVD) on the patterned silicon. The SiO_2 layer was then patterned using the positive photo-lithography resist, S1813, to make the contact holes (Fig. 4.2. (b)) above the silicon pads. The patterned holes in the resist were etched using RIE. The microscope-image of patterned holes is shown in Fig. 4.21. After dry etching of 200 nm-SiO_2 layer, the thin layer of HSQ in the contact holes was also removed using RIE. A 300 nm-thick layer of Al was deposited on the surface using EB evaporator. The cross-section in Fig. 4.22 shows a good step coverage of the evaporated Al over a patterned PECVD-SiO_2 layer on the silicon sample. The Al layer was then patterned in the second photo-lithography step (Fig. 4.2 (c)) using S1813 photo-resist mask and wet etching of Al for making contact pads and wiring. The microscope and SEM images of the patterned Al layer are shown in Fig. 4.23.

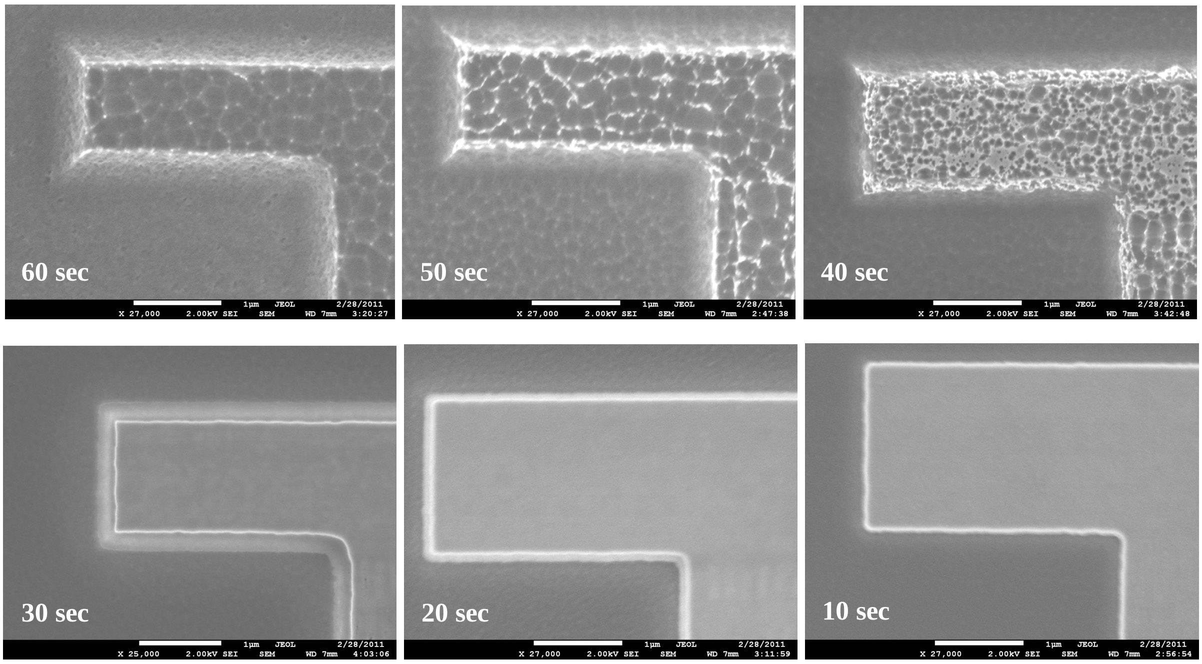

Fig. 4.18 The HSQ surface due to different RIE time steps

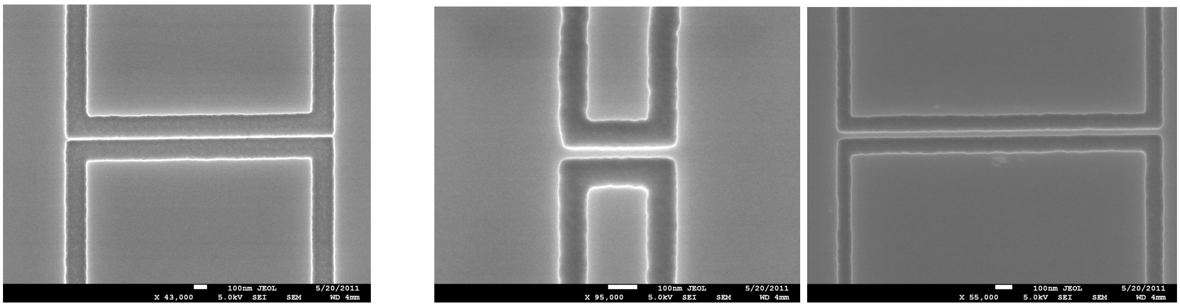

(a) (b)

Fig. 4.19 Etched beams using HSQ mask (a) *w*=15 nm, *g*=160 nm and (b) *w*=45 nm, *g*=80 nm, *l* (left)=400 nm, *l* (right)=2000 nm

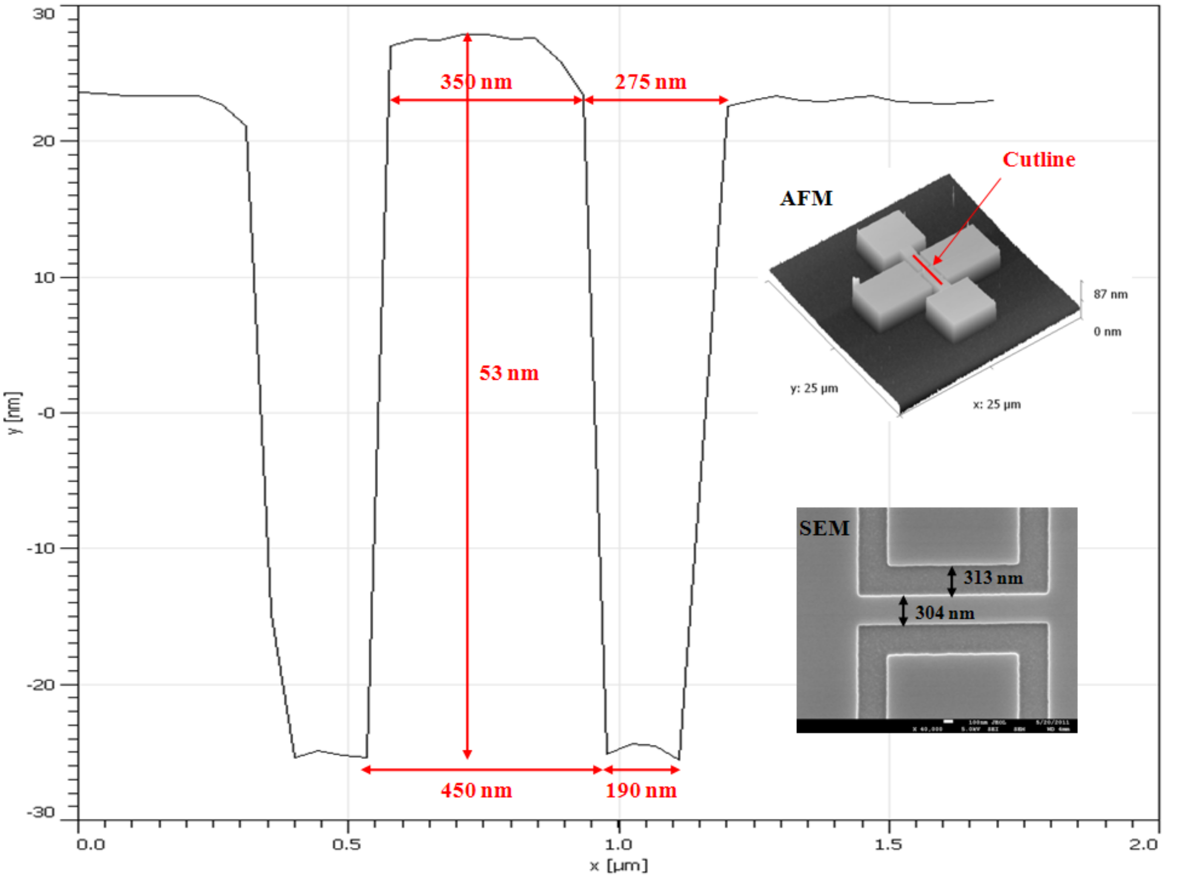

Fig. 4.20 The cross-section of the patterned SOI beam using AFM along the cutline in the AFM 3D image

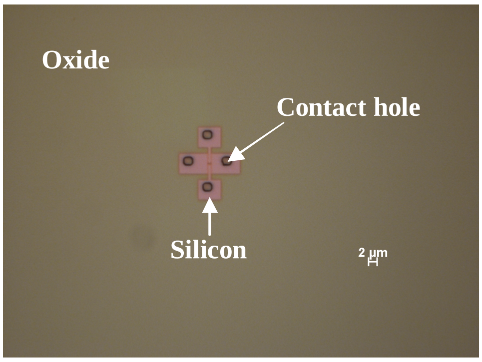

Fig. 4.21 Patterned contact holes in the deposited PECVD-SiO$_2$ layer

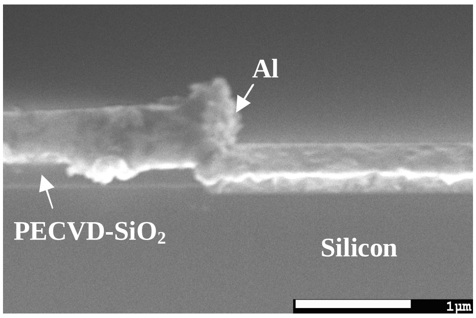

Fig. 4.22 The step coverage of evaporated Al over the patterned PECVD-SiO_2 layer on a silicon sample

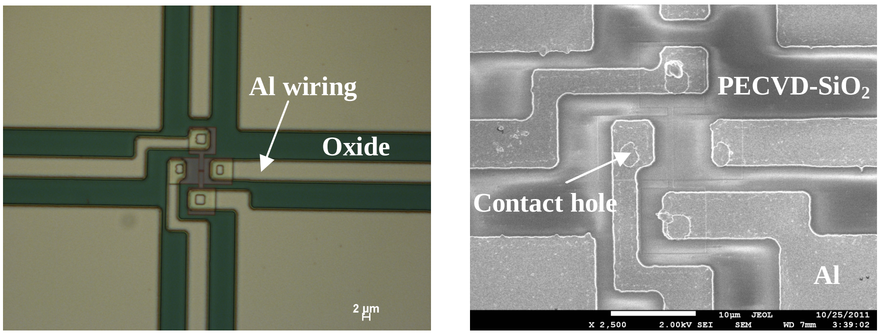

Fig. 4.23 The microscope (left) and SEM (right) images of the patterned wiring in the deposited Al layer

The third photo-lithography step (Fig. 4.2 (d)) was done for the sample A to open a window in the photo-resist above the beam for its subsequent suspension using vapor HF. The microscope-image of the patterned window in resist is shown in Fig. 4.24. Unlike liquid HF, vapor HF is not selective to S1813 photo-resist and it etched the photo-resist as well as the SiO_2 layer. Due to this effect, the surface especially near some of the beams could not be cleared of resist residues after plasma ashing the photo-resist as shown in Fig. 4.25. Subsequent annealing of the sample at 400 °C for 20 minutes in an ambient of forming-gas (96%N_2/4%H_2) was done in collaboration with Dr. Kanad Mallik to reduce the contact resistance between Al and silicon. Without the forming-gas annealing (FGA), the ohmic contact between Al and silicon will be very poor and makes the FGA after the metallization a vital step in the fabrication process [147].

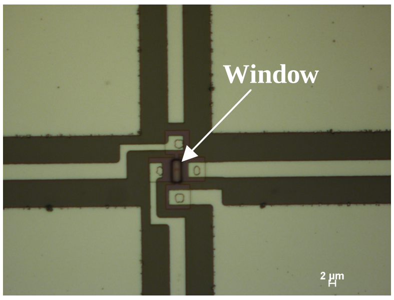

Fig. 4.24 The patterned window in the photo-resist above the beam

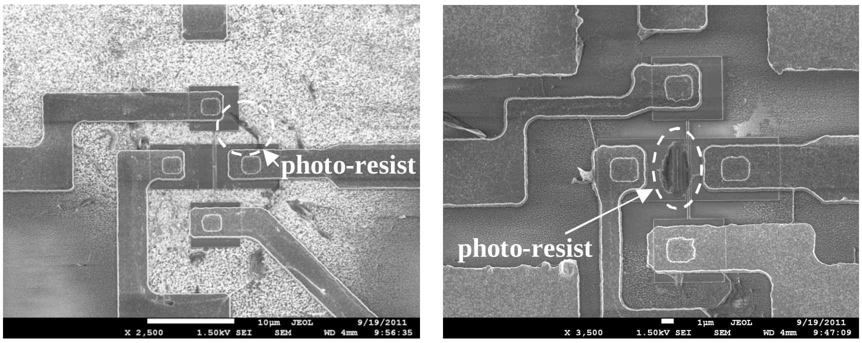

Fig. 4.25 Photo-resist residues on the surface of the sample A

For optimizing the fabrication process, different conditions were used for the samples after the RIE step for the contact holes. Different conditions for the samples are shown in Table 4.4. The sample A showed a good contact between silicon and Al for only a few of devices after characterizing the final devices in the next chapter. This is due to the possible existence of thin HSQ layer or a native oxide layer on silicon. For this reason BHF 20:1 was used for 1 minutes and 30 seconds, 2 minutes and 3 minutes for the samples B, C and D respectively to remove the possible HSQ and native oxide layer on silicon just before transferring the samples to the EB evaporator for the deposition of Al.

Table 4.4 The fabrication steps of four samples after the RIE step for contact holes

Process	Sample A	Sample B	Sample C		Sample D	
			Set A	Set B	Set C*	Set D
HSQ removal using RIE	✓					
HSQ removal using BHF 20:1		✓	✓		✓	
3rd photo-lithography	✓		✓	✓		✓
Suspension using BHF 20:1			✓	✓		✓
Suspension using vapor HF in the presence of photo-resist	✓		✓			
Suspension using vapor HF in the absence of photo-resist		✓		✓	✓	
FGA	✓	✓	✓	✓	✓	✓

* The vapor HF etcher’s reservoir was filled with fresh etchant.

To avoid the photo-resist residues on the surface and beams of the sample A, the third photo-lithography step was ignored for the sample B and beams were suspended using vapor HF in the absence of photo-resist. This was done knowing that vapor HF was selective to Al [141],[148],[149]. Even the surface was cleared of resist residues, it was still contaminated (Fig. 4.26 (a)) and it was assumed it could be due to the long exposure of the silicon surface to vapor HF. In order to reduce the exposure time and decrease the contamination effect in the sample B, an alternative method was used for the suspension of the beam in the sample C. In this method BHF 20:1 was used first after the third photo-lithography step to remove the

200 nm-thick PECVD-SiO_2 layer that was deposited on the beams previously and then using vapor HF for the suspension. After BHF etching of the SiO_2 layer, the sample was cut to sets A and B. It was expected that by reducing the exposure time, the resist will be less affected by vapor HF and therefore the exposure to vapour HF for the set A was done in the presence of photo-resist. Unfortunately the resist residues were still available for the set A even with a short exposure time of resist to vapour HF. So for set B, the same method of the set A was used except that the vapor HF suspension was done after removing the photo-resist by plasma asher. Some of the beams and their side electrodes in the sets A and B were etched mainly by liquid HF as shown in Fig. 4.26 (b).

It was noticed that filling the vapor HF etcher's reservoir with fresh etchant made the problem of contamination in the sample B resolved to some extent. The sample D contained two sets of devices and it was cut to two sets: set D and set C. The same method for the sample B was applied for the set C and consequently all of the beams and electrodes in this set were well-defined with less surface contamination in comparison with the sample B. Another alternative method is using liquid HF for the suspension of beams. So the beams in the set D were released using BHF 20:1 through the patterned windows in the photo-resist as liquid HF is not selective to Al. The only problem with this method is the bending of especially longer beams towards the side gate or the substrate as shown in Figs. 4.27 (a) and 4.27 (b), respectively. Therefore in conclusion, using vapor HF for the suspension of beams in the absence of any protective resist is an easy and producible method for different dimensions of beams. FGA for the samples were done at 400-450 ^{o}C for 20-40 minutes. The best fabricated CC NEM structures from sets B, C and D are shown in Fig. 4.28. The best fabricated FF NEM structures are also shown in Fig. 4.29. The details of the optimized fabrication steps for the sample D is shown in Table 4.5.

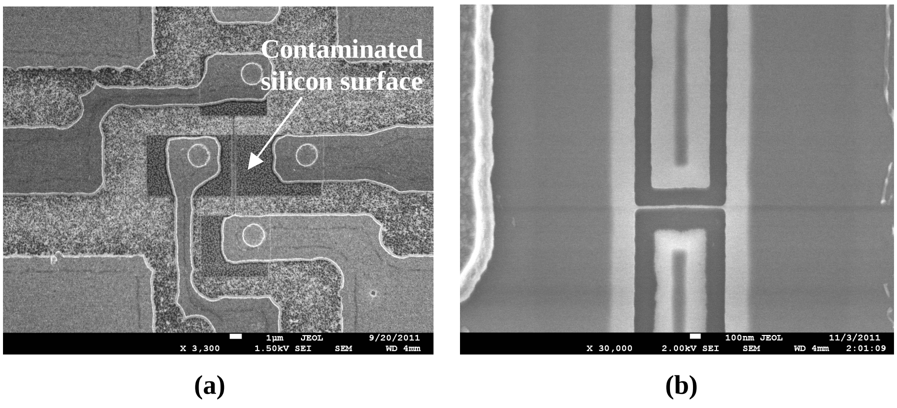

(a) **(b)**

Fig. 4.26 (a) The contaminated silicon surface of the sample B, and (b) the etched beam and side electrode in the sample C

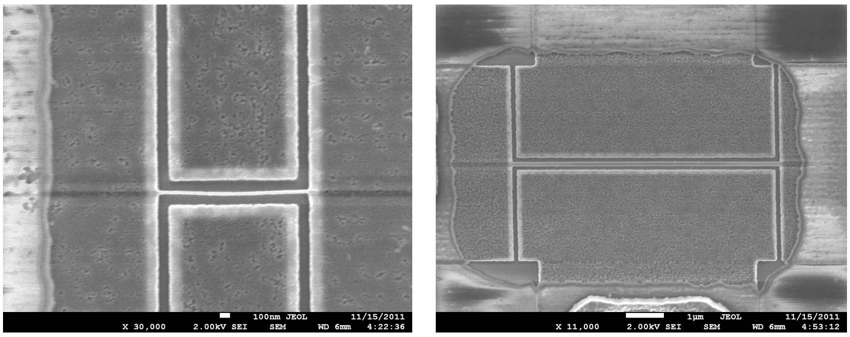

(a) **(b)**

Fig. 4.27 The effect of liquid HF suspension in the sample D-set D: Bending of the beam (a) with *l*=1500 nm, *w*=45 nm, *g*=80 nm towards the side gate, and (b) with *l*=7.20 µm, *w*=135 nm, *g*=80 nm towards the substrate

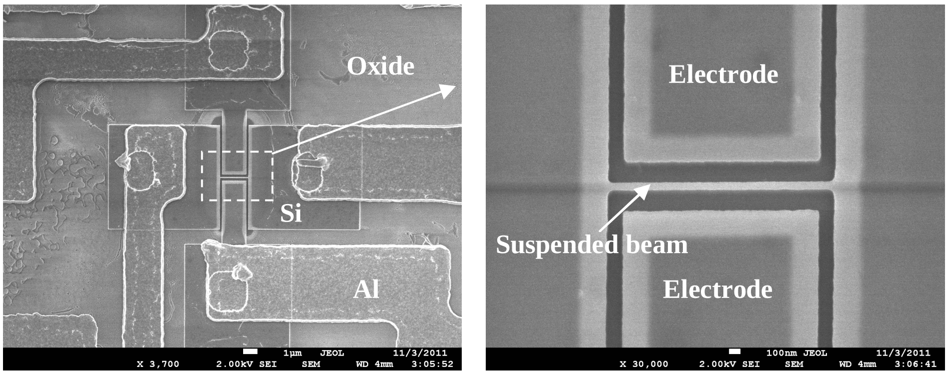

Sample C-set B

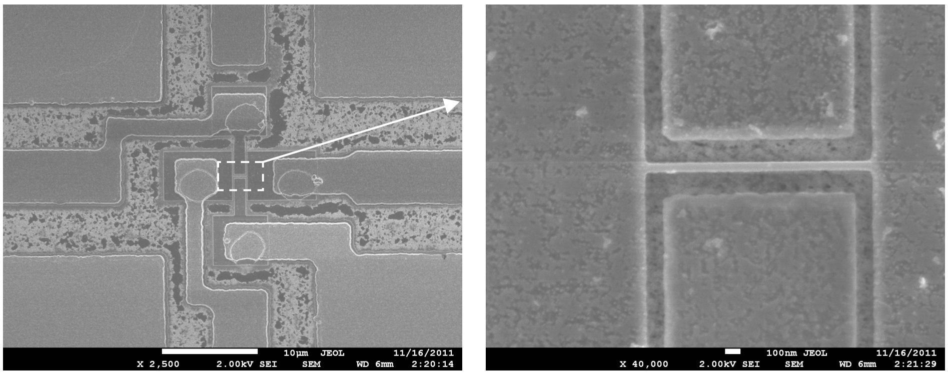

Sample D-set C

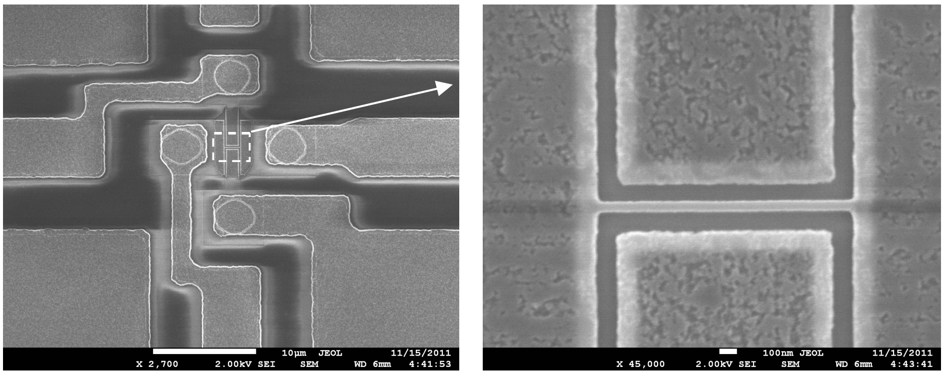

Sample D-set D

Fig. 4.28 SEM views of CC NEM structures with *l*=1500 nm, *w*=75 nm and *g*=80 nm

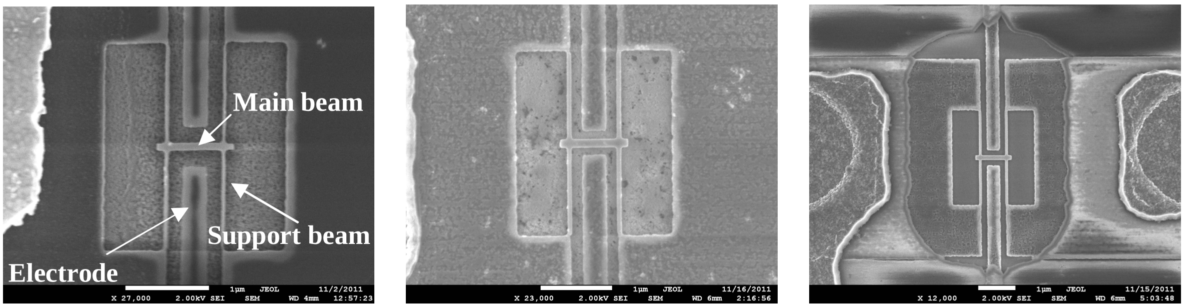

Sample C-set B (*g*=120 nm) **Sample D-set C (*g*=80 nm)** **Sample D-set D (*g*=120 nm)**

Fig. 4.29 SEM views of FF NEM structures with l=1000 nm, w=135 nm, l_s=1192 nm and w_s=81 nm

4.3 Fabrication of IP R-NEM sensors

The mask layout of the IP R-NEM sensor includes variations of beam dimensions, electrode length, channel length of MOSFET, gap size, doping strategies and contact pads' configuration. The details of mask layout and the simplified fabrication process are given in the following sections.

4.3.1 Mask layout

The mask layout includes mainly the IP R-NEM sensor with the working in-plane frequency range, f_0, of 98.2 MHz-2.3 GHz using Cadence-Virtuoso Layout [150] (see Appendix A.5) based on the available fabrication technology process at CEA-LETI. A few number of the mask layers were generated automatically but the rest of layers were defined in the layout design. Figure 4.30 shows the layout of the IP R-NEM sensor and its wiring. Sensors in the layout have two configurations as shown in Fig. 4.31. In Fig. 4.31 (a), a back gate is considered on the SOI for biasing the body while in Fig. 4.31 (b) the back gate is ignored. The variations of dimensions for the sensor are shown in Table 4.6. 65 devices with different dimensions are designed in each chip to cover different possible dimensions and configurations for the sensor.

Based on the configuration of contact pads for the suspended beam in Fig. 4.31, it is not possible to probe the beams in both ends to check their characteristics. For this reason a few NEM structures with the layout of Fig. 4.10 and the same dimensions of beams for IP R-NEM sensors are included in the layout. For doing a complete investigation on the beams' characterization in CEA-LETI's platform the variation of dimensions for the beams in NEM structures are same as Table 4.2 for the frequency range of 98.3 MHz-4.4 GHz.

Table 4.5 The details of fabrication process steps for the NEM structures in the sample D

Step	Properties	More Details
Wafer cleaning	Fuming nitric acid (FNA) for 15 min, BHF 20:1 for 20 sec	SOI thickness=100 nm, BOX thickness= 200 nm,
Oxidation	Gas=O_2 , temp=950 °C , duration=30 min	SiO_2 thickness= 100 nm, SOI thickness=50 nm
Ion implantation	Acceleration voltage= 90 keV, dopant= phosphorous, doping= 1×10^{15} cm^{-3}	
Wafer cleaning	FNA for 15 min	
Furnace annealing	Gas=N_2, temp= 1000°C, duration= 30 min	
SiO_2 layer removal	BHF 20:1 for 4 min and 10 sec	SiO_2 thickness= 100 nm, Etch rate=24 nm/min
Wafer cleaving	To sample sizes of 3.5×3.5 cm^2	
Sample cleaning	FNA for 15 min, BHF 20:1 for 20 sec	
Sample dehydration	Oven bake for 2 hr, temp= 210 °C	
EB lithography	HSQ coating at 5000 rpm for 60 sec, pre-bake at 80 °C for 4 min, exposure dose: 900-1000 $\mu C/cm^2$, development: MF319 for 1 min and 40 sec, rinse: DI water for 60 sec, post bake at 250 °C for 4 min and 30 sec	Patterning Silicon HSQ thickness=63-65 nm
RIE of Silicon	Duration= (1st step) 30 sec+(2nd step)15 sec, SF_6/O_2= 36 sccm/36 sccm, RF power=100 watt, pressure=30 mTorr	Etch rate= ~107 nm/min, selectivity= 8:1
PECVD of SiO_2	SiO_2 thickness= 200 nm	
Sample dehydration	Oven bake for 30 min, temp=120 °C	
Photo-lithography	S1813 coating at 5000 rpm for 30 sec, pre-bake at 115 °C for 1 min, exposure duration: 2 sec, applied pressure for hard contact: 0.5 bar, development: MF319 for 40 sec, rinse: DI water for 30 sec, post bake at 115 °C for 4 min	Mask 1: Patterning contact holes S1813 thickness=1 µm
RIE of SiO_2	Duration= 8 min, Ar/CHF_3= 38 sccm/12 sccm, RF power=200 watt, pressure=30 mTorr	Etch rate= 25 nm/min
HSQ removal	BHF 20:1 for 2 min	HSQ thickness=40-50 nm
S1813 removal	Gas=O_2, duration=10 min	Plasma asher
EB evaporation	Metal= Al, thickness=300 nm	
Sample dehydration	Oven bake for 30 min, temp=120 °C	
Photo-lithography	S1813 coating at 5000 rpm for 30 sec, pre-bake at 115 °C for 1 min, exposure duration: 2 sec, applied pressure for hard contact: 0.5 bar, development: MF319 for 40 sec, rinse: DI water for 30 sec,	Mask 2: Patterning contact pads and wiring S1813 thickness=1 µm
Al etching	Al etchant for 3 min, temp=30 °C	Etch rate= 100 nm/min
Resist removal	Gas=O_2, duration=10 min	Plasma asher
Photo-lithography*	S1813 coating at 5000 rpm for 30 sec, pre-bake at 115 °C for 1 min, exposure duration: 2 sec, applied pressure for hard contact: 0.5 bar, development: MF319 for 40 sec, rinse: DI water for 30 sec, post bake at 115 °C for 4 min	Mask 3: Window opening for beam release S1813 thickness=1 µm
Beam release	Vapor HF, temp=45 °C for 3 min or BHF 20:1 for 4 min	Etched SiO_2 thickness=300 nm
Resist removal	Gas=O_2, Duration=10 min	Plasma asher
Sample cleaning	Ultra-violet ozone cleaning for 10 min	
Furnace annealing	Gas= forming-gas (24:1 N_2/H_2), temp=400 °C, Duration=20 min	

* To use vapor HF for the suspension of the beams, this step was skipped.

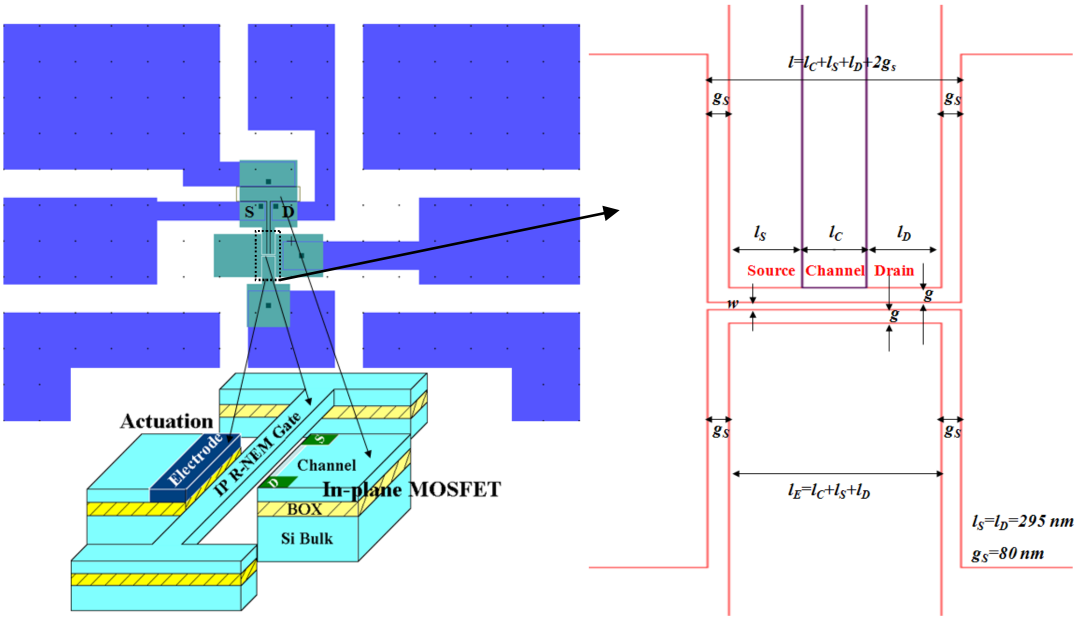

Fig. 4.30 The mask layout for the IP R-NEM sensor

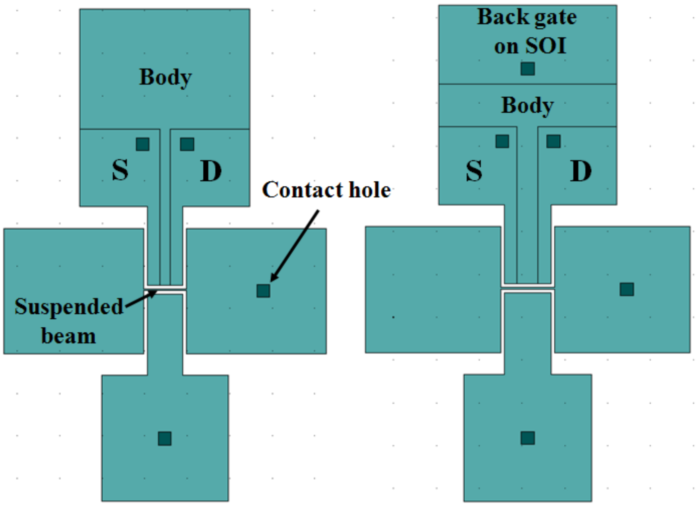

(a) (b)

Fig. 4.31 Different configurations for the IP R-NEM sensor in the mask layout:
(a) Without and (b) with the back gate

Table 4.6 Dimensions for IP R-NEM sensors

l	l_C	g	w
1000, 1250, 1500, 1750, 2000 nm	250, 500, 750, 1000, 1250 nm	80, 140, 200 nm	45, 75, 105, 135 nm

4.3.2 Fabrication process

The CEA-LETI's fabrication process is based on the SOI technology. The thickness of SOI and BOX layers are 40 nm and 145 nm, respectively. P-type doping of P=10^{15} cm^{-3} and P=10^{16} cm^{-3} are considered for the SOI wafers. The fabrication steps are shown in Fig. 4.3.

The SOI wafers are implanted with different dopings of $P^+=10^{19}$ cm^{-3} and $N^+=4\times10^{19}$ cm^{-3} except for the channels of the MOSFETs that are protected by resist in Fig. 4.3 (a). Then the heavily-doped silicon is patterned and the beam is released using vapor HF in Fig. 4.3 (b). Due to the oxidization step (Fig. 4.3 (c)), a 15 nm layer of thermal oxide is grown on the surface of the patterned silicon especially around the suspended beam for passivation and minimizing of the silicon surface states [151]. The two doping strategies for the IP R-NEM sensor are shown in Fig. 4.32. For the first strategy in Fig. 4.32 (left), the whole structure has the doping of $P^+=10^{19}$ cm^{-3} except the channel of the MOSFET with the doping of $P=10^{15}$ cm^{-3}. For the second strategy in Fig. 4.32 (right), the whole structure has the doping of $N^+=4\times10^{19}$ cm^{-3} except the MOSFET-channel with the doping of $P=10^{16}$ cm^{-3}. In Fig. 4.3 (d), poly silicon is deposited to fill the etched area around the beam followed by a step of chemical-mechanical polishing/planarization (CMP). Poly silicon protects the beam from further processing steps. Contact holes above the silicon pads are opened by etching poly silicon with the etch stop layer of thermal oxide (Fig. 4.3 (e). In Fig. 4.3 (f), oxide is deposited and contact holes are patterned in oxide as shown in Fig. 4.3 (g). Al is deposited and patterned for contact pads and wiring in Fig. 4.3 (h). In the final step as shown in Fig. 4.3 (i), a window is opened in oxide and poly silicon above the beam for the suspension of the beam using xenon difluoride (XeF_2). The SEM view of the RF measurement pad, the opened window in oxide and poly silicon above the beam for its suspension, and the IP R-NEM sensor are shown in Figs. 4.33 (a), 4.33 (b) and 4.33 (c), respectively.

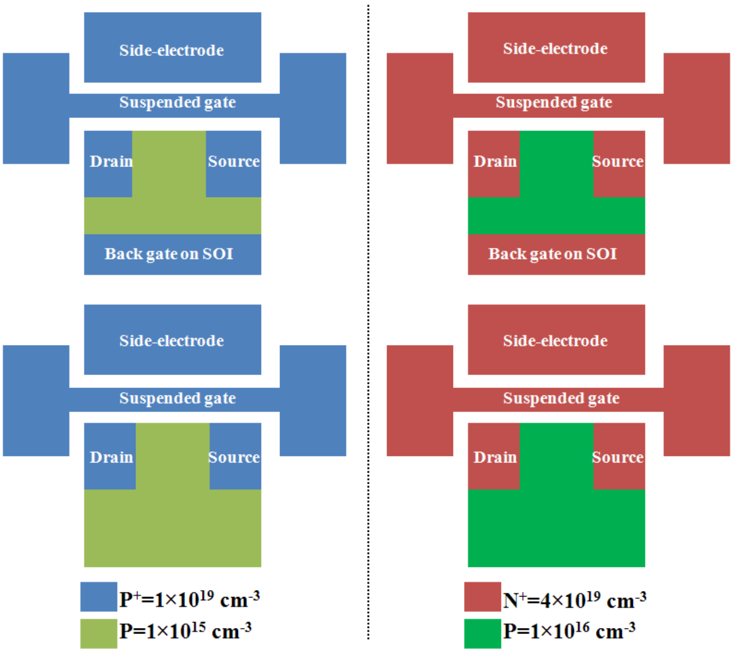

Fig. 4.32 Two doping strategies for the IP R-NEM sensor

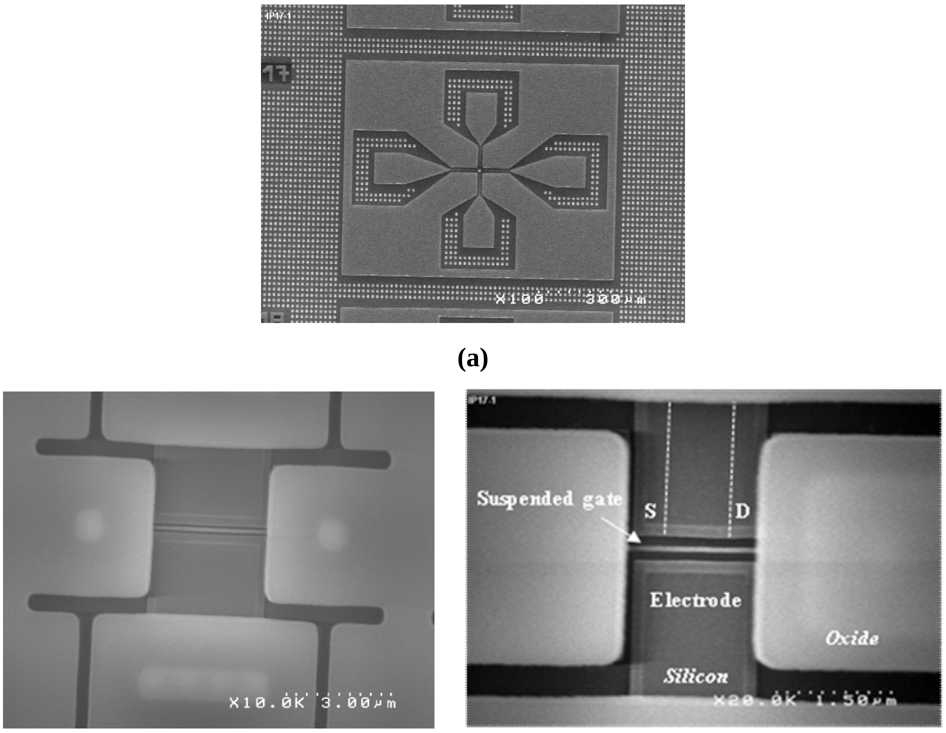

(a)

(b) **(c)**

Fig. 4.33 The SEM view of (a) the RF pad for gas-detecting application, (b) the opened window in oxide and poly silicon for the suspension of the beam, and (c) the IP R-NEM sensor

A cross-section is done using focused ion beam (FIB) in collaboration with Mr. Marek E Schmidt along the line in Fig. 4.34 (left). The cross-section in Fig. 4.34 (right) shows the thickness of 1 µm for oxide, 230 nm for poly silicon, 134 nm for the BOX layer, 480 nm for Al and 55 nm for the SOI layer.

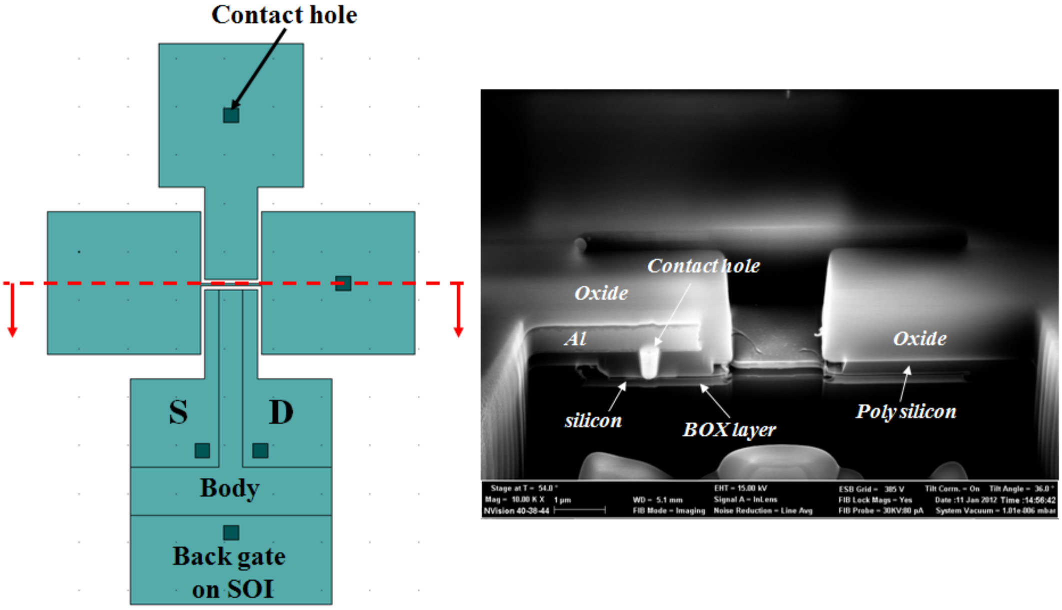

Fig. 4.34 The cross-section of the IP R-NEM sensor (right) along the dotted line (left)

4.4 Summary

In this chapter, the post processing on NW devices was first presented. NWs were suspended using liquid and vapor HF and their characteristics are compared in the next chapter. Vapor HF provided the suspension of NWs without any polymer contamination compared to the liquid HF. Then the mask layout design and fabrication process of CC and FF NEM structures were presented. Vapor HF release of beams provided more reliable suspension method for different dimensions of beams because it reduced the problem of bending and stiction for long beams after the suspension. Finally, the mask layout based on the fabrication process technology at CEA-LETI was designed for the IP R-NEM sensor and the fabrication process was explained afterwards. The characterization of the post-processed and fabricated devices are presented and discussed in the next chapter.

CHAPTER 5

In-plane resonant NEM sensor: Characterization

Characterization of the devices that were explained in the previous chapter will be discussed in this chapter in the same order. The DC characterization of nano-wires (NWs) are first conducted before and after their suspension using both liquid and vapor hydrofluoric (HF) etching and followed by their radio-frequency (RF) measurement. In the second step, the DC and RF characterization for nano-electro-mechanical (NEM) structures are done. Finally, the DC characterization of in-plane resonant NEM (IP R-NEM) sensors that includes the characterization of suspended beams and integrated metal-oxide-semiconductor field-effect-transistors (MOSFETs) are done in order to optimize the applied biasing voltages to the MOSFET for the subsequent RF measurement. Some simulations are done to validate the DC characterization results of the fabricated sensors.

5.1 Characterization of NWs

The DC characterization of NWs in two stated chips in section 4.1 was conducted using Cascade R32 REL3200 probe-station. NWs have the SOI thickness, *t*, of 53 nm, width, *w*, gap, *g*, of 100 nm and different lengths, *l*, of 500 nm, 1000 nm, 1500 nm and 2000 nm. The DC voltage across NWs was swept from -8 mV to 8 mV.

The current of the non-suspended NWs in both chips versus the applied voltage are shown in Fig. 5.1. In Fig. 5.1, by reducing the length of NWs in both chips, the current at non-zero voltages increases and results in smaller resistance that is consistent with the following equation [152]:

$$R = \frac{\rho' l}{A'} \tag{5-1}$$

where l and A' denote, the length in the direction of current flow and the cross-sectional area, respectively and ρ' is the resistivity of the NW. The current in the order of 10^{-10} A for the voltage of 0 V is measured for NWs in both chips in Fig. 5.1. The spikes in the characteristics of NWs in both chips may be explained due to the effect of trapped charges on the surface of NWs. The linear dependencies of the resistance of NWs in each chip to their length are shown in insets to Fig. 5.1.

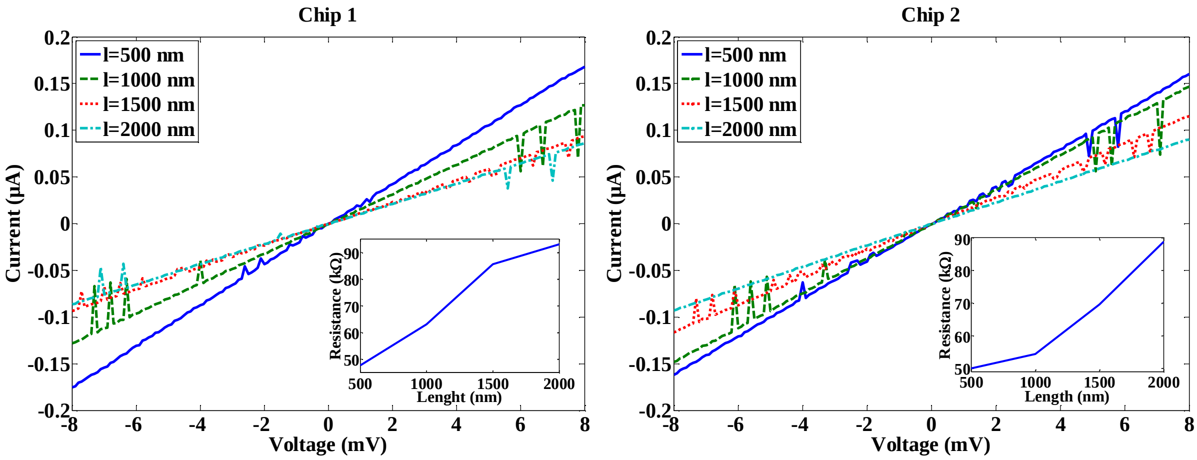

Fig. 5.1 The current versus voltage for NWs with different lengths, and the resistance of NWs versus length in inset to figures

The calculated resistance for non-suspended NWs in chip 1, using eq. (5-1) and the measured resistance from characteristics in Fig. 5.1, are shown in Table 5.1. The ρ' value of 3×10^{-5} Ω.m was used in eq. (5-1) for the assumed N_D doping of 2×10^{19} cm^{-3} for NWs. Measured resistances are about one order of magnitude larger than the calculated resistances and shows the smaller doping than the defined doping of 2×10^{19} cm^{-3} for the fabricated NWs. The same fact was found for NWs in chip 2. The current leakage from side gates (gate1/gate2 in Fig. 4.4) to the NW with l=2000 nm in chip 1 was measured. The leakage current from the gates to the NW is shown in Fig. 5.2 and it is in the order of 10^{-14} A for both gates. The leakage current from gates to the NW with the same length in chip 2 was measured in the order of 10^{-13} A for both gates.

Table 5.1 Comparison of the calculated and measured resistances of NWs in chip 1

l (nm)	Calculated resistance (Ω)	Measured resistance (Ω)
500	2830.18	55749.12
1000	5660.37	69565.21
1500	8490.56	99071.20
2000	11320.75	110880.11

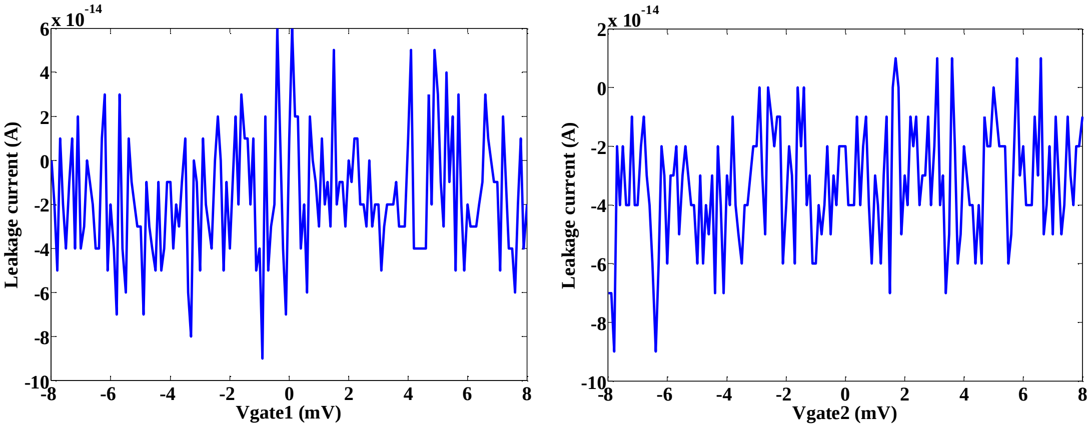

Fig. 5.2 The leakage current versus voltage from gate 1 (left) and gate 2 (right) to the NW with *l*=2000 nm in chip 1

The non-suspended NWs in chip 1 were suspended using BHF 20:1 as explained in section 4.1. The DC characterization was conducted on them to investigate the effect of suspension on their characteristics. The current versus applied voltage for NWs with different lengths are shown in Fig. 5.3. The current in the order of 10^{-9} A was measured for NWs at the zero voltage in Fig. 5.3 that is one order of magnitude larger than the equivalent value in Fig. 5.1. This is due to the trapped charges in the native oxide layer around the nano-wire and to reduce this effect, the oxide was passivated with the additional annealing step that was explained in section 4.1. The current versus the applied voltage for NWs after annealing are shown in Fig. 5.4 and compared to non-suspended NWs. The annealing step reduced the current at zero voltage a bit compared to the equivalent value in Fig. 5.3 but it was still in the order of 10^{-9} A. It was expected that the suspended NWs would show a smaller current than the current through non-suspended NWs at non-zero voltages due to their smaller cross-section after the suspension. Contrary to this expectation, Fig. 5.4 shows a larger current for the suspended NWs that were due to the leakage current from NWs to side gates. The leakage current from side gates to the NW with *l*=2000 nm is shown in Fig. 5.5 that is in the order of nA which is five orders of magnitude larger than the leakage current of non-suspended NW in Fig. 5.2.

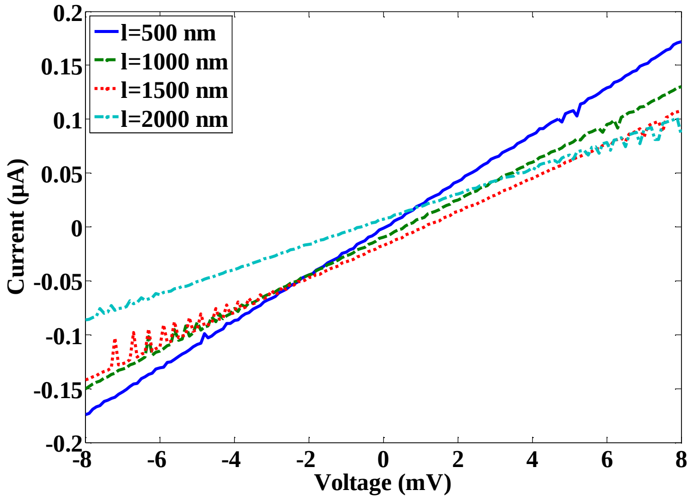

Fig. 5.3 The current versus voltage for the suspended NWs with different lengths

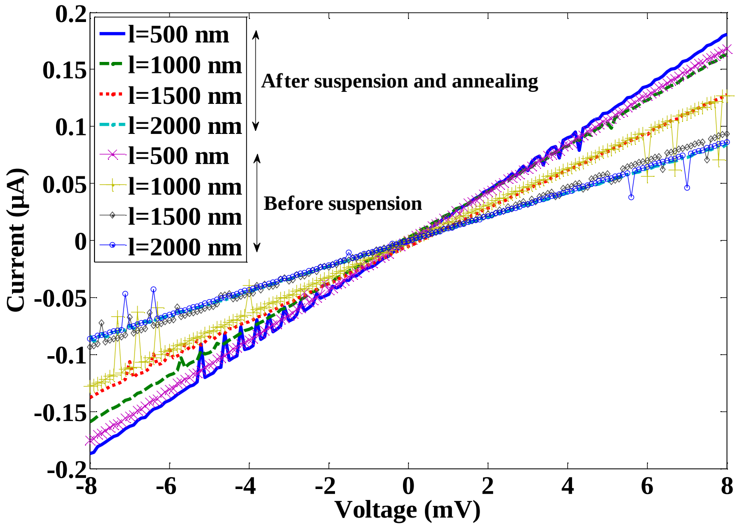

Fig. 5.4 Comparison of the current versus voltage for NWs with different lengths before and after the suspension using BHF and subsequent annealing

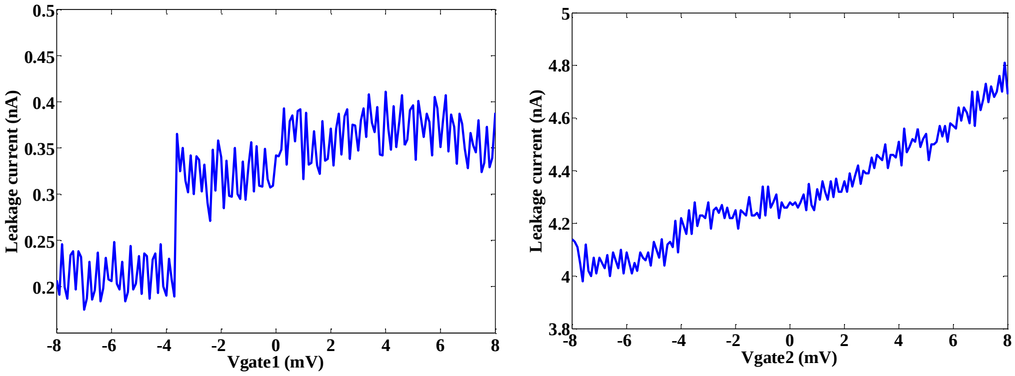

Fig. 5.5 The leakage current versus voltage from gate 1 and gate 2 to the suspended NW with *l*=2000 nm

After using vapor HF for the suspension of non-suspended NWs in chip 2 as discussed in section 4.1, the DC characteristics of suspended NWs were measured using the same measurement setup for the suspended NWs by BHF. Figure 5.6 shows the current of NWs before and after the suspension. The current at non-zero voltages for NWs with *w*=1000,1500,2000 nm is a bit smaller than the current of the non-suspended NWs that is more compatible with the expectation of reduction of the current due to the reduction of beam’s cross-section after the suspension. Not much difference in the current of suspended and non-suspended NWs is explained again because of the leakage current of 10^{-9} A through side gates. The current of NW at zero voltage is measured in the order of 10^{-9} A that is an order of magnitude larger than that of non-suspended NWs. The important point of using vapor HF for the suspension is that no further cleaning and annealing processes on NWs is necessary compared to the suspended NWs using BHF.

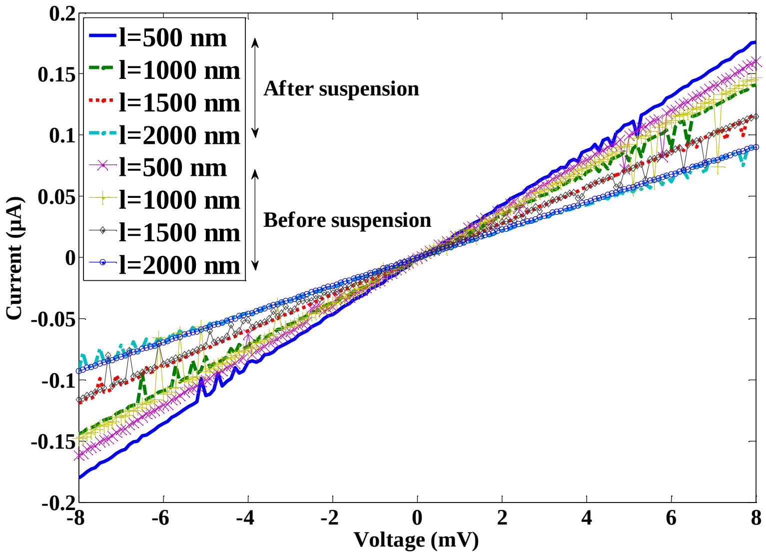

Fig. 5.6 Comparison of the current versus voltage for NWs with different lengths before and after the suspension by vapor HF

For the RF characterization of NWs, Agilent E8361A PNA network analyzer was used to measure S-parameters (see section 2.3.2.1) and the resonance frequency of the suspended NWs. The network analyzer works in the frequency range of 10 MHz-67 GHz. The measurement setup for NWs is shown in Fig. 5.7 (a). As NWs do not have the metal contact pads and the suitable pads configuration in Fig. 4.9, the chip was glued to a chip carrier (cc). The silicon pads of NWs were then wire bonded to the gold pads of the cc that was mounted on the prepared circuit board (cb). The cb has two sub-miniature version A (SMA) connectors that were connected to the 1.8 mm RF cables from the network analyzer. Before doing the measurement, a calibration was needed to remove the measurement errors caused by the imperfections in the instrument [153]. The two-port calibration was done using Agilent electronic calibration (Ecal-85060/90 Series) as shown in 5.7 (b) by connecting the RF cables to its SMA connectors. The range of frequency, number of points in the measurement, power of input AC signal and intermediate frequency (IF) bandwidth were defined before starting the calibration. Important to note that the calibration is valid only for the defined values and it should be repeated in the case of changing these values. Moreover, for this calibration the measurement reference plane is at the end of RF cables.

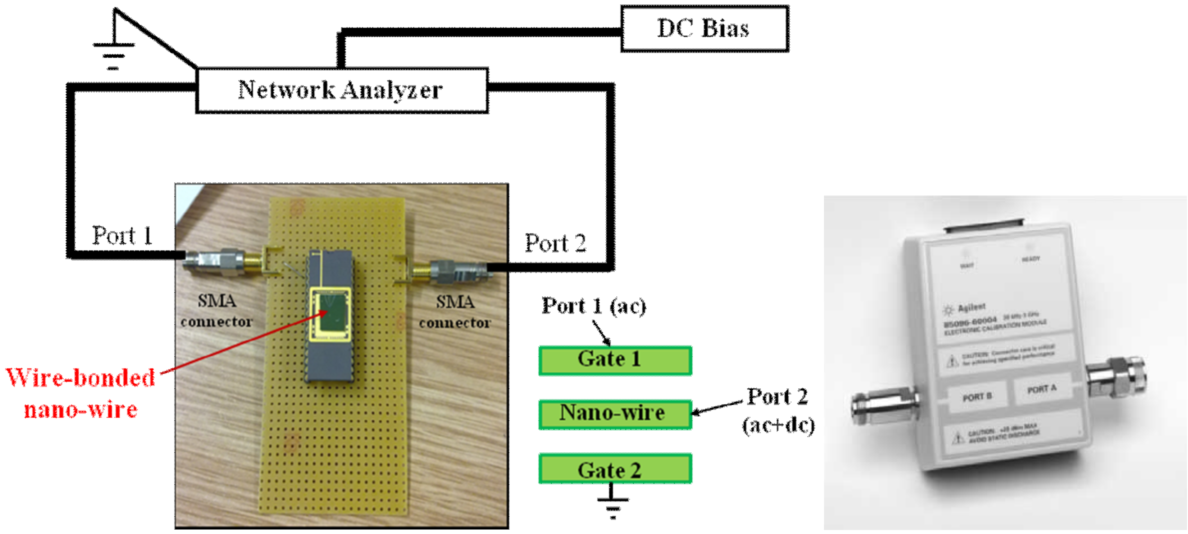

(a) **(b)**

Fig. 5.7 (a) The RF measurement setup for NWs, and (b) Agilent Ecal used for the calibration [153]

Using the cb, cc and wire bonding added some un-wanted parasitic frequencies to the resonance frequencies of the NW especially at higher range of frequencies that is really difficult to distinguish them from the real resonance frequency of the NW. To avoid these parasitic effects as much as possible, the longest NW with l=2000 nm was used for the RF measurement that has the lowest resonance frequency of 218.392 MHz based on the numerical analysis. To be able to differentiate the real resonance frequencies of the suspended NW from the parasitic frequencies, S_{21} signal (the transmitted signal from gate1 to the NW) was measured in five steps and its magnitude versus frequency for all of the steps are shown in Fig. 5.8. For all the measurement steps in Fig. 5.8, the AC voltage with the power of -10 dBmWatt, IF bandwidth of 500 Hz and number of point of 601 were applied based on the measurement setup in Fig. 5.7 (a). Note that, the power of -10 dBmWatt means *10log(power/mWatt)*, so the power is calculated equal to 0.1 mWatt. The DC voltage in Fig.

5.7 (a) is applied to the NW using Agilent semiconductor device analyzer B1500. The measurement was done in the atmosphere and at room temperature.

Before discussing the measurement result in Fig. 5.8, the NW was simulated using CoventorWare in the atmosphere and at room temperature to investigate S_{21} signal of the NW. The circuit model of the NW is shown in Fig. 5.9. The beam and a side electrode are defined using the components and the configuration that was discussed in section 3.5. For simplification, the second electrode is ignored as it is grounded in the measurement setup. V_{dc}=0-100 V is applied to the beam. For the two-port scattering analysis, V_{ac} is applied to the NW within a range of frequency along with V_{dc} and S_{21} signal was measured at the output node shown by *out* in Fig. 5.9. Figures 5.10 (a) and 5.10 (b) show the magnitude and phase of S_{21} signal for the NW, respectively. The magnitude of S_{21} signal at the resonance frequency in Fig. 5.10 (a) increases while the resonance frequency decreases by increasing V_{dc} as was expected from Fig. 3.19. For V_{dc}<60 V, the magnitude of the peak at resonance frequency is much smaller than 1 dB. For V_{dc}=0 V, S_{21} signal does not show any peak at the resonance frequency. This fact is explained using eq. (2-3) in which the electro-static force becomes zero at the resonance frequency by applying V_{dc}=0 V.

In Fig. 5.8, first S_{21} signal was measured for the prepared cb that consists of SMA connectors and the wiring (step 1). Then the cc, without any glued chip, was mounted on the cb and its S_{21} signal was measured (step 2). For the next step, a chip including (chip 2) non-suspended NWs was glued to the cc and mounted on the cb followed by measuring its S_{21} signal (step 3). After that the non-suspended NWs were wire bonded to the cc and the S_{21} signal was measured (step 4). Finally, NWs in chip 2 were suspended using vapor HF as explained in section 4.1 and wire bonded to the cc and mounted on the cb. Then the S_{21} signal was measured for this step (step5). In Fig. 5.8, the S_{21} signal for the suspended NW in the step 5 shows a large peak at 273 MHz that is specified by a dotted circle and at first assumed to be the possible resonance frequency of the suspended NW. This assumption was due to the fact that the peak showed the magnitude and phase of the expected S_{21} signal at resonance frequency as discussed previously for Fig. 5.10 and had a resonance frequency value near the numerical value of 218.392 MHz. The difference in the measured and calculated resonance frequency is explained by the difference in the dimensions of beam in layout and in the fabricated device. Later on, due to the repetition of the peak shown in Fig. 5.8 for the S_{21} signal of other four steps, this assumption was found not to be valid. Moreover, the total quality factor, Q_{Total}, is ~4 that is very low compared to the numerical equivalent value of 4.5×10^3 based on formulas in section 3.3. In order to investigate this case more precisely while considering the effect of DC biasing voltage of the NW on the resonance frequency, different DC voltages from 0-40 V was applied to the NW. If the specified peak for the S_{12} is due to the resonance frequency, its magnitude should be zero at V_{dc}=0 V and increase by increasing V_{dc} as discussed for Fig. 5.10 (a). The S_{21} signal of step 5 for V_{dc}=0-40 V is shown in Fig. 5.11. Figure 5.11 shows that the specified peak by dotted circle at 273 MHz is not zero at V_{dc}=0 V and changes of its magnitude due to changes of V_{dc} is very small and obscure. For this reason, the S_{21} signal at V_{dc}=10-40 V was subtracted from the S_{21} signal at V_{dc}=0 V, ΔS_{21} signal, as shown in Fig. 5.12 (a) to remove the possible parasitic effects and clearly see the dependency of a resonance peak to V_{dc}. The phase of ΔS_{21} signal is shown in Fig. 5.12 (b) for different V_{dc}. The ΔS_{21} signal for all voltages in Fig. 5.12 (a) shows two peaks around 194 MHz and 278 MHz.

The ΔS_{21} signal versus frequency for the suspended NW using BHF in chip 1 with l=2000 nm is shown in Fig. 5.13 using the same measurement setup for Fig. 5.12. Figure 5.13 also shows the peaks around 194 MHz and 278 MHz same as Fig. 5.12 (a). To investigate the origin of these peaks, the same measurement was repeated for two non-suspended NWs in Fig. 5.14 with the same dimensions as the previously measured suspended NWs in chip 1 and 2. Non-suspended NWs show peaks very close to peaks in Figs. 5.12 (a) and 5.13. As a result, these peaks are not due to the mechanical resonance of NW but due to the extra wire-bonding of NW and using of cb and cc especially when the calibration was done at the end of RF cables. The parasitic frequencies can be avoided by designing a metal pad for devices that fits the RF measurement requirements and doing a calibration much nearer to the device.

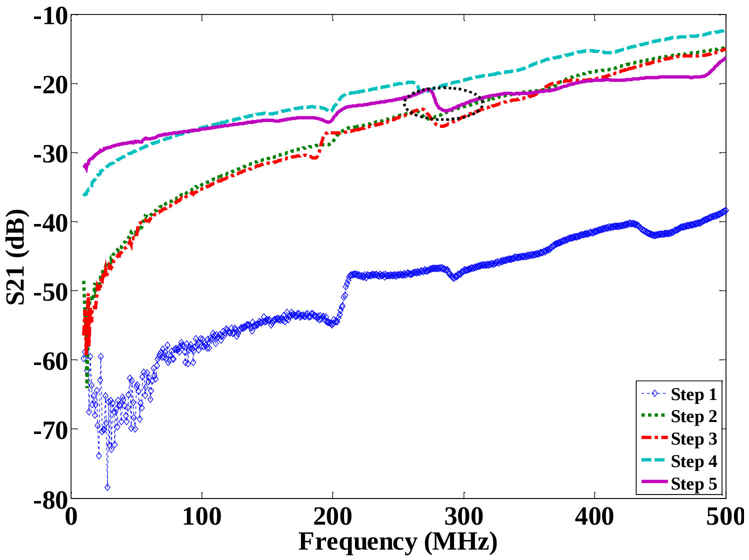

Fig. 5.8 The magnitude of S_{21} signal for 5-step measurement of the suspended NW with l=2000 nm in chip 2

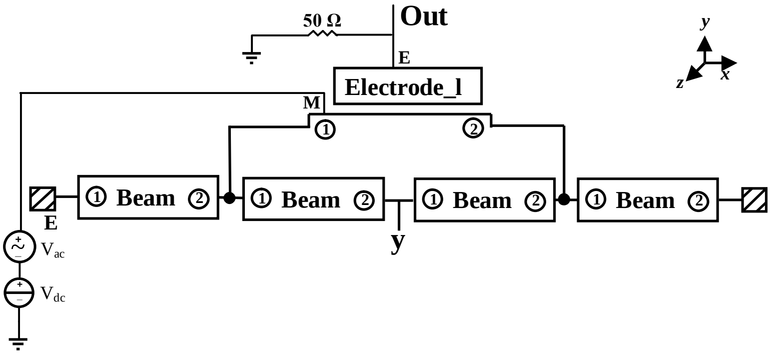

Fig. 5.9 The circuit model using CoventorWare for the NW for extracting S-parameters

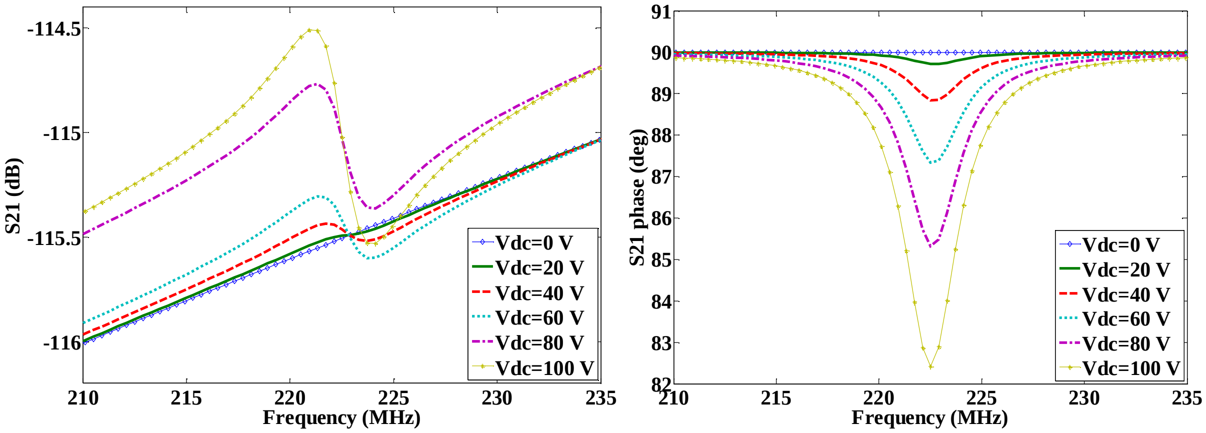

(a) (b)

Fig. 5.10 S_{21} signal for the simulated NW: (a) The magnitude and (b) phase for different V_{dc}

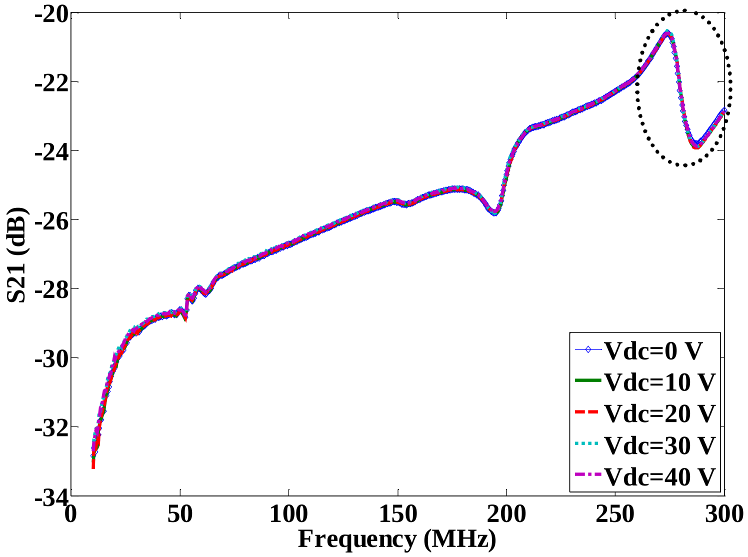

Fig. 5.11 The magnitude of S_{21} signal for the suspended NW of chip 2 in step 5 for different V_{dc}

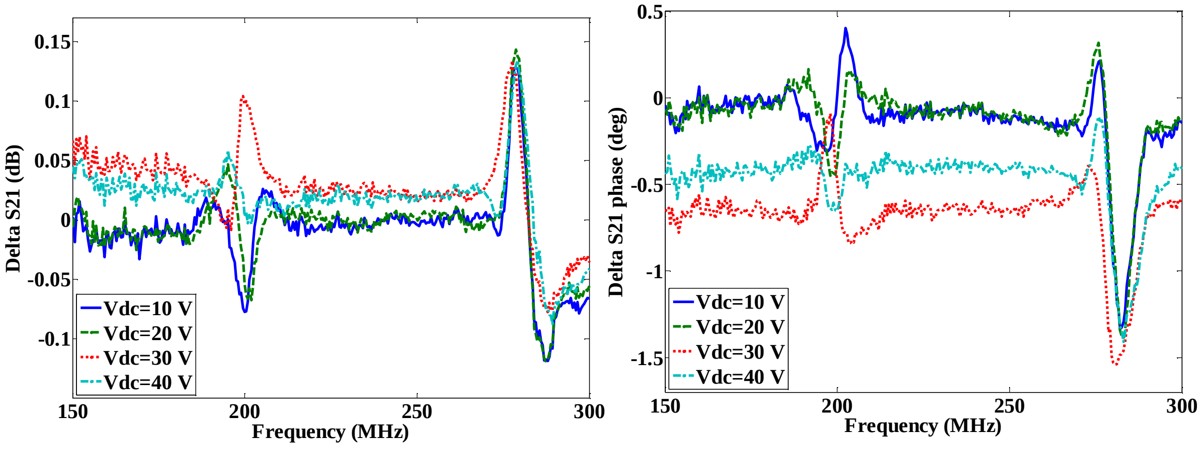

(a) **(b)**

Fig. 5.12 ΔS_{21} signal for the suspended NW of chip 2 in step 5: (a) The magnitude and (b) phase for different V_{dc}

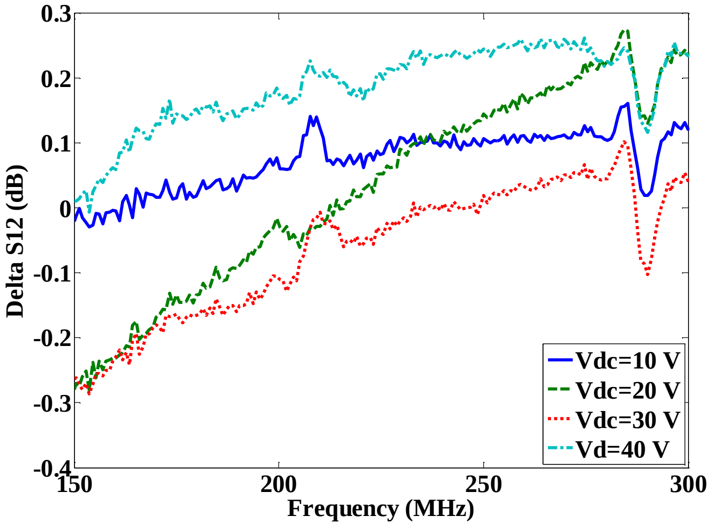

Fig. 5.13 The magnitude of ΔS_{21} signal for the suspended NW with *l*=2000 nm in chip 1 of step 5 for different V_{dc}

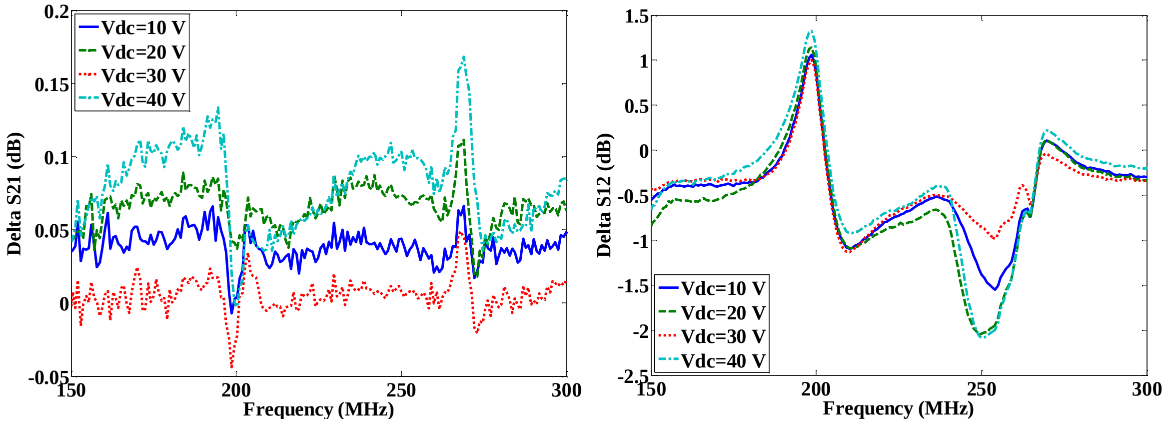

Fig. 5.14 The magnitude of ΔS_{21} signal for the non-suspended NWs with *l*=2000 nm in step 4 for different V_{dc}

5.2 Characterization of NEM structures

The DC characterization of NEM structures in Fig. 4.10 was done using Cascade R32 REL3200 probe-station. NEM structures have t=50 nm, w=45-135 nm, l=400-2000 nm, g=80 nm and N_D doping of 2×10^{19} cm^{-3}. As discussed in section 4.2.2, the effect of forming-gas annealing (FGA) on the contact resistance between Aluminium (Al) and silicon and consequently characteristics of suspended beams are investigated. The DC voltage across the beam with w=105 nm and l=1000 nm was swept from -10 mV to 10 mV before and after FGA and the current versus voltage is shown in Fig. 5.15. The current increases near two orders of magnitude after the annealing that means a reduction of contact resistance between Al and silicon. As a result, FGA is an important step in the fabrication process.

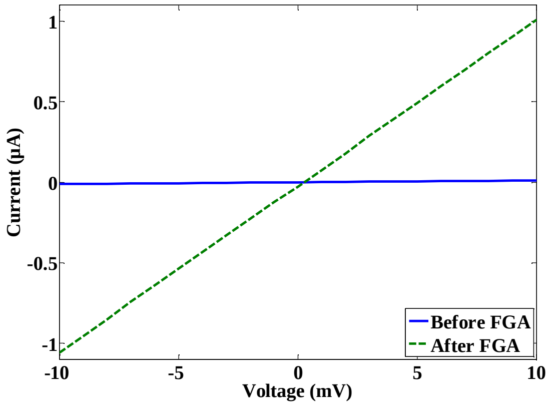

Fig. 5.15 The current of the beam with w=105 nm and l=1000 nm versus voltage before and after FGA

Among the devices in the fabricated six sets in section 4.2.2, a few of the suspended beams show the linear characteristics for the beams. Figures 5.16 (a) and 5.16 (b) show DC characteristics of beams with w=105, l=1000, 2000 nm and w=135 nm, l=400, 800 nm, respectively. The measured resistance values with respect to Fig. 5.16 (a) are three orders of magnitude larger than the calculated resistance using eq. (5-1) while for the beams in Fig. 5.16 (b), the measured and calculated resistance were in the same order. The calculated resistance for the beam with l=2000 nm in Fig. 5.16 (b) gives ρ'=6.91×10^{-5} Ω.m respect to eq. (5-1) that shows the N_D doping of 7.92×10^{19} cm^{-3}. The derived N_D doping for the beam is similar to the expected doping value for the SOI layer. Figure 5.17 shows the non-linear characteristics of the beams with w=135 nm for different lengths by sweeping the voltage from -5 V to 5 V across the beam. The high difference between the measured and calculated resistance in Fig. 5.16 (a) and the non-linear characteristics in Fig, 5.17 is mainly due to the high contact resistance between the Al and silicon in contact holes. Even though in the fabrication process the BHF etching was done to remove any layer above the silicon at the contact holes just before the evaporation of Al and final FGA was done in order to reduce the contact resistance (see section 4.2.2). The following solutions should be considered for the improvement of the ohmic contact between Al and silicon. The temperature of 400-450 ^{o}C was used for FGA of fabricated devices in section 4.2.2. A lower temperature annealing than 350 ^{o}C improves the contact resistance between Al and silicon because the Schottky barrier height of A1 contact to N-type silicon can increase by annealing in the temperature range of 350-550 ^{o}C [154]. As another alternative a SOI wafer with higher doping than 2×10^{19} cm^{-3}, 6×10^{19} cm^{-3}, is used to make a better ohmic contact between Al and silicon.

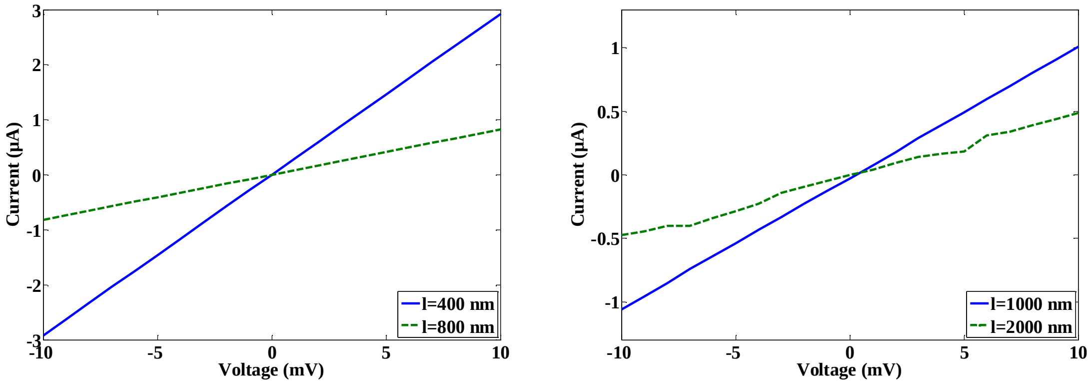

(a) **(b)**

Fig. 5.16 The current of the beam versus voltage with different lengths and: (a) *w*=105 nm and (b) *w*=135 nm

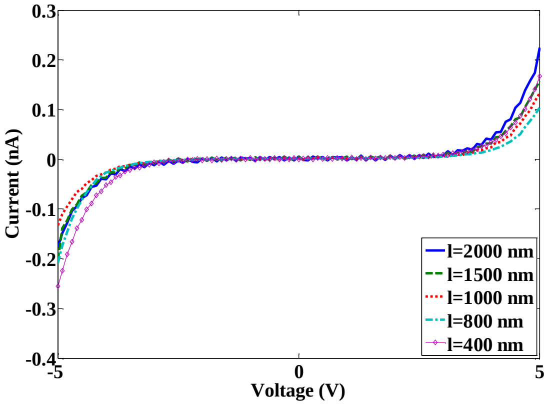

Fig. 5.17 The non-linear characteristics of beams with *w*=135 and different lengths due to the high contact resistance between Al and silicon

For the RF characterization of NEM structures, Cascade SUMMIT 12000B probe station was used. Same as in the RF characterization for NWs, S-parameters for NEM structures were measured using Agilent E8361A PNA network analyzer. Ground-signal-ground (GSG) probes with the pitch of 150 μm were used for the measurement that fit the designed RF pads in Fig. 4.9. The two-port calibration was done using the Cascade impedance standard substrate (ISS) [155] in Fig. 5.18 (a) at the end of GSG probes. The beam with w=135 nm, g=80 nm and l=2000 nm with the DC characteristics in Fig. 5.16 (b) was used for the RF measurement that has the resonance frequency of 285 MHz based on the numerical analysis. The AC voltage with the power of -10 dBmWatt, IF bandwidth of 500 Hz and number of point of 601 were applied based on the measurement setup in Fig. 5.18 (b). The DC voltage is applied to the beam using Agilent semiconductor device analyzer B1500. The measurement was done in the atmosphere and at room temperature.

The magnitude of S_{21} signal versus frequency is shown in Fig. 5.19 (a) for different DC voltages. The smith chart of S_{11} signal for the NEM structure at V_{dc}=20 V and in the same range of frequency of Fig. 5.19 (a) is shown in Fig. 5.19 (b). Respect to Fig. 5.19 (b) and the explanation of the smith chart in section 2.3.2.1, the device works in the “capacitive+resistive” region. By using eqs. (2-12) and (2-15) and Γ_{in}=0.95-1.19j for the device at the frequency of 285 MHz in Fig. 5.19 (b), the capacitance value of 1.13 pF is calculated. None of the peaks of S_{21} signal in Fig. 5.19 (a) show the zero magnitude at V_{dc}=0 V. Therefore these peaks are not due to the resonance of the beams. So the magnitude and phase of ΔS_{21} signal versus frequency for different V_{dc} voltages are shown in Figs. 5.20 (a) and 5.20 (b) respectively to remove the parasitic effects induced by the measurement setup and find the resonance peak. It is not easy to distinguish the resonance peak in Fig. 5.20 (a) from the background noise signal. In order to explain this effect, the NEM structure with the current dimensions is compared to the 14-MHz in-plane NEM resonator by C. Durand et. al in Fig. 5.21 (a) [156]. Their resonator consists of a vibrating gate and a resonant suspended gate MOSFET (RSG-MOSFET) that is fabricated using silicon-on-nothing (SON) technology. The vibrating gate has the dimensions of w=165 nm, t= 400 nm, g=120 nm and l=10 µm and measured parameters for the RSG-MOSFET resonator are: f_0=14.43 MHz, R_x=736 kΩ, C_{gap0}=21.5 fF, Q_{Total}=700. The electrical setup for the capacitive detection of the RSG-MOSFET resonator in Fig. 5.21 (a) is similar to the setup for the NEM structure in Fig. 5.18 (b) and it shows 2 dB for the magnitude of the transmission signal in this setup as shown in Fig. 5.21 (b). With respect to Fig. 2.21, the equivalent circuit model at resonance frequency for a resonator consists of a parallel motional resistance, R_x, and C_{gap} that were studied in section 3.2. Considering the C_{gap0} in the order of atto F for the NEM structure, the magnitude of the transmission signal is strongly dependent to R_x that this dependency was also explained in section 2.3.2.5.

In order to compare the motional resistance of the NEM structure to the RSG-MOSFET, the ratio of key factors for the NEM structure including f_0, Q_{Total}, m_0 and η to the equivalent values for the RSG-MOSFET that are f_0', Q'_{Total}, m_0' and η' are calculated in Table 5.2 using eqs. (3-7), (3-13) and (3-15). Based on the ratios of f_0 / f_0', Q_{Total} / Q'_{Total}, m_0 / m_0' and η / η' in Table 5.2, R_x / R_x' is calculated using eq. (3-11). With respect to Table 5.2, R_x for the NEM structure that works in the atmosphere is higher than R_x' of the RSG-MOSFET and causes higher signal drop across it and consequently smaller output signal than the 2 dB-magnitude transmission signal of the RSG-MOSFET in Fig. 5.21 (b). This reason explains the difficulty in distinguishing the resonance peak with very small magnitude from the back ground noise signal in Fig. 5.20 (a). In order to reduce R_x and improve the transmission signal for the NEM structure in Fig. 5.20 (a), the measurement should be done in high vacuum same as the RSG-MOSFET. The effect of high vacuum on R_x of the NEM structure is shown in Table. 5.2. Important to note is that, the lower working pressure reduces R_x if Q_{Total} is mainly dominated by air damping, Q_{Air}. For example Q_{Total} for the NEM structure with w=135 nm and l=2000 nm is dominated by anchor doping, Q_{Anchor}, and as shown in Table 5.2, its R_x is not reduced much by using high vacuum. In contrast, Q_{Total} for the NEM structure with w=45 nm, g=80 nm and l=400 nm is dominated by Q_{Air} and with respect to Table 5.2, by doing the measurement in high vacuum R_x reduces five orders of magnitude compared to its equivalent value in the atmosphere and consequently the magnitude of transmission signal improves from the magnitude of the signal in the atmosphere. R_x for the NEM structure with w=45 nm in high vacuum is two orders of magnitude smaller than that of the RSG-MOSEFT that means a larger magnitude for the transmission signal will be found for the NEM structure compared to the RSG-MOSFET. Important to note that this NEM structure also shows a larger Q_{Total} than that of the RSG-MOSFET that makes it easy for the recognition of the resonance peak from the back ground noise signal. For further improvement of the signal is necessary to apply larger V_{dc} than 40 V to the beam that improves the magnitude of signal as was discussed in Fig. 5.10 but it causes the pull-in or breaking for the beam. The integration of the NEM structure with an MOSFET improves the transmission signal that is explained in the next section. Moreover, the impedance analyzer can be used as an alternative method for the measurement of the devices with large impedance as explained in section 2.3.2.2.

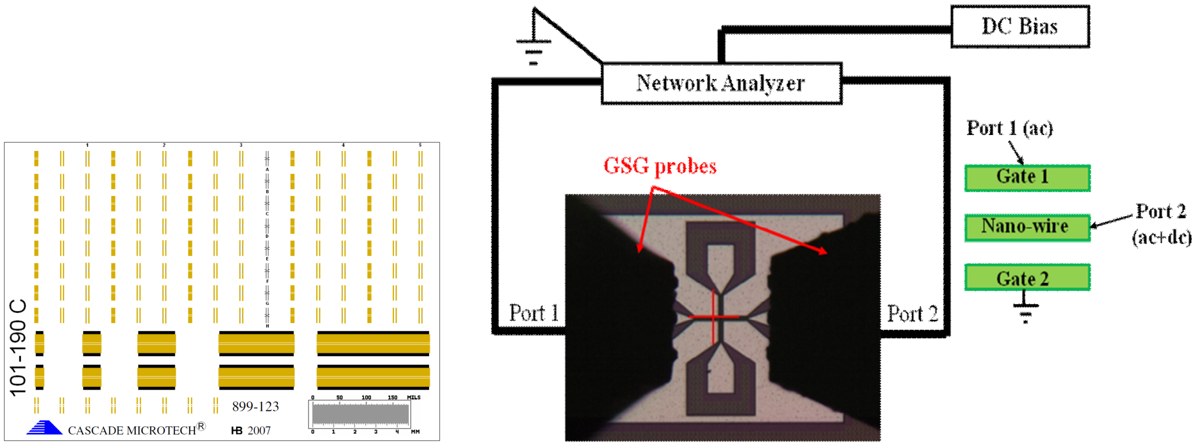

(a) (b)

Fig. 5.18 (a) Cascade ISS used for the calibration [155], (b) the RF measurement setup for the NEM structure

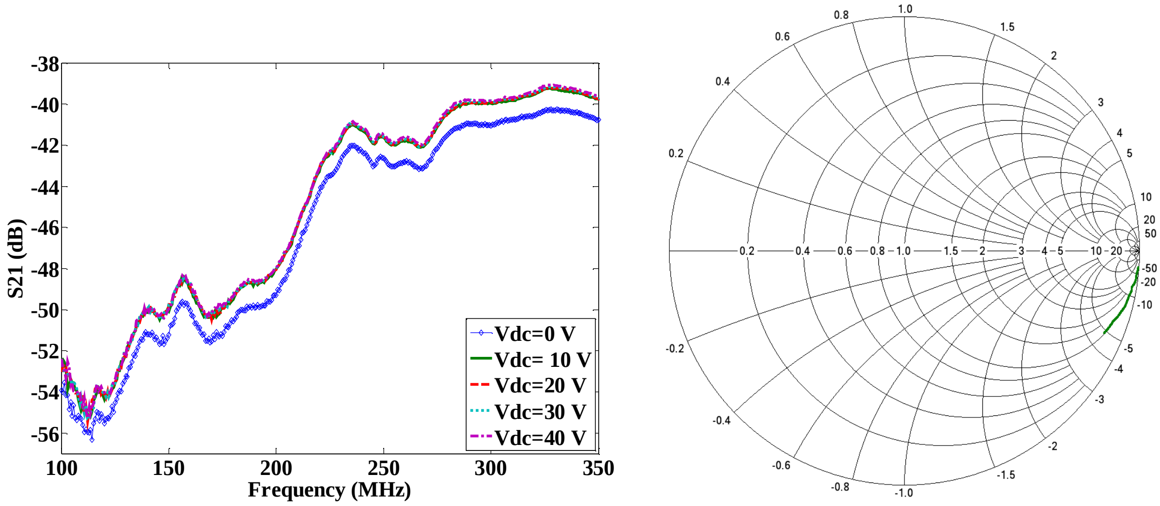

(a) (b)

Fig. 5.19 S-parameters for the NEM structure with *w*=135 nm, *g*=80 nm and *l*=2000 nm: (a) The magnitude of S_{21} signal versus frequency for different V_{dc} and (b) the smith chart for S_{11} signal at V_{dc}=20 V

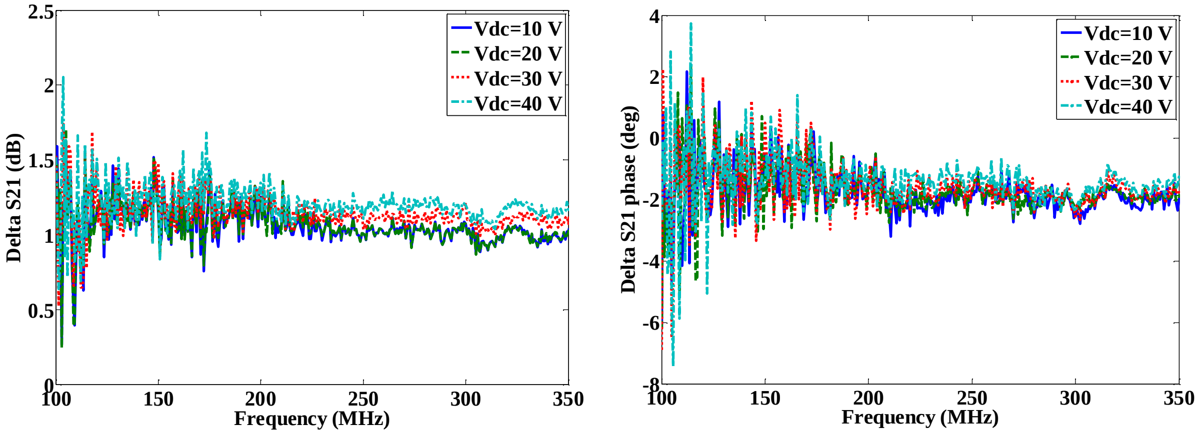

(a) (b)

Fig. 5.20 ΔS_{21} for the NEM structure with *w*=135 nm, *g*=80 nm and *l*=2000 nm: (a) The magnitude and (b) phase for different V_{dc}

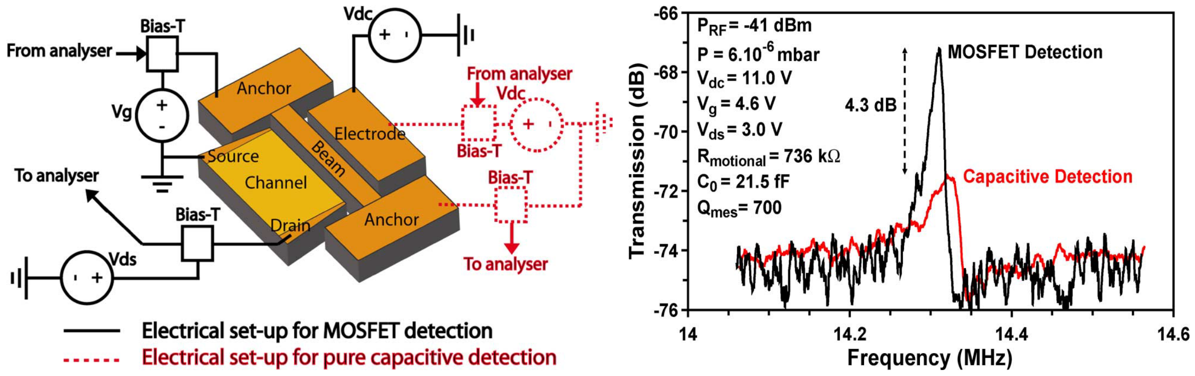

(a) (b)

Fig. 5.21 The 14-MHz RSG-MOSFET resonator [156]: (a) The electrical setup for the capacitive and MOSFET detections and (b) the transmission signal in both setups versus frequency

Table 5.2 The analytical values for NEM structures in the atmosphere and vacuum based on equivalent values for the RSG-MOSFET

Device	Beam dimensions	Working pressure	f_0 / f_0'	m_b / m_b'	Q_{Total} / Q_{Total}'	η / η'	R_x / R_x'
RSG-MOSFET	w=165 nm, t=400 nm, l=10 µm, g=120 nm	High vacuum (6×10^{-4} Pa)	1	1	1	1	1
NEM structure	w=135 nm, t=50 nm, l=2 µm, g=80 nm	Atmosphere	21.2	0.02	0.013	0.57	100.3
		High vacuum			0.014		93.2
	w=45 nm, t=50 nm, l=400 nm, g=80 nm	Atmosphere	204.4	0.001	0.005	0.57	125.8
		High vacuum			49.23		0.01

5.3 Characterization of IP R-NEM sensors

IP R-NEM sensors were fabricated based on SOI technology with t=40 nm, w=45-135 nm, l=400-2000 nm, g=80-2000 nm and different doping strategies as shown in Fig. 4.33. In the beginning, the DC characterization for the beams with different doping types are done by sweeping the voltage from -10 mV to 10 mV across the beam with w=135 nm and different lengths. The current through beams with doping of $N^+=4\times10^{19}$ cm^{-3} and $P^+=10^{19}$ cm^{-3} versus the applied voltage are shown in Figs. 5.22 (a) and 5.22 (b), respectively. In Fig. 5.22 (a), the current at zero voltage is in the order of 10^{-8} A while in Fig. 5.22 (b) it is in the order of 10^{-10} A. The beams with N-type doping show larger current at non-zero voltages than that of P-type beams due to the smaller resistivity of N-type doped silicon. The resistance of N- and P-type beams versus their lengths are shown in Fig. 5.23 (a) and 5.23 (b), respectively. Using eq. (5-1), Fig. 5.23 (a) shows ρ value of 2.71×10^{-3} Ω.cm that gives the doping concentration of ~10^{19} cm^{-3} that is in the same order of previously stated doping. The ρ value of 5.92×10^{-2} Ω.cm for the beams in Fig. 5.23 (b) gives the doping concentration of ~5×10^{17} cm^{-3} that is two orders of magnitude less than the previously stated doping. By reducing the width of beams to 45 nm, the extracted doping concentration will reduce. Fig 5.24 (a) shows the current versus voltage for P-type beams with *w*= 45 nm and lengths from 400 nm to 1500 nm. The resistance versus length for P-type beams are shown in Fig. 5.24 (b). Using curve fitting to Fig. 5.24 (b), the doping concentration of ~9×10^{16} cm^{-3} is calculated that is smaller than the extracted value for the beams with *w*=135 nm.

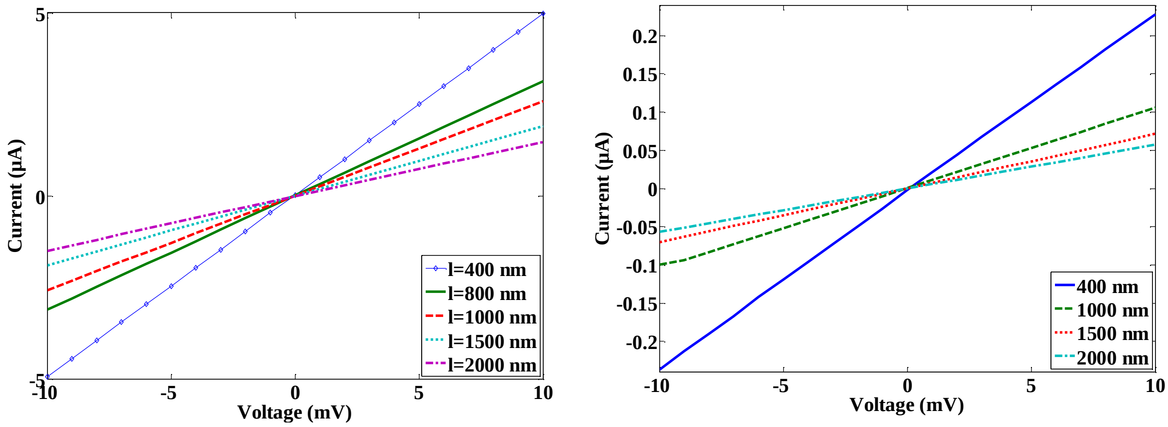

(a) (b)

Fig. 5.22 Comparison of the current versus voltage for beams with *w*=135 nm and different lengths of (a) N-type doping and (b) P-type doping

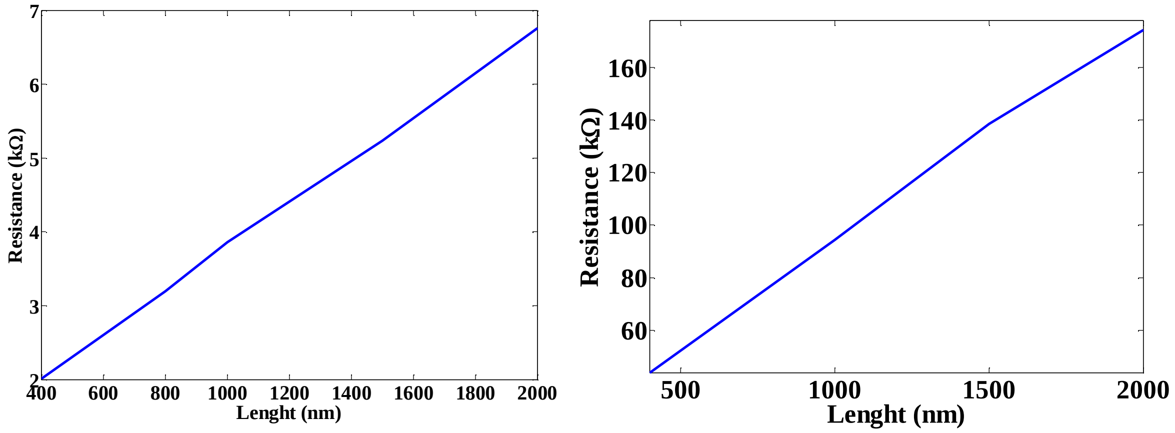

(a) (b)

Fig. 5.23 The resistance versus length of beams with *w*=135 nm for (a) N-type doping and (b) P-type doping

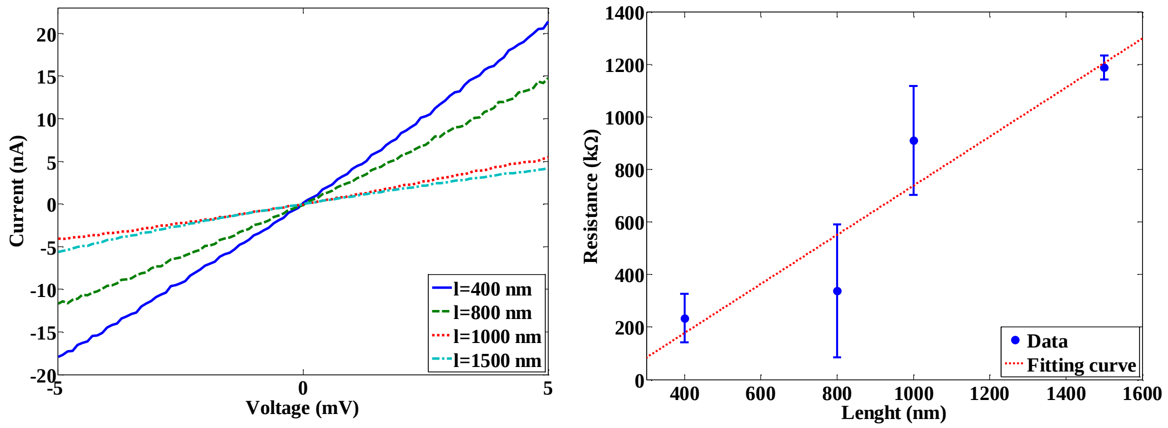

(a) (b)

Fig. 5.24 P-type beams with *w*=45 nm and different lengths: (a) The current versus voltage and (b) the resistance versus length

As discussed for the NEM structure in the previous section, a MOSFET is integrated with the beam for the IP R-NEM sensor in Fig. 4.31 to improve the magnitude of the transmission signal in vacuum. With respect to Fig. 2.32 and eq. (2-20), the output signal from the resonator is amplified by the intrinsic gain of MOSFET, $g_m \times r_o$ where g_m is transconductance and r_o is the output resistance of MOSFET that is in parallel with the 50 Ω-output impedance of analyzer. By optimizing the applied bias voltages in DC characteristics of the MOSFET, the maximum value for g_m is achieved that amplifies the input signal to the MOSFET as much as possible. Based on the fabrication technology at the Commissariat à l'Energie Atomique- Laboratoire d'Electronique et de Technologie de l'Information (CEA-LETI), after the implantation and drive-in steps for dopants, there is an estimated lateral diffusion length of 100 nm, so first the characterization of the MOSFET with the longest channel of 1250 nm was done to minimize the short channel effect. The voltage of 0-0.1 V was applied to drain, V_d, for the enhancement-mode n-channel MOSFET ($N^+/P/N^+$-type) with channel length, l_C, of 1250 nm, l=2000 nm, w=135 nm and g=80 nm as shown in Fig. 5.25 (a). I_d-V_d characteristics for the MOSFET for gate voltages, V_g=0, 20 V are shown in Fig. 5.25 (b). Figure 5.25 (b) shows that even at V_g=0 V, the channel is induced by the drain voltage that is explained by the drain-induce-barrier-lowering (DIBL) or punch through effect [157]. Moreover, increasing of V_g to 20 V slightly changes the drain current in inset to Fig. 5.25 (b) that shows the very small control of gate over the channel. To investigate these effects, I_d-V_g characteristics of the MOSFET are shown in Fig. 5.26 for different V_d. The threshold voltage, V_t, of 1.75 V is analytically calculated using the following formula for the conventional long n-channel MOSFET [157]:

$$V_t = V_{FB} + 2\left|\varphi_p\right| + \frac{1}{C'_{ox}}\sqrt{2\varepsilon_s q N_A 2\left|\varphi_p\right|} \tag{5-2}$$

where V_{FB} is the flat band voltage, φ_p is the substrate potential, C'_{ox} is the gate oxide capacitance per unit area that is calculated using eq. (2-6), silicon permittivity, ε_s, is 0.104 fF/µm, electron charge, q, is 1.602×10^{-4} fC and acceptor substrate doping, N_A, is 10^{16} cm^{-3}. Important to note that, only by applying V_d in the range of 200 to 400 mV the carrier modulation in the channel of MOSFET was seen in I_d-V_g characteristics. With respect to Fig. 5.26, MOSFET has the OFF-current in the order of mA and small ON/OFF current ratio for different V_d and the current is increased by increasing V_d due to the higher impact of drain over the channel instead of the gate. The threshold voltage of $V_t\approx9$ V is found respect to the V_t extraction methods in [158] for the MOSFET in Fig. 5.25 that is much larger than the previously calculated V_t=1.75 V. The increase in the threshold voltage can not be explained with the DIBL effect which should cause reduction in the threshold voltage [157]. Further simulation using the device simulator ATLAS 3D [142] for the MOSFET is done for investigating the reason of high threshold voltage and OFF-current later in this section. Moreover, the reason for the reduction of of V_t by reducing V_d in Fig. 5.26 is discussed in the simulation results later.

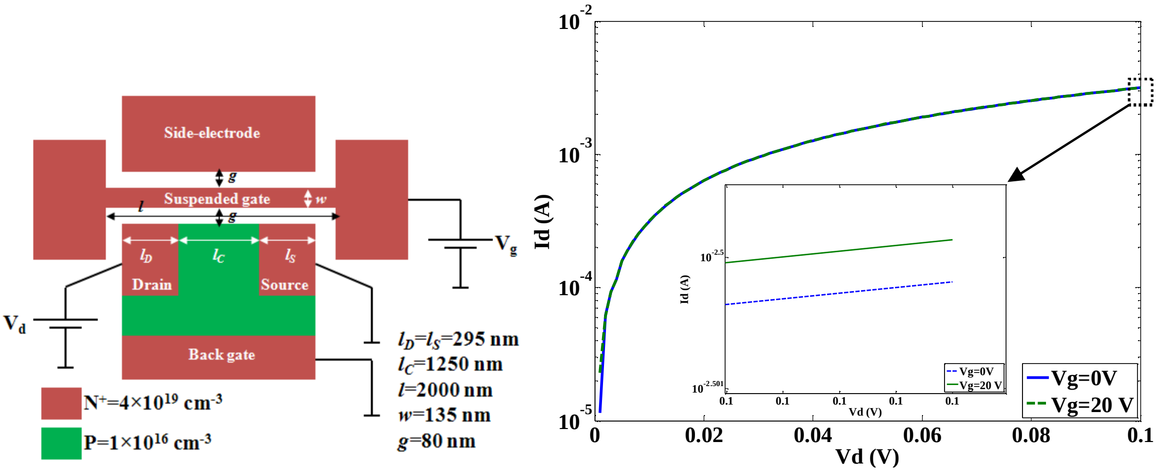

(a) (b)

Fig. 5.25 The N^+/P/N^+-type in-plane MOSFET: (a) Dimensions and the DC characterization setup and (b) the I_d-V_d characteristic at V_g=0 and 20 V

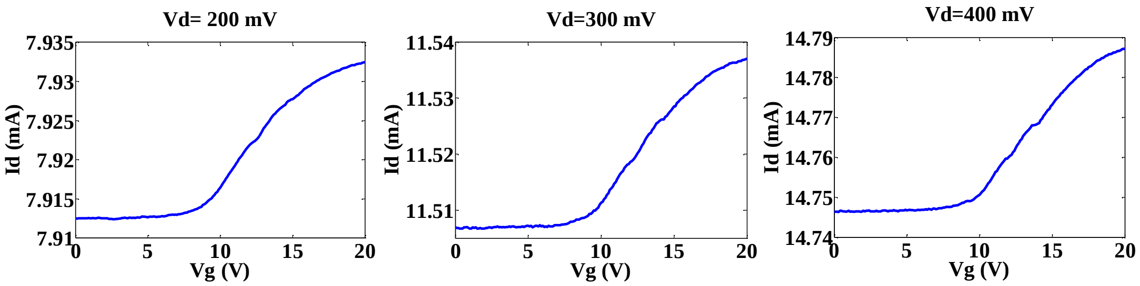

Fig. 5.26 The I_d-V_g characteristic at different V_d for the N$^+$/P/N$^+$-type in-plane MOSFET with *w*=135 nm, *g*=80 nm and *l*=2000 nm

I_d-V_g characteristics for the MOSFET with w=135 nm and different l_C at V_d=300 mV are shown in Fig. 5. 27. OFF-current mostly decreases while ON/OFF current ratio and V_t increase by increasing l_C in Fig. 5.27 that is due to the reduction of drain impact on the longer channel. The fluctuation in the current by increasing l_C is explained by the variation of the diffusion length of dopants in source and drain.

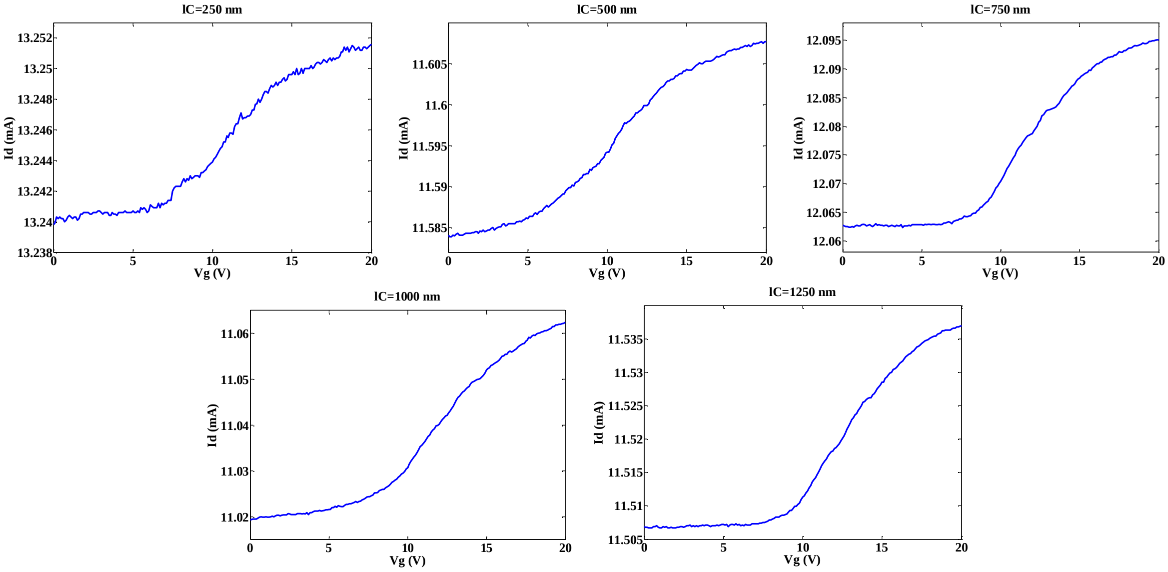

Fig. 5.27 The I_d-V_g characteristic for the MOSFET with *w*=135, *g*=80 nm and different l_C at V_d=300 mV

The transconductance versus V_g for the MOSFET is shown in Fig. 5.28 by taking derivative of I_d-V_g characteristics for different V_d in Fig. 5.26. V_d=400 mV at V_g=13.7 V gives the maximum g_m of 1.5 µS for the MOSFET that is in the same order of measured g_m for the RSG-MOSFET in Fig. 5.21 for the MOSFET detection setup that improves the transmission signal up to 4.3 dB. These biasing values will be used as the optimal values for drain and gate voltages in the subsequent RF measurement. By increasing the back gate voltage more than zero volts, g_m is reduced while the OFF-current is not reduced much. Due to this fact the back gate is grounded as well as the source. Note that, using V_d=400 mV and V_g=13.7 V the MOSFET works in the triode region as $V_{ds}<V_g-V_t$. Further processing on the device is needed for improving its DC characteristics as discussed later.

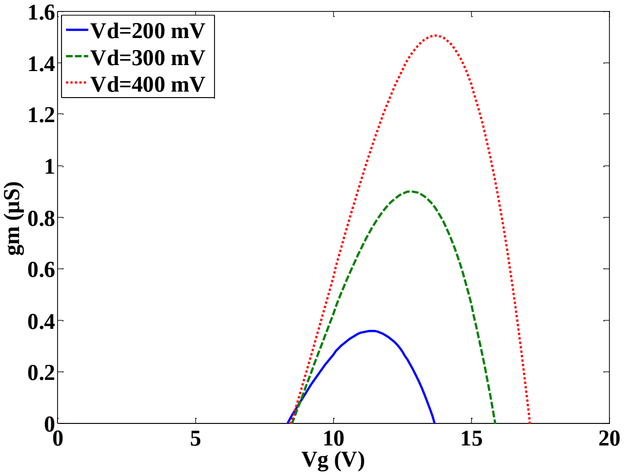

Fig. 5.28 g_m versus V_g at different V_d for the N$^+$/P/N$^+$-type in-plane MOSFET with w=135 nm, g=80 nm and l=2000 nm

In order to investigate the origin of high OFF-current, the leakage from source and drain to the back gate in Fig. 5.25 (a) was measured by sweeping the voltage from -10 mV to 10 mV for the source and drain. The leakage current versus applied voltage for drain and source are shown in Fig. 5.29. The leakage current is in the order of 10^{-4} A for both drain and source and 1 µm-distance of back gate from source and drain shows the dopants diffusion of source and drain towards the back gate is more than the previously stated 100 nm. The value of diffusion length that gives the leakage current in Fig. 5.29 is simulated later.

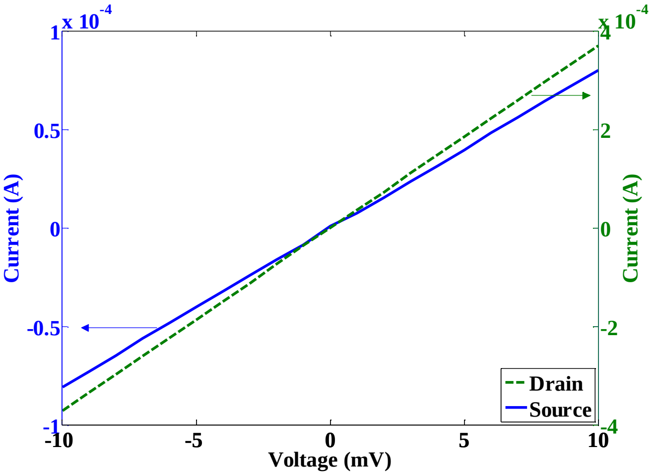

Fig. 5.29 Leakage current from source (solid line) and drain (dotted line) to substrate versus applied voltage to source and drain respectively

In order to isolate the source and drain as much as possible a trench is milled between them, from the end of back gate till 160 nm away from the edge of channel using focused ion beam (FIB) in collaboration with Mr. Marek E. Schmidt. Figures 5.30 (a) and 5.30 (b) show the MOSFET with w=45, g=200 nm, l=1750 nm and l_C=1000 nm before and after the FIB milling, respectively. I_d-V_g characteristics for the MOSFET before and after milling are shown in Fig. 5.31. Figure 5.31 (a) shows the OFF-current of 3.07 mA and a small ON/OFF ratio. After milling in Fig. 5.31 (b), the OFF-current is decreased to 1.5 mA and almost a linearly increasing current is shown for the MOSFET that declares the high OFF-current for the MOSFET is due to the large diffusion length for dopants in drain and source towards the channel. In order to improve the DC characteristics after milling a trench with higher depth should be considered to be sure about the complete isolation of source and drain by trench. Moreover, a smaller distance than 160 nm distance between the trench and edge of channel in Fig. 5.30 (b) should be used in order to be able to deplete the channel by gate voltage.

I_d-V_g characteristics for the MOSFET without the back gate and w=45 and l=2000 nm at V_d=200 and 300 mV in Fig. 5.32 shows the same behaviour in Fig. 5.31 (b). Figure 5.32 shows an OFF-current of mA and a very small ON/OFF current ratio at V_d=200 mV and almost a linearly increasing current for V_d=300 mV that proves the large diffusion length for dopants in source and drain towards the channel. Figure 5.33 shows changing of the I_d-V_g characteristic after the second time measurement that should be taken in account for the subsequent RF measurement. The DC characteristics of MOSFETs change over time mainly due to re-distribution of the trapped charges in oxide that is discussed later in the simulation and this instability makes the situation difficult for the subsequent RF measurement as the optimized bias voltages change.

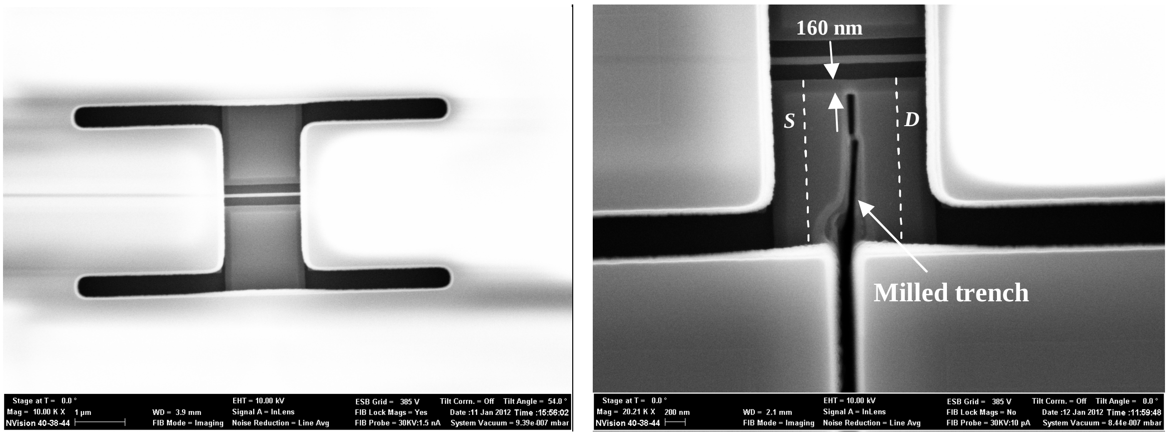

(a) (b)

Fig. 5.30 IP R-NEM sensor with w=45, l=1750 nm and l_C=1000 nm (a) before and (b) after the FIB milling

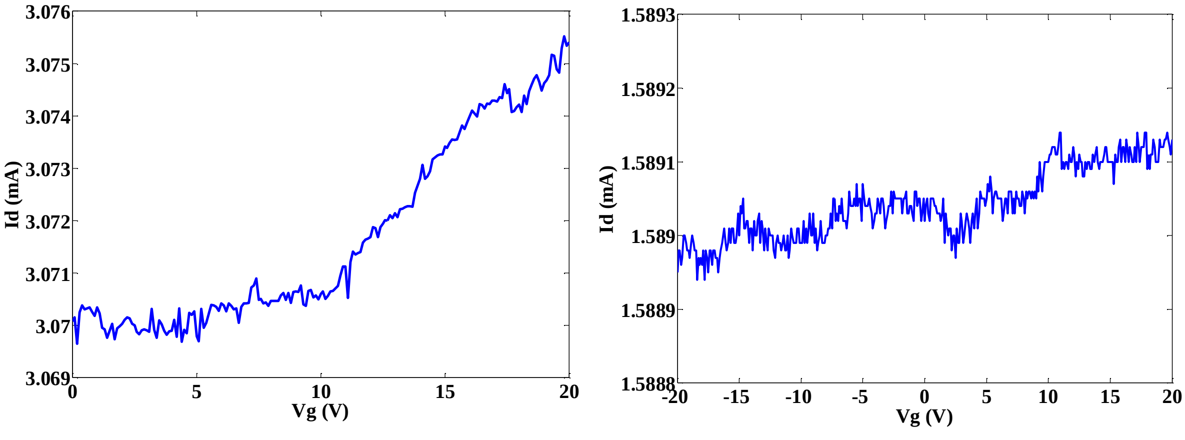

(a) (b)

Fig. 5.31 The I_d-V_g characteristic for the MOSFET with *w*=45, *l*=1750 nm and l_C=1000 nm at V_d=100 mV(a) before and (b) after the FIB milling

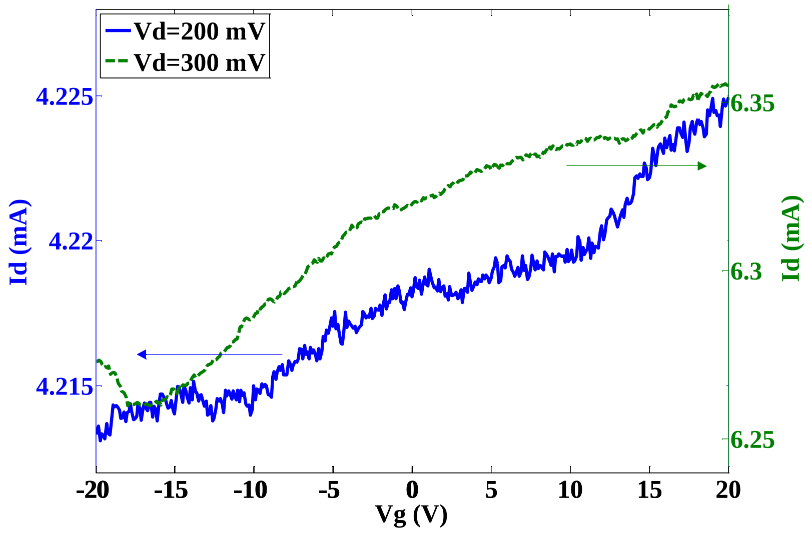

Fig. 5.32 The I_d-V_g characteristic for the $N^+/P/N^+$-type in-plane MOSFET without the back gate and with *w*=45 nm and *l*=2000 nm at V_d=200 and 300 mV

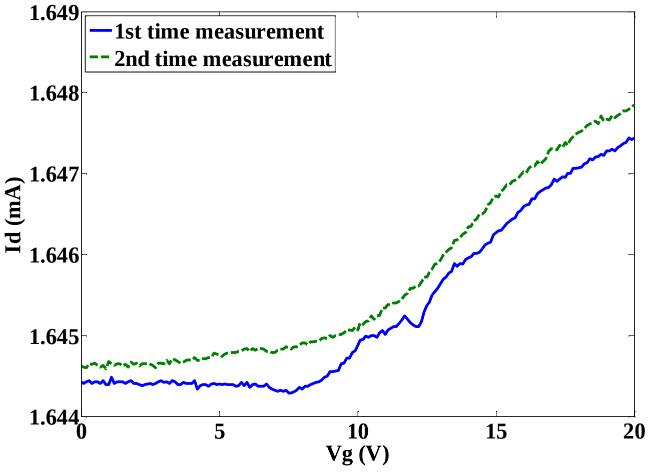

Fig. 5.33 Changes of the I_d-V_g characteristic for the MOSFET with *l*=400 nm, *g*=80 nm and *w*= 105 nm after the second time measurement

Same as the characterization for the MOSFET in Fig. 5.25 (a), the depletion-mode p-channel MOSFET ($P^+/P/P^+$-type) was characterized as shown in Fig. 5.34 (a). The negative voltage in the range of -0.1-0 mV is applied to drain, and the back gate and source are grounded. Similar to Fig. 5.25 (b), the high control of drain over the channel at V_g=0 V is also seen in the I_d-V_d characteristic of $P^+/P/P^+$-type MOSFET in Fig. 5.34 (b). Small changes in the drain current by increasing gate voltage to 20 V is shown in inset to Fig. 5.34 (b). Using eq. (5-2), V_t=1.1 V is calculated that will be compared to the measured V_t of the MOSFET later.

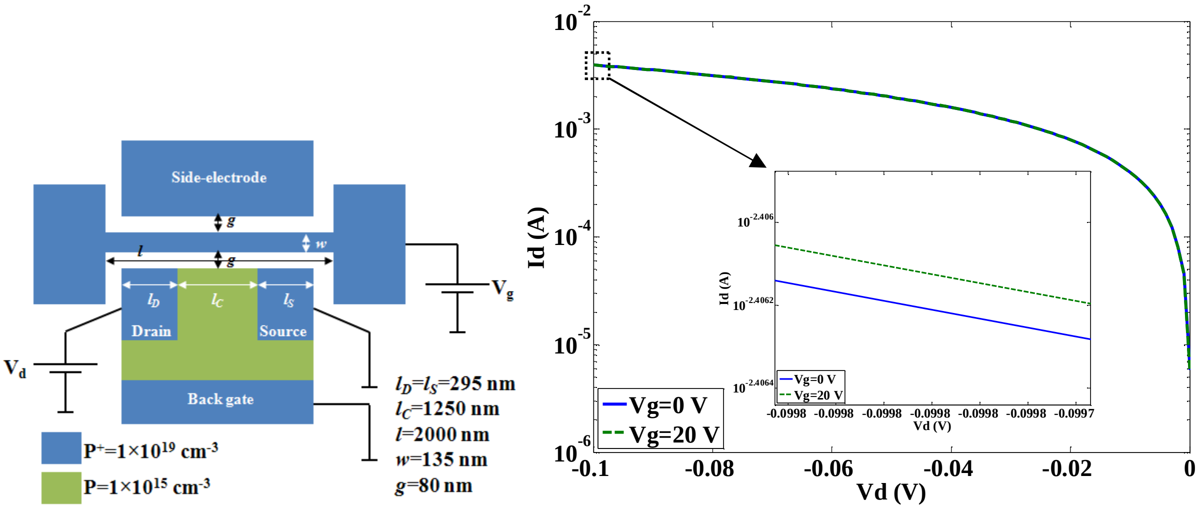

(a) (b)

Fig. 5.34 The $P^+/P/P^+$-type in-plane MOSFET: (a) Dimensions and the DC characterization setup and (b) I_d-V_d characteristics at V_g=0 and 20 V

Fig. 5.35 shows I_d-V_g characteristics of the $P^+/P/P^+$-type MOSFET for different V_d voltages from -100 to -250 mV. With respect to Fig. 5.35, MOSFET has the OFF-current in the order of mA and small ON/OFF current ratio that is similar to Fig. 5.26 for $N^+/P/N^+$-type MOSFET and shows the control of drain over the current in the channel. The threshold voltage of $V_t \approx 9$ V is found for the MOSFET that is larger than the previously calculated V_t=1.1 V. The MOSFET is ON for $V_g<V_t$ and is OFF for $V_g \geq V_t$ due to the depletion of channel so called normally-ON MOSFET. In Fig. 5.35, the current is increased by increasing V_d due to the higher impact of drain over the channel. g_m versus V_g of the MOSFET for different V_d are shown in Fig. 5.36. The applied drain voltage of V_d=-200 mV at V_g=8.7 V gives the highest transconductance of 1.07 mS for the MOSFET that is three orders of magnitude larger than that of the RSG-MOSFET, so these values will be used as the optimal values for drain and gate voltages for the subsequent RF measurement. The $P^+/P/P^+$-type MOSFET works very near to the saturation region. By doing the RF measurement for this MOSFET in high

vacuum the output signal from the resonator is amplified very well. The instability of DC characteristics was seen also for the $P^+/P/P^+$-type MOSFET by passing time that should be considered for the RF measurement.

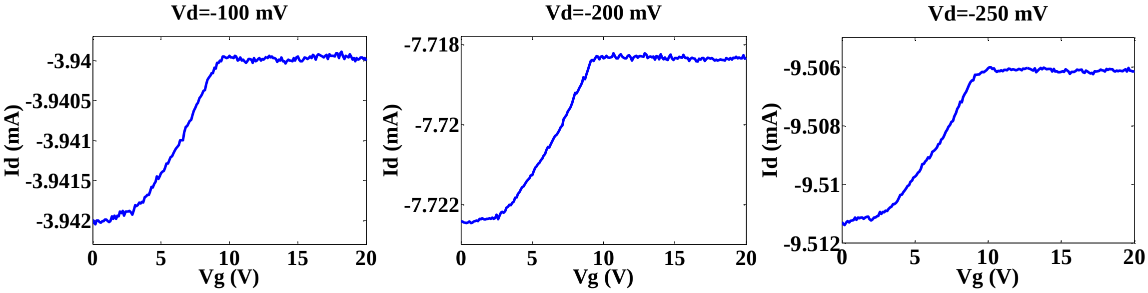

Fig. 5.35 I_d-V_g characteristics at different V_d for the $P^+/P/P^+$-type in-plane MOSFET with w=135 nm, g=80 nm and l=2000 nm

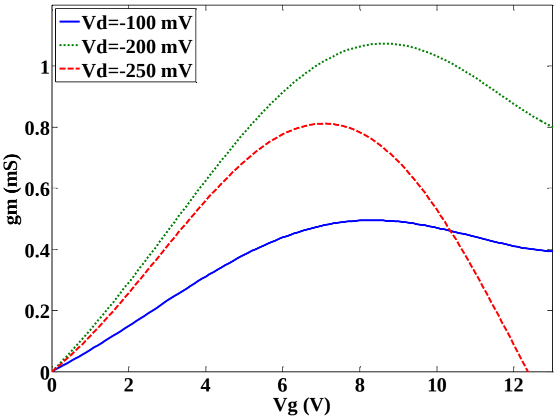

Fig. 5.36 g_m versus V_g at different V_d for the $P^+/P/P^+$-type in-plane MOSFET with w=135 nm, g=80 nm and l=2000 nm

In order to investigate the high OFF-current, small carrier modulation in the channel due to V_g and high threshold voltage of the characterized MOSFET in Fig. 5.25 (a), it was simulated using ATLAS 3D (see Appendix A.6) as shown in Fig. 5.37 (a). The two-dimensional (2D) top view of the MOSFET is shown in Fig. 5.37 (b). A suspended gate is modelled by considering an air region around the beam. To make the structure more consistent with the fabricated device, a 15 nm-SiO_2 layer is considered around the beam and on top of the channel as shown in the zoomed area in Fig. 5.37 (b). The surface mobility model, auger recombination, band gap narrowing and Fermi-Dirac distribution are considered for the carriers in the simulation [142],[159]. In the beginning an ideal uniform doping profile was considered for source, drain and back gate and the I_d-V_g characteristic of the MOSFET is shown in Fig. 5.38 (a). Figure 5.38 (a) shows the OFF-current in the order 10^{-17} A, ON-current in the order of µA and V_t=1.6 V. Then Gaussian doping profile was considered for source, drain and back gate and the value for the diffusion length along with y-axis, vertical diffusion length, was varied to find the value that gives the leakage current between drain and back gate as much as the current order in Fig. 5.29. I_d-V_g characteristics of the MOSFET at V_d=400 mV are shown in Fig. 5.38 (b) with vertical diffusion length of 100 nm (solid line) and 400 nm (dotted line) while the diffusion length along x-axis, lateral diffusion length, is 50 nm for both. The solid line in Fig. 5.38 (b) shows the OFF-current of nA, ON-current of 8 μA and V_t=1.5 V for the vertical diffusion length of 100 nm. By increasing the vertical diffusion length to 400 nm, the OFF-current increases to the order of mA for the dotted line in Fig. 5.38 (b) with the ON-current in the same order that is consistent with the measurement result for V_d=400 mV in Fig. 5.26 and shows that how the leakage from source and drain to the back gate can affect the I_d-V_g characteristic. In Fig. 5.38 (b), the lateral diffusion length of 400 nm gave the leakage current in the order of ~10^{-4} A from drain to the substrate and V_t =1.4 V that is much smaller than the shown V_t in the measurement result for V_d=400 mV in Fig. 5.26.

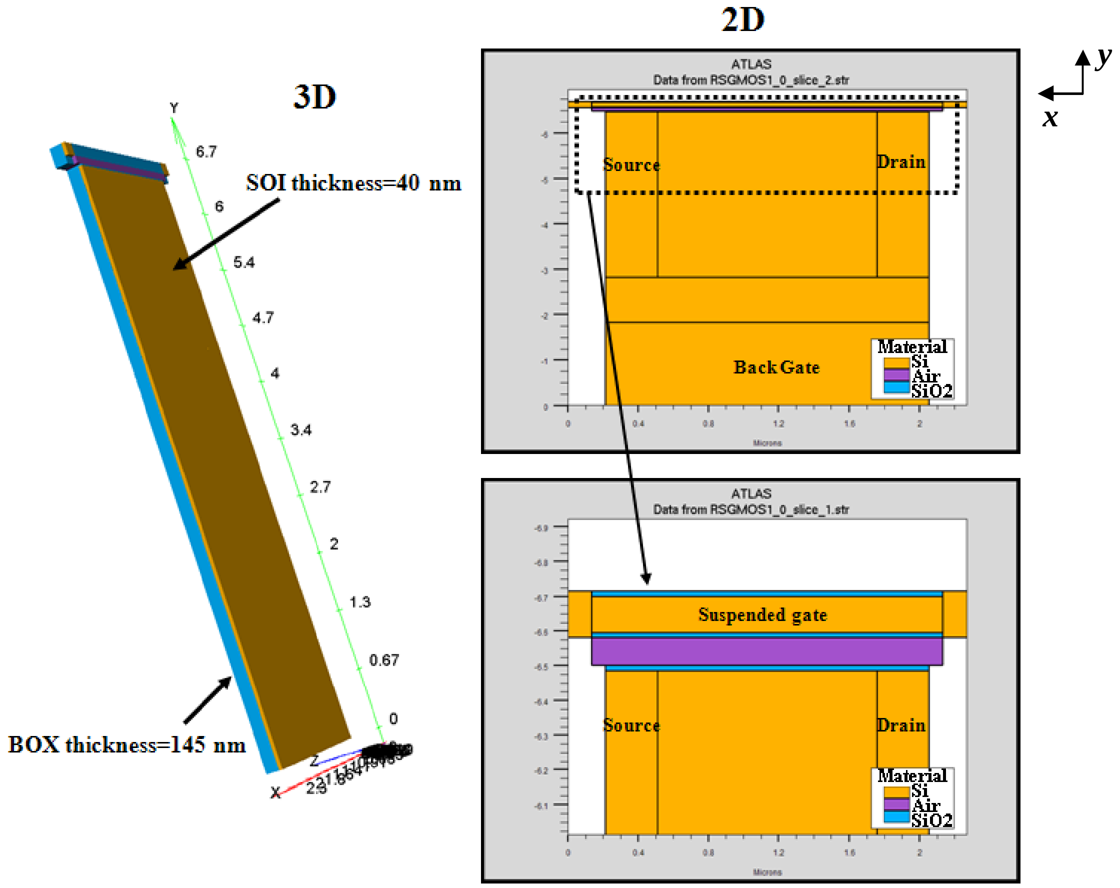

(a) (b)

Fig. 5.37 The simulated IP R-NEM sensor with the suspended gate in ATLAS 3D: (a) The 3D and (b) top 2D view of the device

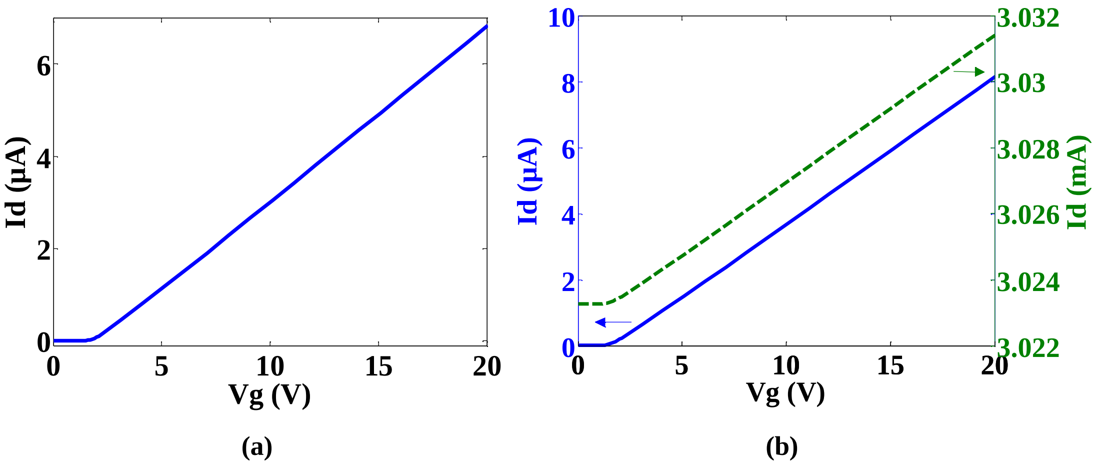

Fig. 5.38 The I_d-V_g characteristic of the N$^+$/P/N$^+$-type in-plane MOSFET in ATLAS 3D with w=135 nm, g=80 nm, l=2000 nm, l_C=1250 nm at V_d=400 mV considering: (a) Uniform doping for source, drain and back gate and (b) Gaussian doping for source, drain and back gate with lateral diffusion of 50 nm and vertical diffusion length of 100 nm (solid line) and 400 nm (dotted line)

The lateral diffusion length is increased from 50 nm in Fig. 5.38 (b) to 150 nm in Fig. 5.39. In Fig. 5.39 (solid line), V_t is decreased to zero volts and OFF-current is increased compared to V_t in Fig. 5.38 (b). Only the introduction of a negative charge (Q_n=-1×10^{12} cm^{-3}) in the interface of 15 nm-oxide layer above the channel and channel surface causes the increase of V_t from zero for solid line to V_t≈11 V for dotted line in Fig. 5.39 that is consistent with the measurement result in Fig. 5.26. The introduced interface charge can be considered as a representative for the surface roughness in the channel-edge and also the possible trapped charges due to the implantation in SiO_2. The dependency of V_t to trapped charges causes the instability of DC characteristics of MOSFETs by passing time in Fig. 5.33. If the same value of 400 nm for the vertical diffusion length is assumed for the lateral diffusion length, larger Q_n than -1×10^{12} cm^{-3} should be considered in the surface to have the same V_t in Fig. 5.26. Based on the dependency of V_t to Q_n, the reduction of V_t by reducing V_d in Fig. 5.26 is explained. Smaller V_d in Fig. 5.26 attracts smaller Q_n in the surface of channel that results in smaller increase of V_t due to Q_n with respect to Fig. 5.39. By reducing the length of channel the amount of Q_n reduces and the impact of V_d on V_t is higher that causes the reduction of V_t as shown in Fig. 5.27.

I_d-V_g characteristics of P$^+$/P/P$^+$-type MOSFET (Fig. 5.34 (a)) at V_d=-200 mV is shown in Fig. 5.40 for the lateral and vertical diffusion length of 150 nm and 400 nm, respectively. Transverse mobility model, Shockley-Read-Hall recombination and Fermi-Dirac distribution are considered for the carries in the simulation [142],[159]. The solid line I_d-V_g characteristic in Fig. 5.40 shows V_t≈18 V that is larger than that of the measurement results in Fig. 5.35. The introduction of a positive charge (Q_p=8×10^9 cm^{-3}) in the interface of 15 nm-oxide layer and channel surface causes the reduction of V_t to ≈8 V for the dotted line I_d-V_g characteristic in Fig. 5.40 that is close to the measured V_t value in Fig. 5.35. Figure 5.40 shows the OFF-current in the order of mA and a small ON/OFF current ratio same as Fig. 5.35. Same as $N^+/P/N^+$-type, if 400 nm is considered for both vertical and lateral diffusion lengths, a larger Q_p than 8×10^9 cm^{-3} should be considered in the surface to have the same V_t in Fig. 5.35 and the instability of DC characteristics of $P^+/P/P^+$-type MOSFETs is also explained by the dependency of their V_t to trapped charges in oxide. Same as the explanation for the $N^+/P/N^+$-type MOSFET in Fig. 5.26, the dependency of V_t to Q_p is used to explain the reason of the increase of V_t by reducing $|V_d|$ in Fig. 5.35. Smaller $|V_d|$ in Fig. 5.35 attracts smaller Q_p in the surface of the channel that results in smaller decrease in V_t with respect to Fig. 5.40.

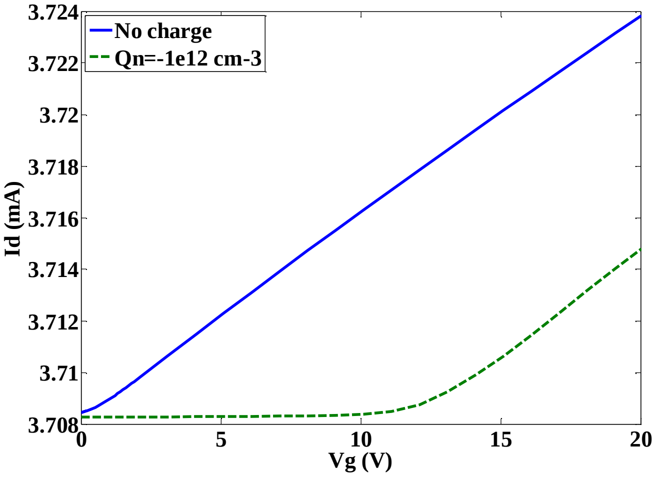

Fig. 5.39 **I_d-V_g characteristics of $N^+/P/N^+$-type MOSFET in ATLAS 3D with w=135 nm, g=80 nm, l=2000, l_C=1250 nm and lateral diffusion length of 150 nm and vertical diffusion length of 400 nm at V_d=400 mV with and without Q_n in the surface of channel**

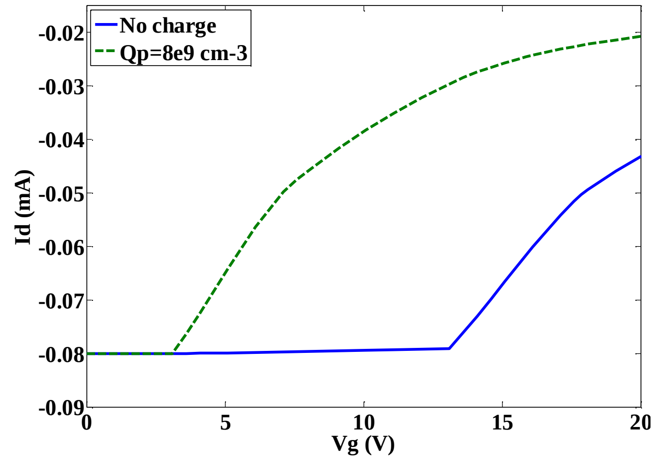

Fig. 5.40 **I_d-V_g characteristics of $P^+/P/P^+$-type MOSFET in ATLAS 3D with w=135 nm, g=80 nm, l=2000, l_C=1250 nm and lateral diffusion length of 150 nm and vertical diffusion length of 400 nm at V_d=-200 mV with and without Q_p in the surface of channel**

5.4 Summary

In this chapter, first characterization of NWs were conducted before and after their suspension to investigate the effect of using liquid and vapor HF etching on the characteristics of NWs. RF characterization for the suspended NWs were done in five steps in order to reduce the effect of parasitic frequencies that were enforced to their measured transmission signal by using SMA connectors, chip carrier and circuit board. It was found that a proper RF measurement pad is necessary for the S-parameter characterization of devices that was considered for NEM structures. Then DC characterization for suspended beams of NEM structures were done following by their RF characterization. The transmission signal for a measured NEM structure was compared to the experimental result for the RSG-MOSFET with the capacitive detection setup. Higher value for the motional resistance of the NEM structure in the atmosphere as the working environment in comparison with the RSG-MOSFET caused the difficulty of finding the resonance peak in its transmission signal. If the quality factor of the NEM structure is dominated by air damping, by conducting the RF measurement in high vacuum the motional resistance reduces a few order of magnitudes and the total quality factor increases that results in ease of distinguishing the mechanical resonance peak from parasitic frequencies. The introduction of an in-plane MOSFET to the suspended beam in IP R-NEM sensor improves the transmission signal by its transconductance. For this reason the IP R-NEM sensor was characterized to optimize the DC bias voltages that could provide the highest transconductance for the sensor that will be used for the subsequent RF measurement. The measured sensors with $P^+/P/P^+$-type MOSFET showed a transconductance higher than the RSG-MOSFET even with high OFF-current and small ON/OFF current but for $N^+/P/N^+$-type MOSFETs the transconductance was in the same order of the transconductance for the RSG-MOSFET and further processing on them such as FIB milling is necessary to improve the DC characteristic of MOSFETs. Further physical-level simulations were done for the investigation of characterized sensors in DC-level.

CHAPTER 6

Summary and future plan

6.1 Summary

In the previous chapters, the most recent NEM-IC devices with different applications such as switch, memory and sensor were presented. The sensing application of NEMS-IC devices especially biosensing was the centre of focus for the developed devices in this thesis. Performance factors of biosensors that include limit of detection (LOD) were discussed after studying their classification. The developed devices particularly targeted DNA molecules by using the mass-detection technique. In this technique the mass of target molecules affects the total mass of the resonator and consequently changes its primary resonance frequency to a new value. For this reason a preliminary method was described to convert the unit of LOD of the mass-detection DNA sensors from mol/L to g/cm^2.

The quartz-crystal microbalance (QCM) biosensor was studied as a commercial example for the mass-detection based biosensors. Mass detection limit, quality factor and mass responsivity of a few QCM biosensors were presented and compared to the equivalent values for the newly developed devices. The previously proposed resonant suspended gate filed-effect-transistor (RSG-FET) was studied and found to have similar operation to the developed sensor in this thesis. RSG-FET consists of a metal-oxide-semiconductor FET (MOSFET) that is integrated with a suspended gate that moves out-of-plane. The network and impedance analyzer as well as lock-in amplifier were discussed as the available measurement instruments for the characterization of high frequency devices like RSG-FET and resonant body FinFET (RB-FinFET).

The newly-proposed in-plane resonant NEM (IP R-NEM) sensor consists of an in-plane MOSFET that is integrated with a suspended clamped-clamped (CC) beam. The resonating CC beam plays the role of a gate for the MOSFET and the sensing block for the sensor. The basic part of the sensor, the NEM structure, that includes a CC beam and two side electrodes was simulated with three-dimensional finite-element-method (3D FEM) to investigate the key parameters of the resonator and then compared to the analytically calculated values. The quality factor of a resonator is an important parameter for the subsequent radio-frequency (RF) characterization. For this reason, different sources of damping in a resonator including air, anchor and thermoelastic damping were studied using both numerical and analytical techniques. The usage of a free-free (FF) beam for the NEM structure was presented as an alternative structure that improved the quality factor by a few orders of magnitude.

The small capacitance of the CC beam in the NEM structure provided a small output signal for the device that needs to be amplified using the integrated MOSFET in the IP R-NEM sensor which was simulated in hybrid NEM-MOS circuit-level. The effect of changing the gap and applied DC voltage on the quality factor, resonance frequency and magnitude of the output signal of the sensor were investigated. In order to make the beam sensitive to target molecules, its surface was functionalized. Functionalization and detection processes of the sensor for both gas- and liquid-phase detection were modelled to calculate the mass responsivity of the sensor that is a determinant factor for mass-detection based sensors. The IP R-NEM sensor showed a unique mass responsivity in the order of zepto g/Hz among the commercialized QCM and other state-of-the-art biosensors. The scaling rule of k^4 was calculated for the mass responsivity of the resonator.

Three types of devices were fabricated in this thesis. First the non-suspended nano-wire (NW) devices that consist of a NW with two side electrodes were suspended using liquid and vapor HF etching. Vapor HF provided non-contaminated suspended NWs along with the reduced possibility of bending or stiction for the longer NWs. Then the mask layout design and the optimized fabrication process of CC and FF NEM structures were discussed. The fabrication process consists of one step of electron beam (EB) lithography followed by two steps of photolithography for final suspension of beams using vapor HF or three steps of photolithography in the case of using liquid HF for the suspension of beams. Finally, the mask layout based on the fabrication process technology at the Commissariat à l'Energie

Atomique-Laboratoire d'Electronique et de Technologie de l'Information (CEA-LETI) was designed for the IP R-NEM sensor and the fabrication process was explained.

The characterization of NWs were conducted before and after their suspension to investigate the effect of using liquid and vapor HF etching on the characteristics of NWs. Using vapor HF gave less current for NWs at zero voltage without the necessity of doing further annealing for the reduction of current. As the contact pads for NWs were not designed for high frequency measurement, a measurement setup consisting of a circuit board, a chip carrier and sub-miniature version A (SMA) connectors were used for the RF characterization of suspended NWs using network analyzer. The measurement was conducted in five steps to reduce the effect of parasitic frequencies caused by SMA connectors, chip carrier and circuit board. It was difficult to recognize the resonance frequency peak in the transmission, S_{21}, signal due to the presence of parasitic peaks even after doing a calibration before starting the measurement.

A proper RF measurement pad was necessary for the S-parameter characterization of devices that was considered for the NEM structures. The DC characterization for suspended beams of NEM structures were done following by their RF characterization in the atmosphere and room temperature using network analyzer. The S_{21} signal for the measured NEM structure was compared to the experimental result for the RSG-MOSFET with the capacitive detection setup because of the difficulty of finding the resonance peak for the NEM structure. This comparison showed the higher value of the motional resistance for the NEM structure that caused a smaller magnitude than the 2 dB-magnitude transmission signal of the RSG-MOSFET and consequently the difficulty of distinguishing this small peak from the background noise signal. Based on the analytical calculations, the RF characterization in high vacuum reduced the motional resistance and increased the quality factor that makes the recognition of the resonance peak much easier. To further reduce the motional resistance, a higher DC voltage than 40 V should be applied to the beam that may cause the pull-in or breaking of it. The impedance analyzer can be used as an alternative measurement method for the RF characterization of the devices with high input impedance.

The integrated MOSFET in the IP R-NEM sensor amplifies the transmission signal by its intrinsic gain. The IP R-NEM sensor was characterized to optimize the DC bias voltages that could provide the highest transconductance for the sensor that can be used for the subsequent RF measurement. Measured sensors with $P^+/P/P^+$-type MOSFETs showed a transconductance higher than the RSG-MOSFET even with high OFF-current and small ON/OFF current ratio. The large gain for the $P^+/P/P^+$-type MOSFETs and the RF characterization at high vacuum improves the output signal from the resonator. For sensors with $N^+/P/N^+$-type MOSFETs, the amplification of transmission signal by the transconductance was in the same order of the RSG-FET and further processing will be needed for the improvement of their DC characteristics that are explained in the future plan. Some physical-level simulations were done for the investigation of characterized sensors in DC-level. The dependency of DC characteristics of MOSFETs to trapped charges in the oxide above the channel was the reason for time-dependency of their characteristics that should be kept in mind during the time optimum biasing voltages is applied to the sensor. Moreover, the origin of high OFF-current for the fabricated sensors is due to a large lateral diffusion of dopants in drain and source.

6.2 Future plan

My research project is a part of European FP7 NEMSIC project that will be finished in April 2012. I will continue my involvement in the project until April and then follow a future plan during the period of submission of my thesis in February and finishing of the project in April:

- As explained in chapter 4, in order to have an ohmic contact between Aluminium and silicon in contact holes of NEM structures, a silicon-on-insulator (SOI) wafer with higher doping than the previously used doping of 2×10^{19} cm^{-3} should be used. For this reason the phosphorus ion was implanted in the oxidized SOI wafer at the University of Surrey with the energy of 90 keV and doping of 5×10^{15} cm^{-3} that provided a doping of 6×10^{19} cm^{-3}. With respect to Table 4.5, fabrication steps were done up to the deposition of SiO_2 layer and the rest of fabrication steps will be completed in the mentioned period. The forming gas annealing after the suspension of beams in the last step of fabrication will be done at temperatures less than 350 ^{o}C and different times to find the optimum recipe with the best conductivity between Aluminium and silicon.
- The in-plane MOSFET for the IP R-NEM sensor showed high OFF-current due to the lateral diffusion of dopants in drain and source. In order to isolate the drain and source, a trench was milled with focused ion beam (FIB) from the end of back gate till near the edge of the channel. The depth and the distance of the trench to the edge of channel would be optimized for further isolation than Fig. 5.30 (b). If the distance can be reduced to less than 160 nm in Fig. 5.30 (b) the possibility of

depletion of the narrow channel by the gate will increase. Some simulations will be conducted using ATLAS 3D to find the optimum distance. Moreover, further annealing will be done to passivate the trapped charges in the thermal oxide layer.

- The RF characterization for the NEM structures and IP R-NEM sensors should be done in high vacuum in order to minimize the motional resistance of the resonator. The available Lakeshore probe station with DC probes at the Southampton Nanofabrication Centre (SNC) will be used for the measurement in vacuum. The existence DC probes can measure the devices with frequencies up to 1 GHz using the newly installed non-magnetic semi-rigid microwave coaxial cables. The only issue for this setup will be the calibration that will be done at the end of RF cables using Agilent Ecal as explained in chapter 5. Some calibration features will be prepared for more accurate calibration to bring the measurement reference plane from the end of RF cables to the tips of the probes.
- The RF characterization for NEM structures and IP R-NEM sensors using lock-in amplifier will be done after preparing the new measurement setup at the University of Southampton (UoS) and also using the currently available setup at the École Polytechnique Fédérale de Lausanne (EPFL).
- After completing the RF measurement of devices and finding the resonance frequency, devices will be sent to the Interuniversitair Micro-Electronica Centrum-Belgium (IMEC-BE) for the functionalization of the beams. For example, the silane couplers such as APTES (Amino-propyltrimethoxysilane) can be used to convert the silanol groups of the native oxide on the beam to the active amino groups. The other method is to make the H-terminated silicon surface active for sensing by using alkenes or alkyne-based molecules. The RF characterization after the functionalization process will be done to calculate the shift of frequency due to the added linker molecules to the beam.
- The functionalized NEM structures and IP R-NEM sensors are suitable for biological detection and introducing the target molecules in liquid to devices and their characterization afterwards will be investigated in my future plan.
- As a main focus of my future plan, I intend to prepare a manuscript to submit to a peer reviewed journal paper that is based on the fabrication and characterization of the NEM structures and IP R-NEM sensors.

CHAPTER 6 Summary and future plan

For my future plan after the PhD, I have submitted a proposal for the short-term post-doctoral fellowship to the Japan Society for the Promotion of Science (JSPS) in collaboration with Prof. Hiroshi Mizuta who will host me at the Japan Advanced Institute of Science and Technology (JAIST). The following plan will be considered after finishing of NEMSIC project in April:

- The host researcher, Prof. Hiroshi Mizuta, is currently building a unique NEM sensor measurement system for gas detection which is an ideal characterization platform for my resonant sensor devices. By using this system, the target molecules such as CO_2 will be introduced to the functionalized NEM structures and IP R-NEM sensors that are suitable for gas detection and the devices will be characterized after this step.
- With respect to the high sensitivity of IP-RNEM sensor to very small changes in mass, the observation of the sparse distribution of target molecules on the surface of the suspended gate of sensor will help me in the atomistic characterization of the sensor. For this reason the availability of the world-best atomic resolution scanning transmission electron microscope (STEM) at JAIST provides me with the best opportunity to investigate the characterization of IP-RNEM sensor before and after the adsorption of CO_2 molecules to the suspended beam.
- Different NEM structures and IP R-NEM sensors with different dimensions of gap, beam size and MOSFET channel length were already considered in the fabricated sensors so studying the effect of dimensions of the resonator on the mass sensitivity after doing functionalization and detection processes will be done as part of my future plan.
- Investigating the noise analysis in low temperature and low vacuum environments besides the operation in the atmosphere and room temperature is also considered in my plan.
- Introducing new designs for the sensor such as those using a free-free suspended beam for the sensor as shown in Fig. 3.10 (a) and studying its operation and characteristics as a possible candidate for the proposed clamped-clamped IP-R-NEM sensor is considered in my future plan. Moreover, I want to investigate the resonance frequency and mass sensitivity of silicon nitride, silicon carbide (SiC)

and graphene-based IP-RNEM sensors that have higher Young's modulus and consequently stiffer beam that leads to higher resonance frequencies.

- My future plan also includes, additional manuscripts submission to journal papers and research proposals based on the new experimental results of the NEM structures and IP R-NEM sensors that I have developed during the fellowship.

Appendices

A.1 CoventorWare

Modelling and simulation of micro/nano-electro-mechanical systems (MEMS/NEMS) is of vital importance to develop innovative products and to reduce time-to-market at a lower total cost. Advanced design methodologies and a variety of software tools are utilized in order to analyze complex geometrical structures, to account for interactions among different physical domains and to capture the cooperative play of micro/nano-devices and connected electronic circuitry or signal processing units. Coventoreware [125] is one of these softwares that have the capability of modelling MEMS/NEMS.

CoventorWare was used for simulating the devices in this project. This suite consists of four parts which are Designer, Analyzer, Integrator and Architect. The design flow of this software is shown in Fig. A.1.

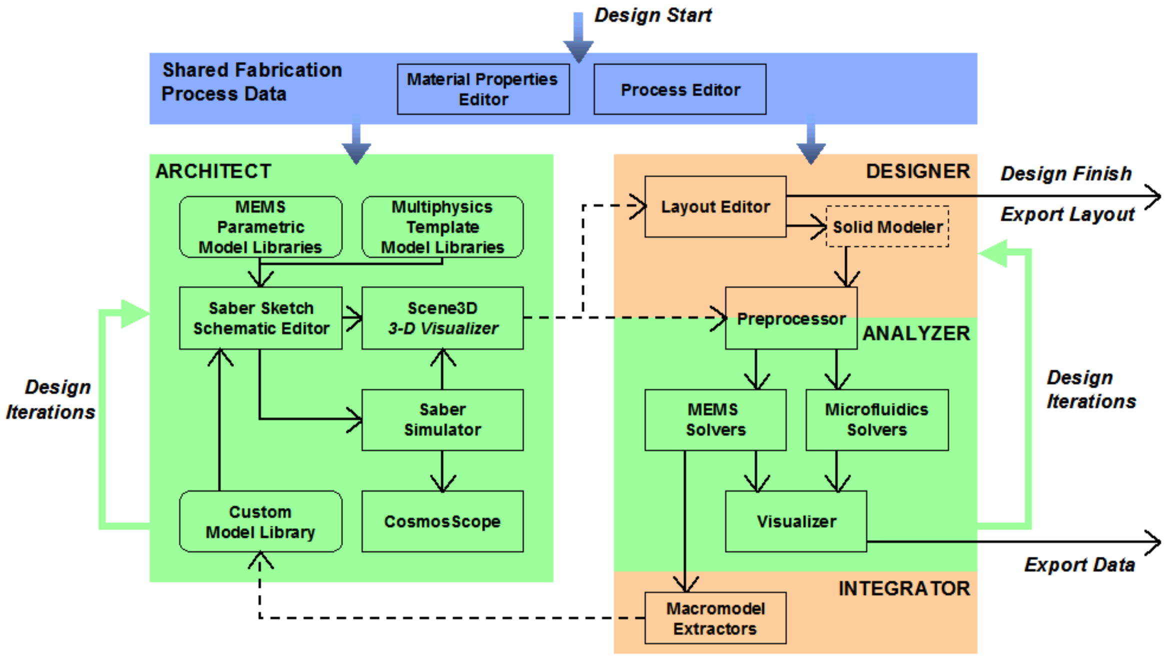

Fig. A.1 The system flow of CoventoreWare [125]

Designer includes process editor, layout editor and solid modeller. After defining the fabrication process and physical structure of the device in Designer, three types of analysis can be done in the Analyzer section.

- Electro-static analysis can be used to calculate capacitance and charge by applying voltage and is called the MemElectro analysis.
- Mechanical analysis is used to study the stress distribution, modal and harmonic analysis and is called the MemMech analysis.
- Coupled electro-mechanics analysis is used to simulate pull-in and pull-out and is named as the CoSolve analysis.

Integrator part is used to provide special features for Architect that analyzes a device at the circuit-level.

A.2 SOI technology-based dimensions for the NEM structure

The dimensions of the structure in Fig. 3.1 (a) are modified for the layout design in order to achieve the targets and limitations of the fabrication process. New dimensions are shown in Figs. A.2 (a) and A.2 (b). The frequency of first 6 modes (out-of-plane and in-plane modes) of NEM structures in Figs. A.2 (a) and A.2 (b) are shown in Figs. A.3 (a) and A.3 (b), respectively. The first in-plane mode in Fig. A.3 (a) is far enough from the out-of-plane mode that will reduce the possibility of mixing in-plane and out-of-plane movements. In Fig. A.3 (b), the second out-of-plane mode is so near to the first in-plane mode and it causes the occurrence of a mixed mode of in-plane and out-of-plane movement that interrupts the wanted behaviour of the device. Based on the effect of dimension on the resonance behaviour of the beam, different dimensions were used for the designed mask layout for the NEM structure

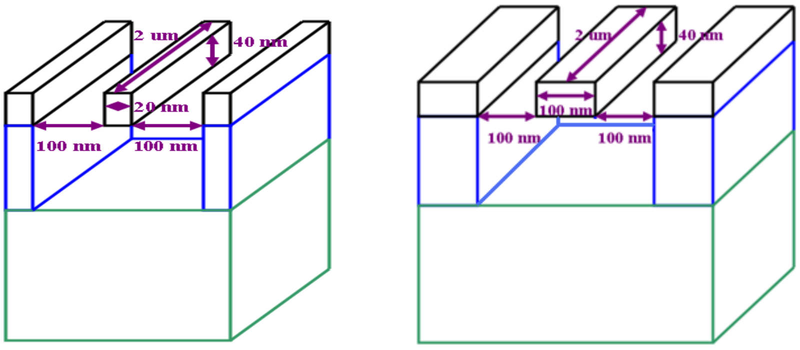

(a) **(b)**

Fig. A.2 Considered dimensions for the NEM structure: (a) The 20 nm-width and (b) 100 nm-width beam

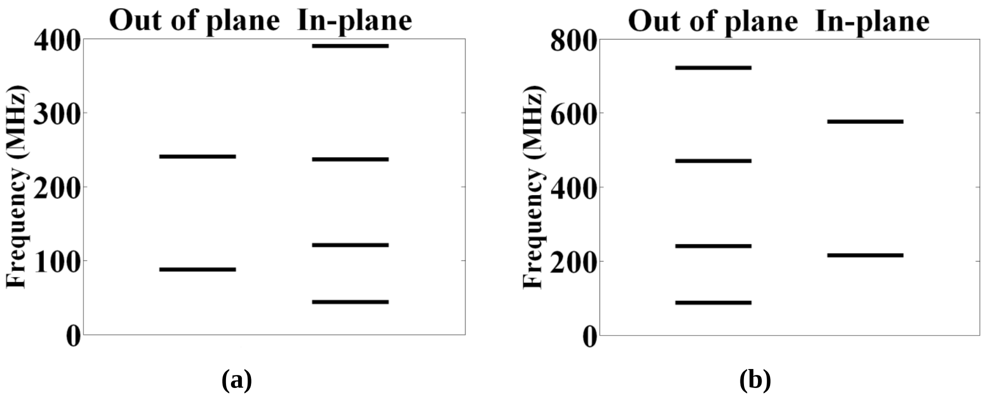

Fig. A.3 The first 6 modes of the mechanical resonance for the NEM structure with: (a) The 20 nm-width and (b) 100 nm-width beam

The comparison of the displacement versus voltage characteristics of the structures in Figs. A.2 (a) and A.2 (b) are shown in Fig. A.4. Using eq. (3-4), k_{bm} is larger for wider beam and it causes larger pull-in voltage due to eq. (3-8). Figure A.4 shows that larger voltage should be applied to the wide beam for having the same value of displacement of the narrow beam.

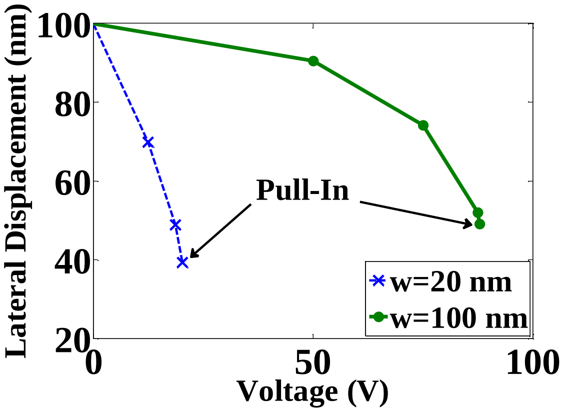

Fig. A.4 The displacement versus voltage for different widths for the suspended beam of the NEM structure

A.3 The vibrating body field-effect-transistor

The vibrating body field-effect-transistor (VB-FET) was presented by D. Grogg et. al [160] as an integrated FET device in the body of a vibrating MEM structure that takes advantage of applying piezo-resistivity to the structure. In contrast with the resonance gate transistor [46] where the channel charge of a MOSFET is modulated by the vibrating gate, the proposed VB-FET utilizes accumulation/inversion channel charge and piezo-resistivity modulation in the body of an active FET integrated on a resonant MEM structure. VB-FETs can offer signal improvement compared with traditional capacitive detection [160]. The VB-FET was introduced as an alternative for the mass-detection based resonant sensor in the NEMSIC project (Fig. A.5).

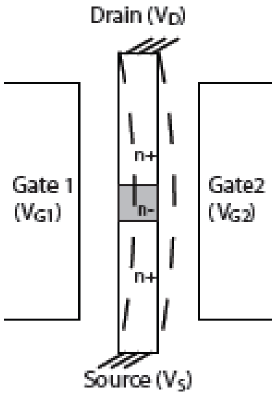

Fig. A.5 Top schematic view of the VB-FET [160]

Monocrystalline silicon has a high piezo-resistivity combined with excellent mechanical properties which makes it particularly suited for the conversion of mechanical deformation into an electrical signal [152]. Due to this fact, the VB-FET has both contributions of charge modulation and piezo-resistivity. For studying the effect of adding piezo-resistivity to the mechanical beam similar to the behaviour of the VB-FET, the piezo-resistive concept was added to the suspended beam with low doping of N_A=2×10^{15} cm^{-3}. The suspended beam acts as the low doping channel for the VB-FET. Constant voltages are applied to ends of the beam that play the role of source and drain of the VB-FET. The used structure in Designer for modelling the piezo-resistive NEM (piezo-NEM) structure is shown in Fig. A.6. Changing of the voltage for the side electrode, V_G, causes changes in the bending of the beam as a result of electro-static behaviour and changes in the bending of the beam means changes in the stress of the beam which varies the electrical resistance of the beam due to the piezo-resistivity.

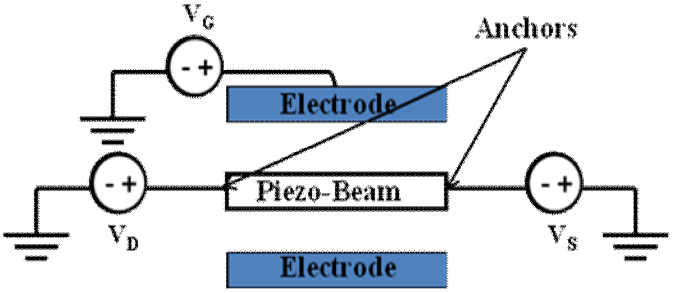

Fig. A.6 The simulated piezo-NEM structure in Designer

A.3.1 Piezo-resistivity

Piezo-resistivity is a material property where the bulk resistivity is influenced by the mechanical stresses applied to the material [152],[161]. A key component of piezo-resistance models is the gauge factor. The gauge factor, *G*, can be defined as the fractional change in resistance, $\Delta R/R$, per unit strain, ε, as follows [161]:

$$G = \frac{\Delta R}{R\varepsilon} \tag{A-1}$$

where *G* is unit less. The implicit differentiation of eq. (5-1) results in [161]:

$$\frac{\Delta R}{R} = \frac{\Delta\rho'}{\rho'} + \frac{\Delta l}{l} - \frac{\Delta A'}{A'} \tag{A-2}$$

The fractional change in area, $\Delta A'/A'$, is expressed in terms of the transverse strain by [161]:

$$\frac{\Delta A}{A} = \frac{\Delta w}{w} + \frac{\Delta h}{h} = -\varepsilon_t - \varepsilon_z \tag{A-3}$$

where $\varepsilon_t = \varepsilon_z$. Including longitudinal strain, $\varepsilon_l = \Delta l/l$, and Poisson's ratio, $\vartheta = -\varepsilon_t/\varepsilon_l$, eq. (A-2) is shown as [161]:

$$\frac{\Delta R}{R} = \frac{\Delta\rho'}{\rho'} + (1+2\vartheta)\varepsilon_l \tag{A-4}$$

Dividing both sides of eq. (A-4) by ε, *G* is [161]:

$$G = \frac{\Delta R}{R\varepsilon} = \frac{\Delta\rho'}{\rho'}\frac{1}{\varepsilon} + 1 + 2\vartheta \tag{A-5}$$

The fractional change in the resistivity, $\Delta\rho'/\rho'$, is the principle source of the piezo-resistance behaviour in semiconductors [162]. For a three-dimensional anisotropic crystal, the electric field vector, *E*, is related to the current vector, *I*, by a 3×3 resistivity tensor [152]:

$$\begin{bmatrix} E_1 \\ E_2 \\ E_3 \end{bmatrix} = \begin{bmatrix} \rho'_1 & \rho'_6 & \rho'_5 \\ \rho'_6 & \rho'_2 & \rho'_4 \\ \rho'_5 & \rho'_4 & \rho'_3 \end{bmatrix} . \begin{bmatrix} i_1 \\ i_2 \\ i_3 \end{bmatrix} \tag{A-6}$$

For the unstressed silicon $\rho'_1 = \rho'_2 = \rho'_3 = \rho'$ and $\rho'_4 = \rho'_5 = \rho'_6 = 0$. These six resistivity components are decomposed into six components: three normal stresses σ_1, σ_2 and σ_3 and three shear stresses τ_1, τ_2 and τ_3. The resistivities are referenced to the isotropic unstressed case and written as [152]:

$$\begin{bmatrix} \rho'_1 \\ \rho'_2 \\ \rho'_3 \\ \rho'_4 \\ \rho'_5 \\ \rho'_6 \end{bmatrix} = \begin{bmatrix} \rho' \\ \rho' \\ \rho' \\ 0 \\ 0 \\ 0 \end{bmatrix} + \begin{bmatrix} \Delta\rho'_1 \\ \Delta\rho'_2 \\ \Delta\rho'_3 \\ \Delta\rho'_4 \\ \Delta\rho'_5 \\ \Delta\rho'_6 \end{bmatrix} \tag{A-7}$$

The piezo-resistance effect can now be described by relating six fractional resistivity changes, $\Delta\rho'_i / \rho'$, to each of the six stress components. The elements of this matrix are called piezo-resistance coefficients, π_{ij}, expressed in Pa^{-1} [152].

$$\frac{1}{\rho'} \begin{bmatrix} \Delta\rho'_1 \\ \Delta\rho'_2 \\ \Delta\rho'_3 \\ \Delta\rho'_4 \\ \Delta\rho'_5 \\ \Delta\rho'_6 \end{bmatrix} = \begin{bmatrix} \pi_{11} & \pi_{12} & \pi_{12} & 0 & 0 & 0 \\ \pi_{12} & \pi_{11} & \pi_{12} & 0 & 0 & 0 \\ \pi_{12} & \pi_{12} & \pi_{11} & 0 & 0 & 0 \\ 0 & 0 & 0 & \pi_{44} & 0 & 0 \\ 0 & 0 & 0 & 0 & \pi_{44} & 0 \\ 0 & 0 & 0 & 0 & 0 & \pi_{44} \end{bmatrix} . \begin{bmatrix} \sigma_1 \\ \sigma_2 \\ \sigma_3 \\ \tau_1 \\ \tau_2 \\ \tau_3 \end{bmatrix} \tag{A-8}$$

The largest piezo-resistance coefficients for silicon are π_{11} in N-type silicon and π_{44} in P-type silicon. As the sign of these coefficients are opposite for N- and P-type silicon, their piezo-resistance behaviour will be in opposite in tension and compression. It has been shown that the resistance of N-type silicon subjected to tensile stress decreases linearly and an applied compressive stress causes a linear increase in resistance [162]. The opposite trend is true in both cases for P-type silicon, with the resistance increasing in tension and decreasing in compression [162].

A.3.2 Impacts of surface modification on the piezo-NEM structure

For the structure shown in Fig. A.6, a long beam with the length of 1.5 μm is used to have a conformal stress distribution throughout the length of the beam. Other dimensions of beam are the same as Fig. 3.1 (a). Constant voltages of -50,50 V are applied to ends of the suspended beam and a voltage range of 0-20 V is applied to the side electrode. The default piezo-resistance coefficients for the low doping silicon are [152]:

(for N-type silicon) π_{11}=-102.2×10^{-5} MPa^{-1}, π_{12}=53.4×10^{-5} MPa^{-1}, π_{44}=-13.6×10^{-5} MPa^{-1}

(for P-type silicon) π_{11}=6.6×10^{-5} MPa^{-1}, π_{12}=-1.1×10^{-5} MPa^{-1}, π_{44}=138.1×10^{-5} MPa^{-1}

The current through the beam versus the side electrode applied voltage is shown in Figs. A.7 (a) and A.7 (b) for N- and P-type silicon beams respectively for different thicknesses of the coating layer in the TB configuration. As shown in Fig. A.7 (a), by increasing the voltage, higher tensile stress applies to the N-type beam and results in smaller resistivity and larger current as expected from previous section for the N-type beam. Figure A.7 (b) shows the opposite trend for larger voltages for the P-type beam with respect to previous section. Adding the coating layer to the beam causes higher compressive stress for the beam that results in a large change in the current at a specific voltage compared to the current of the un-coated beam at the same voltage. Increasing the thickness of the coating layer means higher compressive stress that shows higher resistance and smaller current for the N-type beam and the opposite behaviour for the P-type beam as shown in Figs. A.7 (a) and A.7 (b), respectively. The results show the opposite behaviour for N-type and P-type beams because of their opposite signs for piezo-resistance coefficients. As the N-type beam has smaller gauge factor, changes in current due to changes in stress for Fig. A.7 (a) is smaller compared to the P-type beam in Fig. A.7 (b).

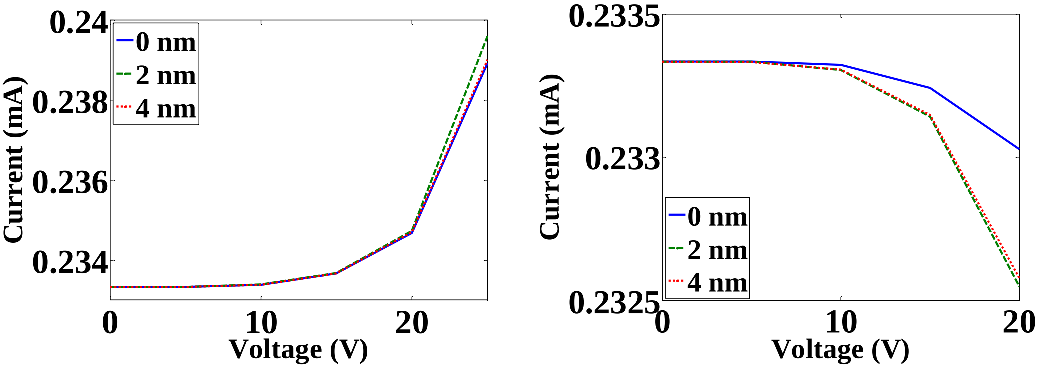

(a) **(b)**

Fig. A.7 The current versus side electrode voltage for different coating layer thicknesses in the TB configuration for: (a) The N-type and (b) P-type beam

A.3.3 Comparison of the IP R-NEM sensor and piezo-NEM structure

The N_A doping of 2×10^{15} cm^{-3} is used for the suspended beam of piezo-NEM structure in Fig. A.6. The same model of Fig. 3.13 (b) is used for the IP R-NEM sensor considering the length of 1.5 μm and N_A doping of 10^{19} cm^{-3} for the suspended beam. The channel of the MOSFET has the P-type doping of 1.7×10^{17} cm^{-3} .The same range of DC voltage is applied to the side electrode for the IP R-NEM sensor and piezo-NEM structure. Then, the induced DC current in the suspended beam for the piezo-NEM structure and the effective current of MOSFET for the IP R-NEM sensor versus the applied DC voltage are compared in Fig. A.8. As shown in Fig. A.8, by applying piezo-resistivity to the NEM structure the current will be a few orders of magnitude larger than the current of the IP R-NEM sensor due to the effect of the piezo-resistance modulation of carriers.

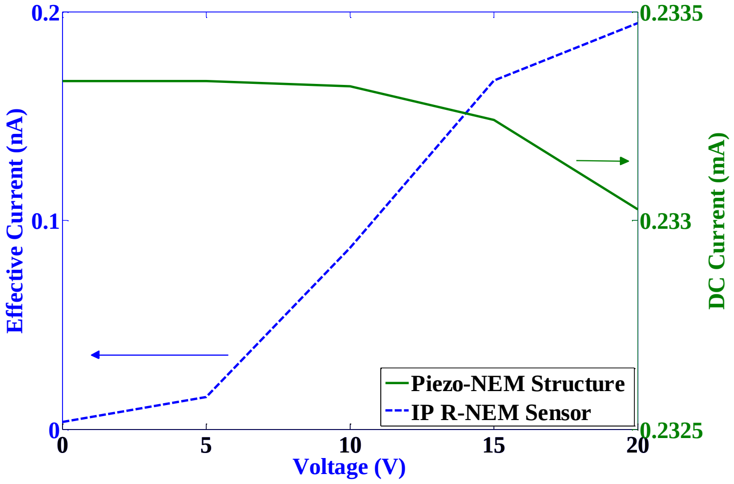

Fig. A.8 The current versus side electrode voltage for the IP R-NEM sensor and the piezo-NEM structure

A.4 ATHENA

ATHENA was used to simulate the doping profile in the SOI layer of the NEM structure after the phosphorus implantation step with the energy of 90 keV and doping of 1×10^{15} cm^{-3} and drive-in step for 30 minutes in nitrogen (N_2) gas at 1000 ^{o}C.

```
go athena

# X CHARACTERISTICS
line x loc=0.00 spac=0.005
line x loc=0.25 spac=0.005
line x loc=0.5 spac=0.005

#Y CHARACTERISTICS
line y loc=0.00 spac=0.0001
line y loc=0.01 spac=0.0001
line y loc=0.02 spac=0.0001
line y loc=0.03 spac=0.001
line y loc=0.04 spac=0.001
line y loc=0.054 spac=0.005

#METHOD
method high.conc full.cpl

# SUBSTRATE
init silicon c.phosphor=1.0e14 orientation=100 two.d
```

```
# DEPOSIT OXIDE
deposit oxide thick=0.096 divisions=96

# IMPLANTATION
implant phosphor dose=1e15 energy=90 monte tilt=5 rotation=0 crystal print.mom

# DRIVE-IN
diffus time=30 temp=1000 nitro

structure outfile=SOI03.str
tonyplot SOI03.str
quit
```

A.5 Cadence-Virtuoso layout editor

The layout of the IP R-NEM sensor was designed using Virtuoso tool in Cadence. The required steps for completing the layout design of the sensor are as follows and shown in Fig. A.9:

- Define a new cell view, select the library and choose the Tool as Virtuoso
- Set display options
- Draw the layout in Virtuoso Layout Editor window based on the defined layers in layer select window (LSW) from library and the design rules of the used technology
- Run the design rules check (DRC)

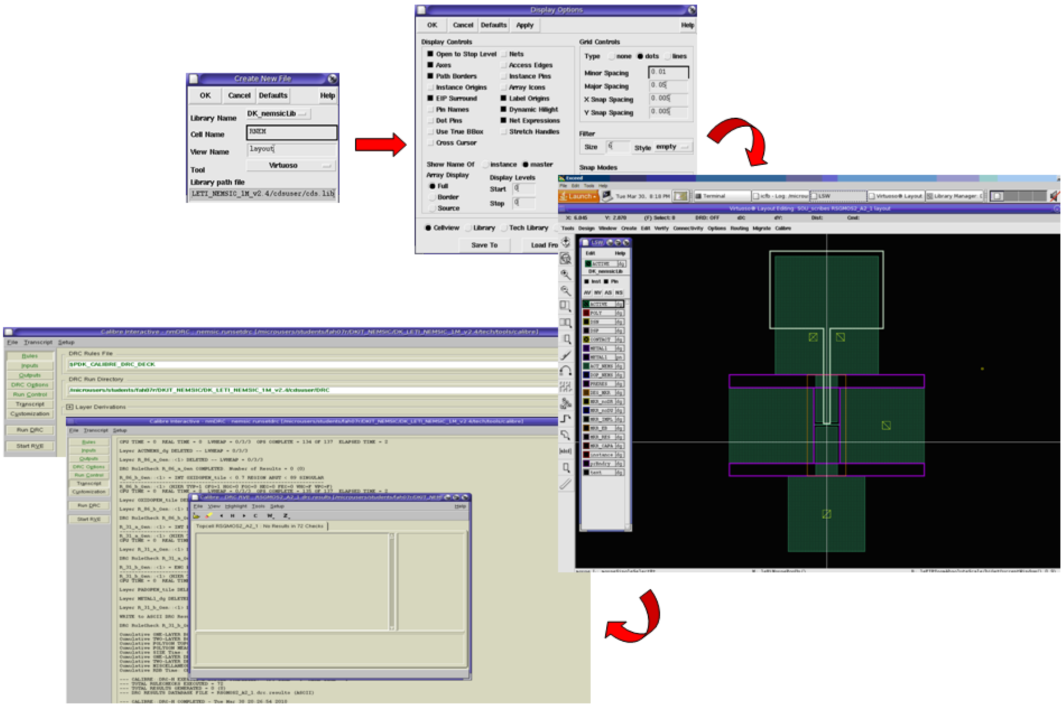

Library Name: DK_nemsicLib
Cell Name: RNEM
View Name: layout
Tool: Virtuoso
Library path file: LETI_NEMSIC_1M_v2.4/cdsuser/cds.lib

■ Open to Stop Level
■ Axes
■ Path Borders
☐ Instance Origins
■ EIP Surround
☐ Pin Names
☐ Dot Pins
☐ Use True BBox
☐ Cross Cursor
☐ Nets
☐ Access Edges
☐ Instance Pins
☐ Array Icons
■ Label Origins
■ Dynamic Hilight
■ Net Expressions
☐ Stretch Handles

Type ○ none ● dots ○ lines
Minor Spacing: 0.01
Major Spacing: 0.05
X Snap Spacing: 0.005
Y Snap Spacing: 0.005
Size: 6 Style: empty
Show Name Of ○ instance ● master
Array Display: ● Full ○ Border ○ Source
Display Levels: Start 0 Stop 0

Fig. A.9 Steps of the layout design using Cadence-Virtuoso

A.6 ATLAS three-dimensional (3D)-Deckbuild

The simulation for the IP R-NEM sensor in ATLAS 3D was defined using Deckbuild that is an interactive runtime and input file development environment within which all Silvaco's TCAD can run. The following script is used for defining the N$^+$/P/N$^+$-type MOSFET in 3D. The required changes for P$^+$/P/P$^+$-type MOSFET are given in the boxes.

```
go atlas
#
TITLE SOI device simulation IP R-NEM sensor
#
# SILVACO International 1992, 1993, 1994, 1995, 1996, 1997
#
# 0.04um of silicon on 0.145um oxide substrate
#
#**** define the mesh ******
#
mesh   three.d  space.mult=1.0
#
x.mesh loc=0         spac=0.01
x.mesh loc=0.135     spac=0.01
x.mesh loc=0.215     spac=0.01
x.mesh loc=0.51      spac=0.01
x.mesh loc=1.76      spac=0.01
x.mesh loc=2.055     spac=0.01
x.mesh loc=2.135     spac=0.01
x.mesh loc=2.27      spac=0.01
#
y.mesh loc=0         spac=0.1
y.mesh loc=1.835     spac=0.1
y.mesh loc=2.83      spac=0.1
y.mesh loc=6.485     spac=0.1
y.mesh loc=6.5       spac=0.1
y.mesh loc=6.58      spac=0.1
y.mesh loc=6.595     spac=0.1
y.mesh loc=6.7       spac=0.1
y.mesh loc=6.715     spac=0.1
#
z.mesh loc=0         spac=0.01
z.mesh loc=0.015     spac=0.01
z.mesh loc=0.025     spac=0.01
z.mesh loc=0.04      spac=0.01
z.mesh loc=0.185     spac=0.01
#
#************* define the regions ************************************************************
#
region   num=1   x.min=0.215   x.max=2.055  y.min=0      y.max=1.835  z.min=0      z.max=0.04  silicon
region   num=2   x.min=0.215   x.max=2.055  y.min=1.835  y.max=2.83   z.min=0      z.max=0.04  silicon
region   num=3   x.min=0.215   x.max=0.51   y.min=2.83   y.max=6.485  z.min=0      z.max=0.04  silicon
region   num=4   x.min=0.51    x.max=1.76   y.min=2.83   y.max=6.485  z.min=0      z.max=0.04  silicon
region   num=5   x.min=1.76    x.max=2.055  y.min=2.83   y.max=6.485  z.min=0      z.max=0.04  silicon
region   num=6   x.min=0.135   x.max=2.135  y.min=6.595  y.max=6.7    z.min=0.015  z.max=0.025 silicon
region   num=7   x.min=0       x.max=0.135  y.min=6.58   y.max=6.715  z.min=0      z.max=0.04  silicon
region   num=8   x.min=2.135   x.max=2.27   y.min=6.58   y.max=6.715  z.min=0      z.max=0.04  silicon
region   num=9   x.min=0.215   x.max=2.055  y.min=0      y.max=6.5    z.min=0.04   z.max=0.185 oxide
region   num=10  x.min=0       x.max=0.135  y.min=6.58   y.max=6.715  z.min=0.04   z.max=0.185 oxide
region   num=11  x.min=2.135   x.max=2.27   y.min=6.58   y.max=6.715  z.min=0.04   z.max=0.185 oxide
region   num=12  x.min=0.135   x.max=2.135  y.min=6.5    y.max=6.58   z.min=0      z.max=0.04  material=Air
region   num=13  x.min=0.135   x.max=2.135  y.min=6.5    y.max=6.715  z.min=0.04   z.max=0.185 material=Air
region   num=14  x.min=0.215   x.max=2.055  y.min=6.485  y.max=6.5    z.min=0      z.max=0.04  oxide
region   num=15  x.min=0.135   x.max=2.135  y.min=6.58   y.max=6.595  z.min=0.015  z.max=0.025 oxide
region   num=16  x.min=0.135   x.max=2.135  y.min=6.7    y.max=6.715  z.min=0.015  z.max=0.025 oxide
region   num=17  x.min=0.135   x.max=2.135  y.min=6.58   y.max=6.715  z.min=0      z.max=0.015 oxide
region   num=18  x.min=0.135   x.max=2.135  y.min=6.58   y.max=6.715  z.min=0.025  z.max=0.04  oxide
#
#*********** define the electrodes ****************************************************
# #1-GATE #2-DRAIN #3-SOURCE  #4-BODY
#
```

```
electrode  name=gate          x.min=0         x.max=0.135    y.min=6.58   y.max=6.715 z.min=0 z.max=0
electrode  name=drain         x.min=1.76      x.max=2.055    y.min=2.83   y.max=6.485 z.min=0 z.max=0
electrode  name=source        x.min=0.215     x.max=0.51     y.min=2.83   y.max=6.485 z.min=0 z.max=0
electrode  name=substrate     x.min=0.215     x.max=2.055    y.min=0      y.max=1.835 z.min=0 z.max=0
0
#
contact   name=gate       workfunction=4.1
contact   name=drain      workfunction=4.1
contact   name=source     workfunction=4.1
contact   name=substrate workfunction=4.1
#
#*********** define the doping concentrations ************************************************************
#
doping   uniform conc=1e16 p.type    x.min=0.215    x.max=2.055  y.min=1.835  y.max=2.83    z.min=0      z.max=0.04
doping   uniform conc=1e16 p. type   x.min=0.51     x.max=1.76   y.min=2.83   y.max=6.485  z.min=0      z.max=0.04
doping   uniform conc=4e19 n.type    x.min=0        x.max=0.135  y.min=6.58   y.max=6.715  z.min=0      z.max=0.04
doping   uniform conc=4e19 n.type    x.min=2.135    x.max=2.27   y.min=6.58   y.max=6.715  z.min=0      z.max=0.04
doping   uniform conc=4e19 n.type    x.min=0.135    x.max=2.135  y.min=6.595  y.max=6.7    z.min=0.015  z.max=0.025
doping   gauss  n.type    conc=4e19 char=0.4 lat.char=0.15  x.min=0.215   x.max=2.055   y.min=0     y.max=1.835  z.min=0  z.max=0.04
doping   gauss  n.type    conc=4e19 char=0.4 lat.char=0.15  x.min=0.215   x.max=0.51    y.min=2.83  y.max=6.485  z.min=0  z.max=0.04
doping   gauss  n.type    conc=4e19 char=0.4 lat.char=0.15  x.min=1.76    x.max=2.055   y.min=2.83  y.max=6.485  z.min=0  z.max=0.04
#
save       outf=NMOS _0.str
#
```

In the case of $P^+/P/P^+$-type MOSFET

```
doping  uniform conc=1e15 p.type
doping  gauss      p.type     conc=1e19
```

```
#******************  define the interface charge  *****************************
#
interface qf=-1e12 x.min=0.51 x.max=1.76  y.min=6.485 y.max=6.485 z.min=0 z.max=0.04
#
```

In the case of $P^+/P/P^+$-type MOSFET

```
qf=8e9
```

```
#************  define models  ***************************************
#
models auger surfmob aln1=-0.16 aln2=-2.17 aln3=1.07 etan=0.5 alp1=-0.296 \
       alp2=-1.62 alp3=1.02 etap=0.33 mrefn1=481 mrefn2=591 mrefn3=1270 \
       mrefp1=92.8 mrefp2=124 mrefp3=534 fermi bgn print numcarr=1 electrons \
       temperature=300
```

In the case of $P^+/P/P^+$-type MOSFET

```
#
models srh conmob fldmob b.electrons=2 b.holes=1 evsatmod=0 hvsatmod=0 cvt \
       fermi print numcarr=2 temperature=300
#
mobility  bn.cvt=4.75e+07 bp.cvt=9.925e+06 cn.cvt=174000 cp.cvt=884200 \
       taun.cvt=0.125 taup.cvt=0.0317 gamn.cvt=2.5 gamp.cvt=2.2 \
       mu0n.cvt=52.2 mu0p.cvt=44.9 mu1n.cvt=43.4 mu1p.cvt=29 mumaxn.cvt=1417 \
       mumaxp.cvt=470.5 crn.cvt=9.68e+16 crp.cvt=2.23e+17 csn.cvt=3.43e+20 \
       csp.cvt=6.1e+20 alphn.cvt=0.68 alphp.cvt=0.71 betan.cvt=2 betap.cvt=2 \
       pcn.cvt=0 pcp.cvt=2.3e+15 deln.cvt=5.82e+14 delp.cvt=2.0546e+14
```

```
#
solve init
solve prev
#
#****  do IDVG characteristic  ***#
method bicgst  maxtrap=4  trap
solve vdrain=0.001
solve vdrain=0.01
solve vdrain=0.1
solve vdrain=0.2
solve vdrain=0.225
solve vdrain=0.25
solve vdrain=0.275
solve vdrain=0.3
solve vdrain=0.325
solve vdrain=0.35
solve vdrain=0.375
solve vdrain=0.4
#
#ramp the gate and store the results
log outf=NMOS_1.log
#
solve vgate=0       vstep=0.01  vfinal=0.2  name=gate
solve vgate=0.21  vstep=0.1     vfinal=2      name=gate
solve vgate=2.1     vstep=1        vfinal=20    name=gate
#
tonyplot NMOS_1.log -set NMOS_1.set
#
#****** do Id-Vd characteristic  ******
#
#ramp the gate to 15 V
log off
solve init
#
method bicgst  maxtrap=4  trap
solve vgate=0
solve vgate=0.01
solve vgate=0.1
solve vgate=1
solve vgate=10
solve vgate=15
```

```
#
#ramp the drain and store the results
#
log outf=NMOS_2.log master
solve vdrain=0.001
solve vdrain=0.01
#
#method    newton  trap  maxtrap=10 autonr
method  bicgst  maxtrap=4  trap
solve vdrain=0.01 vstep=0.01 vfinal=0.1 name=drain
#
save         outf=RSGMOS-thesis2_1.str
tonyplot NMOS_2.log -set NMOS_2.set
tonyplot NMOS_2.log -set NMOS_3.set
#
quit
```

References

[1] O. Brand and G. K. Fedder, *Advanced micro and nanosystems, Volume 2, CMOS- MEMS,* Weinheim: Wiley-VCH Verlag GmbH & Co. KGaA. 2005.

[2] E. Ollier, L. Duraffourg, MT. Delaye, H. Grange, S. Deneuville, J. Bernos, R. Dianoux, F. Marchi, D. Renaud, T. Baron, P. Andreucci, and P. Robert, “NEMS devices for accelerometers compatible with thin SOI technology,” *2nd IEEE Int. Conf. Nano/Micro Engineered and Molecular Systems,* 2007.

[3] M. Villarroya, E. Figueras, J. Montserrat, J. Verd, J. Teva, G. Abadal, F. P. Murano, J. Esteve, and N. Barniol, “A platform for monolithic CMOS-MEMS integration on SOI wafers,” *J. Micromech. Microeng.*, vol. 16, 2006, pp. 2203-2210.

[4] E. Ollier, L. Duraffourg, E. Colinet, C. Durand, D. Renaud, AS. Royet, P. Renaux, F. Casset, and P. Robert, “Lateral MOSFET transistor with movable gate for NEMS devices compatible with “In-IC” integration,” *3rd IEEE Int. Conf. Nano/Micro Engineered and Molecular Systems,* 2008, pp. 764-769.

[5] H. Mizuta, M. A. G. Ramirez, F. A. Hassani, M. A. Ghiass, Y. Tsuchiya, T. Nagami, B. Pruvost, J. Ogi, S. Sawai, S. Oda, and M. Okamoto, “Multi-scale simulation of hybrid silicon nano-electromechanical (NEM) information devices,” *8th Int. Conf. Global Research and Education Inter-Academia*, 2009.

[6] H. F. Dadgour and K. Banerjee, “Design and analysis of hybrid NEMS-CMOS circuits for ultra low-power applications,” *Design Automation Conf.*, 2007.

[7] H. Kam, D. T. Lee, R. T. Howe, and T. J. King, “A new nano-electro-mechanical field effect transistor (NEMFET) design for low-power electronics,” *IEEE Int. Electron Devices Meeting,* 2005.

[8] H. F. Dadgour and K. Banerjee, “Hybrid NEMS-CMOS integrated circuits: a novel strategy for energy-efficient designs,” *IET Comput. Digit. Tech.*, vol. 3, pp. 593-608, 2009.

[9] M. Liao, S. Hishita, E. Watanabe, S. Koizumi, and Yasuo Koide, “Suspended single-crystal diamond nanowires for high-performance nanoelectromechanical switches,” *Adv. Mater.*, vol. 22, pp. 5393-5397, 2010.

[10] X. Wang, S. Narasimhan, A. Krishna, F. G. Wolff, S. Rajgopal, T. -H, Lee, M. Mehregany, and S. Bhunia, “High-temperature (>500°C) reconfigurable computing using

silicon carbide NEMS switches," *Design, Automation and Test in Europe Conf. and Exhibition*, 2011.

[11] K. Alzoubi, D. G. Saab, S. Han, and M. Tabib-Azar, "Complementary nano-electro-mechanical switch for ultra-low-power applications: Design and modeling," *12th Int. Symp. Quality Electronic Design*, 2011, pp. 728-735.

[12] N. Abelé, R. Fritschi, K. Boucart, F. Casset, P. Ancey, and A.M. Ionescu, "Suspended-gate MOSFET: Bringing new MEMS functionality into solid-state MOS transistor," *IEDM Tech. Digest.*, 2005, pp. 479-481.

[13] B. Pruvost, H. Mizuta, and S. Oda, "3-D Design and analysis of functional NEMS-gate MOSFETs and SETs," *IEEE Trans. Nanotechnol.*, vol. 6, no. 2, 2007.

[14] K. Akarvardar, C. Eggimann, D. Tsamados, Y. S. Chauhan, G. C. Wan, A. M. Ionescu, R. T. Howe, and H. -S. Philip Wong, "Analytical modeling of the suspended-gate FET and design insights for low-power logic," *IEEE Trans. Electron Dev.*, vol. 55, no. 1, pp. 48-59, 2008.

[15] Y. Tsuchiya, K. Takai, N. Momo, T. Nagami, S. Yamaguchi, T. Shimada, H. Mizuta, and S. Oda, "High-speed and non-volatile nano electro-mechanical memory incorporating Si quantum dots," *27th Int. Conf. the Physics of Semiconductors,* 2005, pp. 1589-1590.

[16] Y. Tsuchiya, K. Takai, N. Momo, T. Nagami, H. Mizuta, and S. Oda, "Nanoelectromechanical nonvolatile memory device incorporating nanocrystalline Si dots," *J. Appl. Phys.*, vol. 100, 2006.

[17] T. Nagami, Y. Tsuchiya, K. Uchida, H. Mizuta, and S. Oda, "Scaling analysis of nanoelectromechanical memory devices," *Jpn. J. Appl. Phys.*, vol. 49, pp. 044304-1-5, 2010.

[18] M.A. Garcia-Ramirez, Y. Tsuchiya, and H. Mizuta, "Hybrid circuit analysis of a suspended gate silicon nanodot memory (SGSNM) cell," *Microelectron. Eng.*, vol. 87, pp. 1284-1286, 2010.

[19] X. Han, W. Wu, J. Fan, G. Yan, and Y. Hao, "Modeling of nano-resonator testing system by lumped parameter method," *8th Int. Conf. Solid-State and Integrated Circuit Technology,* 2006, pp. 1404-1406.

[20] B. -C. Serban, C. Cobianu, M. N. Mihaila, and V. -G. Dumitru, "Functionalized monolayers for carbon dioxide detection by a resonant nanosensor," U.S. Patent 20110116974, 2011.

[21] S. T. Bartsch, D. Grogg, A. Lovera, D. Tsamados, and A. M. Ionescu, "Very high frequency double-ended tuning fork nano-mechanical FIN-FET resonator," *16th Int. Conf. Solid-State Sensors, Actuators and Microsystems,* 2011, pp. 938-941.

[22] S. -C. Wang, Y. -C. Chang, D. -H. Lien, T. Hsu, and C. -S. Chang, “Resonance frequency shift of a carbon nanotube with a silver nanoparticle adsorbed at various positions,” *Appl. Phys. Lett.*, vol. 97, pp. 133105-1-3, 2010.

[23] J. Arcamone, G. Rius, G. Abadal, J. Teva, N. Barniol, and F. Pe´rez-Murano, “Micro/nanomechanical resonators for distributed mass sensing with capacitive detection,” *Microelectron. Eng.*, vol. 83, pp. 1216-1220, 2006.

[24] S. Jun, “Femtonewton force sensing using SiC nanoelectromechanical resonance at room temperature in moderate condition,” *7th Int. Workshop on Functional and Nanostructured Materials*, 2010, pp. 61-63.

[25] A. K. Naik, M. S. Hanay, W. K. Hiebert, X. L. Feng, and M. L. Roukes, “Towards single-molecule nanomechanical mass spectrometry,” *Nat. Nanotechnol.*, vol. 4, pp. 445-450, 2009.

[26] J. Verd, A. Uranga, G. Abadal, J. Teva, and F. Torres, F. Pérez-Murano, J. Fraxedas, J. Esteve, and N. Barniol, “Monolithic mass sensor fabricated using a conventional technology with attogram resolution in air conditions, ” *Appl. Phys. Lett.*, vol. 91, pp. 013501-1-3, 2007.

[27] J. Teva, G. Abadal, F. Torres, J. Verd, F. Pe´rez-Murano, and N. Barniol, “A femtogram resolution mass sensor platform based on SOI electrostatically driven resonant cantilever. Part II: Sensor calibration and glycerine evaporation rate measurement,” *Ultramicroscopy*, vol. 106, pp. 808-814, 2006.

[28] H. Mizuta, M. Garcia Ramirez, F. A. Hassani, M. A. Ghiass, N. Kalhor, Z. Moktadir, Y. Tsuchiya, S. Sawai, J. Ogi, and S. Oda, “Scaled silicon nanoelectromechanical (NEM) hybrid systems,” *Int. Conf. Solid-State and Integrated Circuit Technology*, 2010.

[29] F. A. Hassani, C. Cobianu, S. Armini, V. Petrescu, P. Merken, D. Tsamados, A. M. Ionescu, Y. Tsuchiya, and H. Mizuta, “Design and analysis of an in-plane resonant nano-electro-mechanical sensor for sub-attogram-level molecular mass-detection,” *Int. Conf. Solid State Devices and Materials*, 2009.

[30] F. A. Hassani, C. Cobianu, S. Armini, V. Petrescu, P. Merken, D. Tsamados, A.M. Ionescu, Y. Tsuchiya, and H. Mizuta, “Numerical analysis of zeptogram/Hz-level mass responsivity for in-plane resonant nano-electro-mechanical sensors,” *Microelectron. Eng.*, vol. 88, pp. 2879-2884, 2011.

[31] C. Cobianu, B. Serban, M. Mihaila, V. Dumitru, F. A. Hassani, Y. Tsuchiya, H. Mizuta, V. Cherman, I. De Wolf, V. Petrescu , J. Santana, C. Dupré, E. Ollier, T. Ernst, P. Andreucci, L. Duraffourg, D. Tsamados, and A. M. Ionescu, “Nano-scale resonant sensors for gas and bio detection: Expectations and challenges,” *Int. Semiconductor Conf.*, 2009, pp. 259-262.

[32] http://www.nemsic.org/

[33] J. L. Arlett, E. B. Myers, and M. L. Roukes, “Comparative advantages of mechanical biosensors,” *Nat. Nanotechnol.*, vol. 6, pp. 203-215, 2011.

[34] J. K. Hart and K. Martinez, “Environmental sensor networks: A revolution in the earth system science?,” *Earth-Sci. Rev.*, vol. 78, pp. 177-191, 2006.

[35] W. Tsujita, S. Kaneko, T. Ueda, H. Ishida, and T. Moriizumi, “Sensor-based air-pollution measurement system for environmental monitoring network,” *12th Int. Conf. Solid State Sensors, Actuators and Microsystem*, 2003, pp. 544-547.

[36] S. Marian, D. Tsiulyanu, T. Marian, and H.-D. Liess, “Chalcogenide-based chemical sensors for atmospheric pollution control,” *Pure Appl. Chem.*, vol. 73, no. 12, pp. 2001-2004, 2001.

[37] C. Durand, F. Casset, P. Ancey, F. Judong, A. Talbot, R. Quenouille`re, D. Renaud, S. Borel, B. Florin, and L. Buchaillot, “Silicon on nothing MEMS electromechanical resonator,” *Microsyst. Technol.*, vol. 14, pp. 1027-1033, 2008.

[38] Y. T. Yang, C. Callegari, X. L. Feng, K. L. Ekinci, and M. L. Roukes, “Zeptogram-scale nanomechanical mass sensing,” *Nano Lett.*, vol. 6, no. 4, 2006.

[39] K. L. Ekinci, Y. T. Yang, and M. L. Roukes, “Ultimate limits to inertial mass sensing based upon nanoelectromechanical systems,” *J. Appl. Phys.*, vol. 95, no. 5, 2004.

[40] K. L. Ekinci and M. L. Roukes, “Nanoelectromechanical systems,” *Rev. Sci. Instrum.*, vol. 76, pp. 061101-1-11, 2005.

[41] M. Li, H. X. Tang, and M. L. Roukes, “Ultra-sensitive NEMS-based cantilevers for sensing, scanned probe and very high-frequency applications,” *Nat. Nanotechnol.*, vol. 2, pp. 144-120, 2007.

[42] K. Jensen, K. Kim, and A. Zettl, “An atomic-resolution nanomechanical mass sensor,” *Nat. Nanotechnol.*, vol. 3, pp. 533-537, 2008.

[43] B. Ilic, H. G. Craighead, S. Krylov, W. Senaratne, C. Ober, and P. Neuzil, “Attogram detection using nanoelectromechanical oscillators,” *J. Appl. Phys.*, vol. 95, no. 7, pp. 3694-3703, 2004.

[44] E. Mile, G. Jourdan, I. Bargatin, S. Labarthe, C. Marcoux, P. Andreucci1 S. Hentz, C. Kharrat, E. Colinet, and L. Duraffourg, “In-plane nanoelectromechanical resonators based on silicon nanowire piezoresistive detection,” *Nanotechnol.*, vol. 21, 2010.

[45] J. Arcamone, G. Rius, G. Abadal, J. Teva, N. Barniol, and F. Pe´rez-Murano, “Micro/nanomechanical resonators for distributed mass sensing with capacitive detection,” *Microelectron. Eng.*, vol. 83, pp. 1216-1220, 2006.

[46] N. Abelé, K. Séguéni, K. Boucart, F. Casset, B. Legrand, L. Buchaillot, P. Ancey, and A. M. Ionescu, “Ultra-low voltage MEMS resonator based on RSG-MOSFET,” *19th IEEE Int. Conf. Micro Electro Mechanical Systems*, 2006, pp. 882-885.

[47] N. Abelé, “Design and fabrication of suspended-gate MOSFETs for MEMS resonator, switch and memory applications,” PhD Dissertation, School of engineering Institute of Microelectronics and Microsystems (IMM) Electronics Laboratories (LEG) and Center of MicroNano Technology (CMI), 2007.

[48] A. M. Ionescu, V. Pott, R. Fritschi, K. Banerjee, M. J. Declercq, P. Renaud, C. Hibert, P. Fluckiger, and G. A. Racine, “Modeling and design of a low-voltage SOI suspended-gate MOSFET (SG-MOSFET) with a metal-over-gate architecture,” *Proc. the Int. Symp. Quality Electronic Design*, 2002.

[49] http://www.comsol.com/

[50] Y. A. Pashkin, T. F. Li, J. P. Pekola, O. Astafiev, D. A. Knyazev, F. Hoehne, H. Im, Y. Nakamura, and J. S. Tsai, “Detection of mechanical resonance of a single-electron transistor by direct current,” *Appl. Phys. Lett.*, vol. 96, pp. 263513-1-3, 2010.

[51] M.A. Garcia-Ramirez, H. Yoshimura, Y. Tsuchiya, and H. Mizuta, “Suspended gate silicon nanodot memory,” *ESSDERC/CIRC Fringe*, 2008.

[52] E. Colinet, C. Durand, L. Duraffourg, P. Audebert, G. Dumas, F. Casset, E. Ollier, P. Ancey, J. -F Carpentier, L. Buchaillot, and A. M. Ionescu, “Ultra-sensitive capacitive detection based on SGMOSFET compatible with front-end CMOS process,” *IEEE J. of Solid-state Circuits*, vol. 44, pp. 247-257, 2009.

[53] F. R. R. Teles and L. P. Fonseca, “Review trends in DNA biosensors,” *Talanta*, vol. 77, no. 2, pp. 606-623, 2008.

[54] R. Bashir, “BioMEMS: state-of-the-art in detection, opportunities and prospects,” *Adv. Drug Deliver. Rev.*, vol. 56, pp. 1565-1586, 2004.

[55] M. Kutz, “Bio Micro Electro Mechanical Systems- BioMEMS Technologies,” in *Biomedical Engineering and Design Handbook, Volume 1, Fundamentals*, 2nd ed. McGraw-Hill, Inc., 2009.

[56] R. Bashir, S. Wereley, and M. Ferrari, “BioMEMS for cellular manipulation and analysis,” in *BioMEMS and biomedical nanotechnology*, New York, NY: Springer Science+Business Media LLC, 2006.

[57] D. R. Theavenot, K. Toth, R. A. Durst, and G. S. Wilson, “Electrochemical biosensors: Recommended definitions and classifications,” *Pure Appl. Chem.*, vol. 71, no. 12, pp. 2333-2348, 1999.

[58] M. Zourob, S. Elwary, and A. Turner, “Label-free microbial biosensors using molecular nanowire transducers,” in *Principles of bacterial detection- Biosensors, Recognition Receptors and Microsystems*, New York, NY: Springer Science+Business Media LLC, 2008.

[59] B. R. Eggins, *Chemical Sensors and Biosensors*, Chichester: John Wiley & Sons Ltd, 2002.

[60] D. van der Voort, C. A. McNeil, R. Renneberg, J. Korf, W. T. Hermens, and J. F. C. Glatz, “Biosensors: basic features and application for fatty acid-binding protein, an early plasma marker of myocardial injury”, *Sensor. Actuator. B*, vol. 105, pp. 50-59, 2005.

[61] International Union of Pure and Applied Chemistry, *Compendium of Chemical Terminology*, version 2.3, 2011.

[62] K. Sun, M. M. A. Hakim, M. Lombardini, M. R. R. d. Planque, H. Morgan, P. L. Roach, D. E. Davis, P. Howarth, P. Ashburn, “Sensors for chemical detection based on top-down fabricated polycrystalline silicon nanowires,” *NanoBioTech*, 2010.

[63] J. Fritz, E. B. Cooper, S. Gaudet, P. K. Sorger, and S. R. Manalis, “Electronic detection of DNA by its intrinsic molecular charge,” *Proc. Natl. Acad. Sci. USA*, vol. 99, no. 22, pp. 14142-14146, 2002.

[64] J. Comley, “Progress in the implementation of label-free detection- part 1: Cell-beased assays,” *Drug Discovery World*, 2008, pp. 77-88.

[65] A. Hierlemann and H. Baltes, “CMOS-based chemical microsensors,” *Analyst*, vol. 128, pp. 15-28, 2003.

[66] D. Lange, C. Hagleitner, A. Hierlemann, O. Brand, and H. Baltes, “Complementary metal oxide semiconductor cantilever arrays on a single chip: mass-sensitive detection of volatile organic compounds,” *Anal. Chem.*, vol. 74, no. 13, 2002.

[67] K. Ramanathan and B. Danielsson, “Principles and applications of thermal biosensors,” *Biosens. Bioelectron.*, vol. 16, pp. 417-423, 2001.

[68] L. Wang, D. M. Sipe, Y. Xu, and Q. Lin, “A MEMS thermal biosensor for metabolic monitoring applications,” *J. Microelectromech. S.*, vol. 17, no. 2, pp. 318-327, 2008.

[69] H. Fujita, *Introduction to Micro and Nano Technology Machine (in Japanese)*, Kogyo Chosakai Publishing, ISBN 4-7693-7117-9, 2003.

[70] H. Campanelle, “Sensor applications,” in *Acoustic wave and electromechanical resonators, concept to key applications*, Norwood, MA: Artech house, 2010.

[71] S. Mandal, J. M. Goddard, and D. Erickson, “A multiplexed optofluidic biomolecular sensor for low mass detection,” *Lab Chip*, vol. 9, pp. 2924-2932, 2009.

[72] C. Li, Y. Liu, L. Li, Z. Du, S. Xu, M. Zhang, X. Yin, and T. Wang, “A novel amperometric biosensor based on NiO hollow nanospheres for biosensing glucose,” *Talanta*, vol. 77, no. 1, pp. 455-459, 2008.

[73] N. Liu, G. J. Li, S. F. Liu, and S. S. Zhang, “Electrochemical DNA biosensor for the detection of interaction between di[azino-di(5,6-azafluorene)-κ^2-NN']dichlormanganous and DNA,” *Sensor. Actuator. B*, vol. 133, pp. 582-587, 2008.

[74] J. A. Lee, S. Hwang, J. Kwak, S. Park, S. S. Lee, and K. C. Lee, “An electrochemical impedance biosensor with aptamer-modified pyrolyzed carbon electrode for label-free protein detection,” *Sensors. Actuator. B*, vol. 129, pp. 372-379, 2008.

[75] J. Kumar, S. K. Jha, and S. F. D'Souza, “Optical microbial biosensor for detection of methyl parathion pesticide using Flavobacterium sp. whole cells adsorbed on glass fiber filters as disposable biocomponent,” *Biosens. Bioelectron.*, vol. 21, pp. 2100-2105, 2006.

[76] S. H. Chen, V. C. H. Wu, Y. C. Chuang, and C. S. Lin, “Using oligonucleotide-functionalized Au nanoparticles to rapidly detect foodborne pathogens on a piezoelectric biosensor,” *J. of Microbiol. Meth.*, vol. 73, pp. 7-17, 2008.

[77] K. Ramanathan, B. R. Jönsson, and B. Danielsson, “Sol-gel based thermal biosensor for glucose,” *Analytica Chimica Acta*, vol. 427, pp. 1-10, 2001.

[78] A. Tsortos, G. Papadakisa, and E. Gizeli, “Shear acoustic wave biosensor for detecting DNA intrinsic viscosity and conformation: A study with QCM-D,” *Biosens. Bioelectron.*, vol. 24, pp. 836-841, 2008.

[79] J. D. Kittle, “Quartz crystal microbalance studies of Dimethyl Methylphosphonate sorption into Trisilanolphenyl-Poss films,” M. Sc. Thesis, Virginia Polytechnic Institute and State University, 2006, pp. 29-39.

[80] F. Höök and M. Rudh, “Quartz crystal microbalances (QCM) in biomacromolecular recognition,” *J. BTi Molecular Biology*, 2005.

[81] Y. Okahata, M. Kawase, K. Niikura, F. Ohtake, H. Furusawa, and Y. Ebara, “Kinetic measurements of DNA hybridization on an oligonucleotide-immobilized 27-MHz quartz crystal microbalance,” *Anal. Chem.*, vol. 70, pp. 1288-1296, 1998.

[82] N. Gufflet. *Quartz Crystal Resonators- Brief Overview.* KVG Quartz Crystal Technology GmbH, 2011.

[83] Y. Okahata, Y. Matsunobu, K. Ijiro, M. Mukae, A. Murakami, and K. Makinolb, “Hybridization of nucleic acids immobilized on a quartz crystal microbalance,” *J. Am. Chem. Soc.*, vol. 114, pp. 8299-8300, 1992.

[84] Y. Okahata, J. Yuyama, A. Itou and M. Nakamura, “QCM bio-sensor,” *ULVAC Technical J. (English)*, no. 63E, 2006.

[85] http://www.initium2000.com/en/products_qn.html

[86] A. Sellborn, M. Andersson, C. Fant, C. Gretzer, and H. Elwing, “Methods for research on immune complement activation on modified sensor surfaces,” *Colloid. Surface. B*, vol. 27, pp. 295-301, 2003.

[87] http://www.qsense.com/q-sense-e4/

[88] http://www.qcmresearch.com/mk21.htm

[89] X. L. Feng, R. He, P. Yang, and M. L. Roukes, “Very high frequency silicon nanowire electromechanical resonators,” *Nano Lett.*, vol. 7, no. 7, pp. 1953-1959, 2007.

[90] C. T. -C. Nguyen, “Vibrating RF MEMS overview: applications to wireless communications,” *Proc. SPIE: Micromachining and Microfabrication Process Technology*, 2005, vol. 5715, pp. 11-25.

[91] N. Abele´, V. Pott, K. Boucart, F. Casset, K. Se´gue´ni, P. Ancey, and A.M. Ionescu, “Comparison of RSG-MOSFET and capacitive MEMS resonator detection,” *Electron. Lett.*, vol. 41, no. 41, 2005.

[92] H. C. Nathanson, W. E.Newell, R. A.Wickstrom, and J. R. J. Davis, “The resonant gate transistor,” *IEEE Trans. on Electron Dev.*, vol. 14, 117-133, 1967.

[93] R. W. Anderson, “S-Parameter techniques for faster, more accurate network design,” *Hewlett Packard J.*, vol. 18, no. 6, 1967.

[94] J. -M. Kang, “Piezoelectric MEMS resonator characterization and filter design,” B. Sc. and M. Sc. Thesis, Massachusetts Institute of Technology, 2004, pp. 31-36.

[95] R. Ludwig and P. Bretchko, “Single- and multiple networks,” in *RF circuit design: Theory and applications*, NJ: Prentice-Hall, Inc., 2000.

[96] S. T Bartsch, D. Grogg, A. Lovera, D. Tsamados, S. Ayoz, and A. M. Ionescu, “Resonant-body Fin-FETs with sub-nW power consumption,” *Int. IEEE Electron Devices Meeting*, 2010, pp. 7.6.1-7.6.4.

[97] A. Arun, S. Campidelli, A. Filoramo, V. Derycke, P. Salet, A. M. Ionescu, and M. F. Goffman, “SWNT array resonant gate MOS transistor,” *Nanotechnology*, vol. 22, pp. 1-5, 2011.

[98] R. Zhu, D. Wang, S. Xiang, Z. Zhou, and X. Ye, “Piezoelectric characterization of a single zinc oxide nanowire using a nanoelectromechanical oscillator,” *Nanotechnology*, vol. 19, pp. 1-5, 2008.

[99] D. M. Pozar, “Microwave resonators,” in *Microwave Engineering*, 3rd ed., NJ: John Wiley & Sons, Inc., 2005.

[100] L. A. Callaghan, “Design, fabrication, and characterization of beam- supported aluminium nitride thin film bulk acoustic resonators,” PhD Dissertation, University of California, Santa Barbara, 2005.

[101] T. Yonekura, “High-frequency impedance analyzer,” *Hewlett Packard J.*, pp. 67-74, 1994.

[102] L. Martens, “High-frequency measurement techniques,” in *High-Frequency Characterization of Electronic Packaging*, Springer, 1998.

[103] *About Lock-In Amplifiers*. Stanford research systems, Application note #3, [Online]. Available: http://www.thinksrs.com.

[104] J. H. Scofield, “A Frequency-domain description of a lock-in amplifier,” *Am. J. Phys.*, vol. 62, no. 2, pp. 129-133, 1994.

[105] A. N. Clenland and M. L. Roukes, “Fabrication of high frequency nanometer scale mechanical resonators from bulk Si crystals,” *Appl. Phys. Lett.*, vol. 69, pp. 2653-2655, 1996.

[106] M. Al_Khusheiny and B. Majlis, “Aluminum based two-port-clamped-clamped resonators,” *Int. Conf. Semiconductor Electronics*, 2006, pp. 188-192.

[107] S. S. Rao, “Continuous systems,” in *Mechanical Vibrations*, 4th ed. Upper Saddle River, NJ: Pearson Education, Inc., Pearson Prentice Hall, 2004, p. 141 and p. 611.

[108] S. Pacheco, P. Zurcher, S. Young, D. Weston, and W. Dauksher, “RF MEMS resonator for CMOS back-end-of-line integration,” *Topical Meeting on Silicon Monolithic Integrated Circuits in RF Systems*, 2004.

[109] Z. Haoa, A. Erbil, and F. Ayazi, “An analytical model for support loss in micromachined beam resonators with in-plane flexural vibrations,” *Sensor. Actuator. A*, vol. 109, pp. 156–164, 2003.

[110] K. L. Ekinci, X. M. Huang, and M. L. Roukes, “Fabrication of high frequency nanometer scale mechanical resonators from bulk Si crystals,” *Appl. Phys. Lett.*, vol. 84, no. 22, pp. 2653-2655, 2004.

[111] K. L. Ekinci, X. M. H. Huang, and M. L. Roukes, “Ultrasensitive nanoelectromechanical mass detection,” *Appl. Phys. Lett.*, vol. 84, no. 22, pp. 4469-4471, 2004.

[112] F. D. Bannon, J. R. Clark, and C. T. -C. Nguyen, “High-Q HF microelectromechanical filters,” *IEEE J. of Solid-State Circuits*, vol. 35, no. 4, pp. 512-526, 2000.

[113] N. Lobontin and E. Garcia, “Static response of MEMS,” in *Mechanics of Microelectromechanical Systems*, Springer Science+Business Media, Inc., 2005.

[114] B. Chouvion, “Vibration transmission and support loss in MEMS sensors,” PhD Dissertation, University of Nottingham, 2010, pp. 1-25.

[115] R. Lifshitz and M. L. Roukes “Thermoelastic damping in micro- and nanomechanical systems,” *Phys. Rev. B,* vol. 61, no. 8, pp. 5600-5609, 2000.

[116] R. Lifshitz, “Phonon-mediated dissipation in micro- and nano-mechanical systems,” *Physica B,* vol. 316-317, pp. 397-399, 2002.

[117] G. D. Cole, I. Wilson-Rae, K. Werbach1, M. R. Vanner, and M. Aspelmeyer, “Phonon-tunnelling dissipation in mechanical resonators,” *Nat. Communication*, vol. 2, no. 231, pp. 1-8, 2011.

[118] A. Berny. *Substrate Effects in Squeeze Film Damping of Lateral Parallel-Plate Sensing MEMS Structures*. [Online]. Available: http://www-bsac.eecs.berkeley.edu/~pister/245/project/.

[119] J. Brotz, “Damping in CMOS-MEMS resonators,” M. Sc. Thesis, Carnegie Mellon University, 2004.

[120] T. Veijola, H. Kuisma, J. Lahdenpera, and T. Ryhanen, “Equivalent-circuit model of the squeezed gas film in a silicon accelerometer,” *Sensor. Actuator. A*, vol. A48, pp. 239-248, 1995.

[121] S. Beeby, G. Ensell, M. Kraft, and N. White, “Inertial sensors,” in *MEMS Mechanical Sensors*, Norwood, MA: Artech House, Inc., 2004.

[122] G. Stemme, “Resonant silicon sensors,” *J. Micromech. Microeng.*, vol. 1, pp. 113-125, 1991.

[123] W. -T. Hsu, J. R. Clark, and C. T. -C. Nguyen, “Q-optimized lateral free-free beam micromechanical resonators,” *Dig. Tech. Papers, 11th Int. Conf. Solid-State Sensors and Actuators*, 2001, pp. 1110-1113.

[124] I. Wilson-Rae, “Intrinsic dissipation in nanomechanical resonators due to phonon tunnelling,” *Physical Review B*, vol. 77, 245418 (31pp), 2008.

[125] http://www.coventor.com/

[126] K. Wang, A. -C. Wong, and C. T. -C. Nguyen, “VHF free–free beam high-Q micromechanical resonators,” *J. Microelectromech. S.*, vol. 9, no. 3, pp. 347-360, 2000.

[127] C. G. Courcimault and M. G. Allen, “High-Q mechanical tuning of MEMS resonators using a metal deposition-annealing technique,” *13th Int. Conf. Solid-State Sensors, Actuators and Microsystems*, 2005, pp.875-878.

[128] A. K. Pandey, K. P. Venkatesh, and R. Pratap, "Effect of metal coating and residual stress on the resonant frequency of MEMS resonators," *Sādhanā*, vol. 34, no. 4, pp. 651-661, 2009.

[129] T. Toriyama, Y. Tanimoto, and S. Sugiyama, "Characteristics of silicon nano wire as piezoresistor for nano electro mechanical systems," *14th IEEE Int. Conf. Micro Electro Mechanical Systems*, 2001, pp. 305-308.

[130] K. Yamazaki, S. Etaki, H. S. J. van der Zant, and H. Yamaguch, "Piezoresistance of suspended InAs/AlGaSb heterostructure nanobeam," *J. of Crys. Growth*, vol. 301-302, pp. 897-901, 2007.

[131] J. H. Kim, K. T. Park, H. C. Kim, and K. Chun, "Fabrication of a piezoresistive pressure sensor for enhancing sensitivity using silicon nanowire," *Int. Conf. Solid-State Sensors, Actuators and Microsystems*, 2009, pp. 1936-1939.

[132] R. He and P. Yang, "Giant piezoresistance effect in silicon nanowires," *Nat. Nanotechnol.*, vol. 1, pp. 42-46, 2006.

[133] H. P. Erickson, "Size and shape of protein molecules at the nanometer level determined by sedimentation, gel filtration, and electron microscopy," *Biological Procedures Online*, vol. 11, no. 1, 2009, pp. 32-51, 2009.

[134] X. L. Feng, C. J. White, A. Hajimiri, and M. L. Roukes, "A self-sustaining ultrahigh-frequency nanoelectromechanical oscillator," *Nat. Nanotechnol.*, vol. 3, pp. 342-346, 2008.

[135] Y. T. Yang, C. Callegari, X. L. Feng, K. L. Ekinci, and M. L. Roukes, "Zeptogram-Scale nanomechanical mass sensing," *Nano Lett.*, vol. 6, no. 4, pp. 583-586, 2006.

[136] H. B. Peng, C.W. Chang, S. Aloni, T. D. Yuzvinsky, and A. Zettl, "Ultrahigh frequency nanotube resonators," *Phys. Rev. Lett.*, vol. 97, pp. 087203-1-4, 2006.

[137] H. G. Craighead, "Nanoelectromechanical systems," *Science*, vol. 290, no. 5496, pp. 1532-1535, 2000.

[138] G. Abadal, Z. J. Davis, B. Helbo, X. Borrisé, R. Ruiz, A. Boisen, F. Campabadal, J. Esteve, E. Figueras, F. Pérez-Murano, and N. Barniol, "Electromechanical model of a resonating nano-cantilever-based sensor for high resolution and high-sensitivity mass detection", *Nanotechnol.*, vol. 12, pp. 100-104, 2001.

[139] J. H. Cho, W. Kim, J. S. Shin, I.S. Song, X.M.H. Huang, and S.C. Jun, "Femtonewton force sensing using SiC nanoelectromechanical resonance at room temperature in moderate condition", *7th Int. Workshop on Functional and Nanostructured Materials*, 2010, pp. 61-63.

[140] J. Ogi, Y. Tsuchiya, S. Oda, and H. Mizuta, “Single-electron tunnelling via quantum dot cavities built on a silicon suspension nanobridge,” *IEEE Silicon Nanoelectronics Workshop*, 2006, pp. 123-124.

[141] A. Witvrouw, P. De Moor, A. Verbist, C. A. Van Hoof, H. Bender, and C. Baert, “Comparison between wet HF etching and vapor HF etching for sacrificial oxide removal,” *Proc. SPIE,* 2000, vol. 4174, pp. 130-141.

[142] http://www.silvaco.com/

[143] A. E. Grigorescu and C. W. Hagen, “Resists for sub-20-nm electron beam lithography with a focus on HSQ: state of the art,” *Nanotechnol.*, vol. 20, 292001 (31pp), 2009.

[144] Y. K. Siew, G. Sarkar, X. Hu, J. Hui, A. See, and C. T. Chuab, “Thermal curing of hydrogen silsesquioxane,” *J. Electrochem. Soc.*, vol. 147, no. 1, pp. 335-339, 2000.

[145] C. -C. Yang and W. -C. Chen, “The structures and properties of hydrogen silsesquioxane (HSQ) films produced by thermal curing,” *J. Mater. Chem.*, vol. 12, 2002, pp. 1138-1141.

[146] K. A. Lister, B. G. Casey, P. S. Dobson, S. Thoms, D. S. Macintyre, C. D. W. Wilkinson, and J. M. R. Weaver, “Pattern transfer of a 23 nm-period grating and sub-15 nm dots into CVD diamond,” *Microelectron. Eng.*, vol. 73-74, pp. 319-322, 2004.

[147] M. L. Reed and J. D. Plummer, “Chemistry of Si-SiO_2 interface trap annealing,” *J. Appl. Phys.*, vol. 63, no. 12, pp. 5776-5793, 1988.

[148] K. R. Williams and R. S. Muller, “Etch rates for micromachining processing,” *J. Microelectromech. S.*, vol. 5, no. 4, pp. 256-269, 1996.

[149] J. Buhlery, F. -P. Steiner, and H. Baltes, “Silicon dioxide sacrificial layer etching in surface micromachining,” *J. Micromech. Microeng.*, vol. 7, pp. R1-R13, 1997.

[150] http://www.cadence.com/

[151] D. J. Black, J. Mattzela, Tsung-ta Ho, Y. Wang, K-K Lew, J. Redwing, and T. S. Mayer, “Plasma-assisted oxidation for surface passivation of silicon nanowires,” *NSF EE REU PENN STATE Annu. Research J.*, vol. 2, pp. 121-128, 2004.

[152] H. H. Bau, N. F. de Rooij, and B. Kloeck, “Piezoresistive sensors,” in *Sensors: A Comprehensive Survey, Volume 7, Mechanical Sensors,* Weinheim: Wiley-VCH Verlag GmbH, 1994.

[153] *Agilent network analyzer basics.* Agilent technologies, Application note, [Online]. Available: http://www.home.agilent.com/

[154] H. C. Card, “Aluminum-silicon schottky barriers and ohmic contacts in integrated circuits,” *IEEE Trans. Electron Dev.*, vol. ED-23, no. 6, pp. 538-544, 1976.

[155] *ISS map 101-190.* Cascade Microtech, [Online]. Available: http://www.cmicro.com/products/calibration-tools/impedance-substrate/

[156] C. Durand, F. Casset, P. Renaux, N. Abelé, B. Legrand, D. Renaud, E. Ollier, P. Ancey, A. M. Ionescu, and L. Buchaillot, “In-plane silicon-on-nothing nanometer-scale resonant suspended gate MOSFET for in-IC integration perspectives,” *IEEE Electron Dev. Lett.*, vol. 29, no. 5, pp. 494-496, 2008.

[157] Y. Tsividis, *Operation and Modeling of the MOS Transistor,* NY: McGraw-Hill, Inc., 1987.

[158] A. Ortiz-Conde, F. J. Garcia Sanchez, J. J. Liou, A. Cerdeira, M. Estrada, and Y. Yued, “A review of recent MOSFET threshold voltage extraction methods,” *Microelectronic. Reliab.*, vol. 42, pp. 583–596, 2002.

[159] http://ecee.colorado.edu/~bart/book/

[160] D. Grogg, M. Mazza, D. Tsamados, and A. M. Ionescu, “Multi-gate vibrating-body field effect transistor (VB-FETs),” *IEEE Int. Electron Devices Meeting*, 2008, pp. 1-4.

[161] S. Middelhoak and S. A. Audet, “Silicon sensors for mechanical signals,” in *Silicon Sensors- Microelectronics and Signal Processing*, London, UK: Academic Press Limited, 1989.

[162] T. L. Waterfall, “Design of piezoresistive MEMS force and displacement sensors,” Master Thesis, Department of Mechanical Engineering, Brigham Young University, 2006.